



Auroral Particle Acceleration at Jupiter

Christopher (Terence Stanley) Lorch, MPhys

Physics: Space and Planetary Physics

Lancaster University

A thesis submitted for the degree of

Doctor of Philosophy

August, 2022

Declaration

I, Christopher T.S. Lorch, declare that this thesis titled “Auroral particle acceleration at Jupiter” and any work presented therein is that of my own. I further confirm that:

- This work was done wholly or mainly while a candidate for a research degree at Lancaster University.
- It is clearly stated in sections of the thesis where any part has previously been submitted for a degree or any other qualification at Lancaster University or any other institution.
- The published work of others used within this thesis is clearly attributed to its respective author/s. With the exception of references to such work, this thesis is entirely my own work.
- Quotes from the published work of others is always and clearly accompanied by a source. With the exception of such quotations, this thesis is entirely my own work.
- I have acknowledged all main sources of help.
- Where the thesis is based on work done by myself jointly with others, I have made clear exactly what was done by others and what I have contributed myself.

Signed: _____

Christopher T.S. Lorch, PhD Candidate

Date: _____

Auroral Particle Acceleration at Jupiter

Christopher (Terence Stanley) Lorch, MPhys.

Space and Plasma Physics Group, Lancaster University

A thesis submitted for the degree of *Doctor of Philosophy*. August, 2022

Abstract

Plasmas naturally occur in our solar system in the form of the Sun, the solar wind, and material within the magnetospheres and ionospheres of planets and satellites. Today, space exploration provides access to ideal natural laboratories, such as Jupiter's unique magnetospheric environment, which provide insights into plasma physics largely irreproducible on Earth.

This thesis begins by outlining fundamental physical concepts needed to understand planetary magnetospheres, before diving into the more subtle and complex details which distinguish Jupiter's magnetosphere from Earth's. The mechanisms resulting in the Jovian magnetosphere-ionospheric coupled system are explained, followed by comparisons of plasma turbulence in Jupiter's, Earth's, and Sun's magnetic environments. This is followed by an overview of the various spacecraft which have visited Jupiter and the instruments that are utilised in this thesis.

Chapter 5 presents work published in Lorch et al. (2020), which investigates equatorial asymmetries in the magnetosphere-ionosphere current system, expanding on previous work with extended magnetic field datasets, new model integration and automated magnetic field signature identification processes. Previously unquantified

height integrated current densities are calculated, and areas where field aligned current topology is equally determined by both radial and azimuthal current divergence are highlighted.

Chapter 6 explores drivers of auroral particle acceleration within the mid-to-high latitude regions of Jupiter's magnetosphere. Lorch et al. (2022) used state-of-the-art Juno magnetometer and plasma data to identify a series of Alfvénic turbulence events which display an energy dissipative spectral index at scales approaching the electron inertial length, which potentially feed energy into wave-particle acceleration mechanisms capable of producing the observed auroral energy flux.

This thesis concludes with a project roadmap aiming to quantify MHD and Alfvénic turbulence within all spatial regions of Jupiter's magnetosphere. This work was initiated but did not reach completion due to the onset of the COVID-19 pandemic.

Acknowledgements

The achievement of the last four years of work, culminated in around 230 pages, is not the product of one person, but the amalgamation of knowledge, experience and support from a mass of individuals for over two and a half decades. To list all those involved in the production of this work would, no doubt, result in an inordinately large page count! That said, there are some special thanks I would like to offer.

First and foremost, the natural world, whose beauty, generosity and mystery enchant those into deepest reverence and awe.

Thank you to Dr. Licia Ray, my supervisor, for the wealth of academic and emotional support over the past 4 years. Your patience and persistence helped shaped me into an actual scientist. From in depth discussion, late night calls with international collaborators, laughing at my extravagant emails/funding applications/feedback, and introducing me to Pho. You have helped me immensely on every bump in the road and I will be sure to approach whatever lies ahead with the same level of empathy (and sass!) you have shown me over the last few years.

Heath and Avril Lorch, who from the beginning have gone above and beyond in encouraging me to keep going, and have helped pull me out of the surfiet of predicaments I have found myself in over the years! Thank you Connor, for being a great friend and brother, and for all the “University Dum-Dum” wisecracks. You only need to read the last chapter.

Thank you to Miss Kelly Harrison, Mr. Richard Jones and Mr. Robert Newsome for shaping my school life and guiding me on the path I have taken. Nathan Jones, for being my rock during difficult times over the years. René Olsen, for our shared experiences and keeping me in high spirits. *Winter's Bane* and *The Peacemakers*, for the great adventures during my write up. In overcoming one of the biggest obstacles in research, I offer my thanks to Alexandra Elbakyan. For providing a seemingly limitless supply of great coffee, food and the occasional procrastination, the staff at the Herbarium, Lancaster. Thank you to my new work colleagues at NPL, for their understanding and support in the final stages of writing up.

Last, but certainly not least, my partner Irene. Thank you for your patience when I was apathetic, supporting me when I was frustrated, and keeping the cat occupied during lengthy Teams meetings. There are very few times in one's life that they find someone so kind and caring. I am truly lucky to have passed this milestone with you at my side. Here's to the next one!

Contents

Declaration	i
Abstract	iii
Acknowledgements	v
List of Figures	xxiv
List of Tables	xxvi
abbreviations	xxvii
1 Space Plasma Physics	1
1.1 Definition of a Plasma	2
1.2 Electric and Magnetic fields	3
1.3 Properties of a Plasma in Electric & Magnetic Fields	5
1.3.1 Kinetic Description	6
1.3.2 Currents in a Plasma	6
1.3.3 Frozen-in Theorem	16
1.3.4 Fluid Description	17
1.3.5 Waves in Plasmas	21
1.4 Conclusion	36
2 Dynamics of the Jovian System	37

2.1	Solar wind and Heliosphere	37
2.2	The Terrestrial Magnetosphere	41
2.2.1	Magnetic reconnection	43
2.3	Jupiter, The Planet	46
2.4	The Jovian Magnetosphere	46
2.4.1	The Galilean Satellites	49
2.4.2	The Plasma Disk	50
2.5	The Terrestrial Ionosphere	53
2.6	The Jovian Ionosphere	57
2.6.1	Jupiter's Auroral Emissions	58
2.7	The M-I Coupled System	62
2.8	Conclusion	64
3	Spatial Distribution of Turbulent Activity	66
3.1	Turbulence in the Solar Wind	69
3.2	Turbulence within the Jovian system	75
3.2.1	Magnetosphere Boundary and Outer region	76
3.2.2	Middle Region	81
3.2.3	Inner Region	86
3.2.4	Polar Region	88
3.2.5	Tail region	93
3.2.6	Conclusion	95
4	Data, Instrumentation and Reference Frames	99
4.1	Spacecraft Instrumentation	99

4.1.1	Magnetometer	100
4.1.2	Electrostatic Analyser	101
4.2	Spacecraft Missions	104
4.2.1	Juno	106
4.2.2	Galileo	109
4.3	Reference Frames	110
4.3.1	Rotation Matrices and Proper Euler Angles	111
4.3.2	System III	112
4.3.3	JSO	115
4.3.4	Mean Field / De Hoffmann-Teller	115
4.3.5	Dynamic Current Disk	116
4.4	Conclusion	118
5	The Structure of the Equatorial Current System	119
5.1	Introduction	119
5.2	Lobe Field Identification from Magnetometer Data	125
5.2.1	Data Selection	125
5.2.2	Current Disk Field Isolation	127
5.3	Methodology	131
5.3.1	Calculation of Magnetodisk Currents and their Divergences . .	131
5.4	Results	136
5.4.1	Height Integrated Current Density	136
5.4.2	Divergence of the Height Integrated Current Density	143
5.5	Discussion	145
5.6	Summary	154

6	Localised Mid-to-High Latitude Alfvénic Turbulence	156
6.1	Introduction	156
6.2	Identification of Events	166
6.3	Energy Regime of Turbulent Events	172
6.4	Discussion and Interpretation	179
6.4.1	Poynting Flux	179
6.4.2	Turbulent Scales	182
6.4.3	Intermittency	185
6.5	Summary	188
7	Future Work and Conclusions	191
7.1	Future work	191
7.1.1	Construction of a Suitable Dataset	191
7.1.2	Numerical Analysis of Wave Evolution	195
7.2	Conclusions	198
A	JRM09 Internal Magnetic Field Model Coefficients	200
	JRM09 Internal Magnetic Field Model Coefficients	201

List of Figures

1.1	The helical motion of a negatively charged particle about the magnetic field. The magnetic field acts as the guiding center of the motion. . .	11
1.2	A Maxwell-Boltzmann distribution for a variety of temperatures. As temperature increases, the mean velocity of the plasma increases, however a wide variety of speeds are still present within the system. .	19
1.3	The phase velocity of the Fast, Slow and Alfvén waves for an electron plasma, displayed as a polar projection. The parameters used in the formation of this figure were: $B = 100 \text{ nT}$, $T = 150 \text{ eV}$, $n = 1000 \text{ m}^{-3}$, and $c_s < v_A$	25
1.4	The perturbation field and associated electric field components for an Alfvén wave. Here, the electric field is represented by green arrows perpendicular to the red magnetic field profile with blue arrows illustrating perturbation vectors. There is a finite component of the perpendicular electric field component parallel to the x-axis. Image Credit: Mottez (2015)	27

1.5	<p>A typical power spectra for a turbulent flow. At low wavenumbers where the power law is less than $-\frac{5}{3}$ energy is supplied to the system. The Kolmogorov regime is located where the power law is $-\frac{5}{3}$, and the energy dissipative regime where the power law is negatively steeper than $-\frac{5}{3}$. Red vertical lines indicate spectral breaks, sharp changes in the gradient which can coincide with a traversal from one regime to the next. The frequency of the spectral breaks can provide information on the plasma mechanism responsible for supplying or dissipating energy from the system.</p>	32
1.6	<p>An example of the modified distribution function following Alfvénic particle acceleration. Electrons with velocities around the Alfvén velocity (black dashed line) are accelerated, leading to a net gain in energy. The dashed red line signifies the portion of the distribution function prior to electron acceleration.</p>	34
2.1	<p>An equatorial projection of the Parker spiral model of the interplanetary magnetic field for varying plasma velocities from (Lhotka et al., 2019). The orbits of Earth, Mars and Jupiter are showed in blue, red and orange respectively. As the interplanetary magnetic field moves radially outward its angle of incidence decreases. For example, the $1,200 \text{ km s}^{-1}$ profile has an almost perpendicular angle of incidence at Earth’s orbit (Blue), but intersects the Jovian orbit at a much shallower angle.</p>	39

2.2	The variation of the solar wind over the solar cycle taken from McComas et al. (2008). The top three panels are polar plots of the solar wind velocity for the three Ulysses orbits. The profile colour denotes the polarity of the IMF, with blue being inward and red being outward. The bottom panel can be used to determine the phase of the solar cycle based off the sunspot number.	40
2.3	A graphical representation of the terrestrial magnetosphere. The dipole geometry of the magnetic field is compressed on the sunward side and elongated on the night side due to the impinging solar wind. Image Credit: ESA/C.T.Russell/ Case (n.d.)	42
2.4	An illustrating of the magnetic reconnection process from Lee et al. (2020)	45
2.5	The flow dynamics of the terrestrial Dungey Cycle as seen from a magnetospheric (left) and ionospheric (right) perspective. Here, (1) the southward solar wind undergoes reconnection with the planetary magnetosphere in the dayside region. (2 - 3) The open magnetic field convects across the polar cap and begins to “pile up” in the nightside magnetosphere. (4) Tail reconnection occurs as magnetic flux increases due to the convection of open field lines, closing the open field lines, (5) ejecting plasmoids downtail and (6) returning the other closed field lines planetward. (7) The planetward flowing field lines convect around the planet, returning to the dayside and beginning the cycle anew. Image Credit: Seki et al. (2015)	45

2.6	An illustration of the Jovian magnetosphere. For scale, the entirety of the terrestrial magnetosphere can fit within the planet Jupiter itself. This illustration demonstrates the distorted nature of Jupiter’s middle magnetosphere when compared with the typical terrestrial example above. The parabolic geometry enforced externally by the solar wind and the extreme extent to which the internal topology is defined by the presence of a current disk (labelled here as the current sheet) is evident to see. One can also notice the opposite polarity of the magnetic field compared with Earth’s. Image Credit: (Bagenal et al., n.d.)	48
2.7	The configuration of the Solar, terrestrial and Jovian magnetosphere. The interaction of the solar wind, coupled with the departure from corotation of the equatorial plasma disk leads to a magnetic field configuration independent of the solar wind and terrestrial geometry. Image Credit: (Khurana, 2001)	52
2.8	An illustration of the cyclic motion of plasma within the Jovian magnetosphere from Kivelson et al. (2005b).	53
2.9	The terrestrial atmospheric profile illustrating the coexistence between the neutral upper atmosphere and ionised ionosphere. Retrieved from Kelley (2003)	55
2.10	A) Jovian atmospheric temperature profile containing data from previous observations and models. B) electron density profile of Jupiter’s upper Atmosphere based of Galileo spacecraft observations. Adapted from figures 9.9 and 9.10 in Yelle et al. (2004)	58

2.11	The auroral emission processes present in a hydrogen dominated atmospheres. Adapted from Badman et al. (2015)	60
2.12	An image of Jupiter’s UV aurora taken by the Hubble Space Telescope. Orange, green and red regions denote the polar flashes, main emission and satellite footprints with wake, respectively. Credit: NASA/HST .	61
2.13	A simplified schematic of the M-I coupled system taken from Cowley et al. (2001). Solid black lines represent the magnetic lines of force, while dashed lines indicate the current system coupling the planet to the plasma disk (dotted region).	64
3.1	A modified version of the Bagenal & Bartlett rendition of the Jovian magnetosphere, illustrating the 5 semi-arbitrary regions discussed in this chapter. Red: Magnetosphere boundary and outer region, blue: Middle region, yellow: Inner region, green: Polar region, purple: Tail region	68
3.2	The variation in solar wind magnetic field magnitude, proton density, and velocity observed by Ulysses and the variation in their respective kurtosis. Figure adapted from Echer et al. (2020).	74
3.3	An illustration of the energetic particles and waves upstream of the terrestrial magnetosphere. The direction of the solar wind is identified via the white arrow, while the black lines correspond to the interplanetary magnetic field impinging upon the system at an angle of approximately 45°. The yellow electron and red ion foreshocks are labeled upstream form the magnetosheath. Image credit: Tsurutani et al. (1981)	79

3.4	Evidence of plasma heating given by the correlation between the ratio of left hand to right hand polarised fluctuations and the proton temperature anisotropy. Image credit: Czaykowska et al. (2001) . . .	81
3.5	The turbulent spectra of the terrestrial magnetosheath during a quiet period as observed by the Cluster spacecraft. The solid line is the power spectra of transverse perturbations, dashed for the compressive perturbations. Image credit: Alexandrova et al. (2008)	82
3.6	The radial temperature profile of the Jovian magnetodisk plasma is given by the dotted lines, the predicted temperature profile based on adiabatic cooling is shown as a dashed line, while the modeled temperature incorporating turbulent heating is shown as the solid profile. Image Credit: Saur et al. (2002)	84
3.7	An illustration of the field perturbation triggered by the presence of a satellite with a velocity difference to the ambient field. In panel a), the unperturbed flow is to the right, and the ambient field is pointing down. Panel b) is the viewpoint of an observer behind the satellite, with the flow velocity coming towards them. Currents flowing along the Alfvén wing are shown as dashed and solid arrows. Solid arrows signify currents traveling on the left side of the satellite in panel b), while dashed arrows signify currents flowing on the right hand side of the satellite in panel b). Image Credit Jia et al. (2010)	87

3.8	Dashed profiles illustrating the polarisation relationship of high latitude kinetic Alfvén waves as stated in Equations 3.4 & 3.5 for components perpendicular (top) and parallel (bottom) to the background field. Solid lines denote constant electron temperatures at 2.5, 10 and 25 keV. Vertical dotted lines denote the ion and electron inertial length scales, λ_i and λ_e , respectively. Image credit: Saur et al. (2018)	90
3.9	The turbulent spectra in the terrestrial cusp region as measured by the Cluster magnetometer (red) and STAFF wave instrument (black). The purple arrow points to the ion cyclotron frequency. Image Credit: Nykyri et al. (2006)	92
3.10	Power spectra of turbulent perturbations in the terrestrial inner central plasma sheet, outer central plasma sheet and plasma sheet boundary layer. Stronger, more dissipative turbulence exists in the inner central plasma sheet than the outer central plasma sheet. Image credit: Bauer et al. (1995).	96
4.1	An illustration of how a flux gate magnetometer measures a magnetic field. Panel a) shows the configuration of the ring core, surrounded by a driver and sensor coil. b) shows the driving waveform, which c) showing the resultant induced field in each half of the ring core in the absence of any background field. If an external field is present, a phase shift is present, resulting in a measurable voltage in the sensor coil as illustrated in panel d) and e). (Image Credit: Imperial College London (n.d.))	102

4.2	Simplified schematic of a top hat 360° field-of-view electrostatic analyzer. Image Credit: Morel et al. (2017)	103
4.3	The orbital trajectories of Jovian missions, in the JSO reference frame, projected onto the three coordinate planes. Yellow trajectories illustrate flyby missions, red is the Galileo orbiter, and green is Juno, the sun is towards the positive x-direction.	105
4.4	The Juno spacecraft with the JADE (left) and MAG (right) instrument highlighted.	108
4.5	The Galileo spacecraft with Magnetometer instrument highlighted. Figure provided by Kivelson et al. (1992)	110
4.6	Three standard definition reference frames for Jupiter. (Top) System III: Here we show the right-handed version of the reference frame, which is the orientation chosen for our study, z is aligned with the Jovian spin axis, x is aligned with the prime meridian, and y completes the right handed triad. (Middle) Jupiter Magnetic: The z axis is aligned with the Jovian magnetic dipole, y is defined by the intersection of the magnetic and geographic equators, illustrated by the overlaid System III axis (black dashed lines), and x completes the right handed triad. (Bottom) JSO: x points towards the sun, y points in the direction of motion of the planet, highlighted by the dashed green line, and z completes the right handed triad.	114
4.7	The De Hoffmann-Teller reference frame is aligned with the background field.	116

4.8	The topography of the Khurana et al. (2005) current sheet. The z axis is in the direction of Jupiter’s spin axis. Warmer (cooler) colours dictate the height above (below) the x-y equatorial plane.	117
5.1	An illustration of the (left) terrestrial and (Right) Jovian current systems. The magnitude of currents within the Jovian system is much larger than those within the terrestrial system. Further to this, the presence of an internal plasma source, and the subsequent internal driving of the magnetospheric dynamics results in a large radial current, comparable to the Jovian ring current. Image Credit: Khurana (2001).	123
5.2	Trajectories of Jovian missions used in this study, projected onto the equatorial plane with the Sun to the right. Also shown are the Joy et al. (2002) bow shock and magnetopause locations for a compressed magnetosphere.	126
5.3	A sample of Galileo magnetometer data in the spherical System III reference frame. Two panels for each component are provided, the upper panel shows (solid grey) the combined field magnitude, (dashed) the JRM09 field model, (solid black) the differenced magnetic field. The lower panel shows the differenced magnetic field, but over a smaller range of y-axis values.	130

5.4	(<i>Top</i>) The radial component of the differenced field can be seen in grey. The dark region indicates a single lobe region determined by the algorithm. The algorithm returns consecutive magnetic field measurements with less than a 7.5% variability for a period of more than 30 minutes. (<i>Bottom</i>) A frequency histogram of the magnetic field strength during the lobe traversal, shown as a thick black line in the top panel. In both panels dashed grey lines indicate the standard deviation of the lobe values, the solid red line indicates the modal value and the dashed red line indicates the mean. The mean is skewed by the large tail in the histogram, associated with part of the recording in the top panel being of the non-lobe field.	135
5.5	The square root of the number of data points recorded within each bin. \sqrt{n} was chosen as it is inversely proportional to the standard error on the mean. Solid black lines represent the magnetopause and bow shock boundaries from Joy et al. (2002).	137

5.6	HICD from lobe regions determined by the algorithm. (a) The height integrated radial current density. Warmer (cooler) colours indicate outward (inward) flowing radial currents. These values are binned and averaged in (b). (c) The height integrated azimuthal current density. Note the log scale on the colour axis. Current flow is in the direction of corotation and again the values are binned and averaged in (d). Concentric dotted rings are placed at intervals of $20 R_J$. 1 hour LT divisions are separated by straight dotted lines. Solid black lines represent the magnetopause and bow shock boundaries from Joy et al. (2002).	139
5.7	The mean radial (<i>left</i>) and azimuthal (<i>right</i>) HICD over all LTs, averaged in radial bins of $5 R_J$. Results are averaged into each sector. Error bars represent the standard error of the mean.	141
5.8	The radial HICD shown against radial distance from the planet binned in LT sectors. HICDs from lobe traversals are represented by black dots. The red line is the mean of the $5 R_J$ bins. Error bars represent the standard error of the mean.	142
5.9	The azimuthal HICD shown against radial distance from the planet binned in LT sectors. HICDs from lobe traversals are represented as black dots. The red line is the mean of the $5 R_J$ bins. Error bars represent the standard error of the mean. The dashed black line is the fitted value to the function $\frac{a}{\rho^b}$, with the corresponding b value labeled.	143

5.10	The divergence of the HICD for the (a) radial (b) azimuthal and (c) perpendicular components, in a similar format to Figure 5.6. The divergence of the perpendicular components is analogous to the parallel current density.	145
5.11	A comparison of the radial and azimuthal divergences. Red regions denote where $\nabla_{\phi} \cdot J'_{\phi} > \nabla_{\rho} \cdot J'_{\rho}$, white regions denote where $\nabla_{\rho} \cdot J'_{\rho} > \nabla_{\phi} \cdot J'_{\phi}$. (In similar format to Figure 5.6)	152
6.1	A comparison of the current-voltage relation derived by Knight (1973) (dot-dashed line) vs the analytical high latitude current choke result. The result of the Knight relation overestimates the current density saturation by almost a factor of 50. The insert is a comparison between the current-voltage relation derived from a 1D spatial, 2D velocity space Vlasov model and the analytical high latitude current choke solution. Taken from Ray et al. (2009)	160
6.2	Two panels from Figure 2 in Mauk et al. (2017) showing Juno energetic electron plasma data from PJ4 over the polar region. Labeled are mono-directional inverted V signatures just prior to 13:39, and a bidirectional broadband signature just after 13:39. Inverted V signatures are associated with field-aligned potentials discussed in the Knight relation, while broadband signatures are associated with wave-particle interactions.	163

6.3	Electron plasma and magnetic field data in the dawn sector for a period during 2017-138. Panel a) shows the high resolution JADE-E electron plasma data. The temperature (black profile) and number density (blue profile) calculated from the plasma moments are overlaid. Panels b) and c) show the perpendicular and parallel components of the magnetic field in the De Hoffmann-Teller reference frame. A detrending procedure was implemented in order to highlight the transient perturbations in the field. Panels e) and f) show the power spectra of the transverse and compressional field respectively. Compressional signals appear absent from the event, while a clear, broad increase in transverse power indicates the presence of Alfvénic turbulence.	170
6.4	The location of the 12 identified events in the magnetic frame of reference. Events are localised in the mid-to-high latitude regions, mapping to equatorial radii, or M shells, between 20 - 50 R_J , conjugate with the main auroral emissions. Mapping was performed using the JRM09 magnetic field (Connerney et al., 2018) and CAN current disk (Connerney, 1981) models. Events used in this study are all within the dawn sector.	171
6.5	The results of the wavelet analysis from event during 2017-138 in the dawn sector. a) The parallel component of the power spectrum. b) the perpendicular component of the power spectrum	174

- 6.6 The calculated power spectral densities of each event. The PSD of each event, shown in red, are scaled by 10^{3n} where n is the number of the event. Scaling was used to aid visualisation. Black lines indicate the fitted power laws. The higher frequency power laws were fitted using the devised optimisation technique, while lower frequency gradients were fitted between the event specific lower frequency cut off and the higher frequency spectral break. The fitted power laws can all be seen to transition from a non-dissipative regime at lower frequencies to a dissipative regime at higher frequencies. 177
- 6.7 The compressibility of each event, represented by light grey lines, over frequency. The frequency has been normalised based off the spectral break in each event to highlight the compressibility within the energy dissipative regions. The black horizontal line marks the value expected for power isotropy. Values above this line indicate a more compressible signal, while values below it are more incompressible. The maroon profile represents the binned median value of each event, with error bars denoting the median absolute deviation. 178
- 6.8 A comparison between the spectral breaking length scale and fundamental plasma lengths. a) Electron inertial length: $\frac{c}{\omega_{p,e}}$, b) electron gyro radius: $\frac{m_e v_{\perp}}{|q|B}$, c) ion inertial length $\frac{c}{\omega_{p,i}}$ and d) ion gyro radius: $\frac{m_i v_{\perp}}{|q|B}$. The χ^2 fit and correlation coefficient for each comparison are included in the upper right section of each panel. Error bars included here represent twice the standard error of the mean. 185

6.9	The flatness of each event normalised by the spectral break frequency of each event. The maroon profile indicates the mean flatness value, with error bars expressing the standard error of the mean. A dashed horizontal line represents a flatness of 3, for a Gaussian distribution. The large values towards the low frequency end are due to boundary effects, while the decrease at high frequencies is due to the instrument sampling boundary. The gradient fit over higher frequency ranges, with a positive value of 0.26, suggests that the turbulent events are multifractal in nature.	188
7.1	A two dimensional projection of the Juno orbits (grey) overlaid in the magnetic frame of reference. Solid black lines represent magnetic field line traces. The Juno orbital trajectory provides a dense coverage over a wide range of magnetic latitudes, making it an ideal candidate for providing a full spatial description of turbulent perturbations.	193
7.2	Two examples of the “turbulent” magnetic field measurements when applying the algorithm outlined in Chapter 6 to the entire Juno magnetometer dataset. (Left) A potentially successful result, as the magnetic field is seen to be fairly constant, and is significantly perturbed in all components over a relatively short period of time. (Right) A likely false return, as the magnetic field is very noisy, and no significant perturbations exist within this window.	196

List of Tables

1.1	An example of the various drift motions arising from the interaction of a plasma with electromagnetic and mechanical forces.	14
2.1	Typical system parameters for the Sun (Verscharen et al., 2019), Earth (Parks, 2015) and Jupiter (Khurana et al., 2004)	65
4.1	A list of the spacecraft missions which have encountered Jupiter. A mission duration ending with (+) signifies missions in operation at the time of writing.	104
5.1	The coefficients used in the Joy et al. (2002) statistical magnetopause and bow shock locations. P_d is the dynamic pressure of the solar wind.	127
6.1	The time, duration, M-shell mapping and Jupiter Solar Magnetic coordinates of the 12 events identified in this study.	172
6.2	A summary of the events' Poynting flux. Given for each event are the field perturbation, local and low altitude Poynting flux. The perturbed field was calculated as the sum of the variance of the band filtered magnetic field. The Poynting flux was scaled to ionospheric values by use of a mirror ratio calculated with the JRM09 magnetic field model.	182

6.3	The parameters calculated for each event. From left to right: event number, mean magnetic field strength, mean number density, mean temperature, mean plasma thermal velocity, plasma beta, electron plasma frequency, electron inertial length, ion plasma frequency, ion inertial length, electron gyrofrequency, electron gyroradius, ion gyrofrequency, ion gyroradius	184
A.1	The spherical harmonic coefficients used in calculation of the JRM09 internal magnetic field model. Values obtained from Connerney et al. (2018).	201

AU - Astronomical Unit
CAN - Connerney Acuña Ness (Jovian current disk model)
ESA - European Space Agency
ESA - Electrostatic Analyser
FAC - Field Aligned Current
FUV - Far Ultraviolet
HICD - Height Integrated Current Density
HST - Hubble Space Telescope
IMF - Interplanetary Magnetic Field
JADE - Jovian Auroral Distribution Experiment
JEDI - Jupiter Energetic Particle Detector
JRM09 - Jupiter Reference Model through perijove 9 (Jovian internal field model)
JSM - Jupiter Solar Magnetic
JSO - Jupiter Solar Orbital
KHI - Kelvin-Helmholtz Instability
LT - Local Time
MAD - Median Absolute Deviation
MAG - Magnetometer
MI - Magnetosphere-Ionosphere
MHD - Magnetohydrodynamic
NASA - National Aeronautics and Space Administration
PJ - Perijove
PSD - Power Spectral Density
 R_J - Jupiter Radius (71,492km at the Equator)

UT - Universal Time

UV - Ultraviolet

ULF - Ultra-low Frequency

Chapter 1

Space Plasma Physics

In order to understand the Jovian magnetosphere in detail, we must first comprehend the fundamental physical concepts that underpin the research in this field. This chapter is dedicated to the background theory relevant to this work, building in complexity until we have the required understanding to describe the complex Jovian magnetosphere-ionosphere coupled system in Chapter 2. We begin with discussing the question, what is a plasma and how are they formed? What are magnetic and electric fields? We then go on to discuss the interaction of plasmas with electric and magnetic fields before moving on to higher order physical phenomena such as reconnection, particle acceleration, and waves and turbulence in plasmas. Throughout this chapter, we make use of the necessary knowledge presented in Kivelson et al. (1995) and Goossens (2003) and prime ourselves to interpret the complex and fascinating dynamics of the Jovian system in the following chapter.

1.1 Definition of a Plasma

A plasma is an electrically conducting, ionised gas. It is by far the most common type of ordinary matter in the universe. Like gases, plasmas consist of a large number of individual elements and molecules which constantly interact with each other, though unlike gases a percentage of these composites are ionised. When sufficient energy is supplied to strip one or more electrons from the parent atom or molecule it becomes ionised. The energy requirement is such that it exceeds the binding potential of the neutral atom or molecule's electron. Additionally atoms or molecules may gain an electron, resulting in a negative ion. Ionised particles can gain or lose more than one electron. After having lost or gained an electron the particle has a net positive or negative electrical charge, respectively, and can freely interact with electric and magnetic fields. Some sources of ionisation include:

- *Photo-ionisation* - High energy photons can remove electrons from their atomic shells.
- *Charge Exchange* - This occurs when an atom or molecule reacts with an ionised atom or molecule, transferring the charge of the ion to the neutral species without any dissociation.
- *Electron impact ionisation* - Unbound electrons with sufficient kinetic energy can collide with atomic electrons, knocking them free from their orbits.

A plasma consists of both positively and negatively charged particles, however over large scales no net charge is present and the plasma is said to be quasi-neutral. A

plasma does not have to be fully ionised in order to behave as an ideal plasma. Often it is an amalgamation of charged and neutral particles. For a plasma to be considered as an ideal plasma, the collision frequency between the charged particles and neutral particles must be lower than the plasma frequency. Being a charged fluid, plasmas display unique behaviours when in the presence of electric and magnetic fields. Charge separation between ions and electrons gives rise to electric fields, and charged particle flows give rise to currents and subsequently magnetic fields.

1.2 Electric and Magnetic fields

An electric field is a physical field surrounding particles with an electric charge. Any additionally charged particles within the electric field will experience a force as a result of that electric field. This electrostatic force is around 36 orders of magnitude greater than that of gravity. Coulomb's law states:

“The magnitude of the electrostatic force of attraction or repulsion between two point charge is directly proportional to the product of the magnitudes of charges and inversely proportional to the square of the distance between them” - Coulomb (1785)

Hence the electrostatic force, \mathbf{F}_C , between two particles is given by

$$F_C = C \frac{q_1 q_2}{r^2} \quad (1.1)$$

where q_i is the charge of the respective particle, separated by a distance r , and C is the Coulomb constant.

From a quantum perspective, the electrostatic force is mediated by massless virtual photons, as such information from this force travels at the speed of light, transmitting the information over an infinite distance. However within the plasma, the length scale over which a charged particle can interact with the surrounding plasma is determined by the Debye length, λ_D , given as

$$\lambda_D = \sqrt{\frac{\epsilon_0 k_B T_e}{n_e q^2}} \quad (1.2)$$

where ϵ_0 is the permittivity of free space, k_B is the Boltzmann constant, T_e is the electron temperature and n_e is the electron density, and q is the particle charge. If the number of electrons within a Debye sphere, with radius λ_D , is sufficiently large, then the central ion is shielded from external particles.

A magnetic field is a vector field resulting from the intrinsic magnetic moment of a material and/or an electrical current. Magnetic and electric fields form the two components of the electromagnetic force and are described in the Maxwell equations

$$\nabla \cdot \mathbf{E} = \frac{\rho}{\epsilon_0} \quad (1.3)$$

$$\nabla \cdot \mathbf{B} = 0 \quad (1.4)$$

$$\nabla \times \mathbf{E} = -\frac{\partial \mathbf{B}}{\partial t} \quad (1.5)$$

$$\nabla \times \mathbf{B} = \mu_0 \left(\mathbf{J} + \epsilon_0 \frac{\partial \mathbf{E}}{\partial t} \right) \quad (1.6)$$

where \mathbf{B} and \mathbf{E} are the magnetic and electric fields respectively, t is time, ϵ_0 is the permittivity of free space, ρ is the charge density, μ_0 is the permeability of free space and \mathbf{J} is the current density.

These four equations form the basis of all following electromagnetic theory. Gauss' law, Equation 1.3, relates gradients in the electric field to the electric charge density. Equation 1.4 shows that magnetic mono-poles do not exist. Equation 1.5 is Faraday's law, which describes the production of an electromotive force via the interaction of a magnetic field with an electric current. Equation 1.6, Ampère's law, relates the total magnetic field around a closed loop to the electric current flowing through the loop. Ampère's law is key to deducing the structure of Jupiter's equatorial currents in Chapter 4. The second term on the right hand side of Ampère's law, the displacement current, is negligible when the particle distributions vary much faster than the configuration of the electric field and is often neglected in what is referred to as the low frequency MHD approximation.

1.3 Properties of a Plasma in Electric & Magnetic Fields

As mentioned, plasmas interact with electric and magnetic fields. Subsequently, their interaction gives rise to additional induced electric and magnetic fields through Equations 1.5 and 1.6. These induced fields can produce additional, higher order

influences on the system, resulting in a highly complex environment which when examined holistically can be overwhelming. Here we dissect several properties of the plasma which are of key importance to this study.

1.3.1 Kinetic Description

An effective way to understand the properties of plasmas is to consider individual particles within the system. Kinetic theory describes the macroscopic properties of a plasma through knowledge of its microscopic attributes, such as particles' velocities and their subsequent kinetic energy. Unless otherwise stated, the velocity of the plasma particles will be described as flowing parallel, v_{\parallel} , or perpendicular, v_{\perp} , to the magnetic field. Note that whilst the kinetic description is suitable for describing certain aspects of plasma physics, it does not explain all physical processes associated with plasma dynamics, such as wave activity, which requires a fluid approach. Be that as it may, a kinetic description provides the necessary starting point in comprehending the workings of a planetary magnetosphere.

1.3.2 Currents in a Plasma

Electric currents are a macroscopic property created by charged particles moving through a conducting medium. Any motion of charged particles within a space plasma, such as drift motion or variations in the magnetic field, produces an electric current. Electric currents play a fundamental role within planetary systems, facilitating the exchange of momentum and energy between the magnetosphere and ionosphere of a planet. Whenever studying currents within space plasmas, it makes more sense to refer to their current densities, \mathbf{J} , which are the flow rates of electric current per

unit area and can be retrieved from the macroscopic equation of motion. Assuming a simplistic plasma containing only one type of positive ion and electrons, we begin with their respective momentum equations

$$n_i m_i \left(\frac{\partial \mathbf{v}_i}{\partial t} + \mathbf{v}_i \cdot \nabla \mathbf{v}_i \right) = n_i Z_i e (\mathbf{E} + \mathbf{v}_i \times \mathbf{B}) - \nabla \cdot \mathbf{\Psi}_i - n_i m_i \nabla \phi + \mathbf{P}_{i,e} \quad (1.7)$$

$$n_e m_e \left(\frac{\partial \mathbf{v}_e}{\partial t} + \mathbf{v}_e \cdot \nabla \mathbf{v}_e \right) = -n_e e (\mathbf{E} + \mathbf{v}_e \times \mathbf{B}) - \nabla \cdot \mathbf{\Psi}_e - n_e m_e \nabla \phi + \mathbf{P}_{e,i} \quad (1.8)$$

$$\mathbf{v}_j = \frac{1}{n_j \Delta V} \Sigma w_j \quad (1.9)$$

$$\mathbf{\Psi}_j = \frac{m_j}{\Delta V} \Sigma (\mathbf{w}_j - \mathbf{v}_j) (\mathbf{w}_j - \mathbf{v}_j) \quad (1.10)$$

where the subscript j denotes the respective species, n is the species particle number density, m is the particle mass, \mathbf{v} is the macroscopic mean particle velocity for a given volume element ΔV , Z is the particle valence, c is the speed of light, \mathbf{E} and \mathbf{B} are the electric and magnetic field vectors respectively, ϕ is the gravitational potential, $\mathbf{\Psi}$ is stress tensor, \mathbf{w} is the particle velocity, and $\mathbf{P}_{i,e}$ accounts for collisional momentum transfer between ions and electrons. The stress tensor, $\mathbf{\Psi}$, typically has 9 components,

for each combination of two directional vectors:

$$\Psi = \begin{bmatrix} \Psi_{xx} & \Psi_{xy} & \Psi_{xz} \\ \Psi_{yx} & \Psi_{yy} & \Psi_{yz} \\ \Psi_{zx} & \Psi_{zy} & \Psi_{zz} \end{bmatrix} \quad (1.11)$$

Components off the diagonal in equation give rise to viscous forces. By assuming an isotropic distribution of random particle velocities, only the three Ψ_{xx} , Ψ_{yy} and Ψ_{zz} components of the tensor remain, which are equal to the scalar pressure, p . Hence we may rewrite the second term of Equation 1.7 & 1.8 as $\nabla \cdot \Psi = \nabla p$. This is valid so long as the collisional mean free path between particles remains short compared with distances over which macroscopic properties change significantly. $\nabla \cdot \Psi = \nabla p$ also remains true for long mean free paths, providing changes with time to the plasma are such that all gradients along the magnetic field lines may be neglected, and for significantly small gyroradii compared with distances over which macroscopic properties change significantly. From Equations 1.7 and 1.8, it can be shown that the macroscopic quantities of velocity, \mathbf{v} and current density \mathbf{J} , are given by:

$$\mathbf{v} = \frac{1}{\rho} (n_i m_i \mathbf{v}_i + n_e m_e \mathbf{v}_e) \quad (1.12)$$

and

$$\mathbf{J} = e(n_i Z \mathbf{v}_i - n_e \mathbf{v}_e) \quad (1.13)$$

Single Particle Motion

Electrons and ions interact with each other to produce plasma oscillations. When a displacement between the electrons and the ions occurs, charge separation forms an electric field which acts to return the constituents to their equilibrium position. The electrons, having a greater mobility, are accelerated more readily back towards the equilibrium position. Ion motion is considered negligible when compared with the electron motion. The electrons will over-shoot and a new electric field is set up in the opposite direction. The result is an oscillation known as the plasma frequency, $\omega_{p,j}$, given by

$$\omega_{p,j} = \sqrt{\frac{n_j q^2}{m_j \epsilon_0}} \quad (1.14)$$

where j denotes the species. For the ions, their much larger mass means their movement is negligible when compared to the motion of the electrons.

In the presence of an electric and magnetic field, a particle with charge q and velocity \mathbf{v} experiences a Lorentz force. With the inclusion of additional non-electromagnetic forces, \mathbf{F}_A , such as gravity or centrifugal forces, we may write the sum of forces on a particle as:

$$m \frac{\partial \mathbf{v}}{\partial t} = q(\mathbf{E} + \mathbf{v} \times \mathbf{B}) + \mathbf{F}_A \quad (1.15)$$

The presence of a magnetic field results in a force perpendicular to the particles velocity and perpendicular to the background field, creating a centrifugal acceleration. The motion of the particle can be determined by taking the derivative of Equation

1.15 assuming $\mathbf{B} = B_z$ and no electric field is present:

$$\frac{\partial v_x}{\partial t} = \frac{qB_z}{m}v_y \quad (1.16)$$

$$\frac{\partial v_y}{\partial t} = -\frac{qB_z}{m}v_x \quad (1.17)$$

$$\frac{\partial v_z}{\partial t} = 0 \quad (1.18)$$

Differentiating Equation 1.16 and substituting Equation 1.17 yields the equation for simple harmonic motion

$$\frac{\partial^2 v_x}{\partial t^2} = -\left(\frac{qB_z}{m}\right)^2 v_x \quad (1.19)$$

which shows that a particle would gyrate about the field with a gyrofrequency, $\omega = \frac{qB}{m}$, and gyration radius, r_g given by:

$$r_g = \frac{v_{\perp}}{\omega} \quad (1.20)$$

Often though, a particle will have a velocity parallel to the magnetic field. This leads to the particle moving in a helical path along the magnetic line of force. The angle the particle's overall velocity makes with the magnetic field line is referred to as the pitch angle, labeled α in Figure 1.1. Pitch angles of 0° and 180° are described as field-aligned particles as their motion is parallel or anti-parallel to the local magnetic field. Particles with a pitch angle of 90° have no parallel velocity, and simply gyrate about their local field line in the manner described above.

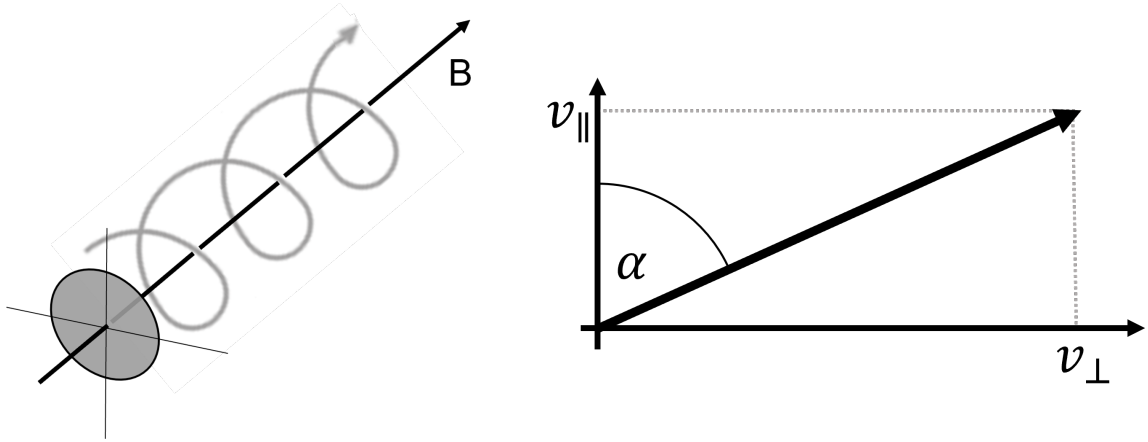


Figure 1.1: The helical motion of a negatively charged particle about the magnetic field. The magnetic field acts as the guiding center of the motion.

Particle Drift

In addition to motion along a magnetic field, particles experience several kinds of drift motions. These occur under varying conditions such as inhomogeneity in the field, the presence of an electric field, and curvatures in the magnetic field. The resultant motion is important in resolving the additional current systems and dynamical processes occurring within planetary magnetospheres. Examples of these drift motions are shown in Table 1.1 at the end of this section. In assuming the plasma is collisionless, it must closely conform to a series of conditions. Firstly, the mean-free path of particles within the plasma is much larger than typical length scales over which macroscopic properties of the plasma vary and secondly, the collisional frequency of particles is less than the time scales over which macroscopic properties vary.

Consider a magnetic field with flux increasing perpendicular to the field direction. A particle gyrating within this field would traverse through an inhomogeneous field. The result is a change in the gyration frequency, and subsequently its gyro-radius. In higher flux regions, the gyro-radius decreases, while in lower flux regions it would expand. The result is a particle drift perpendicular to both the magnetic field direction and the gradient of the magnetic field strength. The velocity of a particle with mass, m , and perpendicular velocity, v_{\perp} undergoing this motion, often called the grad B drift, is given by:

$$\mathbf{v}_{\nabla\mathbf{B}} = \frac{1}{2}mv_{\perp}^2 \left(\frac{\mathbf{B} \times \nabla\mathbf{B}}{qB^3} \right) \quad (1.21)$$

Recalling that the direction of gyration is dependent on the charge of a particle, then the drift direction is opposite for electrons and positive ions. The differential motion of particles creates a current, which in the magnetosphere manifests as a ring current.

In the case where the magnetic field is curved, such as that of a dipole, and in the absence of an electric field another type of drift occurs. Particles moving along a curved magnetic field experience a centrifugal force acting perpendicular to the field curvature. Over a gyration a particle will experience an acceleration and deceleration, varying the radius of its orbit. This produces a drift analogous to the grad B drift. Again, due to the opposite gyro-motion of positive and negative particles, a charge separation will occur producing a current. Additionally the curvature of the field produces a Coriolis force, however it cancels out over the course of a gyro-period.

Quantitatively, the curvature drift is given by

$$\mathbf{v}_{curv} = \frac{mv_{\parallel}^2}{qB^2} \frac{\mathbf{R}_B \times \mathbf{B}}{R_B^2} \quad (1.22)$$

where \mathbf{R}_B is the radius of curvature of the magnetic field. The currents produced by this differential drift would act to enhance the ring currents.

The final drift we discuss arises under the presence of an electric field, aligned perpendicularly to the magnetic field. The presence of an electric field acts to accelerate the particles perpendicularly to the magnetic field, in a similar way to the curvature drift. However the opposing gyration of the particles means the overall drift is in the same direction, as such no charge separation occurs with this kind of drift. The motion of the particles is perpendicular to both \mathbf{E} and \mathbf{B} , and is referred to as the $\mathbf{E} \times \mathbf{B}$ drift. The value of which is expressed by

$$\mathbf{v}_{\mathbf{E} \times \mathbf{B}} = \frac{\mathbf{E} \times \mathbf{B}}{B^2} \quad (1.23)$$



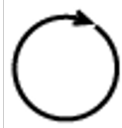

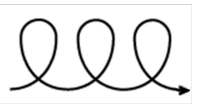


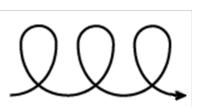




Drift	Conditions	Negative Charge Motion	Positive Charge Motion
Gyromotion	\mathbf{B} 		
Gradient B Drift	\mathbf{B}  $\uparrow \nabla \mathbf{B}$		
$\mathbf{E} \times \mathbf{B}$ Drift	\mathbf{B}  $\uparrow \mathbf{E}$		
Curvature Drift	\mathbf{B}  $\uparrow \mathbf{F}_c$		

Table 1.1: An example of the various drift motions arising from the interaction of a plasma with electromagnetic and mechanical forces.

The First Adiabatic Invariant

The magnetic moment relies on the assumption that the magnetic field is slowly varying. That is that temporal changes are much longer than a gyro-period, or that spatial variations are much larger than a gyro-radius. The magnetic moment is the first adiabatic invariant, and is given as

$$\mu = -\frac{W_{\perp}}{B} \quad (1.24)$$

where $W_{\perp} = \frac{mv_{\perp}^2}{2}$ is the perpendicular kinetic energy. In the case where the magnetic field is spatially varying such that the magnetic flux is increasing along the direction of the field, particles will be reflected. As the particle traverses through the converging field, its parallel energy will decrease, whilst its perpendicular energy will increase. Hence its pitch angle will increase to the point where it is reflected. This is referred to as a magnetic mirror and results in a particle's bounce motion along the magnetic field.

$$W = W_{\perp} + W_{\parallel} = \mu B + W_{\parallel} \quad (1.25)$$

The Second Adiabatic Invariant

The second invariant is associated with the periodic gyration of a particle about its magnetic guide. A charged particle, trapped in a magnetic mirror, will remain trapped on the same magnetic field line. This is often referred to as the longitudinal invariant and is proportional to the loop integral of the parallel velocity over a bounce orbit

$$J = m \int v_{\parallel} ds \quad (1.26)$$

where m is the mass of the particle, v_{\parallel} is the particle's parallel velocity, ds represents an element of the field line with length S . This invariant is conserved when the time variation of the magnetic field is less than the particle bounce period.

The Third Adiabatic Invariant

The third invariant relates to the drift of a charged particle about the axis of its magnetised planet. This invariant requires that magnetic flux through a given drift

surface is conserved. In realistic cases the longitudinal drift motion is slow compared with the orbital velocity, so this invariant is often broken.

1.3.3 Frozen-in Theorem

For a plasma within a magnetic field, the rate of change of magnetic flux is given by:

$$\frac{\partial \mathbf{B}}{\partial t} = \nabla \times (\mathbf{u} \times \mathbf{B}) + \frac{\nabla^2 \mathbf{B}}{\mu_0 \sigma} \quad (1.27)$$

The first term on the RHS of the equation is the convective term, which determines how the plasma and magnetic field are frozen together. The second term is the diffusive term, which influences how the plasma diffuses through the magnetic field. The ratio of these two terms is referred to as the magnetic Reynolds number, which is often used to determine whether the frozen-in approximation is applicable. For the case where the Reynolds number is large, the diffusive term is negligible and the plasma is frozen-in. For the case where the Reynolds number is less than one, plasma can diffuse from the magnetic field, and the frozen-in condition no longer applies. The Alfvén frozen-in theorem states:

“In a fluid with infinite electric conductivity, the magnetic field is frozen into the fluid and has to move along with it” - Alfvén, 1942

Similarly, the motion of the magnetic field would act to drag/push the plasma along with it. Depending on the strength of the magnetic pressure or the thermal pressure, the system is either governed by the motion of the magnetic field or the motion of the plasma respectively. This is expressed as the plasma beta, which is the

ratio of the two pressures:

$$\beta = \frac{nkT}{\frac{B^2}{2\mu_0}} \quad (1.28)$$

Motion of a plasma with $\beta \ll 1$ is controlled by the magnetic field, while a plasma with $\beta > 1$ is dominated by the plasma thermal motion.

1.3.4 Fluid Description

As mentioned at the beginning of the last section, plasma dynamics cannot be completely encapsulated by a single particle description. A plasma consists of a collection of readily mobile particles and as such behaves similar to a fluid. The presence of and interaction with magnetic and electric fields introduces a new dimension of complexity to that of a neutral fluid however. Magnetohydrodynamics, or MHD, is a branch of mathematical physics which attempts to describe the properties of an electrically conducting fluid in the presence of electric and magnetic fields.

In order to apply the MHD description to a plasma, there are several conditions which must be met. Firstly, the plasma is assumed to be quasi-neutral over characteristic length and time scales. Additionally, the gyro-radii of particles (Eq 1.20) within the plasma are smaller than characteristic length scales of the system and the gyro-period of particles within the plasma are smaller than characteristic time scales within the system. When these conditions are met, the frozen-in condition is met and the MHD approach can be applied.

Describing a plasma as a fluid is relatively straight forward. This is done by applying the standard fluid equations with the consideration of electromagnetic forces arising from the charged nature of the fluid. These fluid equations are as follows:

$$\frac{\partial \rho}{\partial t} + \nabla \cdot (\rho \mathbf{v}) = 0 \quad (1.29)$$

$$\rho \left[\frac{\partial \mathbf{v}}{\partial t} + (\mathbf{v} \cdot \nabla) \mathbf{v} \right] = -\rho \nabla \phi - \nabla \cdot \mathbf{P} + \nabla \cdot \mathbf{F} \quad (1.30)$$

$$PV^\gamma = \text{constant} \quad (1.31)$$

Equation 1.29 is the conservation of mass equation, stating that in the absence of sources or sinks, the local mass of the system will be conserved. For an open system of constant mass, the equation states that the total mass entering through a source must equal the total mass exiting through a sink.

Equation 1.30 shows that the rate of change of momentum for a system of particles is equal to the sum of the forces acting on that system. Components on the LHS represent the temporal and spatial variations of velocity, respectively. On the RHS, the terms represent the gravitational force, ϕ , forces arising due to pressure gradients, \mathbf{P} , and additional forces, \mathbf{F} , such as viscous friction, electromagnetic forces and collisions.

Equation 1.31 is an equation for an adiabatic process, a process in which no heat enters or leaves the system. Here, γ is the ratio of the specific heats at constant pressure, P , and volume, V . This condition allows the derivation of the work done on or by a system.

Plasma Thermal Distribution

The energy distribution of plasma particles follow a Maxwell-Boltzmann, or Maxwellian, distribution. Figure 1.2 shows a series of Maxwellian distributions with varying temperature and hence thermal velocity. The thermal velocity, v_t , is linked to the particle kinetic energy through:

$$v_t = \sqrt{\frac{2k_B T}{m}} \quad (1.32)$$

The plasma distribution function, f_m , is given by

$$f_m = \frac{n}{\sqrt{2\pi}v_t} e^{-\frac{v^2}{2v_t^2}} \quad (1.33)$$

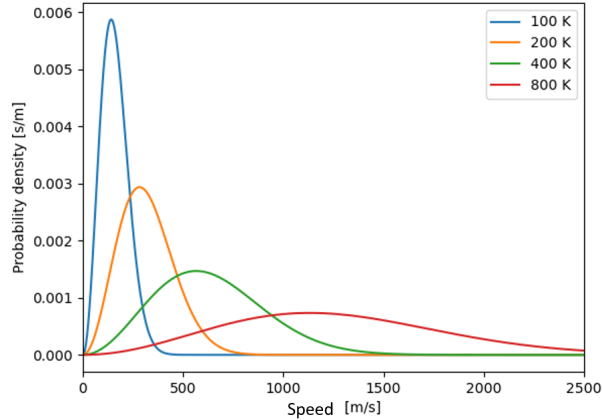


Figure 1.2: A Maxwell-Boltzmann distribution for a variety of temperatures. As temperature increases, the mean velocity of the plasma increases, however a wide variety of speeds are still present within the system.

In the case of an anisotropic plasma, the distribution function can be approximated

with a kappa distribution. If v_{\parallel} is parallel to the magnetic field and v_x and v_y are perpendicular to it, then the distribution function is given by:

$$f_m = \frac{n}{(\sqrt{2\pi}v_{t,\parallel})(\sqrt{2\pi}v_{t,\perp})^2} e^{-\frac{v_{\parallel}^2}{2v_{t,\parallel}^2} - \frac{v_x^2 + v_y^2}{2v_{t,\perp}^2}} \quad (1.34)$$

Plasma Distribution Function

The properties of a plasma particle at a point in time can be described in terms of a 6 dimensional phase space distribution, that is a 3 dimensional position, and a 3 dimensional velocity. This is often represented as $f(\mathbf{r}, \mathbf{v}, t)$ and is referred to as the plasma distribution function.

The plasma density of a given population can be calculated by integrating the distribution function over velocity space at that instance in time:

$$n = \int_{-\infty}^{\infty} f(\mathbf{r}, \mathbf{v}, t) d\mathbf{v} d\mathbf{r} dt \quad (1.35)$$

Vlasov Theory

A volume within an isolated particle population, i.e., one with no source or sink, experiences a rate of change of particle population based on the number of particles moving through the surface of said volume. For a collisional plasma discontinuities can be created resulting in sources and sinks, however for a collisionless plasma, with no external forces, the distribution function obeys the Vlasov equation

$$\frac{\partial f}{\partial t} + \mathbf{v} \cdot \nabla f + \frac{d\mathbf{v}}{dt} \cdot \nabla_{\mathbf{v}} f = 0 \quad (1.36)$$

where $\nabla_{\mathbf{v}}$ is the gradient in velocity space. The Vlasov equation is the basis by which the dispersion relation of wave-particle interactions are derived using kinetic theory. For a collisionless plasma, energy dissipation is assumed to largely be facilitated through resonant wave-particle interactions. The work presented in this thesis demonstrates the presence of such interactions at Jupiter, and so knowledge of Vlasov theory is essential to understanding the auroral particle acceleration mechanisms.

1.3.5 Waves in Plasmas

The simplest way in which a system responds to a disturbance is through the generation of waves (Cramer, 2001; Spitzer, 2006). Waves play a vital role in the transfer of energy and momentum in a collisionless plasma. Understanding the processes behind wave generation, propagation and dissipation is necessary to understand the information transfer process they mediate. At the most basic level, a property, u , undergoing wavelike oscillations can be described with the one-dimensional, planar wave equation

$$\frac{\partial^2 u}{\partial t^2} = c^2 \frac{\partial^2 u}{\partial x^2} \quad (1.37)$$

where the property u , can be described by its wavenumber, k , and frequency, ω , in the polar form:

$$u(x, t) = Ae^{i(kx - \omega t)} \quad (1.38)$$

There are two velocities associated with the propagation of a wave packet: its group velocity and its phase velocity. The wave packet travels at the group velocity,

given by:

$$v_g = \frac{\partial \omega}{\partial k} \quad (1.39)$$

The phase velocity denotes the speed at which the phase of the wave propagates and is given by:

$$v_p = \frac{\omega}{k} \quad (1.40)$$

A perturbation in a physical system often results in the emission of waves. These plasma waves differ between sound waves and electromagnetic waves. Analysis of the plasma waves can allow the deduction of the system's properties. The structure of oscillatory action within a closed system is often a superposition of standing waves with frequencies dependent on the system's conditions. Plasma waves have an additional layer of complexity compared with standard fluid waves due to the electromagnetic properties of the medium. The interplay between mechanical and electromagnetic forces give rise to a unique species of waves known as MHD waves.

MHD waves are predicted through an amalgamation of the fluid conservation equations and Maxwell's equations. One of the first of these to be discovered was a type of incompressible MHD wave known as an Alfvén wave. Its existence can be proven by taking the curl of Equation 1.5 and the time derivative of Equation 1.6, eliminating $\nabla \times \frac{\partial \mathbf{B}}{\partial t}$ and obtaining the wave equation for electromagnetic waves:

$$\nabla^2 \mathbf{E} - \nabla (\nabla \cdot \mathbf{E}) = \frac{1}{c^2} \frac{\partial^2 \mathbf{E}}{\partial t^2} + \mu_0 \frac{\partial \mathbf{J}}{\partial t} \quad (1.41)$$

Consider the case where the velocity and change in magnetic field are both in the y direction and the ambient magnetic field is in the z direction. Assuming an infinitely conducting medium, and neglecting higher order terms, Equation 1.15 and Ohm's law, (see 1.51), can be rewritten as

$$\rho \frac{\partial V_y}{\partial t} = J_x B_z \quad (1.42)$$

$$E_x - v_y B_z = 0 \quad (1.43)$$

From this, we can write $J_x = \frac{\rho}{B_z} \frac{\partial E}{\partial t}$, and substitute into the wave equation, 1.41, to find

$$\nabla^2 E_x = \left(1 + \frac{\mu_0 \rho c^2}{B_z^2}\right) \frac{1}{c^2} \frac{\partial^2 E_x}{\partial t^2} \quad (1.44)$$

through which one can identify the Alfvén velocity

$$v_A^2 = \frac{B^2}{\mu_0 \rho} \quad (1.45)$$

where v_A is the Alfvén velocity, B is the local magnetic field strength, μ_0 is the permeability of free space and ρ is the local plasma mass density.

For the case of a warm plasma, the resultant dispersion relations can be derived for MHD and Alfvén waves

$$\left(\frac{\omega}{k}\right)^2 = v_A^2 \cos^2 \theta \quad (1.46)$$

$$\left(\frac{\omega}{k}\right)^2 = \frac{1}{2} \left(c_s^2 + v_A^2 \pm \sqrt{[(c_s^2 + v_A^2)^2 - 4c_s^2 v_A^2 \cos^2 \theta]} \right) \quad (1.47)$$

where ω is the wave frequency, k is the wave number, θ is the angle of propagation with respect to the background magnetic field and c_s is the local sound speed. These two equations predict the existence of the shear Alfvén wave and the magneto-acoustic waves respectively. A shear Alfvén wave is one which propagates at frequencies below the ion-cyclotron frequency. Other sub-types of Alfvén waves, which are defined based on their dispersive length scales include the kinetic and inertial Alfvén wave, with respective dispersive scales at the proton gyroradius and electron inertial length (Dubinin et al., 2005). While Alfvén waves are incompressible, the magneto-acoustic wave has a compressional component. Given the phase velocity of these waves is $\frac{\omega}{k}$, we can illustrate the three solutions to equations 1.46 and 1.47 as a polar diagram in Figure 1.3.

Wave phenomena has been investigated under laboratory conditions for decades, however these experiments are costly, difficult to construct, and produce waves which decay rapidly under laboratory conditions (Amatucci, 2006). For a wave to exist, the damping distance must be significantly larger than the wavelength of the wave. The Lundquist number (Lundquist, 1949a; Lundquist, 1949b), S_L , representing the ratio of Alfvén timescales to diffusive timescales, provides the conditions in which such waves can exist

$$S_L = B_0 L \sigma \sqrt{\frac{\mu_0}{\rho}} \gg 1 \quad (1.48)$$

where L is the typical length scale associated with the system and σ is the plasma

conductivity. Fortunately, in sufficiently large systems the decay rate is small and this condition is met. Planetary magnetospheres provide such a system, making them an ideal natural laboratory in which this phenomenon may be investigated.

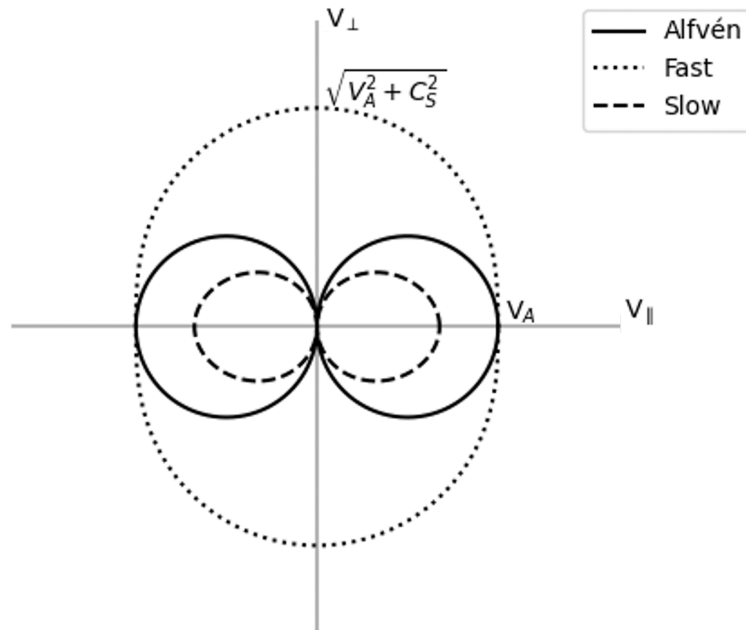


Figure 1.3: The phase velocity of the Fast, Slow and Alfvén waves for an electron plasma, displayed as a polar projection. The parameters used in the formation of this figure were: $B = 100$ nT, $T = 150$ eV, $n = 1000$ m⁻³, and $c_s < v_A$.

Waves can be excited in a variety of ways. Generally, a change in the equilibrium of the plasma and/or magnetic field through some dynamic mechanism will act as a

source of energy to drive waves. Such drivers in planetary magnetospheres might include the solar wind and radial interchange of plasma. Wave growth can be facilitated when the plasma velocity-space distribution is anisotropic. Instabilities are non-linear growths arising from certain plasma conditions. A few conditions include beams, anisotropic distributions and non-equilibrium spatial distributions.

Alfvén Waves

Energy within Alfvén waves is divided between electric and kinetic energy. In an infinitely conducting fluid, the wave kinetic energy is equal to the magnetic energy density:

$$\frac{1}{2}\rho v^2 = \frac{B^2}{2\mu_0} \quad (1.49)$$

Alfvén waves with perpendicular wavelengths comparable to the ion gyroradius carry electrical energy comparable to the magnetic energy density. Alfvén waves can also carry a parallel electric field, which can be shown by considering Ohm's law with Hall effects included. The full form of Ohm's law is given as

$$\mathbf{E} + \mathbf{v} \times \mathbf{B} = \eta \mathbf{J} + \frac{\mathbf{J} \times \mathbf{B}}{qn} - \frac{\nabla \cdot \mathbf{P}_e}{qn} + \frac{m_e}{q^2 n} \left[\frac{\partial \mathbf{J}}{\partial t} + \nabla \cdot \left(\mathbf{u} \mathbf{J} + \mathbf{J} \mathbf{u} - \frac{\mathbf{J} \mathbf{J}}{nq} \right) \right] \quad (1.50)$$

where, from left to right on the RHS, terms represent the plasma resistivity term, the Hall term, the electron pressure term, and the inertial term. The electron pressure and inertial terms are negligible, and can be omitted, and the plasma resistivity term vanishes under the approximation of an infinitely conducting plasma, thus we are left

with a simplified version of Ohm's law:

$$\mathbf{E} + \mathbf{v} \times \mathbf{B} = \frac{\mathbf{J}}{qn} \times \mathbf{B} \quad (1.51)$$

The above equation demonstrates that the electric and magnetic fields are orthogonal to one another. The parallel electric field component associated with the perturbed magnetic field is shown in Figure 1.4 from Mottez (2015).

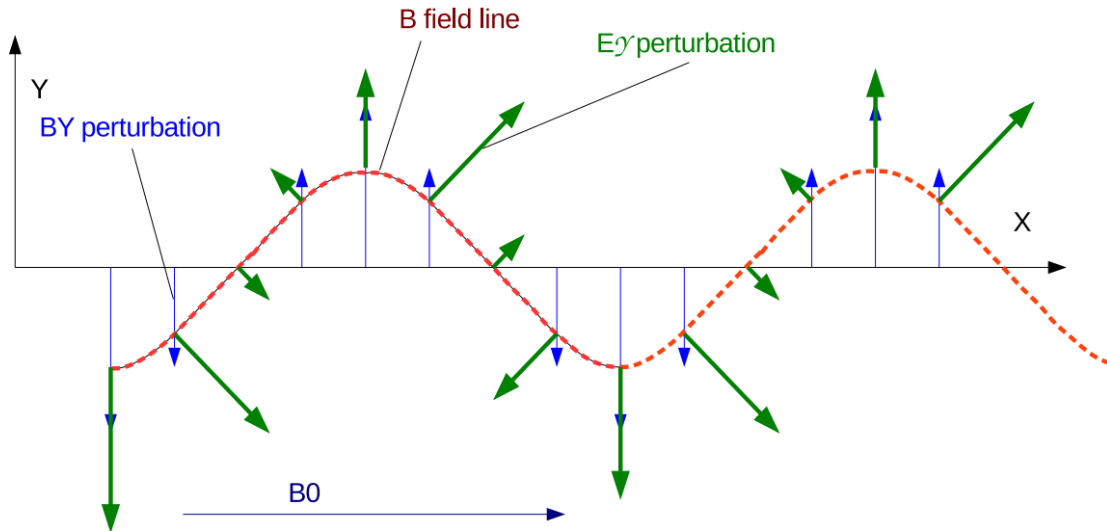


Figure 1.4: The perturbation field and associated electric field components for an Alfvén wave. Here, the electric field is represented by green arrows perpendicular to the red magnetic field profile with blue arrows illustrating perturbation vectors. There is a finite component of the perpendicular electric field component parallel to the x-axis. Image Credit: Mottez (2015)

At scales corresponding to the Alfvén resonance point, fast magneto-acoustic

modes may undergo a strong mode conversion to a small perpendicular wave mode or quasi-electrostatic wave. This phenomena arises from coupling between the fast magneto-acoustic mode and the pure shear Alfvén mode. In warm plasmas, these new modes are referred to as kinetic Alfvén waves, while in the cold plasma they are called inertial Alfvén waves. These subspecies of Alfvén waves have significant parallel electric fields and can efficiently interact with the plasma to accelerate charged particles. Such waves can be responsible for the formation of electron beams and the transfer of energy within a system.

Wave Instabilities

Instabilities are key components when discussing the configuration and transport properties of a planetary magnetosphere. In an instability, the plasma distribution has deviated from its equilibrium state, perturbations grow and non-linear waves act to return the system to a minimal energy configuration. A wave described by an exponential function experiences growth or dampening dependent upon the sign of the imaginary component of its frequency, $\omega = \omega_o + i\gamma$ where γ is the growth rate. For a positive imaginary component the wave undergoes growth, while for a negative imaginary component the wave is damped.

Non-linear interactions within a plasma can produce turbulence. Turbulent flows consist of vortices which in turn are made up of increasingly smaller vortices. This can also be thought of in terms of wave numbers. In a magnetosphere, waves reflecting by boundaries interact non-linearly and produce a turbulent cascade from larger to smaller scales. The energy flow, ϵ , in the turbulent flow is linked to the vortex scale

(or wavenumber in this case), k . Energy spectra of turbulent cascades obey a power law relationship with k . This follows some relationship

$$E(k) \approx C\epsilon^x k^y \quad (1.52)$$

where C is a dimensionless constant and $E(k)$ is the energy per unit mass carried by waves over an interval $\Delta k = k_1 - k_2$. By applying several assumptions and a dimensional analysis, it is possible to derive the expected values of x and y in Eq 1.52. One must assume the following for this analysis to hold true:

- For large Reynolds numbers, small-scale vortices are statistically steady, isotropic, and independent of the detailed structure of large-scale motion.
- Energy is not lost through viscous dissipation, but is transferred from large to smaller vortices through inertial forces.
- For sufficiently high Reynolds numbers, all small-scale motions statistically follow a universal form dependent on viscosity and dissipation rate.

In the dimensional analysis, the energy flow, ϵ , has base units

$$\frac{\text{energy}}{\text{mass} \cdot \text{time}} = \text{length}^2 \text{time}^3 \quad (1.53)$$

the wavenumber has units

$$\frac{1}{\text{length}} \quad (1.54)$$

and finally, $E(k)$ has units

$$\frac{\text{energy}}{\text{mass} \cdot \text{wavenumber}} = \frac{\text{length}^3}{\text{time}^2} \quad (1.55)$$

By substituting the dimensions defined in Equations 1.53, 1.54 and 1.55 into Equation 1.52 we achieve:

$$\frac{\text{length}^3}{\text{time}^2} = \left(\frac{\text{length}^2}{\text{time}^3} \right)^x \cdot \left(\frac{1}{\text{length}} \right)^y \quad (1.56)$$

Equating distance and temporal dimensions, we achieve a pair of simultaneous equations for x and y :

$$\text{length}^3 = \text{length}^{2x} \cdot \text{length}^{-y} \Rightarrow 3 = 2x - y \quad (1.57)$$

$$\text{time}^2 = \text{time}^{3x} \Rightarrow 2 = 3x \quad (1.58)$$

Solving this pair of simultaneous equations results in the completed form of Equation 1.52

$$E(k) \approx C\epsilon^{\frac{3}{2}} k^{-\frac{5}{3}} \quad (1.59)$$

where the dependency on the wavenumber is the well known Kolmogorov value $-\frac{5}{3}$.

Energy enters a system at large scales and is transferred to increasingly smaller scales through non-linear interactions between comparable scale structures. At the smallest scales, turbulent fluctuations eventually dissipate, raising the entropy of the

surrounding medium (Kiyani et al., 2015). The multi-scale nature of the turbulent perturbations in the magnetic field leads to a broad power-law in the measured power spectral density, which can change over the range of scales. As shown previously, for a constant rate of energy transfer in the inertial range, the range between the large energy input scales and small energy dissipation scales, the power law is expected to have a value of $-\frac{5}{3}$. Sharp gradient changes in this power law can indicate a transition from one range to the next. For example, in the solar wind, the typical power laws associated with the energy injection, inertial and dissipative scales are -1, $-\frac{5}{3}$ and -2.8 (Verscharen et al., 2019). Dissipation acts to steepen the power spectra of magnetic field fluctuations, as such a transition from typical inertial values to larger magnitude gradients could indicate a transition into the dissipative regime (Chandran et al., 2013; Schekochihin, 2022). Figure 1.5 shows a typical power spectra for a turbulent flow.

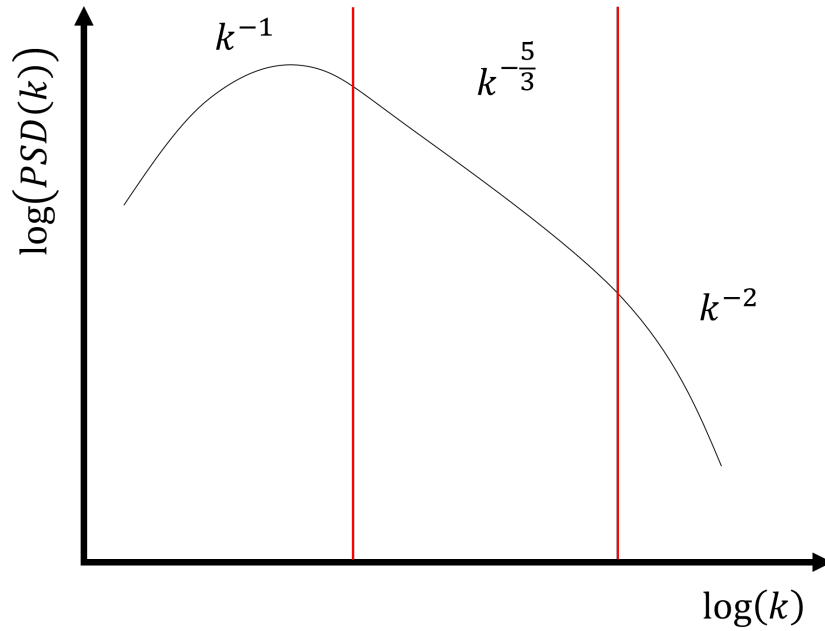


Figure 1.5: A typical power spectra for a turbulent flow. At low wavenumbers where the power law is less than $-\frac{5}{3}$ energy is supplied to the system. The Kolmogorov regime is located where the power law is $-\frac{5}{3}$, and the energy dissipative regime where the power law is negatively steeper than $-\frac{5}{3}$. Red vertical lines indicate spectral breaks, sharp changes in the gradient which can coincide with a traversal from one regime to the next. The frequency of the spectral breaks can provide information on the plasma mechanism responsible for supplying or dissipating energy from the system.

Resonance

Landau resonance occurs when the particle velocity is equal to the parallel phase velocity of the wave, as given in Equation 1.40. This results in a beam-like distribution. Particles traveling at a similar velocity will be accelerated by the

resonant interaction as they experience a relatively stationary electric field from their reference frame. Particles with a slightly greater velocity will be decelerated, while those with a slightly lower velocity will be accelerated. Within the Maxwellian distribution, there are more particles with a lower velocity than a higher velocity, and so there is a net increase in particle energy. When the wave frequencies are some integer multiple of the particle gyro frequency, a resonant interaction occurs perpendicular to the background field. Such resonance produces whistler mode waves and often manifests as an anisotropy in the pitch angle distributions.

Alfvén wave acceleration

Interactions between magnetospheric electrons and Alfvén waves can produce the spectrogram signature associated with stochastic acceleration. Alfvén waves induce a parallel electric field which can act to accelerate electrons. The phase velocity of the electric field is equal to the Alfvén velocity. For a reference frame traveling at the Alfvén velocity, the parallel electric field associated with the Alfvén wave would appear stationary. As such, electrons with velocities approaching the Alfvén velocity would have their velocities modified by the associated electric field. The overall velocity distribution, such as that shown in Figure 1.2, would be modified at the point near the Alfvén velocity. For an Alfvénic acceleration process, the adjustment to the distribution would reflect an energy increase, such as the example given in Figure 1.6

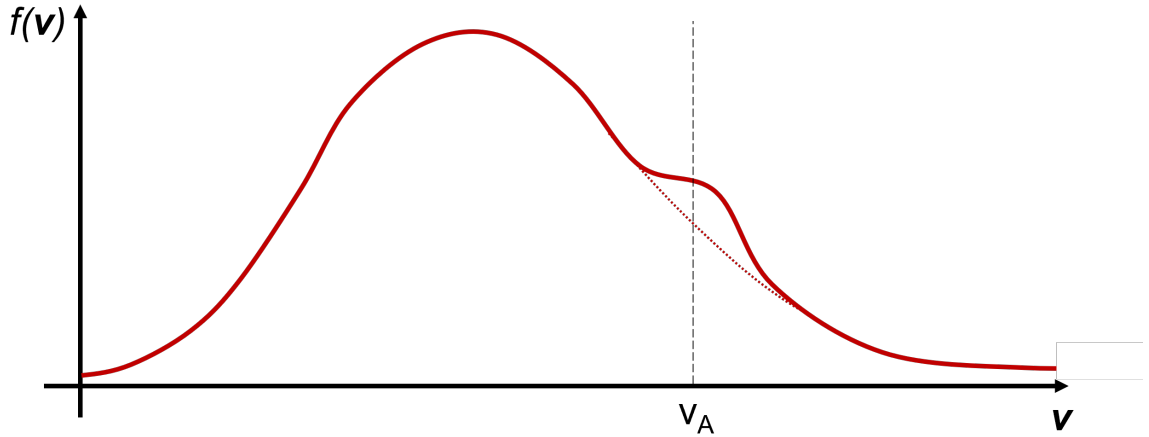


Figure 1.6: An example of the modified distribution function following Alfvénic particle acceleration. Electrons with velocities around the Alfvén velocity (black dashed line) are accelerated, leading to a net gain in energy. The dashed red line signifies the portion of the distribution function prior to electron acceleration.

Stochastic Acceleration

Stochastic acceleration is the name given to an energisation mechanism which produces a broadband feature in plasma energy spectrograms by non-resonant energy diffusion processes (McChesney et al., 1987; Chen et al., 2001; Johnson et al., 2001; Chaston et al., 2004; Fiksel et al., 2009; Karimabadi et al., 1994; Bourouaine et al., 2013). Turbulent perturbations, with spatial scales comparative to the local gyroradii of diffusing particles, distort the circular gyro-orbits of the particles, causing them to become disordered or stochastic in the plane perpendicular to the ambient magnetic field. The interactions of these particles with the time-varying electric fields causes diffusion in the perpendicular kinetic energy, which leads to heating in the

perpendicular direction (Chandran et al., 2013; Verscharen et al., 2019). Unlike Landau resonance or Alfvénic acceleration though, stochastic acceleration occurs over a much broader range of energies.

Poynting Flux

Waves are a transport mechanism for energy, the flow of which is quantifiable using the group velocity. The product of the group velocity and the energy density of the waves gives the energy transfer per unit area per unit time, or energy flux. For a purely electromagnetic wave the energy flux is given by the Poynting vector, \mathbf{S} ,

$$\mathbf{S} = \frac{\mathbf{E} \times \mathbf{B}}{\mu_0} \quad (1.60)$$

where \mathbf{E} and \mathbf{B} are the electric and magnetic fields respectively, and μ_0 is the permeability of free space. For Alfvén waves, one only needs knowledge of the magnetic field and Alfvén velocity in order to determine the Poynting vector. Since $\mathbf{E} = v \times \mathbf{B}$, $\frac{\delta E}{\delta B} = v_A$ for an Alfvén wave, where δE and δB is the value of the perturbed electric and magnetic field respectively, and v_A is the Alfvén velocity of the wave, the Poynting flux of an Alfvén wave can be written as:

$$S = \frac{\delta B^2 v_A}{\mu_0} \quad (1.61)$$

This is fundamental to the work in Chapter 6, where only plasma and magnetic field data are available to infer the Poynting flux from. A direct comparison between the Poynting flux and auroral energy flux can then be used to infer the significant contribution Alfvén waves have in the generation of auroral emissions, which is

discussed in further detail in Chapter 6.

1.4 Conclusion

This chapter has provided the relevant knowledge describing the origins of electric and magnetic fields, and the definition of a plasma. Additionally we explain the kinetic and fluid descriptions used to understand the dynamics of plasma systems, such as the motions of particles in the presence of varying electric and magnetic field configurations, how currents arise, and the generation of waves and their dissipation mechanisms. After exploring the relevant background theory needed to understand the more complex aspects of space plasma physics we proceed into Chapter 2, where we apply these concepts in describing the dynamic interaction of the solar wind with planetary magnetic fields, which drives magnetospheric dynamics and the mechanisms associated with the generation of planetary aurorae.

Chapter 2

Dynamics of the Jovian System

This chapter builds upon the fundamental physics outlined in Chapter 1 to describe the dynamics of the Jovian system. Although much further from the sun than Earth, the Jovian system is still influenced by variations in the solar wind. As such, this chapter begins with an outline of the solar cycle and solar wind. Following this, a description of planetary magnetospheres is given, using the terrestrial magnetosphere as a base model, before comparing and contrasting it with Jupiter's. This transitions to a discussion of the Galilean satellites, the global current disk and the coupling of the global current disk to the planetary ionosphere. Finally, observations of the Jovian aurora and current theories on their generation mechanism are communicated.

2.1 Solar wind and Heliosphere

We cannot discuss the physics of the Jovian magnetosphere without first giving some attention to Sol, the star at the center of, and the eponym to, our solar system. Powered by the nuclear fusion of hydrogen into helium, the sun is the primary source

of energy for all bodies within the solar system. The sun's magnetic field is also a driver of auroral activity on magnetised bodies within the solar system, which is facilitated in part through the solar wind.

Plasma in the upper atmosphere of the sun undergoes continuous heating to the point where its velocity exceeds the sun's escape velocity. The result is a continuous outward expansion of plasma along the sun's magnetic field, referred to as the solar wind. The solar wind is a highly conducting tenuous plasma, comprising mainly of protons and electrons which flow radially away from the sun. This plasma has a typical velocity of 400 km s^{-1} , density of 7 cm^{-3} and magnetic field strength of 5 nT at 1 AU (Suess et al., 2003). The solar magnetic field remains frozen into the streaming plasma due to its high conductivity and, with its foot point anchored to the rotating sun, produces an Archimedean spiral as it travels radially outward forming the interplanetary magnetic field (IMF), as illustrated in Figure 2.1. This spiral-like structure is known as the Parker spiral (Parker, 1958). For increasing radial distances the Parker spiral is wound tighter and tighter, resulting in the interplanetary magnetic field developing a stronger azimuthal component at larger radial distances. This structure extends out to what is known as the heliopause, the point where the pressure from the solar wind balances with the pressure of the interstellar medium. The region known as the heliosphere is the volume of space bounded by the heliopause surface.

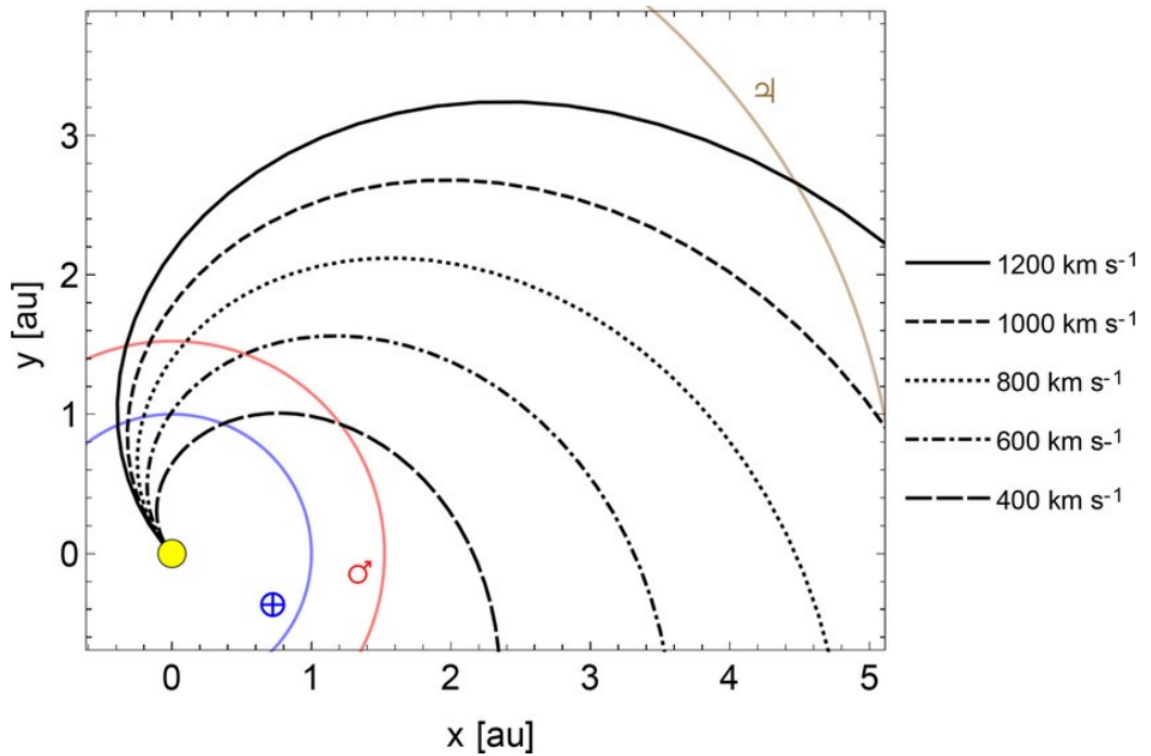


Figure 2.1: An equatorial projection of the Parker spiral model of the interplanetary magnetic field for varying plasma velocities from (Lhotka et al., 2019). The orbits of Earth, Mars and Jupiter are showed in blue, red and orange respectively. As the interplanetary magnetic field moves radially outward its angle of incidence decreases. For example, the $1,200 \text{ km s}^{-1}$ profile has an almost perpendicular angle of incidence at Earth's orbit (Blue), but intersects the Jovian orbit at a much shallower angle.

Over a 22-year process, known as the solar cycle, the sun goes through periods of increasing and decreasing activity as its magnetic field reverses. This is often quantified by the distribution of sunspots over its surface (McComas et al., 2003). The frequency of solar flares and coronal mass ejections also vary with cycle, as well

as the velocity and pressure of the solar wind. Figure 2.2 demonstrates the variation in the solar wind over half of the solar cycle. As can be seen in this figure, the IMF becomes highly disordered during solar maximum, and the polarity of the IMF flips in the approximately 11 year period. When the solar wind reaches obstacles, such as a planetary magnetosphere, the consequences of these variations can be quite pronounced.

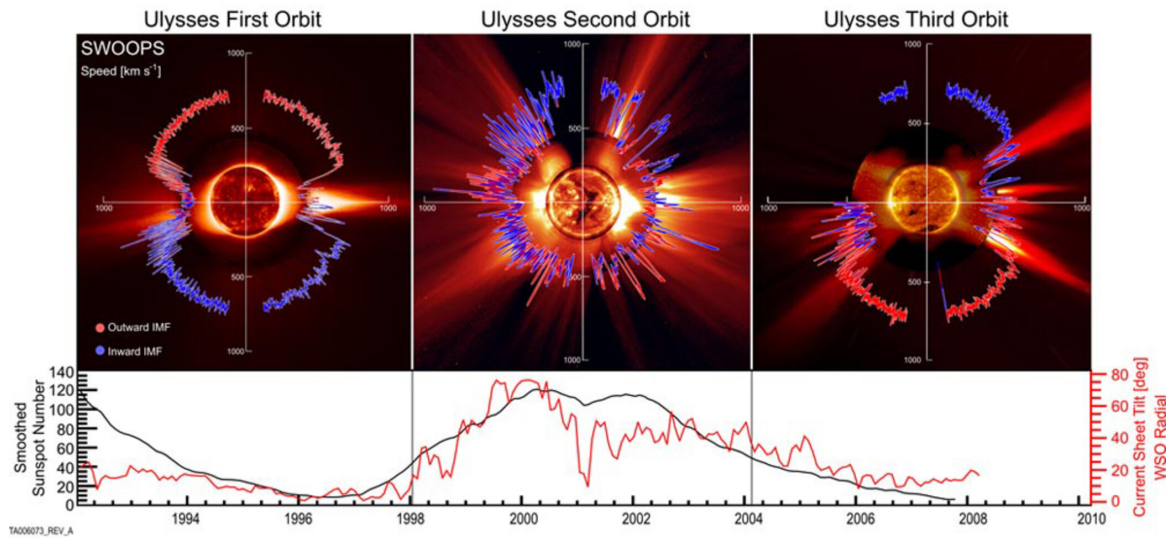


Figure 2.2: The variation of the solar wind over the solar cycle taken from McComas et al. (2008). The top three panels are polar plots of the solar wind velocity for the three Ulysses orbits. The profile colour denotes the polarity of the IMF, with blue being inward and red being outward. The bottom panel can be used to determine the phase of the solar cycle based off the sunspot number.

2.2 The Terrestrial Magnetosphere

A magnetosphere is a cavity within the heliosphere carved out by the magnetic field of a planet or satellite. The magnetosphere is defined as the region in which the forces associated with the magnetic field of the body dominate over the external forces. Due to the interaction with the impinging interplanetary magnetic field, the magnetosphere assumes a paraboloidal geometry, being compressed by the solar wind on the sun-ward side and elongated in the direction of the solar wind flow on the night side (Chapman et al., 1930; Hughes, 1995).

Figure 2.3 illustrates the anatomy of Earth's magnetosphere, which labels several points of interest. The bow shock is the point where the supersonic solar wind velocity becomes subsonic, while the magnetopause denotes the area where the solar wind pressure is in equilibrium with the planet's internal magnetic pressure.

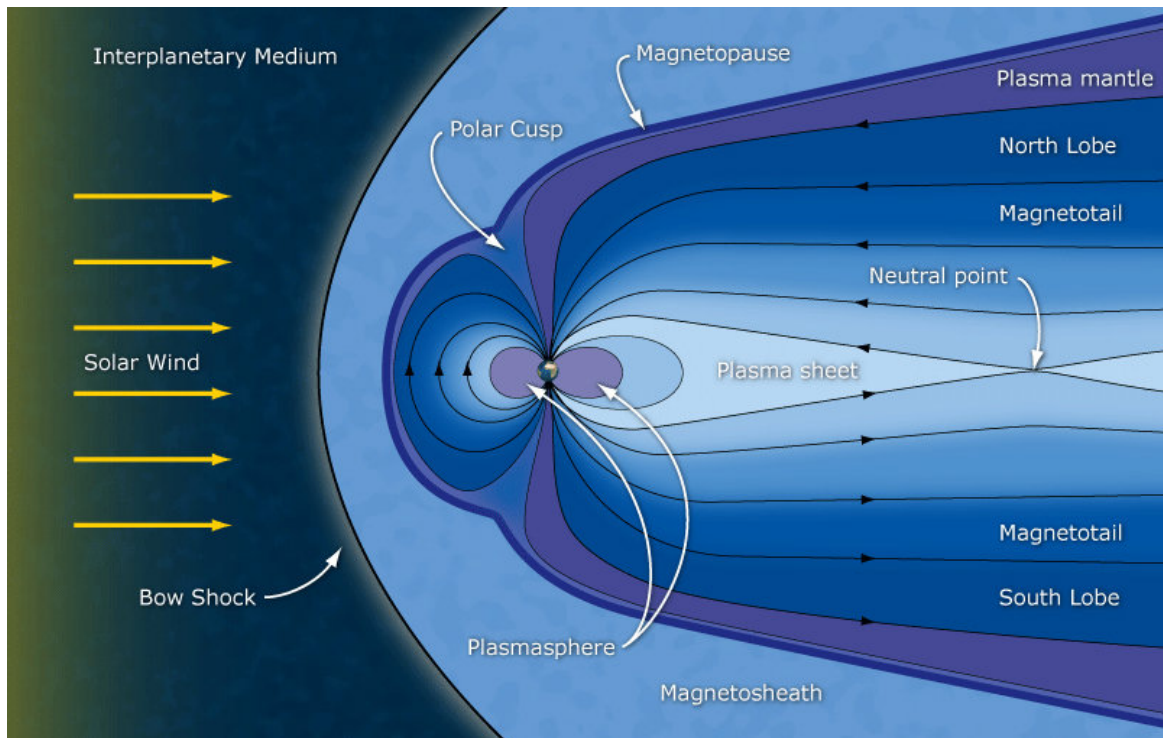


Figure 2.3: A graphical representation of the terrestrial magnetosphere. The dipole geometry of the magnetic field is compressed on the sunward side and elongated on the night side due to the impinging solar wind. Image Credit: ESA/C.T.Russell/Case (n.d.)

The terrestrial magnetosphere comprises of several substructures which form as a consequence of the interaction of the intrinsic field with either the solar wind, or internal processes. Where these magnetic fields interact there is a change in the local magnetic field strength which, according to Ampère’s law, forms a current sheet at the interaction boundary. Current sheets act to deform the magnetic field topology, and play host to magnetic reconnection events (Dungey, 1961).

On the sunward facing side of the magnetosphere, the interaction between the solar magnetic field and the planetary field forms a current sheet boundary known as the magnetopause (Chapman et al., 1930). Its distance from the planet, or standoff distance, can be estimated by balancing the internal pressure, $P_B = \frac{B^2}{2\mu_0}$, within the magnetosphere with the external solar wind dynamic pressure, $P_d = \rho v_{sw}^2$. The standoff distance can be estimated, assuming the magnetic field falls off at a rate of $B(r) = \frac{B_0}{r^3}$, with

$$r = \left(2 \frac{B_0^2}{\mu_0 \rho v_{sw}^2} \right)^{\frac{1}{6}} \quad (2.1)$$

where B_0 is the magnetic field strength at the equatorial surface, μ_0 is the permeability of free space, and ρv_{sw}^2 is the solar wind dynamic pressure. The factor of two accounts for the induced magnetopause currents.

2.2.1 Magnetic reconnection

One key interaction in space plasma physics is the process of magnetic reconnection, hereafter referred to simply as reconnection. This is the process under which oppositely directed magnetic fields within a plasma “break” and reconnect. The process results in energy trapped in the magnetic field being converted to kinetic energy or Poynting flux. Reconnection between the solar wind and the Earth’s magnetic field is known to accelerate particles into the high-latitude regions and generate aurora.

The simplest case of reconnection can be considered as two opposing magnetic

fields moving towards one another. Owing to Ampère’s law, a current sheet is formed between these opposing fields. Thermal pressure from the compressed plasma and magnetic pressure resulting from the $\mathbf{J} \times \mathbf{B}$ force brought on by the induced current sheet forces the plasma together. Due to the frozen in nature of the field, the field is also drawn in, compressing the magnetic field topology. Thermal and magnetic pressure continue to compress the magnetic field lines, thinning the current sheet. The gradient of the magnetic field becomes large enough that the diffusive term in Eq 1.27 dominates over the convective term. A diffusion region forms, where the magnetic field can separate from the plasma and reconnect with the opposing field. The point at which reconnection occurs, at the centre of the diffusion region, is known as the “X-line”. Magnetic tension forces then carry reconnected field lines away from the reconnection site, perpendicular to the compressed field lines.

At Earth, reconnection occurs at the dayside and nightside magnetosphere. Dayside reconnection reconfigures the Earth’s magnetic field, forming “open” field lines. Realistically the field lines are connected to the solar magnetic field. Field lines which have undergone reconnection on the dayside then convect over the Earth’s polar regions where they begin to pile up on the nightside magnetosphere, forming a current sheet. As more field lines build up, reconnection is triggered. The closed reconnected field lines are no longer connected to the solar IMF and convect back round to the dayside magnetosphere. Once back in the dayside magnetosphere these magnetic field lines can then undergo further reconnection, repeating the process in what is known as the “Dungey Cycle” (Dungey, 1961), which is illustrated in Figure 2.5.

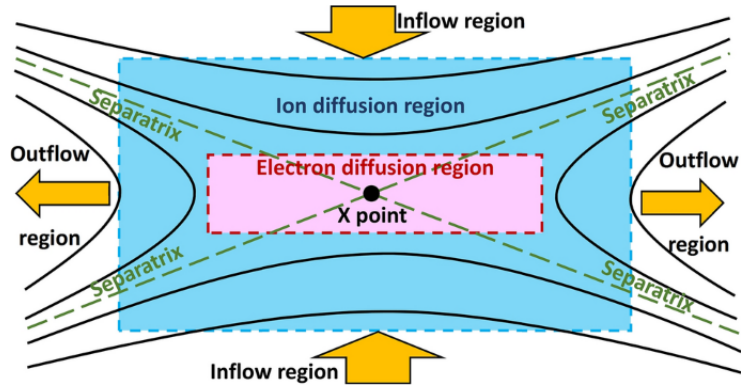


Figure 2.4: An illustrating of the magnetic reconnection process from Lee et al. (2020)

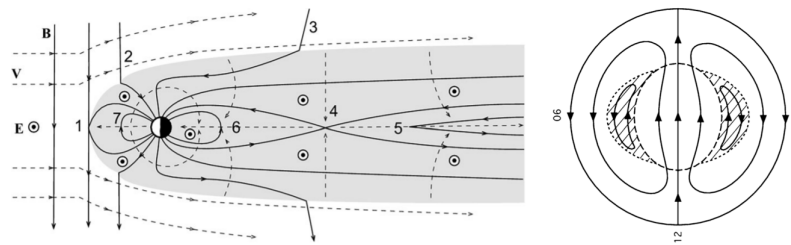


Figure 2.5: The flow dynamics of the terrestrial Dungey Cycle as seen from a magnetospheric (left) and ionospheric (right) perspective. Here, (1) the southward solar wind undergoes reconnection with the planetary magnetosphere in the dayside region. (2 - 3) The open magnetic field convects across the polar cap and begins to “pile up” in the nightside magnetosphere. (4) Tail reconnection occurs as magnetic flux increases due to the convection of open field lines, closing the open field lines, (5) ejecting plasmoids downtail and (6) returning the other closed field lines planetward. (7) The planetward flowing field lines convect around the planet, returning to the dayside and beginning the cycle anew. Image Credit: Seki et al. (2015)

2.3 Jupiter, The Planet

Discovered in 1610 by Italian astronomer Galileo Galilei, Jupiter is the largest planet within our solar system, with an equatorial radius of $R_J = 71,492\text{km}$. Initially appearing more like a failed star than a planet, Jupiter is mainly comprised of hydrogen and helium, making up over 87% of its mass. Its structure consists of a potentially rocky core, surrounded by a churning hydrogen mantle, above which lies its iconic cloud layer (Guillot et al., 2004).

Gravitational collapse and remnant heat from formation heat the planet's interior, causing convection within the liquid hydrogen layer. The churning of the metallic hydrogen creates a sufficient dynamo effect to form an powerful magnetic field, making Jupiter's magnetosphere is the largest object in the solar system (Khurana et al., 2004).

2.4 The Jovian Magnetosphere

The magnetosphere of Jupiter is similar to that of Earth, displaying many of the same characteristics, however it is much stronger and larger, with a magnetotail extending outwards past the orbit of Saturn. Furthermore, the presence of a dense internal plasma source, coupled with the rapid rotation of the system, produces a global current sheet, hereafter referred to as the current disk. This acts to deform the magnetic field topology, as can be seen in Figure 2.6, and facilitates the exchange of momentum between the planet and the magnetospheric plasma through a $\mathbf{J} \times \mathbf{B}$ force associated with corotation breakdown. This is discussed in more detail in Chapter 4.

In addition to deforming the magnetic field topology, the plasma disk also acts to inflate the magnetosphere. This is evident by substituting typical parameters at 5 AU into equation 2.1. Taking a solar wind dynamic pressure of around 0.4 nPa (Tao et al., 2005a) and a magnetic field strength of 450,000 nT (Connerney et al., 2018), the magnetopause standoff distance should be around 31 R_J , which is much less than observed bi-modal probabilistic magnetopause standoff distance at 62 to 93 R_J (Joy et al., 2002), indicating Jovian magnetosphere inflation is driven by additional forces. The bi-modal nature of the magnetopause is believed to be, in part, from the bi-modal nature of the solar wind at 5 AU. The solar wind exhibits bi-modal distributions in its velocity, proton density, temperature and magnetic field (Larrodera et al., 2020) due to it originating from different sources, producing two “types” of solar wind. “Fast” solar wind, originating from open magnetic field regions is has a higher temperature, and is less dense than the “slow” solar wind, which originates from regions of closed magnetic (Owens, 2020). The subsequent bi-modal dynamic pressure resulting from the distribution is believed to produce the bi-modal magnetopause standoff distances observed at Jupiter.

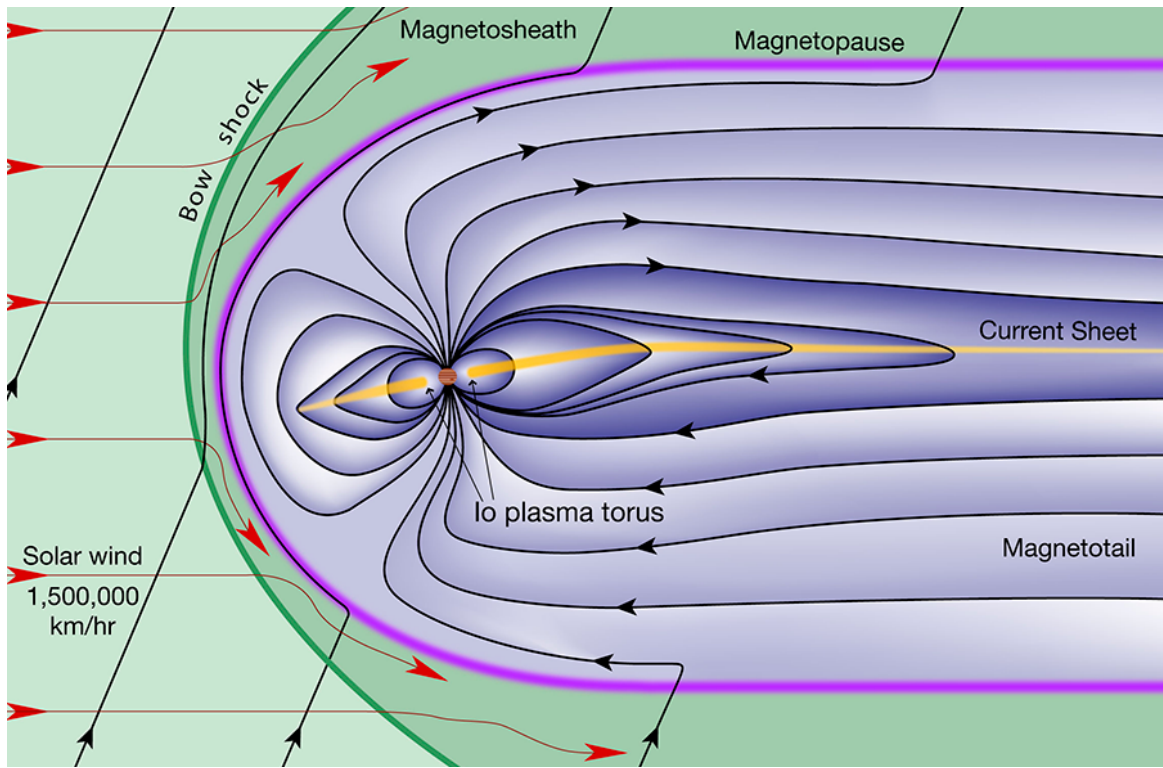


Figure 2.6: An illustration of the Jovian magnetosphere. For scale, the entirety of the terrestrial magnetosphere can fit within the planet Jupiter itself. This illustration demonstrates the distorted nature of Jupiter's middle magnetosphere when compared with the typical terrestrial example above. The parabolic geometry enforced externally by the solar wind and the extreme extent to which the internal topology is defined by the presence of a current disk (labelled here as the current sheet) is evident to see. One can also notice the opposite polarity of the magnetic field compared with Earth's. Image Credit: (Bagenal et al., n.d.)

2.4.1 The Galilean Satellites

Within its assortment of over 63 satellites are Io, Europa, Ganymede and Callisto. These are the Galilean satellites, discovered and named after Galileo Galilei shortly after his discovery of Jupiter. They are the largest of Jupiter's satellites and their proximity to the planet and unique orbits play a defining role in the system's magnetospheric dynamics. The satellites exist in unique resonant orbits, whose tidal forces influence a profound effect on the entire magnetosphere (Schubert et al., 2004). The harmonic orbits of the 4 Galilean satellites provide a slight "kick" to each of the moons' orbital velocities, resulting in a slightly elliptical orbit. The associated variation in the gravitational forces acting on the moons by Jupiter produce a tidal heating effect in the core, driving volcanic activity and resulting in potentially habitable oceans on Europa and Ganymede (Khurana et al., 1998; Kivelson et al., 1999; Kivelson et al., 2000).

Io's volcanic activity extends the influence of this tiny satellite out into the whole magnetosphere. Io's extremely thin atmosphere (3.5 g cm^{-3}) is dominated by volcanic sulphur dioxide. This atmosphere, coupled with a low escape velocity allows out-gassing to supply large amounts of sulphur and oxygen derived compounds to the surrounding magnetosphere. Out-gassing to the magnetosphere occurs at a rate of between $700 - 1300 \text{ kg s}^{-1}$ of material (Bagenal et al., 2011; Hill et al., 1983), producing a neutral cloud source. Electron impact and charge exchange ionises the neutral clouds. It is expected that less than 20% of the mass outflow from Io is ionised (Saur et al., 2003). Once ionised the resultant plasma is caught up in the planetary magnetic field and accelerated from its initial Keplerian velocity up to corotation with

the planetary magnetic field (Schneider et al., 2007). The result is a dense plasma torus.

2.4.2 The Plasma Disk

The existence of a plasma disk at Jupiter was long established since the flybys of the Pioneer probes in the 1970s (Smith et al., 1974; Hill et al., 1976). Neutral gasses, ionised by electron impact and charge exchange, form the plasma torus. At the Io orbital distance, the ambient field is mostly dipolar. Charged particles within the torus oscillate along the magnetic field about the centrifugal equator, a plane defined by points along the magnetic field line furthest from the planetary spin axis. The angle of inclination of this plane to the magnetic equator is approximately two-thirds of the tilt angle between the magnetic and rotational equator (Thomas et al., 2004). This centrifugal equator is a product of large centrifugal forces acting on plasma within the Jovian magnetosphere. At greater radial distances, up to $25 R_J$, the equilibrium point deviates from the centrifugal equator towards the dipole equator (Phipps et al., 2020).

The evolution of the Io plasma torus to the magnetospheric plasma disk occurs through flux tube interchange events, which act to diffuse Iogenic plasma into the system whilst conserving magnetic flux (Thomas et al., 2004; Kivelson et al., 2005b; Achilleos et al., 2015). Additionally, fluctuations in the electric and magnetic field with temporal variations occurring over time periods shorter than the particle bounce period will break the third adiabatic invariant and lead to radial diffusion (Brice et al., 1973; Schulz, 1979; Walt, 1994).

The strong centrifugal forces acting on the plasma produce a thin radial disk, the spatial distribution of which is non-uniform in both density and temperature (Bagenal et al., 2011). The regions above and below the plasma disk are referred to as the “lobe” regions which are regions of closed magnetic field lines in contrast with the terrestrial magnetosphere, in which the lobe field is open. The plasma disk dominates the dynamics of the middle magnetosphere, and couples to the planet through a complex current system. Within this system is a partial ring current, arising due to the drift motions detailed in Chapter 1. In the middle magnetosphere, these currents act to diminish the equatorial magnetic field, resulting in a distension of the magnetic field topology (Vasyliunas, 1983) into a disk like configuration. In the middle magnetosphere, large-scale injection events dominate the mass transportation process. Injection events, hot inward flowing plasma observed in plasma data as transient enhancements of energy-time-intensity spectrograms, have been reported to occur as frequently as 5 times per Jovian day (Mauk et al., 1999).

The departure from rigid corotation of the frozen-in equatorial plasma disk in the middle magnetosphere drags the magnetic field into a bent back configuration with respect to the Jupiter-sun line. This can be seen in magnetometer data, manifesting as a strong azimuthal component. The resulting topology is independent of the terrestrial and solar wind configurations. Figure 2.7 illustrates the similarities between the magnetic field topology.

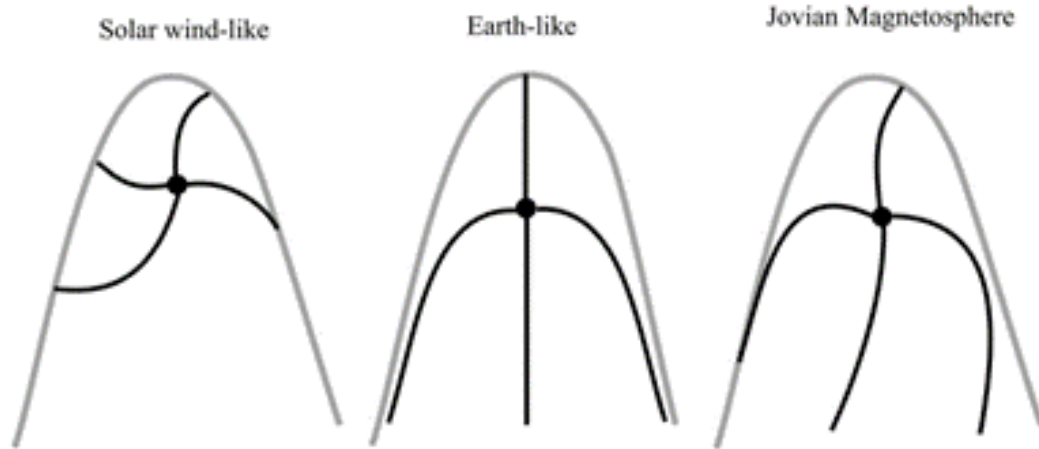


Figure 2.7: The configuration of the Solar, terrestrial and Jovian magnetosphere. The interaction of the solar wind, coupled with the departure from corotation of the equatorial plasma disk leads to a magnetic field configuration independent of the solar wind and terrestrial geometry. Image Credit: (Khurana, 2001)

Plasma must be lost from the system eventually, lest the magnetosphere continue to inflate indefinitely. The Vasylunas (1983) cycle describes the periodic loss of material through centrifugally driven reconnection events. Once a flux tube reaches a critical plasma content the local plasma sheet becomes unstable. Rotating past the dusk sector, the expansion of the magnetopause offers no boundary to support the loaded tube. As such, plasmoids are ejected downtail as a mass loss mechanism (Kivelson et al., 2005b). Furthermore, large pressure anisotropies act to expand flux tubes into unstable configurations before ejecting their plasma contents. This cyclic process can be seen in Figure 2.8.

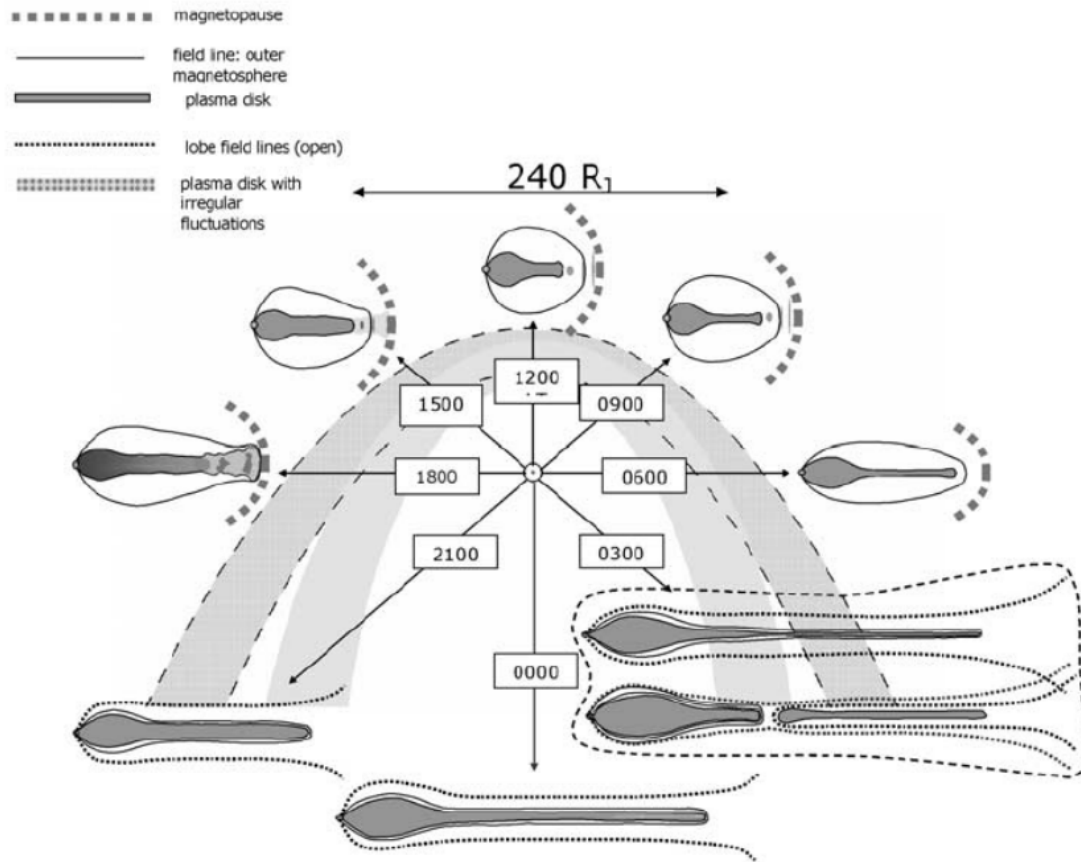


Figure 2.8: An illustration of the cyclic motion of plasma within the Jovian magnetosphere from Kivelson et al. (2005b).

2.5 The Terrestrial Ionosphere

In upper planetary atmospheres there exists a region in which ionised and neutral particles coexist. The ionised portion of this region is referred to as the ionosphere. In its simplest form, the ionosphere can be approximated as a thin conducting slab,

however it extends over a range of altitudes up to approximately 1000 km. Due to its much higher plasma number density being embedded in a dense neutral plasma, the ionosphere is collisional and is not an ideal plasma. This is essential for the generation of auroral emissions (Luhmann, 1995) as charged magnetospheric particle transfer their energy to atmospheric particles through collisions.

Ionisation of neutrals within the upper atmosphere provide one source of plasma for the ionosphere. Chapman's theory of ionospheric layer formation (Chapman, 1931) is used in modelling the ion production as a function of altitude. The theory states that peak ion production occurs in the vicinity of an altitude specified where the total number of particles in a unit column is equal to the inverse of the absorption cross section. Chapman theory therefore provides a model describing ion production as a function of the neutral density and the solar radiation intensity. The resulting altitude of maximum production is named the Chapman Layer, while the functional profile of electron density over altitude is named the Chapman profile. Electron precipitation will also play an important role in the ionisation of upper atmospheric neutrals, however it is not considered in Chapman theory. The terrestrial atmospheric profile is displayed in Figure 2.9, in which a Chapman layer can be seen at approximately 300 km, denoted by the F region.

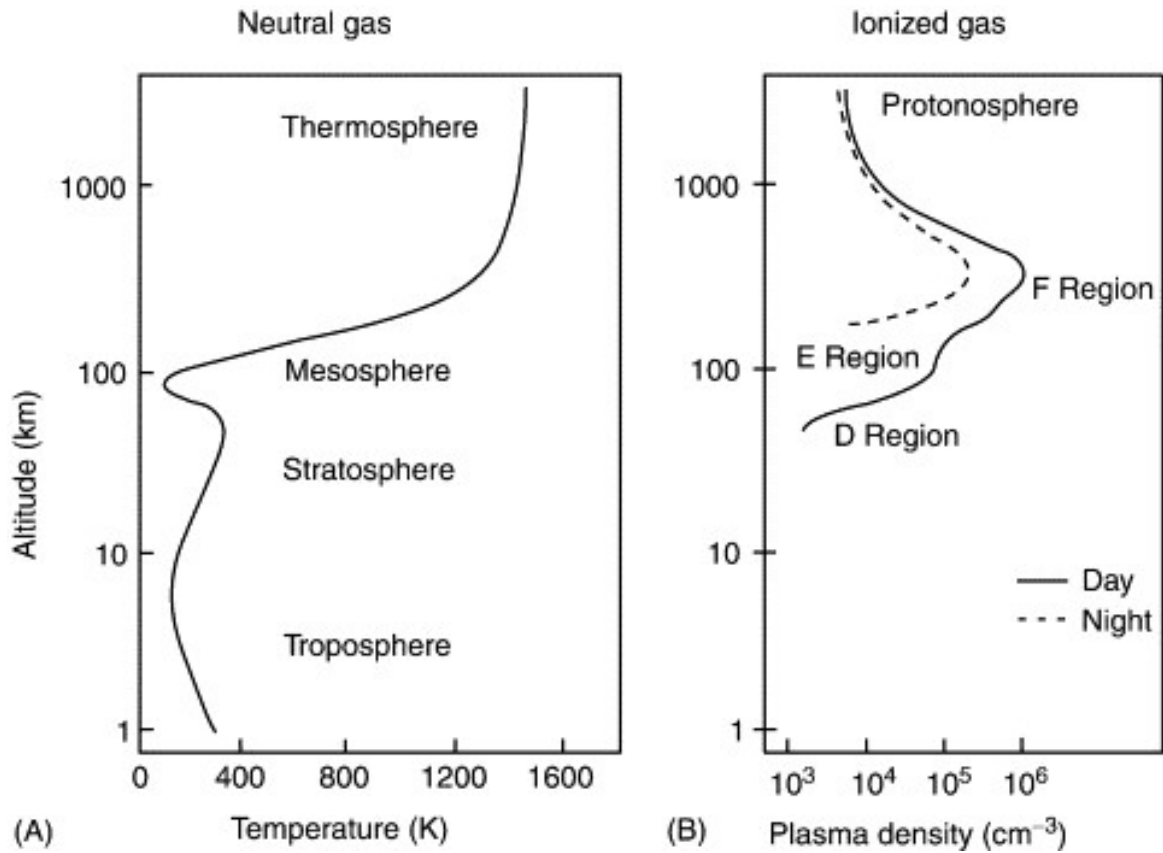


Figure 2.9: The terrestrial atmospheric profile illustrating the coexistence between the neutral upper atmosphere and ionised ionosphere. Retrieved from Kelley (2003)

One property of this ionised layer is its ability to reflect electromagnetic radiation. Waves in a magnetosphere are dependent on the boundary conditions of the system. The ionosphere would function as one such boundary. The density of charged species directly affects the degree of refraction experienced by incident waves. For a highly conducting ionosphere, dense layers of charged particle populations act as a refractive layer for electromagnetic waves, subsequently resulting in a reflection of incident waves on the ionosphere back along the field line away from the planet. Ionospheres with a

lower conductivity will still partially reflect waves, though reflection only occurs for select harmonic frequencies.

The presence of atmospheric neutrals leads to collisions with ionospheric ions. These collisions give rise to a phenomenon known as Joule heating, a mechanism which dissipates energy within an ionosphere through collisional friction. At Earth and Jupiter, this process also mediates the transfer of momentum and energy between the planet and its magnetospheric plasma.

Current systems arise within the ionosphere because of the interplay between magnetic and collisional forces controlling the plasma motion. Birkeland, or field-aligned currents are associated with auroral particle precipitation. They act to couple the ionosphere to the magnetosphere. Electrons can precipitate into the upper atmosphere along upward field-aligned currents, producing visible auroral emissions. Field-aligned currents alone are not sufficient to cause electron precipitation. Some form of acceleration is required to account for observed auroral emissions. The Knight relation (Knight, 1973) gives the expected field-aligned potential required to promote electron precipitation. This relationship is explained in further detail in Chapter 5.

Ionospheric closure of the M-I coupled system occurs via currents flowing perpendicularly to the ambient field. These occur in the region of the ionosphere when the collision frequency is approximately equal to the ion gyrofrequency and collisions between atmospheric neutrals and ions becomes significant (Kaepler et al., 2012). The currents flow through regions of increased conductivity, while their orientation is

determined by the perpendicular electric field. Pedersen currents flow parallel to the perpendicular electric field, while Hall currents are perpendicular to the electric and magnetic field.

2.6 The Jovian Ionosphere

Jupiter's ionosphere boasts many similarities to that of the terrestrial ionosphere. Extreme ultraviolet radiation and charged magnetospheric particles dissociate and ionise upper atmospheric neutrals. Unlike Earth however, Jupiter's main atmospheric constituent is hydrogen which isolates itself in the upper atmosphere due to its low mass. This leads to an upper atmosphere which is relatively pure by comparison to Earth's.

Figure 2.10 shows the temperature and electron density profiles in the upper Jovian atmosphere. As there is no apparent surface, it is more intuitive to refer to altitudes either by pressure, as is the case in panel a, or as a distance above the 1 bar level. Within this region, the typical collisional mean free path ranges between 10 cm to 150 km. This is lower than the atmospheric scale height in this region (≈ 200 km), meaning ion-neutral collisions facilitating momentum exchange are important (Yelle et al., 2004).

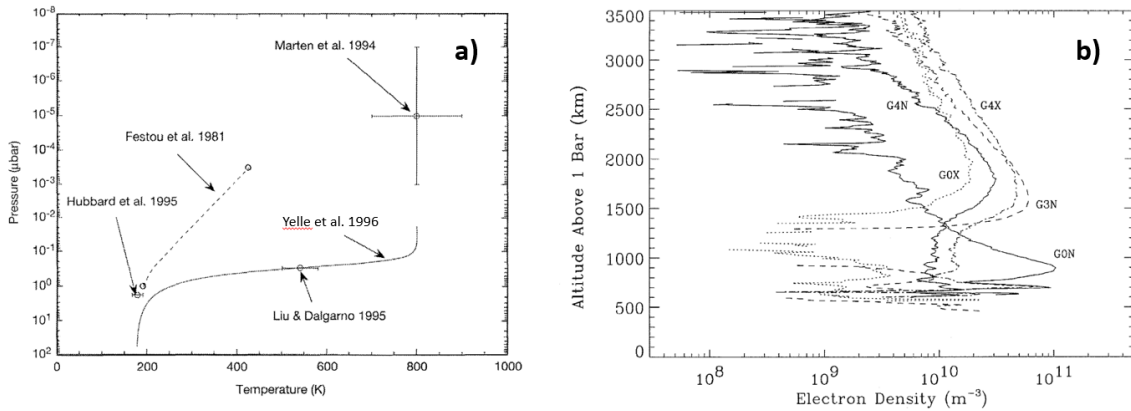


Figure 2.10: A) Jovian atmospheric temperature profile containing data from previous observations and models. B) electron density profile of Jupiter's upper Atmosphere based of Galileo spacecraft observations. Adapted from figures 9.9 and 9.10 in Yelle et al. (2004)

2.6.1 Jupiter's Auroral Emissions

Any planet or satellite with a collisionally thick atmosphere and an internal magnetic field of sufficient strength to resist the solar wind or plasma flow will exhibit an aurora process. An aurora is part of the exchange of energy and momentum between a magnetised body's magnetosphere and its atmosphere in the form of electromagnetic radiation. Energetic particles with sufficient parallel energy, most often electrons, traveling along high latitude magnetic field lines penetrate into a planetary atmosphere and excite atmospheric particles. Atmospheric neutrals enter an excited state where their bound electrons move to a higher energy state. When the electrons relax to a lower energy state they emit a photon of light at a wavelength corresponding to the difference in energy shells.

Precipitation of electrons can occur in a number of ways. There exists a range of equatorial pitch angles over which the particle has sufficient parallel energy to precipitate. This range is referred to as a loss cone. Increasing the parallel velocity of a particle can place it within this loss cone and hence allow it to penetrate into the upper atmosphere. Parallel velocity increases can be facilitated via an acceleration of electrons by quasi-static electric fields. Waves within the magnetosphere can also act to accelerate electrons, or in other cases scatter them into the loss cone.

The Jovian aurora is by far the most powerful aurora in the solar system, with energies one hundred times that of Earth's and a brightness up to ten times greater. The first observations of Jupiter's auroral emissions have been present since the Voyager 1 flyby (Broadfoot et al., 1979). Using ultraviolet spectroscopy, Waite et al. (1983), identified the auroral emissions as originating from excitation of atomic and molecular hydrogen in Jupiter's upper atmosphere. Several factors determine the driving mechanism behind the auroral emissions, such as the orientation of the solar magnetic field, the plasma density and distribution within the planet's magnetosphere and its proximity to the sun. Unlike Earth, Jupiter's aurora is driven by internal influences, such as the density of its plasma disk. Jupiter's aurora has been primarily imaged in the ultraviolet and infrared ranges. Ultraviolet emissions are the result of energised atomic and/or molecular hydrogen, while ionisation of H₂ molecules are responsible for the infrared emissions. Figure 2.11 depicts the process responsible for generation of auroral emissions in hydrogen dominated atmospheres.

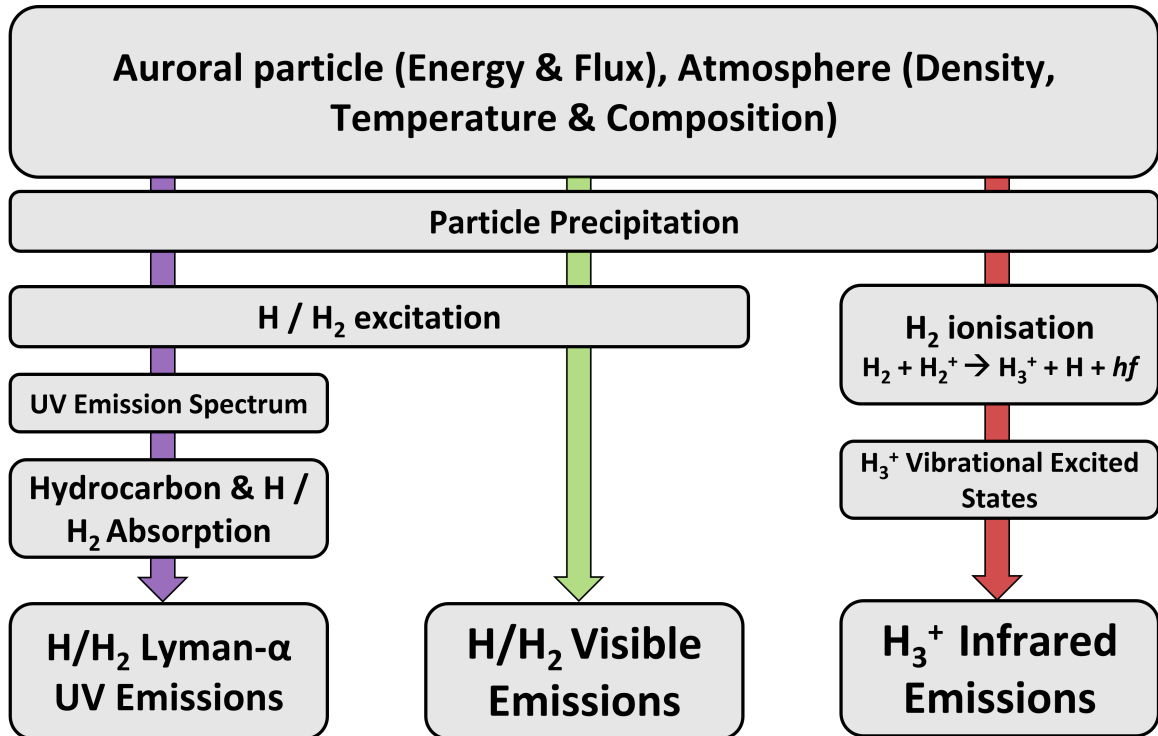


Figure 2.11: The auroral emission processes present in a hydrogen dominated atmospheres. Adapted from Badman et al. (2015)

Jupiter’s auroral emissions can be split into three main constituents. These can be seen highlighted in Figure 2.12. Conjugate features associated with these regions are commonly observed in both hemispheres, though the northern emissions form a distorted, “kidney-bean” shape owing to the northern magnetic anomaly associated to a local weakening in the surface magnetic field (Grodent et al., 2008b). This thesis focuses on the mechanics responsible for the generation of Jupiter’s main auroral emission, a continuous circumpolar emission associated with mechanisms within the middle magnetosphere. The corotation of the middle magnetosphere is conserved

by a viscous torque formed by collisions between upper atmospheric neutrals with the lower velocity ions (Hill, 1979; Hill, 2001). Coupling of the system is facilitated through field-aligned currents, as illustrated in Figure 2.13.

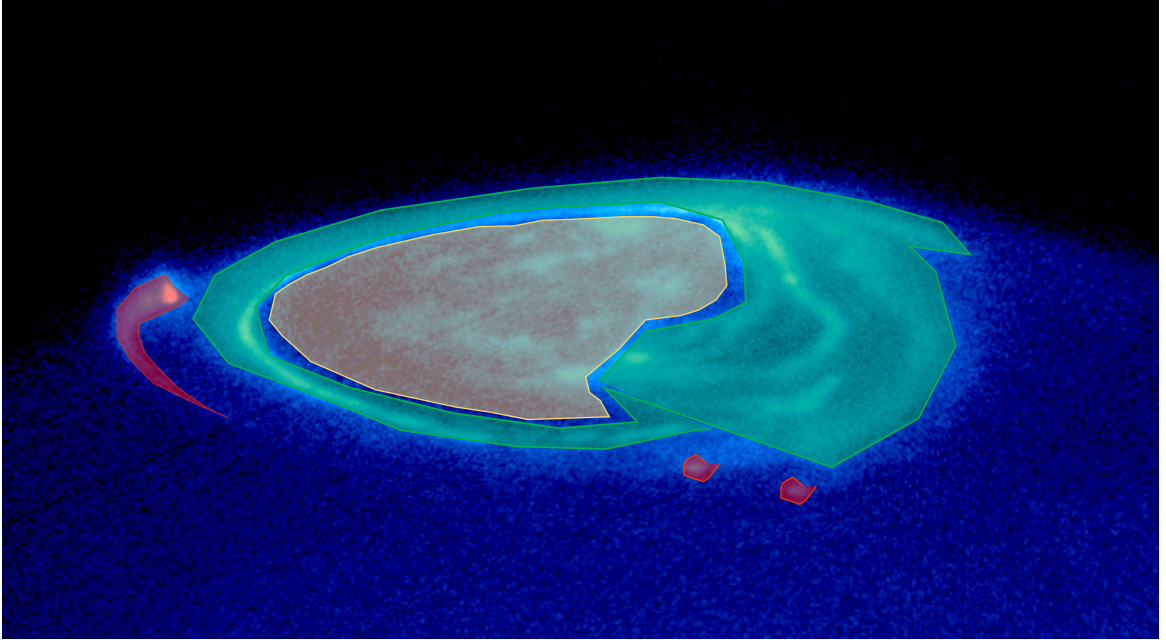


Figure 2.12: An image of Jupiter's UV aurora taken by the Hubble Space Telescope. Orange, green and red regions denote the polar flashes, main emission and satellite footprints with wake, respectively. Credit: NASA/HST

Momentum exchange is inhibited at greater radial distances due to external forces or the plasma's inertia. Corotation breakdown occurs at a critical radius. The distance at which the deviation from corotation is significant is given in Hill (1979) as

$$R_c = \left(\frac{\pi \Sigma' B_E^2 R_J^2}{\dot{M}} \right)^{\frac{1}{4}} \quad (2.2)$$

where R_c is the characteristic distance in units of Jovian radii, Σ' is the effective Pedersen conductance, B_E is the equatorial surface magnetic field strength and \dot{M} is the rate of outward mass transport. Substituting in reasonable values for each variable, $\Sigma' = 0.2$ mho (Cowley et al., 2001), $\dot{M} = 1000$ kg s⁻¹ (Bagenal et al., 2011), and $B_E = 644,000$ nT (Connerney et al., 2018), R_c is found to be around $15 R_J$, at the lower end of the generally accepted range, $15 - 30 R_J$ (Khurana et al., 2004; Clarke et al., 2004). It should be noted that other factors, such as ionospheric conductance and magnetic configuration will influence this value significantly. Increases in volcanic activity at Io would lead to a greater mass outflow rate, resulting in corotation breaking down at smaller radial distances.

Alfvén waves and parallel electric fields associated with field-aligned currents linking the system would be responsible for facilitating electron precipitation into the main auroral emissions, which maps to field lines within $15 - 30 R_J$ (Khurana et al., 2004; Clarke et al., 2004). Due to its internal driving, the main auroral emission corotates with the planet and has discrete regions associated with specific magnetospheric dynamics such as intense dawn storms. The main auroral emission has a peak brightness around the MR intensity, with visible and UV emissions intensities around 100 kR or 10 times brighter than Earth's (Clarke et al., 2004).

2.7 The M-I Coupled System

It is almost impossible to discuss an individual region of the Jovian system. The entire system is dynamically coupled. The magnetosphere-ionosphere coupled system

is comprised of several components. Figure 2.13 presents a simplified two dimensional illustration of the M-I coupled system. Ω_J denotes the rotational velocity of Jupiter, while ω denotes the lower rotational velocity of the plasma. The dotted region is representative of the plasma disk. Distortion of the magnetic field lines (solid black) are more exaggerated at greater radial distances, with the azimuthal component included as a result of field bend-back. The subsequent current system coupling the plasma disk to the ionosphere via upward and downward field-aligned currents is shown as a dashed line, with arrows indicating the motion of the currents. Currents flowing perpendicularly in the current disk exert a $\mathbf{J} \times \mathbf{B}$ force on the magnetospheric and ionospheric plasma. The main auroral emission discussed in Section 2.6 is a direct signature of the M-I coupled system. A more detailed description of this system is given in Chapter 4 of this thesis, which examines the structure of the current system threading the current disk and quantifies the spatial asymmetries within the system.

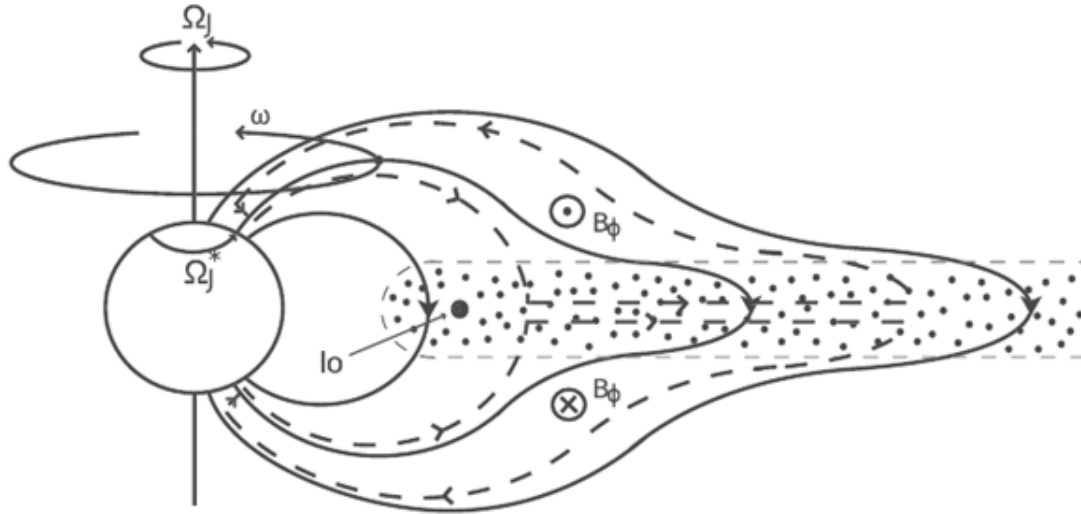


Figure 2.13: A simplified schematic of the M-I coupled system taken from Cowley et al. (2001). Solid black lines represent the magnetic lines of force, while dashed lines indicate the current system coupling the planet to the plasma disk (dotted region).

2.8 Conclusion

Table 2.1 highlights some key parameters in the three systems discussed in this chapter. The space environment around Jupiter is a dynamic, rotationally coupled system displaying a series of complex phenomena. It is coupled by a complex current system responsible for the transfer of planetary momentum to the equatorial plasma disk. This current system facilitates the precipitation of electrons, generating the main auroral emission. Whilst certain aspects of the system have been well established,

there remains a number of unanswered questions. The aim of this thesis is to investigate some of these questions, namely:

- What asymmetries are present in the equatorial current disk?
- Where are the upward and downward field-aligned currents that couple the magnetosphere to the main auroral emission located?
- What is the mechanism driving the precipitation of electrons at latitudes conjugate to the middle magnetosphere?
- What other energisation mechanisms might exist within the system and how do they vary throughout the magnetosphere?

In response to the final question, we devote the next chapter to discuss turbulence within the system, and examine its energisation potential in Chapter 6.

Property	System		
	Sun	Earth	Jupiter
Radius at equator [km]	696,340	$R_E = 6,371$	$R_J = 71,492$
Surface equatorial magnetic field [T]	0.001	3.05×10^{-5}	4.17×10^{-4}
Typical equatorial rotation rate	587 hr 17 min	23 hr 56 min	9 hr 56 min
Distance from Sun [AU]	-	1	5.2
Magnetopause standoff distance	≈ 123 AU	$\approx 10 R_E$	$\approx 63 R_J / 92 R_J$
Typical plasma density ranges [cm^{-3}]	$10^{-3} - 10^6$	$10^{-2} - 10^2$	$10^{-2} - 10^4$
Typical plasma temperature ranges [K]	$10^5 - 10^6$	$10^3 - 10^4$	$10^5 - 10^6$

Table 2.1: Typical system parameters for the Sun (Verscharen et al., 2019), Earth (Parks, 2015) and Jupiter (Khurana et al., 2004)

Chapter 3

Spatial Distribution of Turbulent Activity

Throughout the terrestrial and Jovian magnetosphere, spacecraft observations have identified a plethora of turbulent activity linked to auroral emissions (see Borovsky et al. (2003), Zimbardo et al. (2010), Zhao et al. (2012), El-Alaoui et al. (2021), and Saur (2021) and references therein). They have been shown to play a pivotal role in the injection of energy and its cascade from large scale vortices to smaller scales where dissipation occurs. While the spatial distribution of turbulence at Jupiter is still relatively unknown, much work has been done in identifying and understanding turbulence in other systems. Providing a detailed insight into not only the spatial distribution of magnetospheric turbulence but also its evolution, from initial perturbation, through the turbulent cascade, to its final energy dissipation would aid in explaining the generation of Jovian aurora, and energisation processes occurring within the magnetosphere.

In the quest to understand turbulence in space plasmas, many studies have successfully quantified the behaviour of turbulent features within the solar wind (e.g. Chen et al. (2012), Kuznetsov et al. (2016), Verscharen et al. (2019), and Yang (2019)), and Earth (see citations in previous paragraph). However, the expansive variability in space environments means that there is a much greater breadth to turbulence which we do not fully understand. The Jovian system is a turbulent environment much different from the solar wind and Earth's magnetosphere. Firstly, magnetospheric turbulent perturbations are much smaller than the background field. They also exist within a finite magnetosphere, which implies that a maximum length scale exists for the turbulent cascade, and the turbulent scales are confined to a maximum length scale. Additionally, plasma composition, reflections at boundaries, such as the ionosphere and plasma disk, and the inhomogeneity of the magnetic field at high latitudes and the plasma disk create additional levels of complexity within the system (Saur, 2021).

This chapter provides a literature review of known properties of turbulence with implications towards auroral emissions. Comparisons and differences are also noted between the solar wind, terrestrial and Jovian systems. In comparing and contrasting turbulence we split the Jovian system into 5 components, and systematically work through each one, noting key findings within the region and making comparisons to other similar regions in other known systems. Figure 3.1 highlights the 5 regions discussed in this chapter. Although this distinction between regions has been made based on knowledge of the system, it should not represent solid physical boundaries. The system is incredibly complex and wave related phenomena within one region are known to influence and diffuse into other regions. Following the review, our work in

Chapter 6 builds upon this knowledge by identifying turbulence within the mid-to-high latitudes of Jupiter's magnetosphere and quantifies its nature. Chapter 7 then uses information from the review to outline considerations needed for expanding the Chapter 6 study in future work.

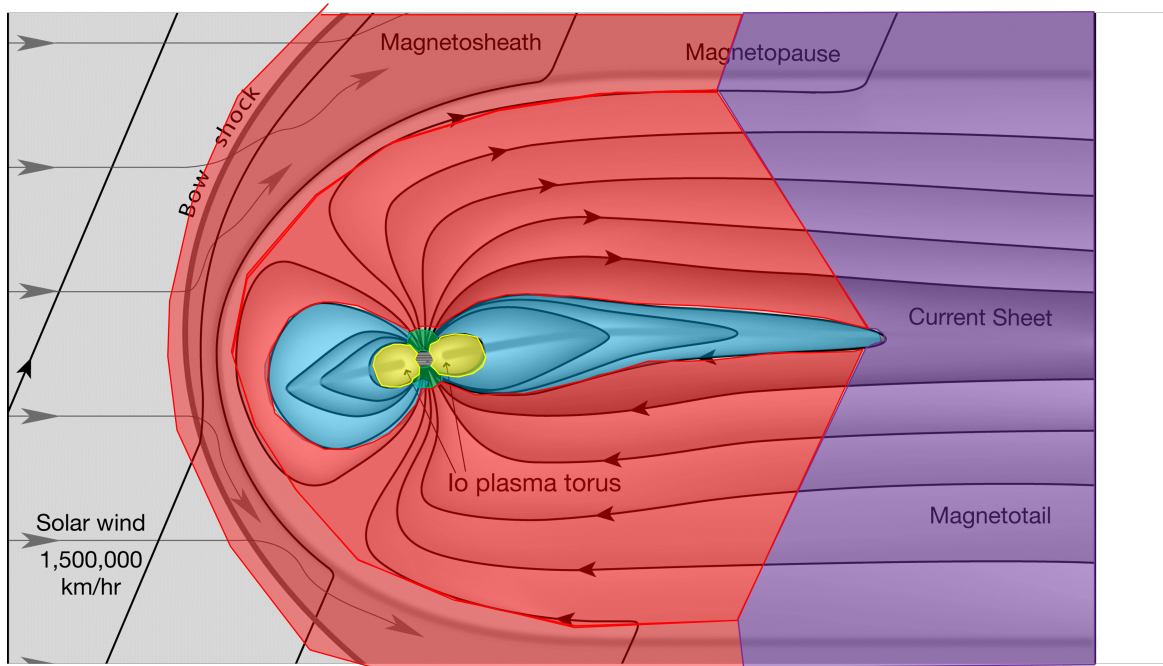


Figure 3.1: A modified version of the Bagenal & Bartlett rendition of the Jovian magnetosphere, illustrating the 5 semi-arbitrary regions discussed in this chapter. Red: Magnetosphere boundary and outer region, blue: Middle region, yellow: Inner region, green: Polar region, purple: Tail region

3.1 Turbulence in the Solar Wind

The solar wind is a highly turbulent media (Coleman, 1968). Such perturbations are produced by the non-linear interaction of Alfvén waves (Belcher et al., 1971; Belcher et al., 1975) and range in scale from approximately 0.3 AU (Podesta et al., 2008), down to proton and electron gyroradii. Studies of turbulence in the solar wind have been pivotal as a benchmark in understanding turbulence in a homogeneous media. On its outward journey, the solar wind encounters planetary magnetospheres which it is able to transfer energy and momentum to through a variety of processes including, but not limited to: direct entry from magnetic reconnection, and cross-field transport due to the scattering of particles by waves across the closed magnetopause field lines (Lakhina et al., 2000). Hence, any turbulent activity within the solar wind has some influence on the magnetosphere it is interacting with and is therefore an important consideration for understanding the global distribution of turbulence within a planetary system.

Magnetic field fluctuations are often seen in conjunction with velocity perturbations, and are highly intermittent in nature (Tu et al., 1995; Sorriso-Valvo et al., 1999; Sorriso-Valvo et al., 2001). Intermittency is a general feature known from fluid turbulence (McComb, 1990). It is seen as extended tails in the probability distribution functions of magnetic field perturbations, indicating sharp changes in the magnetic field are occurring more frequently than predicted by Gaussian statistics. Intermittent turbulence manifests as bursty patches of increased turbulence and localised regions of enhanced fluctuations (Verscharen et al., 2019). Polarised features are not expected to be present in fully developed turbulence, as this is a property of linear waves. Jupiter’s system is sufficiently large compared to the terrestrial system that turbulence can

develop further than what it would at Earth, but not so much as it would in the solar wind, allowing researchers to quantify a different developed stage of MHD and Alfvénic turbulence.

Coleman (1968) found Alfvén waves within the solar wind with a turbulent spectra, which extends through a non-linear cascade to much smaller scales where energy dissipation is expected to occur. The order of magnitude difference between the Alfvén velocity, 40 km s^{-1} , and the solar wind velocity, 400 km s^{-1} , results in perturbations appearing frozen into the solar wind. When investigating turbulence, a crucial consideration is as to whether the Taylor hypothesis (Taylor, 1938) is satisfied. Take the turbulent parameter n which varies with time. This can be split into a convecting and advecting component like so

$$\frac{\partial n}{\partial t} = \frac{Dn}{Dt} - \mathbf{U} \cdot \nabla n \quad (3.1)$$

where \mathbf{U} is the plasma velocity. For Equation 3.1, the first term on the right hand side is the convecting term, while the second term is the advecting term. The Taylor hypothesis is said to be satisfied when the perturbation velocity is less than half the velocity of the medium. Under these conditions, it is assumed that the convection term becomes negligible. For turbulent eddies, applying the assumption means features can be considered as frozen in as they advect past the sensor. This allows one to obtain the wavevector for a turbulent feature via $k = \frac{\omega}{U}$, where ω is the frequency associated with the turbulent feature, and U is the plasma velocity. Neglecting the convection

term allows Eq 3.1 to be reduced to:

$$\frac{\partial n}{\partial t} = -\mathbf{U} \cdot \nabla n \quad (3.2)$$

For the solar wind, this condition is satisfied, however plasma speeds within the terrestrial magnetosphere are comparable to the local Alfvén velocity, and in the Jovian magnetosphere the Alfvén velocity is relativistic and much larger than the plasma flow velocity. These differences mean that the Taylor hypothesis is rarely satisfied. The implications for an observer means that it is difficult to resolve temporal variations of the turbulent eddies from observed changes due to the advecting turbulent medium. Additionally, incorrectly applying the Taylor hypothesis through Equation 3.2 may lead to an overestimation of the plasma bulk velocity. Subsequently, this would lead to an overestimation of the magnetic Reynolds number, possibly resulting in an incorrect application of the frozen-in theorem. In this case, a model must be used to relate the wavenumber to the flow velocity. In the case of wave activity, the respective dispersion relation, such as Eq 1.46, can be used. In the regions of the magnetosphere discussed in Chapter 6, the Alfvén velocity is found to be relativistic, as such the Eq 1.46 reduces to $\omega = \frac{c}{k}$.

Because of the large difference in plasma velocity when compared with Alfvén velocity, the Alfvén effect, which tends to divide energy between the perpendicular velocity and magnetic field perturbations via a similar scaling factor, results in non-linear interactions being slowed down in the presence of a strong magnetic field. The

partition between the mean square velocity, u , and magnetic field, B , is expressed by

$$\frac{1}{8\pi}\langle B^2 \rangle = \kappa \frac{1}{2}\rho\langle u^2 \rangle \quad (3.3)$$

where ρ is the plasma density, and κ is the scaling factor (Chandrasekhar, 1957). Equation 3.3 is applicable in the inertial sub-range, where eddy sizes are small compared to the largest energy containing eddies but still sufficiently large that they experience a non-linear exchange of energy.

Turbulent perturbations in the solar wind are found to be anisotropic, favouring perpendicular fluctuations and are expected to have spectral indices at $-\frac{3}{2}$ (Iroshnikov, 1964; Kraichnan, 1965), but more often are found at $-\frac{5}{3}$, as shown in Eq 1.59. The angle of incidence of the impinging solar wind and local plasma beta determine properties of the bow shock, such as its topology, dynamics and dissipation processes. At Earth this is relatively well understood, however more exploration of this is required in the Jovian system. The increasingly coiled nature of the Parker spiral as it travels into the outer solar system means that the angle of incidence will vary significantly at Jupiter, and present an exciting opportunity for investigation.

Work by D'Amicis et al. (2020) revealed that turbulence within the solar wind plays a significant role in driving geomagnetic activity, particularly in the high latitude regions. A common feature of high frequency terrestrial magnetospheric turbulence is the presence of a steep, oftentimes greater than -2.3, spectral index which is

comparable with values observed in the solar wind. Investigations into geomagnetic responses to the solar wind at Earth reveal the presence of significant activity even when large perturbations, such as coronal mass ejections or corotating interaction regions, are not present (Gonzalez et al., 1999; Yermolaev et al., 2005). Borovsky et al. (2003) have analysed the correlation between the level of solar wind turbulence and measures of geomagnetic activity at Earth. Their findings indicate that stronger upstream turbulence can lead to the generation of higher viscosity eddies within the magnetosheath, which in turn results in a larger transport of solar wind momentum and energy into the system, producing stronger magnetosphere-ionosphere coupling currents.

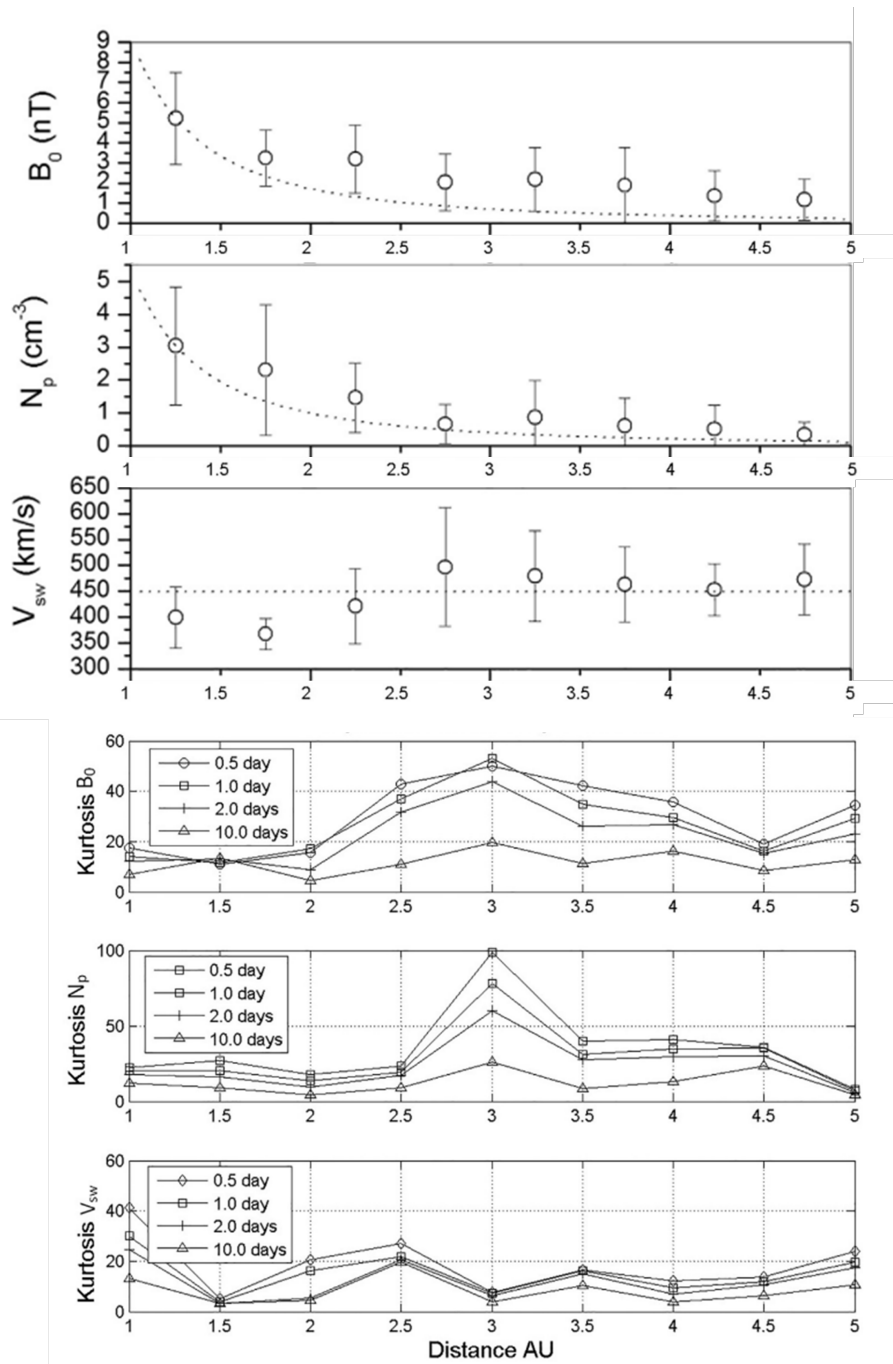


Figure 3.2: The variation in solar wind magnetic field magnitude, proton density, and velocity observed by Ulysses and the variation in their respective kurtosis. Figure adapted from Echer et al. (2020).

No studies have yet been published in determining the affect of solar wind turbulence on the magnetospheres of the outer planets. Undertaking such a study at Jupiter would provide a unique insight into how the solar wind impacts a rotationally dominated magnetosphere. In addition to the magnetospheric driving mechanism, the solar wind turbulence is significantly different than at 1AU (Pine et al., 2020). Kurtosis analysis of the solar wind magnetic field, proton density and velocity data from Ulysses indicates a change of regime somewhere between 2 and 3 AU (Echer et al., 2020), with the respective probability distribution functions exhibiting a spreading shape as a result of intermittence. The findings of Echer et al. (2020) are illustrated in Figure 3.2. The outer planetary magnetospheres therefore offer an opportunity to investigate solar wind interactions that are not possible at Earth.

3.2 Turbulence within the Jovian system

As we showed in Chapter 2, Jupiter exists in an environment much different to the Earth. Orbiting at an appreciably greater distance from the sun, possessing a significantly stronger, larger and faster revolving magnetosphere than the Earth, with inhomogeneous internal plasma sources, this system offers an unprecedented opportunity to expand our knowledge of planetary magnetospheric dynamics (Saur, 2021). It is not enough to know the location and direction of field-aligned currents, which will be found in Chapter 4, in order to understand the Jovian M-I coupled system. One must also understand the acceleration processes present within the system. This Section reviews observations of turbulence within the Jovian magnetosphere, and comments on the similarities and differences between it and our terrestrial system. The information presented here forms the basis of the work in

Chapter 6, and aided in the formulation of a potential project roadmap discussed in Chapter 7.

3.2.1 Magnetosphere Boundary and Outer region

This region is defined as encompassing the interface between the solar wind and the planetary magnetic field, as well as the outer magnetosphere of Jupiter where the distended field returns to a quasi-dipolar topology and into the high latitude lobes. This demarcation allows one to encompass the solar wind interaction at the bow shock, magnetopause, magnetosheath and outer magnetosphere, all regions susceptible to changes in the solar wind conditions.

When Cluster traversed Earth's bow shock, it witnessed an increase in turbulent activity. This is suggested to be locally produced through the shock thermalisation process (Yordanova et al., 2008). Large perturbations are found within the magnetosheath, most likely compressive as the magnetosheath is a region of strong compression after the bow shock. Eastwood et al. (2003) observed Alfvén waves in the terrestrial foreshocks. Where $\beta < 4$, Alfvénic perturbations dominate the turbulent spectra. The turbulent perturbations continue to evolve, as seen by intermittency and anisotropies increasing, past that seen in the solar wind, with distance from the shock. Above the spectral break frequency, measured turbulence displays an anisotropy in its wavevector. At higher β values, fluctuations become isotropic, as such the influence of the ambient field on the magnetic turbulence is negligible.

The terrestrial magnetopause is a highly perturbed region, defined by its intense

turbulence. Ultralow-frequency (ULF) waves, electromagnetic waves with frequencies less than 1 mHz, are found within the Jovian magnetopause. The energy from these perturbations are eventually deposited in the middle and inner magnetosphere, and so are of considerable importance in understanding the dynamics of the system. ULF wave generation on the terrestrial magnetopause is found to be a product of magnetopause perturbations (Kepko et al., 2003; Zhang et al., 2010) or Kelvin-Helmholtz instabilities (Hasegawa et al., 2004), a type of fluid instability occurring in the presence of a velocity shear in a homogeneous fluid, or velocity differential at the interface of two fluids. In the Jovian magnetosphere, Manners et al. (2020) observed multiple occurrences of ULF waves close to the noon and dusk magnetopause, which they suggested were also the product of external drivers. Results from the Juno spacecraft reveal magnetopause compressions are a driver of low-frequency wave activity and an enhancement mechanism for dawnside reconnection (Gershman et al., 2017). Additionally, simulations show that the presence of the plasma disk results in an enhancement of Kelvin-Helmholtz instabilities, which again drive ULF waves (Masters, 2017).

The interaction of energetic solar wind particles on the terrestrial magnetosphere forms an ion and electron foreshock, the structure of which is seen in Figure 3.3. Perpendicular plasma velocities increase due to the compression of the shocked solar wind and conservation of the first adiabatic invariant, leading to a temperature anisotropy. Breuillard et al. (2018) used the Magnetospheric MultiScale spacecraft to determine the properties of turbulence within the subsolar magnetosheath. They found the subsolar magnetosheath can be divided into the quasi-perpendicular and

quasi-parallel magnetosheath shocks, based on its angle of incidence. The quasi-parallel and quasi-perpendicular shocks exhibit different turbulent perturbations. Between 0.01 and 0.04 Hz, perturbations are around 4 nT in the quasi-parallel shock, and up to an order of magnitude larger in the quasi-perpendicular shock (Czaykowska et al., 2001). One explanation for this difference is the presence of upstream propagating reflected ions in the quasi-parallel ion foreshock, which can amplify magnetic power by a factor of 4 through ion cyclotron wave generation at the shock interface. There are no reflected ions upstream of the quasi-perpendicular shock, however downstream is dominated by left hand polarised ion-cyclotron waves with amplitudes of 3 nT. The power spectra of downstream turbulence does not show significant variations, suggesting turbulent energy transfer is prevalent.

Voyager 1 and 2 data from quasi-parallel and quasi-perpendicular bow shock crossings revealed bi-Maxwellian ion distributions in the Jovian magnetosheath (Richardson, 1987). Thomsen et al. (1988) later deduced that these observations originate from the same mechanisms generating similar distributions in the terrestrial ion foreshock. Whilst this process was found to be similar to that observed at Earth, the difference between the two system parameters presents an opportunity to expand our understanding of the reflection process.

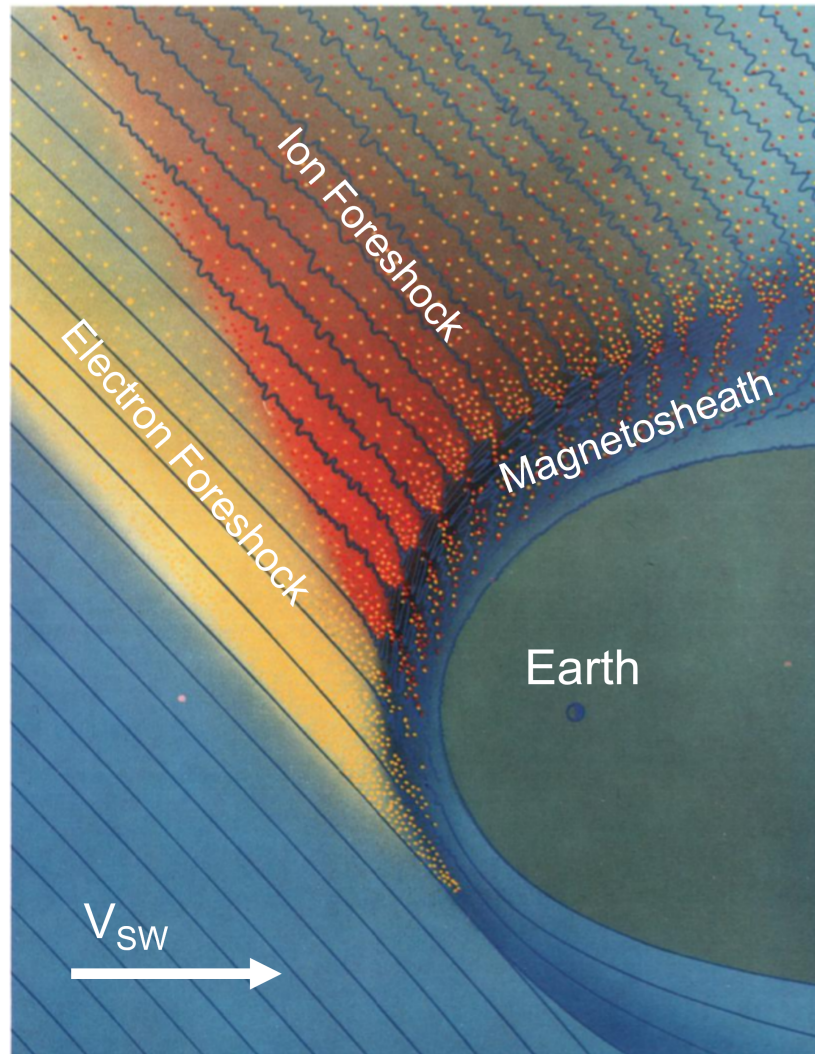


Figure 3.3: An illustration of the energetic particles and waves upstream of the terrestrial magnetosphere. The direction of the solar wind is identified via the white arrow, while the black lines correspond to the interplanetary magnetic field impinging upon the system at an angle of approximately 45° . The yellow electron and red ion foreshocks are labeled upstream from the magnetosheath. Image credit: Tsurutani et al. (1981)

In the terrestrial magnetosheath, evidence of shock wave heating of heavy ions is given by the existence of a strong correlation between the proton temperature anisotropy and the intensity of polarised waves (Zimbardo et al., 2010). Figure 3.4, from Czaykowska et al. (2001), shows the ratio of left hand to right hand polarised fluctuations and the proton temperature anisotropy. Similar work has yet to be undertaken at Jupiter, however Manners et al. (2019) successfully used hodograms of 22, 14, 7 and 4 minute averaged magnetic field signatures to identify the polarisation properties of standing Alfvén waves in the Jovian plasma disk. It therefore seems feasible that a similar technique could be applied alongside an analysis of plasma data to generate results akin to those shown in Figure 3.4.

Magnetosheath turbulence is highly dependent upon the field-flow angle (Mangeney et al., 2006). The reflection of solar wind ions at the quasi-perpendicular shock create ion beam instabilities, which can influence the power of magnetic perturbations between the quasi-perpendicular and quasi-parallel shocks (Sckopke et al., 1983; Czaykowska et al., 2001). These highly disturb the system, generating magnetic turbulence, introducing temperature anisotropies and producing velocity shears (Zimbardo et al., 2010). Temperature anisotropies can also result in kinetic instabilities, and have also been found to exhibit wave-particle interactions generating wave emission rather than acting as medium for wave dissipation. Figure 3.5 shows a typical quiet magnetosheath turbulent spectra, with a plasma beta around 1. The localised peak at approximately 10^2 Hz corresponds to an energy injection associated with whistler modes.

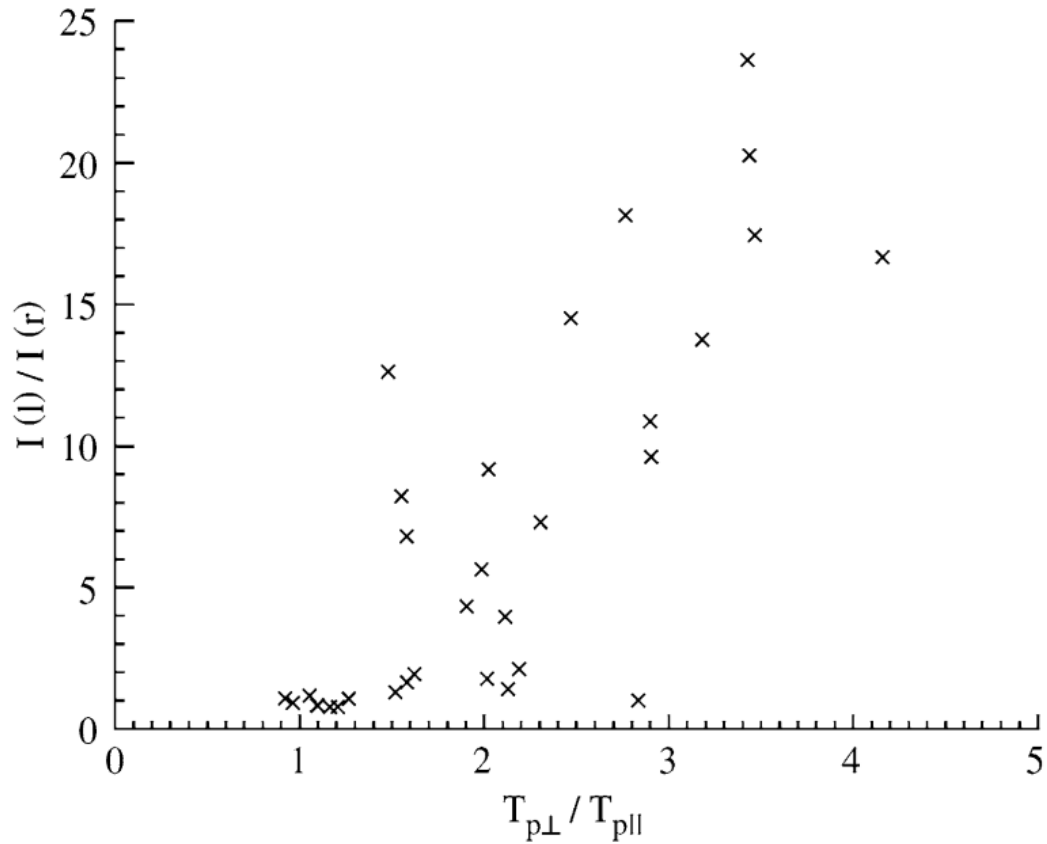


Figure 3.4: Evidence of plasma heating given by the correlation between the ratio of left hand to right hand polarised fluctuations and the proton temperature anisotropy.

Image credit: Czaykowska et al. (2001)

3.2.2 Middle Region

The middle region is loosely defined here as the area through which corotation breaks down and the topology of the magnetic field is distended. This corresponds largely to the middle magnetosphere of Jupiter. This area encompasses the highly turbulent

plasma disk and lobe regions. It is one of the more extensively investigated regions of the Jovian magnetosphere for turbulence and wave-particle interactions.

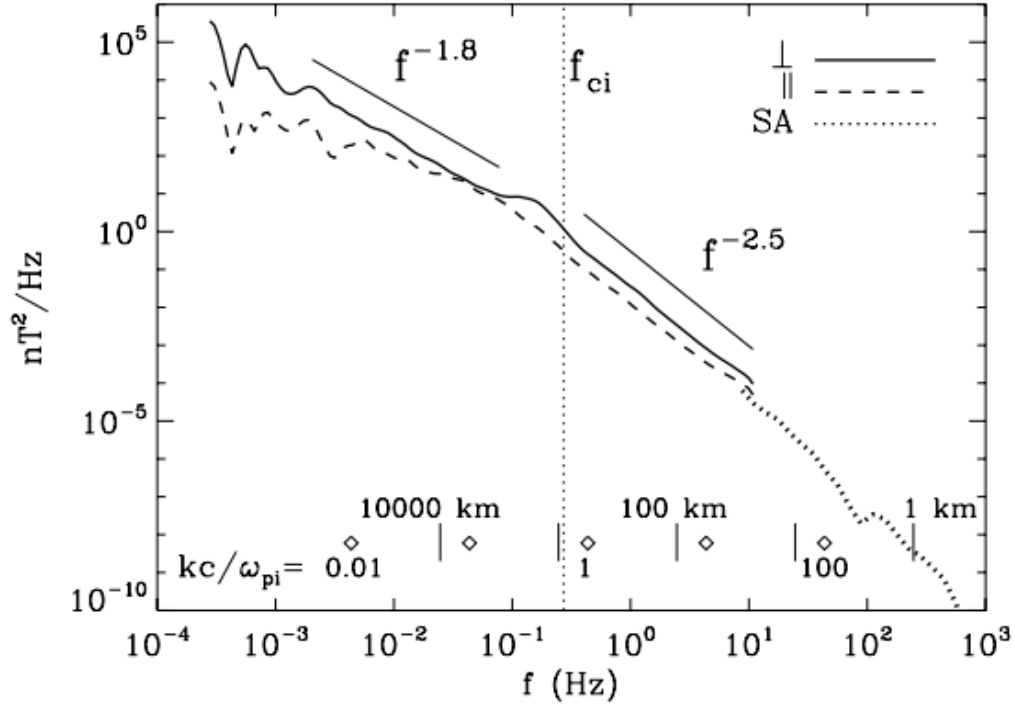


Figure 3.5: The turbulent spectra of the terrestrial magnetosheath during a quiet period as observed by the Cluster spacecraft. The solid line is the power spectra of transverse perturbations, dashed for the compressive perturbations. Image credit: Alexandrova et al. (2008)

Central to the dynamics of the Jovian magnetosphere is the plasma disk. Equilibrium is maintained through the continuous production and loss of mass from the disk. Centrifugal forces, plasma pressure, gravity and magnetic tension

all act to drive radial transport in the system (Southwood et al., 1987). Plasma interchange events have been suggested to initialise perturbations, which later go on to accelerate and energise plasma (Saur et al., 2002; Saur et al., 2003; Saur, 2004). Centrifugal interchange instabilities, analogous to gravitational Rayleigh-Taylor instabilities, present a possible mechanism enabling radial interchange in a low beta plasma (Gold, 1959). A centrifugally unstable plasma torus arises when the mass content per unit of magnetic flux decreases with radial distance. This destabilisation is balanced at Jupiter however by the increasing flux tube entropy over radial distances (Paranicas et al., 1991; Mauk et al., 2004). Wilson et al. (2000) were able to identify multiple occurrences of ULF wave activity within the current disk region using Galileo data. By sectioning the magnetometer time series into 2 hour sections, they were able to identify multiple wave signatures with periods ranging between 10 to 20 minutes.

At Jupiter, in the plasma disk, temperatures increase dramatically with radial distance, up to two orders of magnitude (Frank et al., 2002; Bagenal et al., 2011). Without a large energy input to achieve this, adiabatic cooling, where the plasma temperature decreases due to expansion, would dominate and reduce the temperature of the plasma with radial distance. This can be seen in Figure 3.6, whereby temperature observations closely match predicted heating and are vastly different than adiabatic cooling expectations. The investigation of ion heating is not a new topic. The majority of plasma waves observed in the equatorial plasma disk have a largely perpendicular wave component (Wilson et al., 2000). Barbosa (1981) & Barbosa et al. (1984) looked into high frequency plasma wave turbulence, and low frequency Alfvén turbulence, respectively, as a potential heating mechanism for magnetospheric ions.

A variety of studies have been made since to explain this phenomena, including the turbulent heating arising from flux tube diffusion (Saur, 2004) and advection (Ng et al., 2018). MHD turbulence has the potential to account for the required energy responsible for the observed increase in plasma temperature.

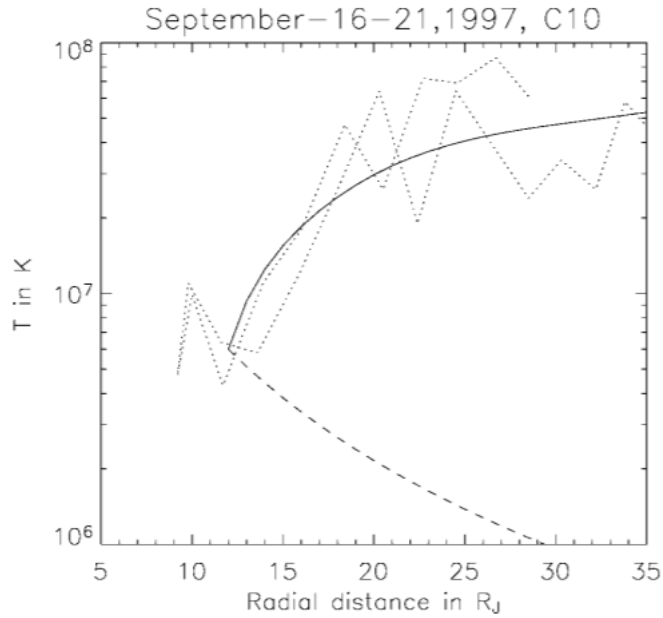


Figure 3.6: The radial temperature profile of the Jovian magnetodisk plasma is given by the dotted lines, the predicted temperature profile based on adiabatic cooling is shown as a dashed line, while the modeled temperature incorporating turbulent heating is shown as the solid profile. Image Credit: Saur et al. (2002)

A fundamental process in the creation of MHD and plasma turbulent cascade is where counter-propagating wave packets interact non-linearly (Goldreich et al., 1995; Howes et al., 2013). In the middle region radial transport of Iogenic plasma perturbs the Jovian magnetic field, triggering waves which, reverberating off the plasma disk

and ionospheric boundary, interact non-linearly to form a turbulent cascade.

Studies have been made of local time variations of turbulence in the plasma disk of the Kronian system. Again, the relative amplitude of Kronian turbulent perturbations with respect to the background field is much less than in the solar wind (Papen et al., 2014). Similar to studies at Jupiter by Tao et al. (2015), Kronian turbulence is intermittent and consistent with kinetic Alfvén wave turbulence. At Saturn however, Papen et al. (2016) investigated the spatial and temporal structure of the magnetospheric turbulence. They observed an enhancement of fluctuations at noon, which they suggest is due to flux tube interchange events, a primary driver of turbulence. Additionally at Saturn, these fluctuations are seen to correlate with planetary periodic oscillations (Espinosa et al., 2000; Gurnett et al., 2009; Provan et al., 2009; Papen et al., 2016). No periodic oscillations exist at Jupiter, and so investigating the turbulent spatial distributions in its system would also be beneficial in untangling the current knowledge of the Kronian system.

There exists a broad diffuse auroral emission in the Jovian aurora. Nishida (1976) was the first to investigate Jovian whistler driven pitch angle diffusion of energetic electrons and ions. Recent observations by Juno, using the Juno Energetic-particle Detector Instrument (JEDI) and Jovian Auroral Distributions experiment (JADE) instrument revealed electrons within the 0.1 - 700 keV energy range as it passed over the diffuse auroral region. Measured electrons were almost entirely within the loss cone, which Li et al. (2017) postulate are caused by equatorial whistler mode waves, generated via anisotropic electron injections. Outside of 10 R_J , perturbations

as small as 25 pT are expected to be sufficient to produce strong pitch angle diffusion (Bhattacharya et al., 2005).

3.2.3 Inner Region

We define the inner region as from the ionosphere, out to the point of corotation breakdown. The Galilean satellites orbit within this region, interacting with the surrounding plasma, and through wave-particle interactions, produce conjugate auroral footprints.

As touched upon in Chapter 2, the Galilean satellites undergo a significant interaction with the Jovian magnetosphere. The most notable manifestations of this interaction are the auroral footprints conjugate with the moons Io, Europa and Ganymede. The thin atmospheres, or potential conducting subsurface oceans, present an obstacle to the ambient magnetic field. Since the satellites rotate at a Keplerian velocity, much less than the corotational velocity of the plasma disk, the plasma is perturbed as it passes the satellite. Such perturbations propagate along the magnetic field in the form of Alfvén waves which can accelerate magnetospheric electrons which go on to precipitate into the upper atmosphere and trigger auroral emissions (Hess et al., 2012). Figure 3.7 illustrates the development of Alfvén wings from the perturbed ambient field due to the presence of a conducting obstacle.

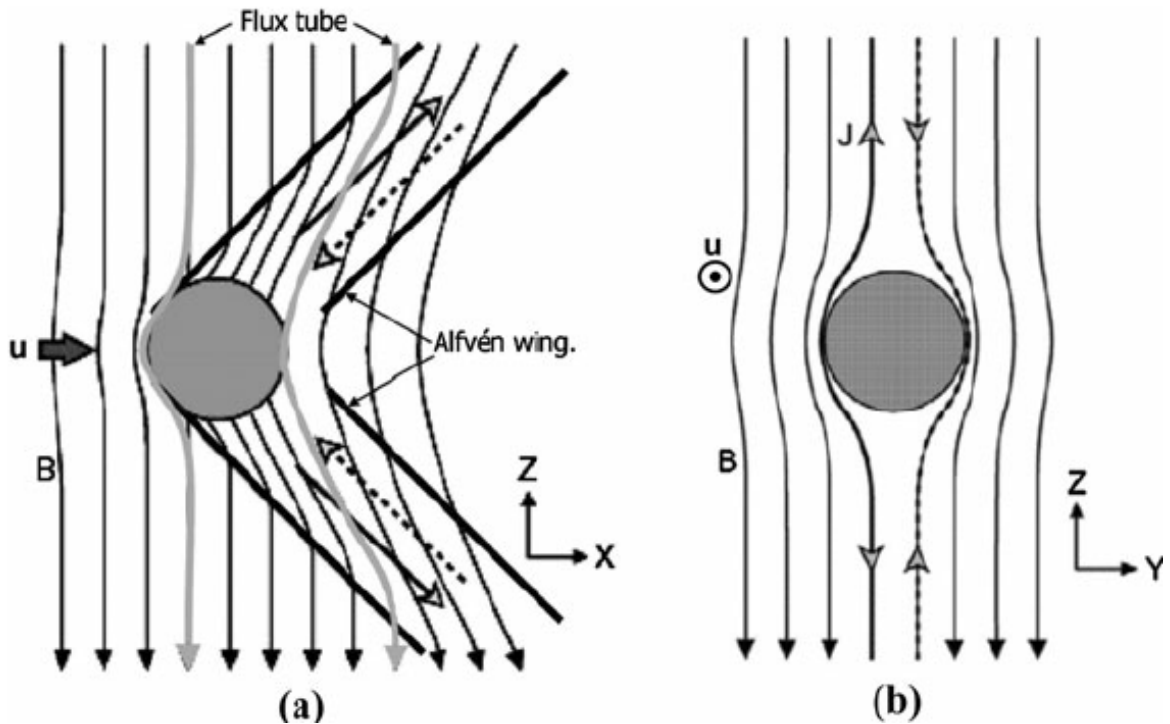


Figure 3.7: An illustration of the field perturbation triggered by the presence of a satellite with a velocity difference to the ambient field. In panel a), the unperturbed flow is to the right, and the ambient field is pointing down. Panel b) is the viewpoint of an observer behind the satellite, with the flow velocity coming towards them. Currents flowing along the Alfvén wing are shown as dashed and solid arrows. Solid arrows signify currents traveling on the left side of the satellite in panel b), while dashed arrows signify currents flowing on the right hand side of the satellite in panel b). Image Credit Jia et al. (2010)

The auroral footprint associated with Io is the most well researched. Auroral images show a series of secondary spots attributed to the excitation of electrons in opposing hemispheres and/or the reflection of plasma waves generated via the

satellite/plasma torus interactions. Examination of the width, vertical extent and intensity of the auroral footprint can indicate the size of the interaction region, precipitating electron energy distributions and the interaction mechanisms respectively (Bonfond, 2012). It should be noted therefore, that one could expect a larger density of perturbations detectable along magnetic shells conjugate with the Galilean satellites.

As well as satellite interactions, the inner region is also the home of Jupiter's intense radiation belts. The inner radiation belt is located at approximately $1.5 R_J$, and is the product of particle injection processes and whistler wave driven electron acceleration (Woodfield et al., 2014). Since Juno's orbit was specifically engineered to limit exposure to the radiation belts, they will not form a part of the study in Chapter 6, or future work detailed in Chapter 7. They are, however, a key feature of the Jovian system driven by resonant wave activity.

3.2.4 Polar Region

The polar region is defined here as encompassing all latitudes through which auroral emissions are present, loosely extended out to $2 R_J$. Juno, with its polar orbit, has allowed for an in depth study of this region where it was theorised that large quasi-static electric fields energised auroral electrons.

Within the auroral regions, there is evidence of significant stochastic acceleration processes, now believed to dominate over the previously hypothesised quasi-static

electric fields (Ebert et al., 2017; Kotsiaros et al., 2019). At least three of the Galilean satellites are intrinsically coupled to the planetary ionosphere via Alfvén wave mediated FACs.

As highlighted in section 3.1, turbulent heating can be inferred based on the ratio of right- and left-handed polarised waves. Saur et al. (2018), using the dispersion relationship from Lysak (2008) has derived the polarisation relationship for small ion gyroradii, semi-relativistic, kinetic Alfvén waves, such as those observed by Gershman et al. (2017) in the Jovian auroral regions. The perpendicular polarisation relationship is

$$\frac{\delta E_x}{\delta B_y} = \frac{k_z}{\omega} \left(\frac{c^2}{1 + \left(\frac{c}{v_A}\right)^2} \right) \quad (3.4)$$

and the parallel polarisation relationship is

$$\frac{\delta E_z}{\delta B_y} = \frac{k_z}{\omega} \left(\frac{c^2 \frac{k_z}{k_x}}{1 + \left(\frac{c}{v_A}\right)^2} \right) - \frac{\omega}{k_x} \quad (3.5)$$

where δB_i and δE_i denote the perturbation magnetic and electric fields in the i^{th} direction respectively, k_i is the i^{th} component of the wavevector, ω is the wave frequency, and c and v_A are the speed of light and Alfvén velocity respectively. Figure 3.8 shows the profiles resulting from the polarisation relationships for kinetic Alfvén waves in the high latitude region of Jupiter’s magnetosphere.

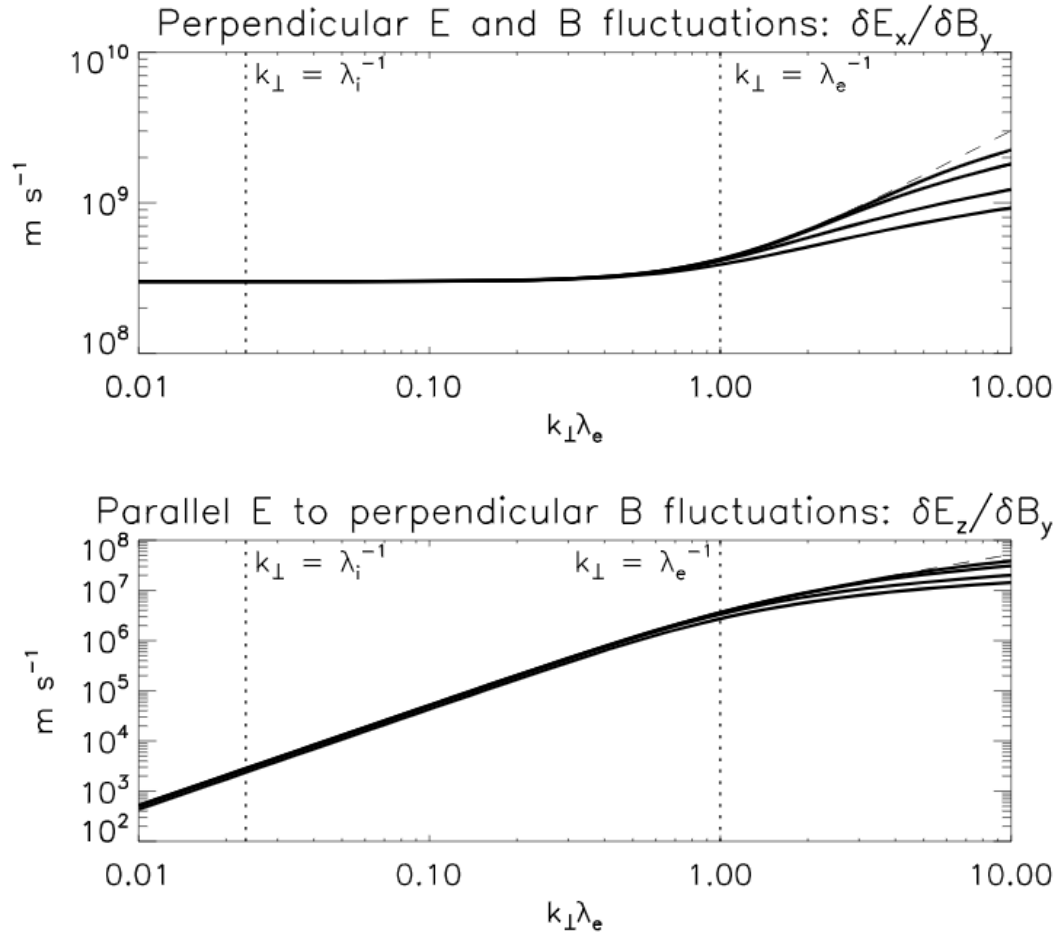


Figure 3.8: Dashed profiles illustrating the polarisation relationship of high latitude kinetic Alfvén waves as stated in Equations 3.4 & 3.5 for components perpendicular (top) and parallel (bottom) to the background field. Solid lines denote constant electron temperatures at 2.5, 10 and 25 keV. Vertical dotted lines denote the ion and electron inertial length scales, λ_i and λ_e , respectively. Image credit: Saur et al. (2018)

Saur et al. (2018) stressed the importance of the profiles in Figure 3.8, as for perpendicular length scales smaller than the electron inertial length the ratio exceeds

the speed of light by almost an order of magnitude. They stress that this effect should be taken into consideration in identifying wave modes. This is because when the Alfvén wave group velocity approaches the speed of light, Alfvén waves become ordinary electromagnetic waves. therefore failure to apply this consideration could result in the incorrect classification of wave species.

At Earth, the orientation of the cusp with respect to the solar wind influences the turbulent nature of the region. Nykyri et al. (2006) found a strong correlation between the magnetic turbulence, with field-aligned plasma flow for northward IMF in the less sunward orientated cusp. This had a spectral index between 4.2 - 4.9 after the spectral break around the proton gyrofrequency. Though there is a clear spectral break around the proton gyrofrequency, it has been found that a variety of potential dissipation and energisation mechanisms exist within the cusp region. Figure 3.9 shows a sample of the cusp’s turbulent spectra, obtained from the Cluster spacecraft. Evidently several spectral slopes are present, as well as local peaks in the spectra near the ion cyclotron frequency signifying energisation. Similar observations have been made in the terrestrial magnetosheath (Alexandrova et al., 2006).

Unlike Earth, the “Cusp” region of Jupiter changes its orientation with respect to the solar wind due to its internal driving mechanisms. This constant change in the orientation presents a unique opportunity to expand our current knowledge of the solar wind interaction with cusp regions. A caveat to this however, is that solar wind driven reconnection is much less prevalent at Jupiter than at Earth (Vasyliunas, 1983; Krupp et al., 2004).

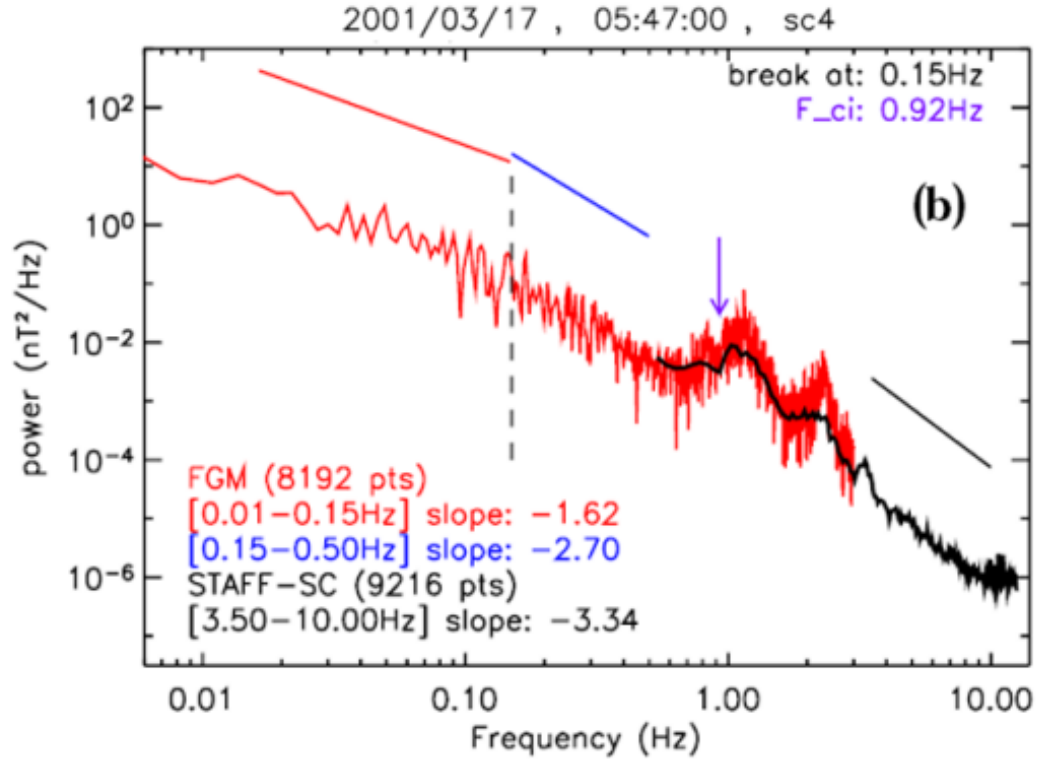


Figure 3.9: The turbulent spectra in the terrestrial cusp region as measured by the Cluster magnetometer (red) and STAFF wave instrument (black). The purple arrow points to the ion cyclotron frequency. Image Credit: Nykyri et al. (2006)

The direct interaction of magnetosheath plasma with the cusp produces a turbulent boundary layer, which acts to amplify magnetosheath turbulence. Coherent structures, including plasma bubbles, Alfvén vortices and magnetosonic jets have been identified in the terrestrial magnetopause and cusp regions. Coherent structures are widely believed to be a product of a turbulent cascade (Perri et al., 2012) and can be

used to identify likely dissipation and acceleration regions. In simulations, coherent structures are characterised by the enhancement of work done on particles. Measuring this as the product of the current density with the electric field gives a measure on the magnetic energy dissipation within the turbulent structure (Wan et al., 2015).

The Cluster spacecraft constellation has observed Alfvén vortices at scales in the region of 100 km, near the ion gyroradius (Sundkvist et al., 2005). It should be noted that these are drift-kinetic Alfvén vortices, which are not the same as the Kelvin-Helmholtz vortices which develop at the magnetosheath flanks via shear flows and have scales around 40,000 km (Hasegawa et al., 2004).

Broadband radio emissions and plasma wave observations by Ulysses while at Jupiter has been fruitful in identifying magnetospheric boundaries. One such observation is of auroral-like hiss associated with low plasma density region around the vicinity of Io and taken to be analogous to the terrestrial cusp (Stone et al., 1992). In the same sense as the terrestrial cusp, ion-cyclotron waves, at the gyrofrequency of SO_2^+ ions, are present within the vicinity of Io, having been generated through the interaction of the satellites exosphere with Jupiter’s powerful magnetic field (Russell et al., 2007).

3.2.5 Tail region

The tail region is loosely defined as the region extending from the x-line anti-sunward from the planet. It is the region through which the magnetic field becomes highly distended due to its interaction with the solar wind, and continues out some several

AU to the orbit of Saturn. Despite its large size, we focus primarily on *in situ* observations made relatively close to the planet.

It is possible to infer the generation mechanisms of turbulence based on their scale size. For example, in the terrestrial magnetotail perturbations with frequencies larger than 0.03 Hz and with wavelength scales smaller than the typical magnetotail size are considered to be due to local non-linear cascades. At frequencies lower than 1 mHz and with wavelengths exceeding the size of the plasma sheet, perturbations are theorised to be triggered by the solar wind. Simulations of reconnection in the terrestrial plasma sheet by Onofri et al. (2004) found a turbulent spectra with an index of -2.3, comparable with observed magnetotail values. Within the terrestrial magnetotail, the structure functions were largely Gaussian prior to a substorm event, however after an event exhibited extended tails and hence an increase of intermittency. This might signify an energy injection during substorms, feeding the cascade of energy to smaller scales.

In addition to substorm driven enhancement, Klimas et al. (2010) showed that kinetic energy injections within the magnetotail can be facilitated through turbulent driven reconnection. Reconnection events in the middle and outer Jovian magnetosphere, where the magnetic field topology is highly distended, are a potential governor of radial transport (Delamere et al., 2015a). Reconnection events in this region are suggested to occur over a complex and patchy spatial distribution. Radial and azimuthal stresses are generated by the radial transport and sub-corotation of magnetospheric plasma (Hill, 2001; Goldreich et al., 2007). This is because the stress

balance of the system is not in a steady state. It is regularly disturbed by the non-continuous radial transport of plasma, observed to occur through interchange of mass loaded magnetic flux tubes with adjacent less loaded flux tubes further out (Kivelson et al., 1997).

When determining the nature of observed turbulence it is important to consider the observation location. If one were to take measurements over significantly long intervals with relatively uniform flow speeds, magnetotail activity would exhibit a Kolmogorov spectral index and a relative size of $\frac{\delta B}{B_0} \in [0.2 - 0.8]$. Figure 3.10 shows stronger turbulence with a steeper spectral index, around 2-2.5, at the inner central plasma sheet rather than at the outer central plasma sheet (Bauer et al., 1995). This is steeper than that observed in the solar wind, and can be explained as a consequence of the plasma sheet boundary (Hoshino et al., 1994). (Borovsky et al., 1997) suggests that though the spectral index is steeper within the magnetotail, perturbations should not be considered as fully developed turbulent flows, but rather strongly driven.

3.2.6 Conclusion

We have presented a systematic breakdown of turbulence within space plasmas relevant to the scope of this thesis. This namely centers around the solar wind, and the terrestrial and Jovian magnetospheres. Key features currently understood about turbulence and wave activity within the Jovian magnetosphere are outlined, and areas where new observations by Juno could uncover more information about the system are identified. Comparisons between the three systems were made, and several similarities and differences identified.

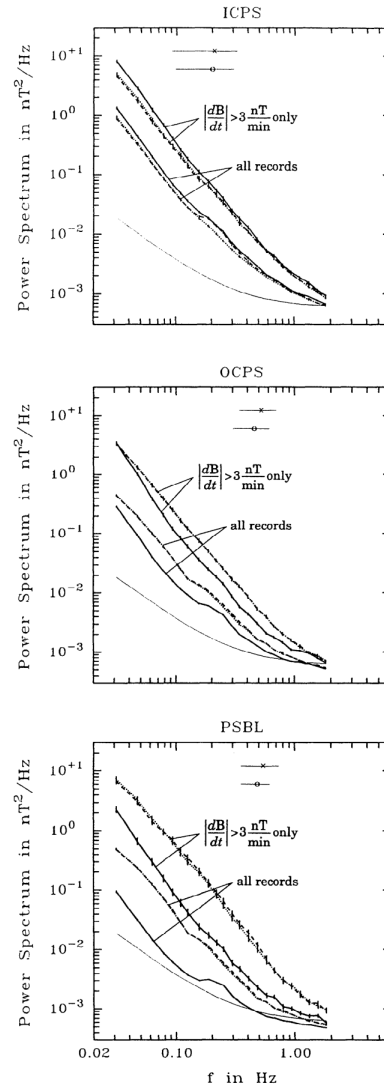


Figure 3.10: Power spectra of turbulent perturbations in the terrestrial inner central plasma sheet, outer central plasma sheet and plasma sheet boundary layer. Stronger, more dissipative turbulence exists in the inner central plasma sheet than the outer central plasma sheet. Image credit: Bauer et al. (1995).

As stated at the beginning of this chapter, the Jovian system is vastly different to that of the solar wind and Earth. Perturbations are much smaller than the

background field and exist within a finite magnetosphere implying a confinement to a maximum length scale. The inhomogeneity of the system results in non-resonant interactions playing a more significant role in wave-particle interactions than at Earth. In a homogeneous system, non-resonant interactions are equally accelerated and decelerated over a wave phase. For an inhomogeneous system, accelerated particles can escape the acceleration region before the second half of the wave phase has an opportunity to decelerate them. This opens an avenue into the study of non-resonant interactions within the Jovian magnetosphere. In addition to this, the presence of a dense, global plasma disk results in an additional boundary through which waves can undergo reflections and facilitate a non-linear energy cascade.

The dense plasma and intense magnetic field in Jupiter's magnetosphere result in an Alfvén velocity which approaches relativistic speeds. In this scenario, the Taylor hypothesis is not satisfied, and one must use another method to relate the wavevector with the frequency. Though despite these differences, the properties of turbulence in the magnetotail and magnetosheath potentially exhibit universal properties. A full spatial study of turbulence within the system would help determine if this is the case.

Instrumentation onboard Juno offers one the possibility of investigating plasma heating by applying a similar method used by Czaykowska et al. (2001). The Hodogram technique utilised by Manners et al. (2019) can be applied to determine the polarisation properties of turbulent perturbations, while JADE/JEDI data can be used to obtain the parallel and perpendicular plasma temperatures. It should be noted however, that as Juno precesses through its orbit, the orientation of its particle

sensors will move such that the angle of the viewing cone will decrease, meaning the parallel plasma velocities will be unresolvable (McComas et al., 2017).

Inspired by the work undertaken in the other systems, we use Chapter 6 to apply some of these techniques within the mid-to-high latitude regions of the Jovian magnetosphere. This work identifies turbulent Alfvén waves within this region and quantifies their potential energy input into the auroral regions. Following this, Chapter 7 utilises the knowledge presented above to discuss future applications in quantifying the full spatial distribution of turbulence in the Jovian system.

Chapter 4

Data, Instrumentation and Reference Frames

This chapter focuses its discussion on spacecraft and their instrumentation utilised in this thesis. Particular focus is given to the Galileo and Juno orbiter missions, whose measurements forms the bulk of the data used within the work discussed in Chapter 5 and 6. We begin with a discussion on the magnetometer and electrostatic analyser instruments, which supply all the data used in this work, followed by a look at the various spacecraft to visit Jupiter. Finally, an overview of the different reference frames employed in analysing and presenting the results are outlined, and the mathematical transforms used in converting to these frames are detailed.

4.1 Spacecraft Instrumentation

There exists a range of instruments on board the various spacecraft which have visited Jupiter. As more information has been unravelled about the system, these

instruments have become more refined. Two instruments are of particular importance in this thesis; magnetometers and electrostatic analysers. Magnetometer data is used in Chapter 5 to calculate the height integrated current densities around the Jovian current disk, and in Chapter 6 to identify turbulent perturbations and calculate their associated compressibility and Poynting flux. Electrostatic analysers provide detailed information regarding plasma velocity and flux, which provides a measure of the plasma density, temperature and pitch angle distribution. This is used in Chapter 6 to identify plasma perturbations associated with wave activity, and provide *in situ* measurements of the local plasma conditions.

4.1.1 Magnetometer

In the 1970s, extremely reliable, low power and high performance magnetometers were developed for outer planetary exploration. Vector magnetometers are the most widely used instrument aboard spacecraft missions for magnetic field measurements. They provide information about the magnitude and direction of the field. A tri-axial, orthogonal arrangement of single sensors is used to measure the three components of a local magnetic field in a frame aligned with the sensor axis.

The detector is made up of highly magnetically susceptible ring cores around which two lengths of wire are coiled. These are referred to as the driver and sensor coils. A simple illustration of this design is shown in Figure 4.1a. Driving an alternating voltage through the driver coil varies the magnetization of the core such that opposite sides of the core will induce a field in opposition to each other. For a given waveform, such as the example shown in of Figure 4.1b, the alternation of the induced field in

the absence of an external field will have a profile similar to that in Figure 4.1c. In the presence of an external field however, there is a phase shift between the two induced signals. This phase difference means a net change in flux passes to the sensor coil, which under Faraday's law, Eq. 1.5, produces a measurable voltage in the sensor coil, the size and phase of which provides information about the magnitude and direction of the external field (Primdahl, 1979). Positioning three such cores in an orthogonal arrangement provides a three dimensional vector of the magnetic field.

Vector magnetometers must be calibrated using accurately generated magnetic fields, carried out at specialist facilities. The calibration can be checked during flybys and gravitational assists. The instruments can operate over a wide temperature range and are found to be tolerant of high radiation doses (Acuña, 2002).

4.1.2 Electrostatic Analyser

Measurements of plasma velocity-space distributions can be obtained through the use of an electrostatic analyser. The analysers consist of three main components: a velocity space filter, a detector and a counter. Below we detail the basic functionality of a top-hat electrostatic analyser, mission specific details, such as the energy ranges, are detailed in section 3.2.1 for Juno.

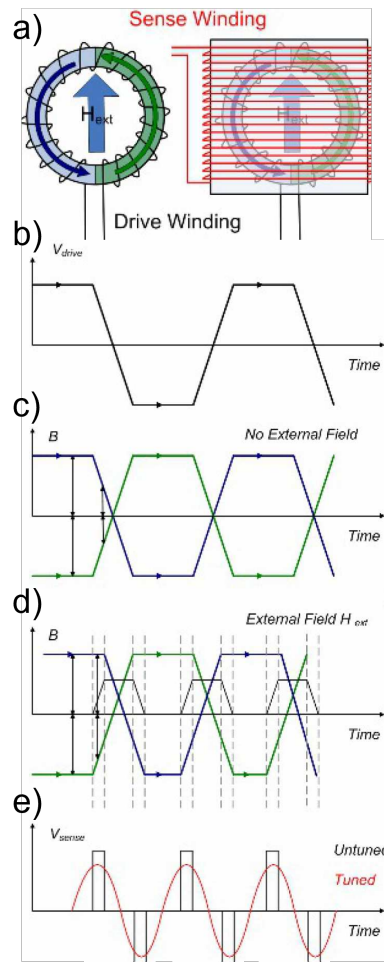


Figure 4.1: An illustration of how a flux gate magnetometer measures a magnetic field. Panel a) shows the configuration of the ring core, surrounded by a driver and sensor coil. b) shows the driving waveform, which c) showing the resultant induced field in each half of the ring core in the absence of any background field. If an external field is present, a phase shift is present, resulting in a measurable voltage in the sensor coil as illustrated in panel d) and e). (Image Credit: Imperial College London (n.d.))

Electrons incident upon a spacecraft are part of a six dimensional spatial and velocity volume. An electrostatic analyser measure parts of this distribution by

allowing electrons within a select energy and angular range to pass through an entrance slit and reach a detector plate. The energy selection is achieved by using a pair of hemispherical electrodes consisting of an inner and a grounded outer hemisphere. A charged particle must navigate the curvature of the cavity between the plates in order to reach a detector. Applying a voltage to the inner hemisphere produces an electric field within the cavity. The magnitude of the electric field determines the extent to which incident electrons are curved around the hemispheres. Thus varying the voltage allows for a precise energy selection. An angular selector is achieved through the implementation of a third shell located above the aperture and a collimator (Collinson et al., 2010). A simplified example of a 360° field-of-view electrostatic analyzer is illustrated in Figure 4.2.

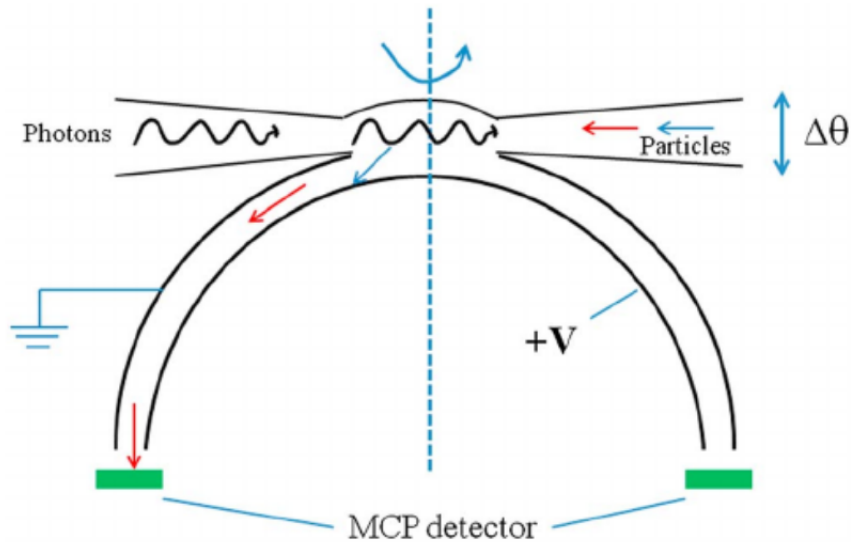


Figure 4.2: Simplified schematic of a top hat 360° field-of-view electrostatic analyzer. Image Credit: Morel et al. (2017)

4.2 Spacecraft Missions

There have been several spacecraft missions to Jupiter. The size and position of the planet make it useful as a gravity assist mechanism. As such, Jupiter has been visited by more spacecraft than any other outer planet system. Here we detail some of these missions which have been critical to the success of this study.

Mission	Insertion/Closest Approach	Mission Duration
Pioneer 10	04/12/1973	30Y, 10M, 22D
Pioneer 11	03/12/1974	22Y, 5M, 25D
Voyager 1	05/03/1979	43Y, 10M, 7D (+)
Voyager 2	09/07/1979	43Y, 10M, 22D (+)
Ulysses	08/02/1992	18Y, 8M, 24D
Galileo	08/12/1995	13Y, 11M, 3D
New Horizons	29/02/2007	15Y, 5M, 23D (+)
Cassini	30/12/2000	19Y, 11M, 0D
Juno	05/07/2016	9Y, 11M, 7D (+)

Table 4.1: A list of the spacecraft missions which have encountered Jupiter. A mission duration ending with (+) signifies missions in operation at the time of writing.

With the exception of Galileo and Juno all spacecraft encounters with Jupiter have been flybys, taking advantage of the planet’s large gravitational pull to perform slingshot maneuvers. Galileo and Juno were sent exclusively to investigate the Jovian system, and account for the majority of data used in throughout this work.

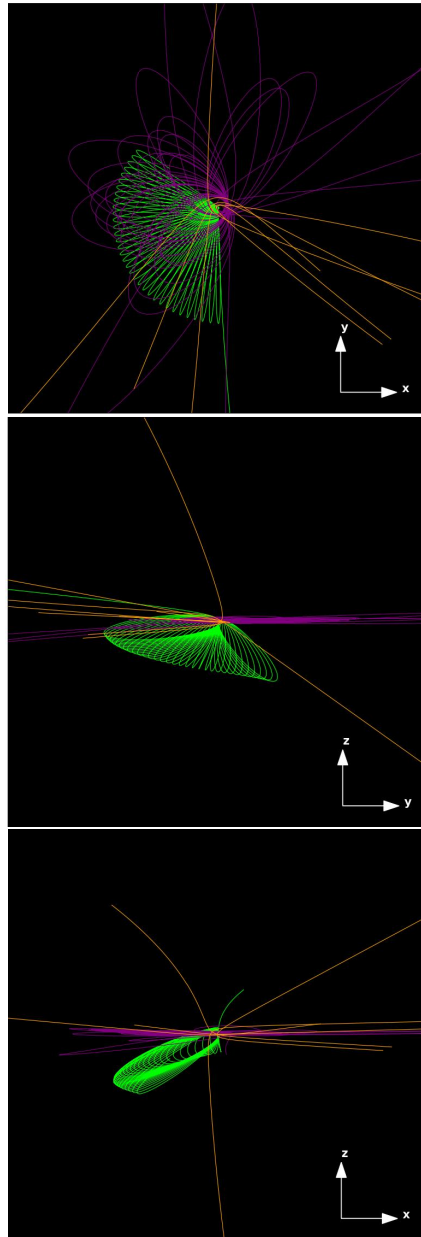


Figure 4.3: The orbital trajectories of Jovian missions, in the JSO reference frame, projected onto the three coordinate planes. Yellow trajectories illustrate flyby missions, red is the Galileo orbiter, and green is Juno, the sun is towards the positive x-direction.

4.2.1 Juno

Launched on August 5th 2011, Juno is the second mission in NASA's New Frontiers Program. The spacecraft is powered by three solar arrays arranged on three 9 m arms, making it the first solar-powered mission to Jupiter. The spacecraft weighs over 3.5 tonnes, carrying a selection of instruments including vector magnetometers, high and low energy charged particle detectors, radio and plasma wave antennas, and UV and IR spectroscopic imagers used in addressing its scientific objectives which are to investigate the planet's interior, deep atmosphere, complex magnetic field and its polar magnetospheric regions (Bolton et al., 2017). The majority of these instruments are contained within a radiation shield to protect them from the harsh conditions found within the planetary magnetosphere.

The spacecraft was engineered to spin at a rate of 2 rpm whilst performing elliptical polar orbits of the planet. The orbital configuration, whilst minimising exposure to radiation, allows the spacecraft to provide a wide, three dimensional spatial coverage of the Jovian system, whereas its predecessor, Galileo, only managed to cover an approximate disk shaped region owing to its equatorial orbit. The elliptical trajectory of the Juno spacecraft brings it as close as 8,000 km from the planet's 1 bar level, and as far as 113 R_J . Its baseline science objectives would be satisfied with 32 of these polar orbits. Orbital insertion was achieved on July 5th, 2016.

Two of the nine instruments on board Juno were used in the research presented here: the magnetometer, MAG (Connerney et al., 2017), and JADE (McComas et al., 2017).

The Juno MAG instrument consists of two independent tri-axial flux-gate (or vector) magnetometers and a pair of co-located imaging sensors for accurate altitude measurements when recording magnetic field data. The two magnetometers are located at 10 and 12 m along a magnetometer boom attached to the outer end of a solar array. Locating the magnetometers away from the body of the spacecraft is necessary to mitigate interference by induced fields from other spacecraft instruments. Simultaneous measurements of the magnetic field are made by both magnetometers at a rate of 64 vector samples per second. The instruments have a wide dynamic range between 1 nT - 1.6×10^7 nT spaced over 6 range settings, with resolutions between ± 0.05 nT - ± 25 nT depending on the range setting.

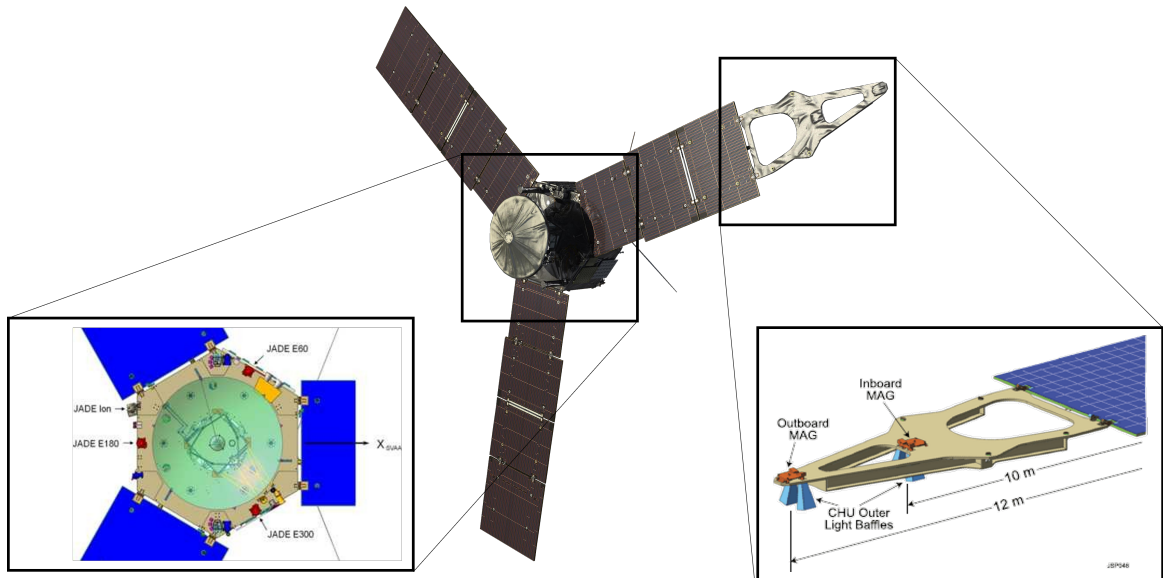


Figure 4.4: The Juno spacecraft with the JADE (left) and MAG (right) instrument highlighted.

JADE is comprised of three identical electron sensors (JADE-E), one ion sensor (JADE-I) and an electronics box. The three electron sensors are located at equidistant positions around the spacecraft body, providing full electron pitch angle coverage depending on orientation with respect to the background field. JADE-I provides a $270^\circ \times 90^\circ$ instantaneous field of view, with a full spatial observation available every spacecraft rotation (30s). This work exclusively uses JADE-E data as the ion dynamics were not of primary concern.

The JADE-E instrument is capable of measurements of energetic electrons in the range 100 eV - 95 keV, covering a field of view of $360^\circ \times 70^\circ$ at 1s resolution. It should be noted however, that due to instrumentation issues, one JADE-E sensor was

rendered unusable, and so only $240^\circ \times 70^\circ$ field of views were available for this work.

4.2.2 Galileo

Galileo was the first spacecraft to orbit and provide extended observations of an outer planetary system. The mission was made up of an orbiter and entry probe. It was launched from the Kennedy Space Center on October 18th, 1989 and entered into orbit around Jupiter on December 8th, 1995.

The Galileo mission was designed to cover a wide range of scientific objectives aimed at a holistic understanding of the Jovian system, including the dynamical relationship between the planet and its satellites. Galileo also carried an atmospheric probe which was jettisoned into the planet's atmosphere. The probe was able to supply data for almost an hour before being crushed by the immense atmospheric pressure. The orbiter was fitted with 13 separate instruments to fulfill its demanding scientific objectives (Johnson et al., 1992). The magnetometer, again abbreviated to MAG, was a principle component in this work.

Galileo MAG was a pair of boom-mounted dual tri-axial flux-gate magnetometers, located 6.87m and 11.03m along the boom (Kivelson et al., 1992). The boom-mounted design allowed for isolation of the sensors from the induced fields associated with the spacecraft and its instrumentation. The dynamic range of the two sensors ranged between ± 32 nT - ± 512 nT for the outboard sensor, suitable for the solar wind and distant Jovian magnetosphere, and ± 512 nT - $\pm 16,384$ nT for the inbound sensor, designed for analysis of the inner magnetosphere during perijoves. The magnetometer

boom can be seen in Figure 4.5.

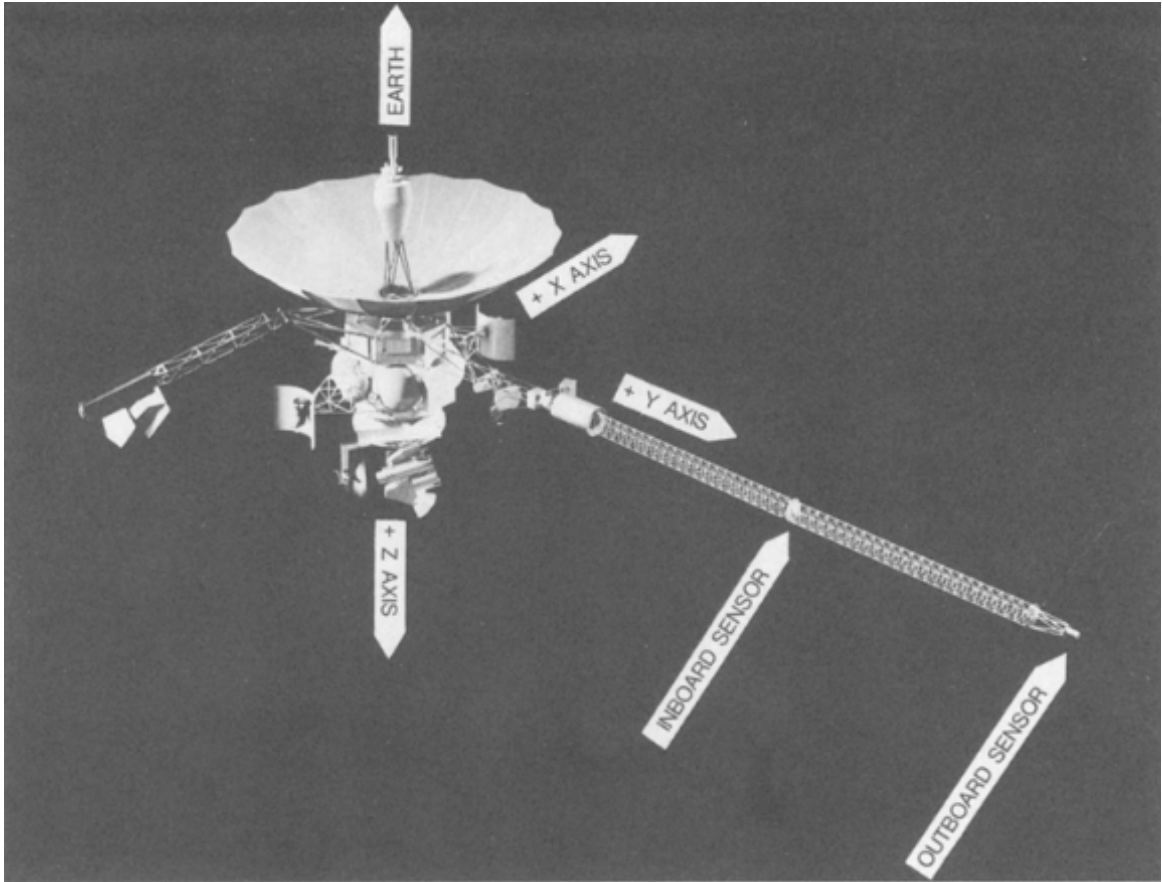


Figure 4.5: The Galileo spacecraft with Magnetometer instrument highlighted. Figure provided by Kivelson et al. (1992)

4.3 Reference Frames

A key feature in our data analysis methods is a choice of reference frame suitable to the work being undertaken. Here we review the key reference frames used throughout this thesis and detail the methods required to transform from one reference frame

to the next. Reference frames utilised in this work may be spherical, cylindrical or cartesian in nature or in a frame inherent to the physical system. For consistency and visualisation purposes in this chapter, we will describe each reference frame's alignment in the form of a cartesian triad.

4.3.1 Rotation Matrices and Proper Euler Angles

Throughout this thesis we use two main methods for obtaining reference frames. Firstly the SPICE method, using inbuilt python functions which draw positional information from publicly available data kernels to calculate the position and frame of the spacecraft. Secondly through custom frame rotations. The custom frame rotations work by rotating the reference frame about an axis by some angle. In order to rotate a reference frame about an axis, i , we must apply one of three matrices, R_i . Depending on the axis, i , these are referred to as roll, pitch and yaw rotations. Their respective matrices are given by:

$$R_x(\theta) = \begin{bmatrix} \cos(\theta) & -\sin(\theta) & 0 \\ \sin(\theta) & \cos(\theta) & 0 \\ 0 & 0 & 1 \end{bmatrix} \quad (4.1)$$

$$R_y(\theta) = \begin{bmatrix} \cos(\theta) & 0 & \sin(\theta) \\ 0 & 1 & 0 \\ -\sin(\theta) & 0 & \cos(\theta) \end{bmatrix} \quad (4.2)$$

$$R_z(\theta) = \begin{bmatrix} 1 & 0 & 0 \\ 0 & \cos(\theta) & -\sin(\theta) \\ 0 & \sin(\theta) & \cos(\theta) \end{bmatrix} \quad (4.3)$$

Knowing the rotation matrices is not the complete story however. One must also obtain angles of rotation. In order to maintain consistency and correctly rotate from one reference frame to the next proper Euler angle rotation chains must be implemented. These are specific orders one must rotate their frame by, for example rotation using matrices $R_z - R_x - R_z$. The angles of rotation can be obtained through rearrangement of the dot product when considering the axis of the intended reference frame, and the intermediary reference frame one achieves during the stages of transformation.

4.3.2 System III

The system III reference frame is a planetocentric, rotating spherical reference frame defined in the left handed coordinate system. The x component of the reference frame is aligned with the prime meridian, a point defined by radio astronomy in 1956. z is aligned with the planet's rotation axis and y completes the left handed triad. The reference frame rotates at the speed of Jupiter's magnetosphere. System III is the standard reference frame almost all Jovian data is accessible in via the PDS/PPI website. It is included in the SPICE kernels associated with Jovian missions and as such is relatively simple to obtain from the SPICEYPY package.

System I & II reference frames are used when dealing with the planetary

atmosphere. As Jupiter is mostly gaseous it experiences differential rotation. System I is used for the mid latitude to equatorial atmosphere while system II is used for the polar atmosphere. Each of these three reference frames rotates at slightly different velocities. As our work deals mainly with the magnetospheric dynamics of the system we do not consider the System I or II reference frames, but have included them here for completeness.

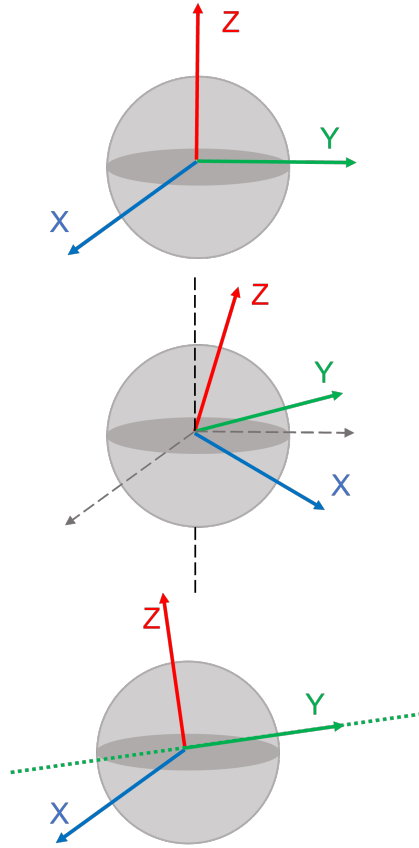


Figure 4.6: Three standard definition reference frames for Jupiter. (Top) System III: Here we show the right-handed version of the reference frame, which is the orientation chosen for our study, z is aligned with the Jovian spin axis, x is aligned with the prime meridian, and y completes the right handed triad. (Middle) Jupiter Magnetic: The z axis is aligned with the Jovian magnetic dipole, y is defined by the intersection of the magnetic and geographic equators, illustrated by the overlaid System III axis (black dashed lines), and x completes the right handed triad. (Bottom) JSO: x points towards the sun, y points in the direction of motion of the planet, highlighted by the dashed green line, and z completes the right handed triad.

4.3.3 JSO

The Jupiter-Solar-Orbital reference frame is defined with x pointing towards the sun, y points in the direction of motion of the planet and z completes the right handed triad. Throughout this work, we will make use of the “local time” to define the azimuthal position around the planet. The local time (LT) is given in hours based on a local, planetary meridian, defined by the Jupiter-Solar line. For example, the noon-meridian is 12 hours LT, and local dusk is located 90° in the direction of corotation from the noon-meridian.

The Jupiter-Solar-Magnetic or JSM reference frame is defined similarly, with the x component pointing towards the sun. However this frame wobbles such that the magnetic moment of the planet remains in the xz plane. y completes the right handed triad. It is important to note that this is not the same as the Jupiter Magnetic reference frame shown in Figure 4.6, in which the z axis rotates with the planet and remains aligned with the magnetic dipole. Transformation into these reference frames is made simple through the use of the SPICEYPY package and inbuilt functions.

4.3.4 Mean Field / De Hoffmann-Teller

The De Hoffmann-Teller frame of reference is one such that the z axis of the triad is aligned with the direction of the background magnetic field. The y component is given by the cross product of the z axis and the relative bulk plasma motion. Finally, the x axis is given by the cross product of the z and y axis. Both the x and y axis are perpendicular to the background field direction. This reference frame is particularly useful in discerning perturbations in the magnetic field and as such is key in detecting

the presence of Alfvénic or MHD wave modes. In order to obtain the transformation angles to convert to this reference frame, one must take a long period running average of the magnetic field data which is to be transformed in order to smooth out transient perturbations in the field and obtain an average magnetic field vector. Using the dot product, the proper Euler angles can then be obtained and used to convert to the desired reference frame.

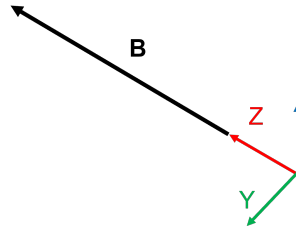


Figure 4.7: The De Hoffmann-Teller reference frame is aligned with the background field.

4.3.5 Dynamic Current Disk

When examining the magnetic field and subsequent currents associated with the current disc, one must rotate into a current disk reference frame. Failure to do so will mean certain aspects of the magnetic field will be indeterminable. The current disk is a complex three dimensional, time dependent system and as such obtaining a suitable reference frame is no simple task. We may define a cylindrical reference frame such that z is normal to a simplified current disk surface, ρ points radially outward and tangential to the local surface geometry. Finally ϕ completes the right hand triad. The surface of the current disk is defined by an empirical model. Rotation angles can be found by obtaining the normal to this surface.

The normal of a surface described by $F(x, y, z)$ where the conditions $F(x, y, z) = f(x, y) - z = 0$ and $\nabla F(x, y, z) \neq 0$ are applicable, can be determined by:

$$n = \frac{\nabla F}{\|\nabla F\|} \quad (4.4)$$

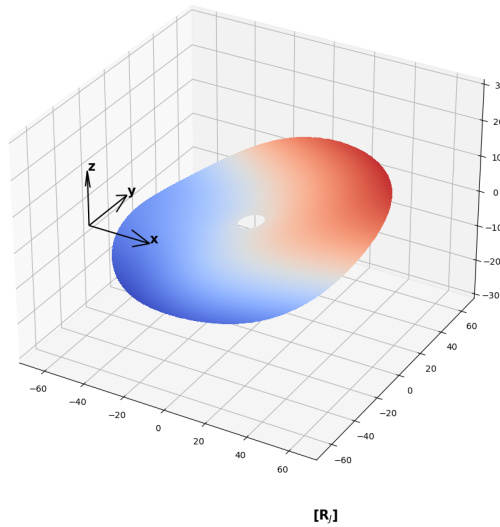


Figure 4.8: The topography of the Khurana et al. (2005) current sheet. The z axis is in the direction of Jupiter's spin axis. Warmer (cooler) colours dictate the height above (below) the x - y equatorial plane.

4.4 Conclusion

Since the flyby of the Pioneer missions in the early 70's a plethora of studies have been made in understanding Jupiter's complex magnetosphere using the limited data available. Galileo gave researchers the first Jovian orbiter mission, which was confined to equatorial latitudes. Galileo performed a de-orbiting and burning up upon entry into Jupiter's atmosphere. The Juno mission, orbiting Jupiter at the time of writing this thesis, presents a new opportunity to provide a detailed study of the planetary system. This thesis makes use of data primarily from Juno and Galileo in the following chapters to understand the structure of the magnetosphere-ionosphere coupling current system outlined in Chapter 2, and in understanding mechanisms which have the potential to explain the large precipitating electron energies. This is achieved through the use of magnetometer and electrostatic analyser data, the functionality of which has been outlined in this chapter.

Chapter 5

The Structure of the Equatorial Current System

This chapter contains work from *Local Time Asymmetries in Jupiter's Magnetodisk Currents* (Lorch et al., 2020). L.C. Ray was the primary academic supervisor, C.S. Arridge was the secondary academic supervisor, K.K. Khurana, C.J. Martin and A. Bader supported scientific discussions and analysis techniques.

5.1 Introduction

As discussed in Chapter 2, the current disk is a consequence of the strong rotationally driven dynamics of the Jovian magnetosphere. It is coupled to the planet through field-aligned currents. At Earth, acceleration regions associated with Alfvénic activity, and upward and downward field-aligned currents are observed. The same acceleration regions observed at Earth are also expected to be seen at Jupiter (Ergun et al., 2002), however there is expected to be a lesser influence on its magnetosphere-ionosphere (M-

I) coupled system owing to its greater distance from the sun and stronger magnetic field. In a planetary magnetosphere, flow patterns imposed by solar wind driven reconnection result in sunward flows through the equatorial magnetosphere (Dungey, 1961). A flow stagnation point develops at the point defined in (Kivelson, 2005) as

$$R_{stag} = \sqrt{\left(\frac{\Omega_J B_E R_J^2}{0.1 v_{sw} B_{sw}}\right)} \quad (5.1)$$

where Ω is the planetary rotational velocity, B_E is the equatorial field strength, v_{sw} and B_{sw} are the solar wind velocity and magnetic field respectively. Substituting in typical Jovian values produces a stagnation point much larger than the typical magnetopause standoff distance, signifying that rotational stresses dominate over Solar Wind influences.

Baron et al. (1996) was the first study to give evidence that the Jovian aurora are modulated by conditions in the interplanetary magnetic field. HST images suggest a coupling between the solar wind and the Jovian magnetosphere (Grodent et al., 2003; Bunce et al., 2005). A region of outer emissions, defining a region equatorward of the main oval, not coupled to the solar wind, experienced a considerable increase in brightness during a main emission expansion in spring 2007 (Nichols et al., 2009; Bonfond, 2012). It has been postulated that solar wind compressions would act to decrease the auroral brightness as the compressed magnetopause would confine plasma to smaller radial distances, increasing its angular momentum and decreasing the viscous drag on the ionosphere (Southwood et al., 2001), however more recent work has found correlations between the total emitted auroral power and the solar wind dynamic pressure (Nichols et al., 2007; Clarke et al., 2009; Nichols et al., 2009)

(Nichols et al., 2017; Kita et al., 2019). It is difficult to infer the influence of the solar wind on Jovian auroral emissions. This is due to difficulties in accurately predicting the solar wind magnetic field pressure and dynamic pressure, as there is significant error propagation from forward modeling of solar wind conditions at 1 AU to 5 AU (Tao et al., 2005b; Owens et al., 2005; Nichols et al., 2017).

Khurana (2001) explored this influence with the use of magnetometer data from Jovian missions. Although they were limited by the data coverage available at the time, they showed dawn-dusk asymmetries associated with solar wind interactions. However the influence of the solar wind is second to that of the current disk. The magnetic field geometry of Jupiter’s magnetosphere is heavily influenced by the presence of the plasma disk and associated current disk. The resultant topology, shown in Figure 2.7, is analogous to a hybrid of the solar wind and the terrestrial magnetosphere. The influence of the plasma disk can be seen to produce a strong azimuthal field component, creating a bent-back appearance in the magnetic field. With net mass outflow in the magnetodisk, the presence of a bent-back configuration is expected. A bent-forward configuration is a consequence of rapid inward motion of tenuous flux tubes following a reconnection event (Delamere et al., 2015a).

One crucial aspect of the current disk is its role in the coupling of the magnetosphere to the ionosphere. Radial mass transport rate and ionospheric conductivity characterises the magnetosphere-ionosphere coupling that can generate internally driven aurora, [e.g Nichols et al. (2004), Ray et al. (2010), and Delamere et al. (2013)]. The resultant electrical currents play a key role in the interchange of

forces within the plasma disk. Radial motion of plasma requires an increase in angular momentum, which is balanced by a decrease in planetary angular momentum through the viscous interaction of the ionosphere and the neutral atmosphere. Voyager plasma parameters substituted into the equation for corotation breakdown distance, Eq 2.2 by Hill (1979) discussed in Chapter 2, indicated a significant departure from corotation occurring at $20R_J$.

Initial theories of M-I coupling at Jupiter neglected the influence of azimuthal currents. The total radial current, i_r , arising from corotation breakdown was expressed as

$$i_r = \dot{\mu} \frac{v_{\perp}}{B} \quad (5.2)$$

where $\dot{\mu}$ is the rate of plasma mass production per unit radial distance. Since the plasma velocity perpendicular to the magnetic field and the magnetic field magnitude varied with radial distance, this self consistently resulted in the radial current being a function of radial distance (Pontius et al., 1982). Figure 5.1 shows a comparison between the terrestrial and Jovian current systems. It can be seen that the internal driving within the Jovian magnetosphere produces an additional radial current, which is comparable in magnitude to the Jovian ring current. Lorch et al. (2020) aimed to answer the question: What are the local time asymmetries in this magnetodisk current system?

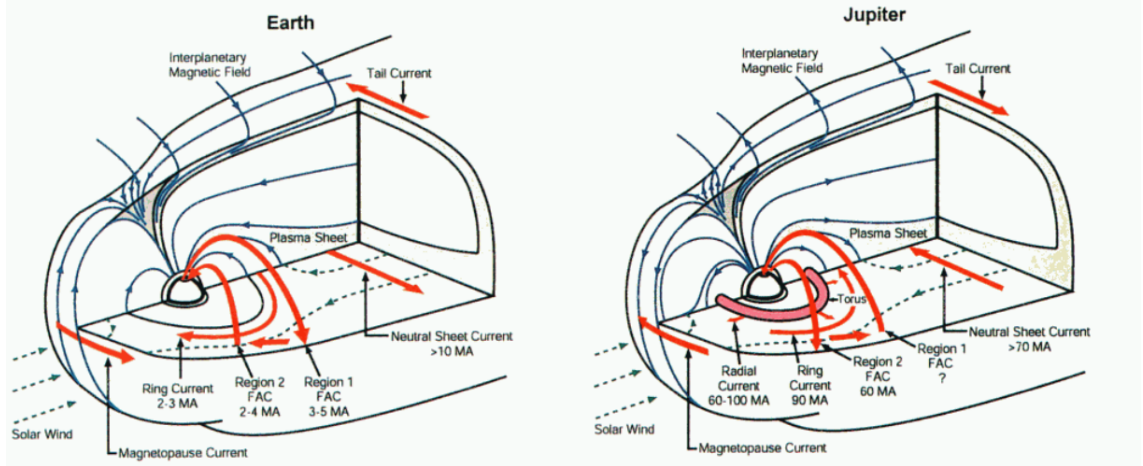


Figure 5.1: An illustration of the (left) terrestrial and (Right) Jovian current systems. The magnitude of currents within the Jovian system is much larger than those within the terrestrial system. Further to this, the presence of an internal plasma source, and the subsequent internal driving of the magnetospheric dynamics results in a large radial current, comparable to the Jovian ring current. Image Credit: Khurana (2001).

Cowley et al. (2002), building off the Hill-Pontius model, showed upward currents existed throughout a range of radial distances covering the typical corotation breakdown region ($\approx 20 R_J$) to an outer boundary of $100 R_J$. At the time it was suggested that return currents existed outside of this region at greater radial distances. Furthermore, this work highlighted the importance of a current disk in understanding the current structure throughout the system and to better quantify the magnitude of the field-aligned currents. This showed that when accounting for a current disk in the Hill model, the currents are an order of magnitude larger. The field-aligned current densities within this region were found to peak around $0.4 \mu\text{A m}^{-2}$.

The most commonly used models of the Jovian system invoke the assumption that

the currents are symmetric about the rotational axis, however this simply cannot be the case. Dynamical variations in the current disk would form from changes in the plasma environment, such as radial transport or velocity differentials. Certain features in the main emission are known to be fixed in local time, such as discontinuities in the emission near noon and bright dawn storms (Radioti et al., 2008; Gustin et al., 2006; Chané et al., 2018). Ray et al. (2014) demonstrated such variations in these currents by applying a 1D M-I coupling model at 1 hour LT intervals throughout the Jovian magnetosphere. Using a local time dependent magnetic field they showed that the auroral currents were stronger in the dawn sector than the dusk or noon sector by an order of magnitude. The authors emphasised that this approach did not consider azimuthal currents or the azimuthal bend-back in the magnetic field, and explicitly called for their consideration in future studies.

LT asymmetries have been observed in the UV auroral emissions. Using 1663 FUV Hubble space telescope images Bonfond et al. (2015) showed that 93% of southern and 54% of northern hemispheric images suggested a larger emitted power in the dusk sector than the dawn sector. The southern dusk sector was approximately three times brighter than its dawn counterpart, while northern sectors displayed a relatively similar brightness. The authors attributed this difference to magnetic field variations between hemispheres, arguing also that the southern values are a better representation of the field-aligned current system associated with the main auroral emission (MAE) as they lack the superimposed uncertainty of the northern magnetic anomaly.

This chapter details the methodology, data analysis techniques and results found

in pursuit of this question. Firstly, details of the data selection and pre-processing is expanded upon, followed by a derivation of the key equations used in determining the height integrated current density (HICD). Finally, presentation and discussion of the results highlights the key discoveries in this project.

5.2 Lobe Field Identification from Magnetometer Data

5.2.1 Data Selection

Understanding the structure of the currents within the current disk requires magnetometer data with vast spatial coverage of the magnetosphere. This was achieved by utilising all available Jovian spacecraft missions except for New Horizons and Cassini, as they do not provide sufficient data relevant to this study during their flybys. An equatorial projection of the spacecraft trajectories can be seen in Figure 5.2.

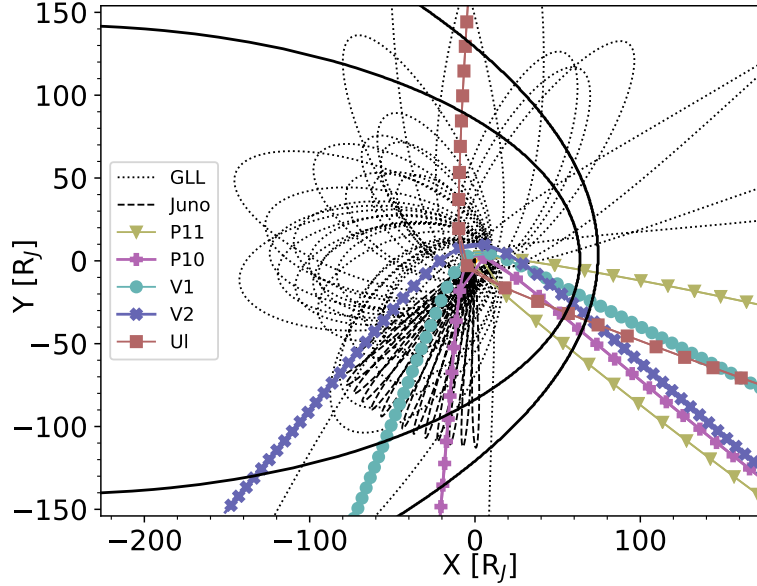


Figure 5.2: Trajectories of Jovian missions used in this study, projected onto the equatorial plane with the Sun to the right. Also shown are the Joy et al. (2002) bow shock and magnetopause locations for a compressed magnetosphere.

Data was further constrained within a probabilistic magnetopause and bow shock region from Joy et al. (2002). The equatorial profiles of the bow shock and magnetopause were calculated by numerically minimising the second order polynomial

$$z^2 = A + Bx + Cx^2 + Dy + Ey^2 + Fxy \quad (5.3)$$

in the JSO coordinate frame where x points towards the sun, z is along the Jovian spin axis and y completes the right handed triad. Values A through F , as defined in Joy et al. (2002), are shown in Table 5.1.

Coefficient	Bow Shock	Magnetopause
A	$-1.107 + \frac{1.591}{\sqrt[4]{P_d}}$	$-0.134 + \frac{0.488}{\sqrt[4]{P_d}}$
B	$-0.566 - \frac{0.8112}{\sqrt[4]{P_d}}$	$-0.581 - \frac{0.225}{\sqrt[4]{P_d}}$
C	$0.048 - \frac{0.059}{\sqrt[4]{P_d}}$	$-0.186 - \frac{0.016}{\sqrt[4]{P_d}}$
D	$0.077 - \frac{0.038}{\sqrt[4]{P_d}}$	$-0.014 + \frac{0.096}{\sqrt[4]{P_d}}$
E	$-0.874 - \frac{0.299}{\sqrt[4]{P_d}}$	$-0.814 + \frac{0.811}{\sqrt[4]{P_d}}$
F	$-0.055 + \frac{0.124}{\sqrt[4]{P_d}}$	$-0.050 + \frac{0.168}{\sqrt[4]{P_d}}$

Table 5.1: The coefficients used in the Joy et al. (2002) statistical magnetopause and bow shock locations. P_d is the dynamic pressure of the solar wind.

5.2.2 Current Disk Field Isolation

Spacecraft magnetometers within the Jovian system measure a summation of several field components. These include, but are not limited to, the internal dynamo field, the current disk magnetic field, the magnetic field arising from Chapman-Ferraro currents associated with the magnetopause and the induced field associated with spacecraft electronics. To ascertain the magnetic field contribution solely from the current disk, these additional field components must be either eliminated or minimised. Magnetic fields associated with the spacecraft electronics are accounted for in the data pipeline

prior to data acquisition. To account for the magnetopause currents, the data is limited to regions within the middle magnetosphere, distant from the magnetopause. However it is important to consider that towards the boundary of this region the magnetopause currents would increasingly vary the structure of the current system. The internal magnetic field is accounted for by subtraction of an internal field model.

For the study detailed in this chapter, the JRM09 internal field model (Connerney et al., 2018) was subtracted from the raw magnetometer data. JRM09 is a tenth order spherical harmonic expansion of Jupiter’s magnetic field with coefficients derived from Juno perijove data (PJ01 through PJ09). The coefficients of this model are provided in Appendix A, at the end of the thesis. Previous models were constructed using data from Pioneer and Voyager flybys, and constrained to the Io auroral footprint (Connerney et al., 1998; Hess et al., 2011), or had an additional dipole superimposed to agree with Hubble space telescope observations (Grodent et al., 2008a). The JRM09 model was the ideal candidate for this study as the model exploits low altitude measurements of the magnetic field and so contamination by external fields is negligible. One additional consideration was the long-term variations in the Jovian magnetic field between missions. Stallard et al. (2018) gave evidence supporting an immutable intrinsic field between the Galileo era and the Juno era, hence the JRM09 model was applicable through these periods.

To best isolate the magnetic field associated with the current disk from the magnetopause and intrinsic planetary magnetic field, two techniques are applied. Firstly, data collection was limited to a region inside a predicted compressed

magnetopause boundary. This was achieved by estimating the magnetopause standoff distance using the Joy et al. (2002) model under a relatively high solar wind pressures of 0.331 nPa (Walker et al., 2001). These values produced a magnetopause standoff distance of around 60 R_J . Data outside of this bounded region was rejected from the analysis. Varying the solar wind pressure parameter expands or compresses the magnetopause boundary, subsequently adding or removing data from the final selection used in the analysis. Compared to the 7382 used in the overall analysis though, the amount of data added or removed in this way does not significantly affect the results of this work. Isolation of the remaining data from the intrinsic planetary field was achieved by subtracting the JRM09 magnetic field model (Connerney et al., 2018) from the raw data. The choice of magnetic field model did not vary the results significantly, as the estimations of the magnetic field are comparable in the middle magnetosphere. Figure 5.3 shows a sample of the raw magnetic field data from the Galileo magnetometer, alongside the JRM09 modeled internal field and differenced field. It is clear to see that subtraction of the internal field does dramatically alter the profile of the magnetic field data, but the periodic reversals of the radial magnetic field component remains prominent.

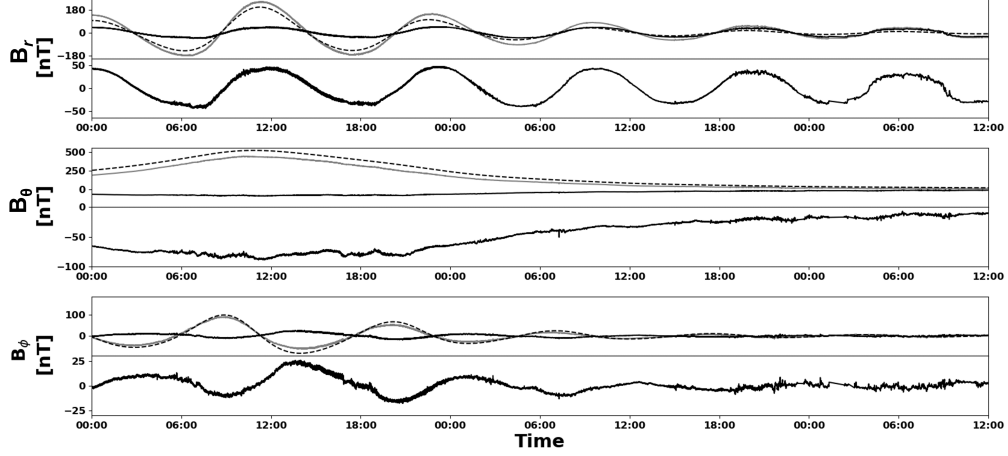


Figure 5.3: A sample of Galileo magnetometer data in the spherical System III reference frame. Two panels for each component are provided, the upper panel shows (solid grey) the combined field magnitude, (dashed) the JRM09 field model, (solid black) the differenced magnetic field. The lower panel shows the differenced magnetic field, but over a smaller range of y-axis values.

In order to both correctly isolate the magnetic field associated with the current disk and apply $\nabla \cdot \mathbf{J} = 0$, it is crucial to perform the data analysis in a reference frame defined by the current disk geometry. This rotating cylindrical reference frame is defined by a ρ component pointing radially outward from the planet and locally tangential to the current disk surface, z is defined as the normal to the surface, while ϕ completes the right handed triad. This work assumes that the plasma azimuthal velocity is equal to the rotational velocity of the defined current disk reference frame. As described in Chapter 4, transformation matrices are applied to rotate the pre-

defined System III coordinate frame into this dynamic current disk reference frame. The angles of rotation are given by the proper Euler angles obtained through analysis of the surface gradients to the model current disk provided in Khurana et al. (2005)

$$Z_{cs} = \sqrt{\left[\left(x_H \tanh \frac{x}{x_H} \right)^2 + y^2 \right]} \cdot \tan(\theta_{CS}) \cos(\phi - \phi') + x \left(1 - \tan \left| \frac{x_H}{x} \right| \right) \tan(\theta_{sun}) \quad (5.4)$$

where x_H is the hinging distance of the current disk, set to be $-47 R_J$; x and y are the Jupiter-Sun-Orbital positions of the spacecraft, where \vec{x} points towards the sun and \vec{y} points anti-parallel to Jupiter's orbital velocity; θ_{CS} is the tilt angle of the current disk; ϕ is the west longitude of the spacecraft; ϕ' is the prime meridian of the current disk, and θ_{sun} is the angle between the Sun-Jupiter line and the Jovigraphic equator. The model incorporates hinging of the current disk due to solar wind forcing and information delay as a function of radial distance due to wave travel time and field geometry. For further information on this model the reader is referred to Khurana et al. (2005) and Khurana (1992).

5.3 Methodology

5.3.1 Calculation of Magnetodisk Currents and their Divergences

Local measurements of the magnetic field, obtained by a small number of spacecraft in a constellation arrangement can provide an excellent approximation of the current density (Kivelson, 2005). Unfortunately, no such mission is present, or planned, for

the outer planets. However, it is possible to derive the radial and azimuthal height integrated current density. Beginning with the cylindrical formulation of Ampère's law, Eq 1.6 from Chapter 2, and neglecting the displacement current

$$\mu_0 J_\rho = \frac{1}{\rho} \left(\frac{\partial B_z}{\partial \phi} - \rho \frac{\partial B_\phi}{\partial z} \right) \quad (5.5)$$

$$\mu_0 J_\phi = - \left(\frac{\partial B_z}{\partial \rho} - \frac{\partial B_\rho}{\partial z} \right) \quad (5.6)$$

where J_ρ and J_ϕ are the radial and azimuthal current densities respectively. Within the current disk, azimuthal variations in B_z are negligible and hence are not considered in the determination of the radial HICD. The HICD is given as the integral of these equations over the height of the current disk. For the radial component this is

$$\int_{-w}^w J_\rho \partial z = \frac{1}{\mu_0} \int_{-w}^w \partial B_\phi \quad (5.7)$$

The saw-tooth like structure of a Harris current sheet means that over the width of the current disk, the half-width of which is w , $\int_{-w}^w \partial B_\phi = 2B_\phi$, hence the radial HICD, J'_ρ is given as:

$$J'_\rho = -\frac{2B_\phi}{\mu_0} \quad (5.8)$$

Under similar derivation, the azimuthal component is found to be:

$$\int_{-w}^w J_\phi \partial z = \frac{1}{\mu_0} \left(\int_{-w}^w \partial B_\rho - \frac{\partial B_z}{\partial \rho} \int_{-w}^w \partial z \right) \quad (5.9)$$

Again, over the width of the current disk, $\int_{-w}^w \partial B_\phi = 2B_\phi$. The second integral

on the right-hand side gives the current disk thickness, $\int_{-w}^w \partial z = 2w$. Hence the final solution for the azimuthal HICD, J'_ϕ , is

$$J'_\phi = \frac{1}{\mu_0} \left(2B_\rho - 2w \frac{\partial B_z}{\partial \rho} \right) \quad (5.10)$$

where for each equation B_ρ , B_ϕ and B_z are the differenced radial, azimuthal and normal field strengths in the lobe regions respectively. The lobe field, at Jupiter, refers to the magnetic field in regions above and below the current disk. The half thickness of the current disk is assumed to be $2.5 R_J$ to align with other studies (Connerney, 1981; Khurana et al., 1993). In reality however, the current disk has a spatially varying half thickness. In this study, varying the current disk half thickness between $2 R_J$ and $10 R_J$ does not produce a significant difference in the HICDs outside of $60 R_J$. However positive and negative variations are found in the azimuthal HICD, up to 20% within $50 R_J$, and a variance of up to 100% localised at $50 R_J$. B_z was determined by fitting a polynomial of the form $B_z(\rho) = \frac{a}{\rho} + \frac{b}{\rho^2} + \frac{c}{\rho^3}$, bounded between $6 R_J$ and $100 R_J$, to the total set of returned values of the z component of the differenced magnetic field. Coefficients of best fit were found to be $a = -1.825 \times 10^2 \text{ nT } R_J$, $b = 1.893 \times 10^4 \text{ nT } R_J^2$ and $c = -8.441 \times 10^4 \text{ nT } R_J^3$. This was then differentiated to give $\frac{\partial B_z}{\partial \rho}$.

As described in Chapter 2, the $\sim 10.3^\circ$ tilt of Jupiter's magnetic field (Connerney et al., 2018) with respect to its spin axis results in a periodic reversal of the radial magnetic field for an observer at the spin equator. This periodic reversal in B_ρ can be exploited in a numerical algorithm to return the lobe magnetic field. The algorithm was constructed such that it identified plateaus in the radial magnetic field measurements, coincident on when the spacecraft was traversing the lobe region.

These plateaus were identified, using an iterative process, as regions where consecutive measurements of B_ρ do not deviate by more than $\pm 7.5\%$ for a period of 30 minutes or more. The applied value of $\pm 7.5\%$ provided a *juste milieu* by allowing for small fluctuations in the field whilst ignoring the larger variations associated with the traversal of lobes.

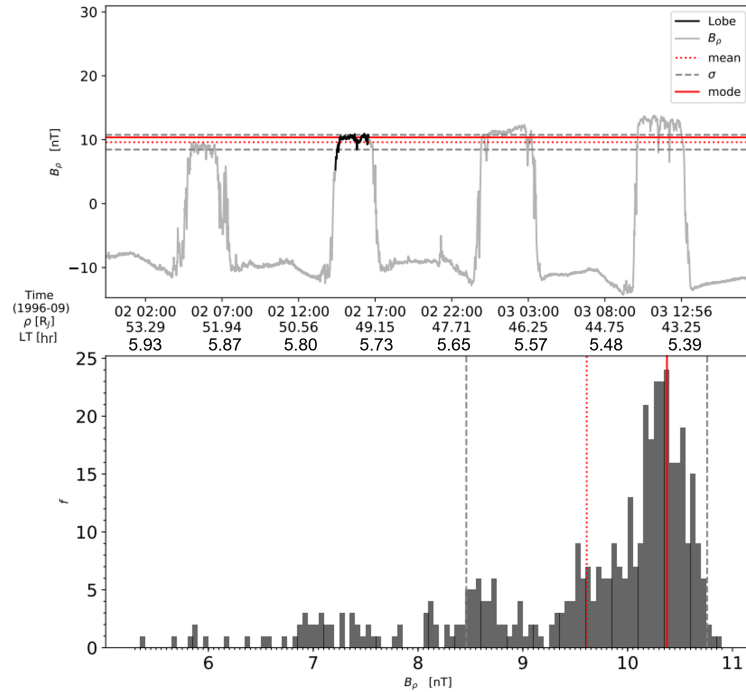


Figure 5.4: (*Top*) The radial component of the differenced field can be seen in grey. The dark region indicates a single lobe region determined by the algorithm. The algorithm returns consecutive magnetic field measurements with less than a 7.5% variability for a period of more than 30 minutes. (*Bottom*) A frequency histogram of the magnetic field strength during the lobe traversal, shown as a thick black line in the top panel. In both panels dashed grey lines indicate the standard deviation of the lobe values, the solid red line indicates the modal value and the dashed red line indicates the mean. The mean is skewed by the large tail in the histogram, associated with part of the recording in the top panel being of the non-lobe field.

The modal value of B_ρ , B_ϕ and B_z were chosen to represent the magnetic field in the lobe regions. The mode gives a more accurate value of the lobe field strength, as opposed to the mean which is often skewed by the slowly varying field signatures

recorded whilst still within the current disk. Figure 5.4 demonstrates how the non-lobe field skews the mean, while the modal value lies within a more reasonable estimate of lobe value. In the event where no modal value was present, a median value was instead adopted. A total of 7382 lobe field values were retrieved, however a systematic bias is expected to be present in this value. For example, a sharp fluctuation in the lobe field will result in two readings being returned, one prior to and one after the fluctuation. Both of these recordings are returned and used in this study. The number of true lobes recorded will be less than what were retrieved, however the magnitude of the fluctuation is still a good representation of the lobe field.

5.4 Results

5.4.1 Height Integrated Current Density

The radial and azimuthal HICD, obtained through the calculation outlined above, are illustrated in Figure 5.6. The radial and azimuthal individual values and their binned averages are shown in Figures 5.6a and c, and Figures 5.6b and d, respectively. Bin sizes are $5 R_J$ radially by 1 hr LT. Binning values was achieved by defining a series of concentric ring segments and determining which of these bins the spacecraft was in whilst the lobe value was recorded. For this, the mean position of the spacecraft at that time was used. Figure 5.5 illustrates the number of returned readings per cell as \sqrt{n} , which is inversely proportional to the standard error on the mean. In most cases, measurements from different orbits are recorded in the same bin. It is assumed that the magnetic field does not change significantly over the course of each orbit. If this was the case however, by taking the average of the calculated height integrated

current density it is reasonable to assume that any transient variations are smoothed out of the final result. Red/blue diverging colours indicate outward and planetward radial currents, while the azimuthal currents all flow in the direction of corotation. The azimuthal currents fall off rapidly with distance, as such a natural log scale was implemented to highlight variations in the structure.

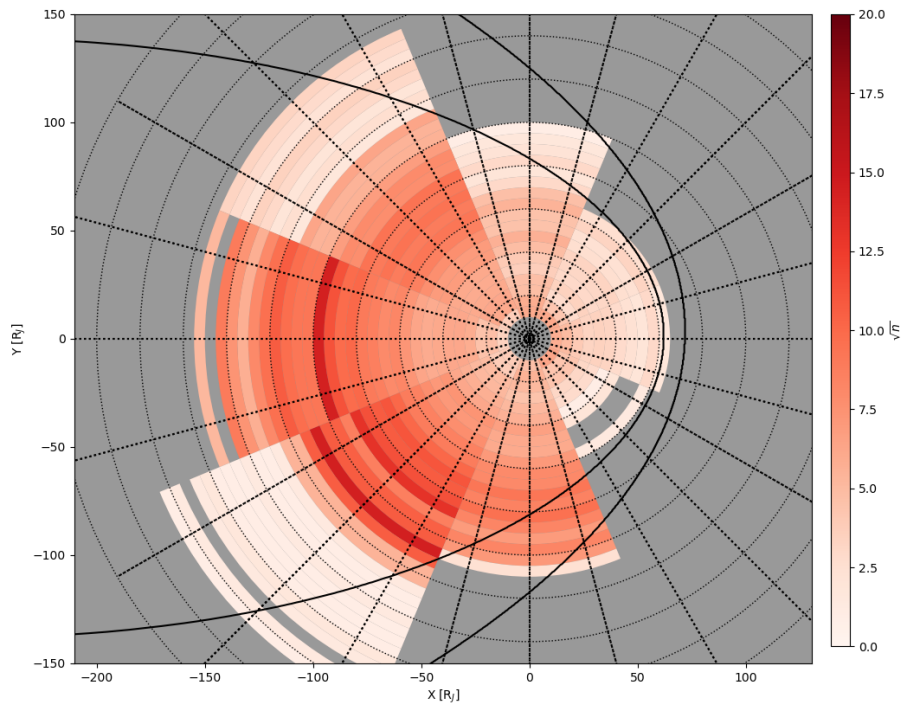


Figure 5.5: The square root of the number of data points recorded within each bin. \sqrt{n} was chosen as it is inversely proportional to the standard error on the mean. Solid black lines represent the magnetopause and bow shock boundaries from Joy et al. (2002).

When initially viewing the radial HICD presented in Figure 5.6, it is apparent that a clear asymmetry exists. This manifests in the form of strong outward radial currents dominating the midnight through dawn magnetosphere, with weaker planetward currents present from noon through dusk. Within $40 R_J$ strong outward radial currents are present, but weaken at noon. Planetward of this, at radial distances below of $20 R_J$, radial currents appear to be weaker in the post dusk sector than at other LTs. Azimuthal currents are seen to decay with radial distance, though are larger in the midnight through dawn sectors than in the noon through dusk sectors.

The asymmetrical nature of the HICDs is better visualised by splitting the results of Figure 5.6 into concentric rings of incremental radial distance. Figure 5.7 illustrates the magnitude of each $5 R_J \times 3$ hr bins concentric ring, centred at $5 R_J$ intervals. Due to the larger bin sizes some features, such as the reversal of the radial HICD in the outer dusk region, are not evident in Figure 5.7. This is the same for Figures 5.8 and 5.9, which use 6 hr LT bins. Both the radial and azimuthal components begin to exhibit local time asymmetries from a distance of $15 R_J$. For the radial currents, a maxima develops around 6LT with a minima at noon. This minima shifts to around 18UT at larger radial distances. This might coincide with the loading and unloading of plasma through the Vasyliunas cycle. Azimuthal currents exhibit a noon-midnight asymmetry, peaking around midnight and minimising at noon, possibly indicating a solar wind influence on the system. Whilst dominating the inner magnetosphere, the azimuthal currents fall off rapidly with increasing distance, becoming comparable to the radial currents further from the planet.

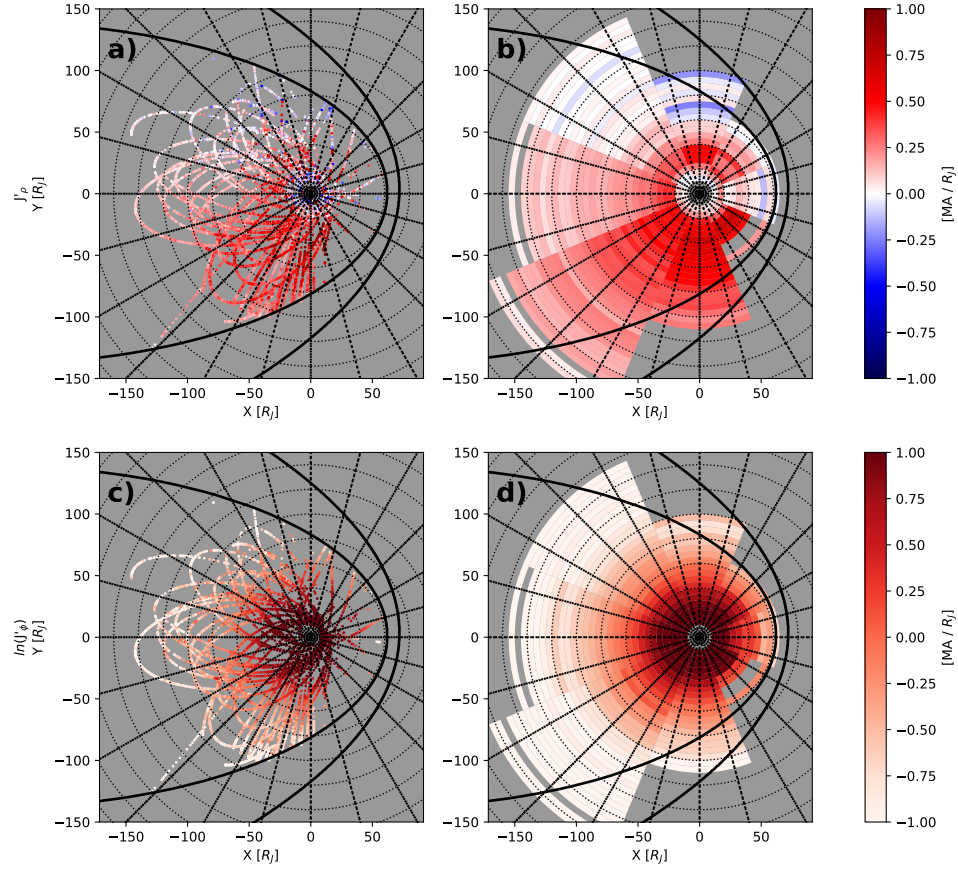


Figure 5.6: HICD from lobe regions determined by the algorithm. (a) The height integrated radial current density. Warmer (cooler) colours indicate outward (inward) flowing radial currents. These values are binned and averaged in (b). (c) The height integrated azimuthal current density. Note the log scale on the colour axis. Current flow is in the direction of corotation and again the values are binned and averaged in (d). Concentric dotted rings are placed at intervals of $20 R_J$. 1 hour LT divisions are separated by straight dotted lines. Solid black lines represent the magnetopause and bow shock boundaries from Joy et al. (2002).

Further emphasis can be placed on the local time asymmetries in the system by

separating the results into their local time sectors coinciding with midnight, dawn, dusk and noon. This is shown in Figures 5.8 and 5.9, where 6 hr LT bins were used, centred on the respective regions. Black dots represent the HICD calculated from lobe values and the red line represents the mean binned every 5 R_J . Radial currents are seen to peak around 30 R_J then steadily decrease. The azimuthal currents fall off with radial distance, following a $\frac{a}{r^b}$ relationship. By fitting the data to such a function, the exponent b , can be determined. For both the radial and azimuthal components, currents in the noon sector are weaker than the other sectors. For the azimuthal currents, the night sector has the most rapid decrease of magnitude with radial distance, as determined by the fitting routine, while dawn has the slowest fall off. This might be related to the loading and unloading of plasma, where the azimuthal current is carried by the rotating plasma.

For the azimuthal and radial height integrated current densities in each bin, the results are distributed in the form of a normal distribution. As such, the errors in Figures 5.7, 5.8 and 5.9 are given by the standard error of the mean, ϵ , calculated as:

$$\epsilon = \frac{\sigma}{\sqrt{n}} \quad (5.11)$$

where σ is the standard deviation of the averaged data, and n is the number of data points within the bin. The mean was chosen over the median to represent the results, as the associated error was considerably less than the median absolute error obtained from the median average.

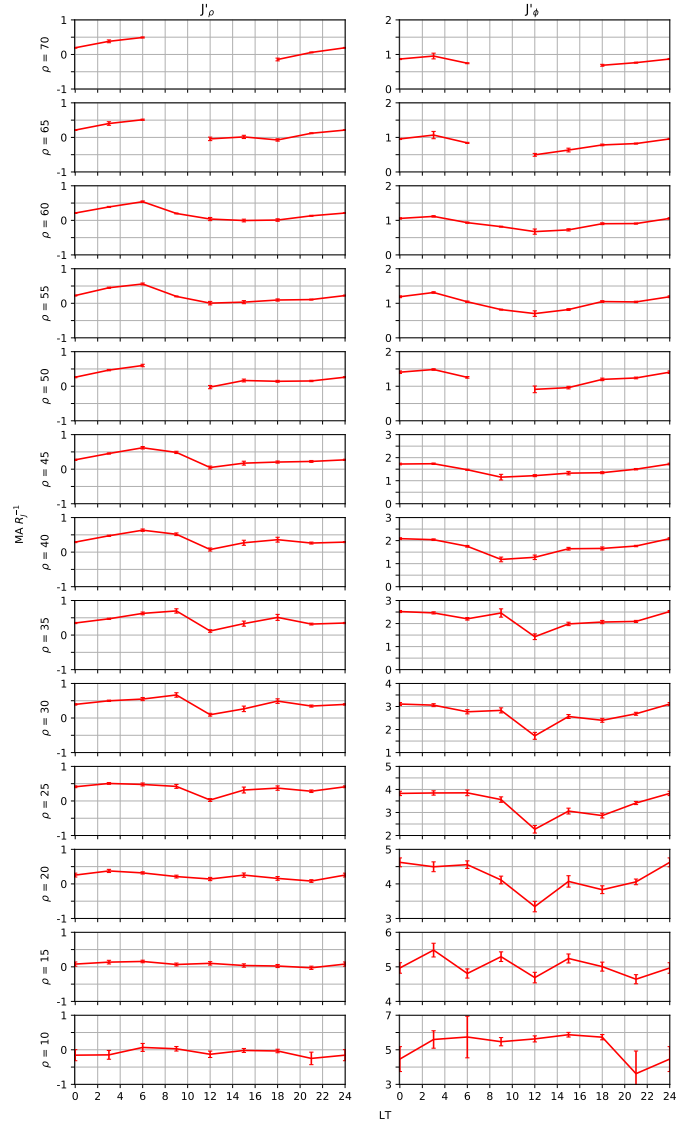


Figure 5.7: The mean radial (*left*) and azimuthal (*right*) HICD over all LTs, averaged in radial bins of $5 R_J$. Results are averaged into each sector. Error bars represent the standard error of the mean.

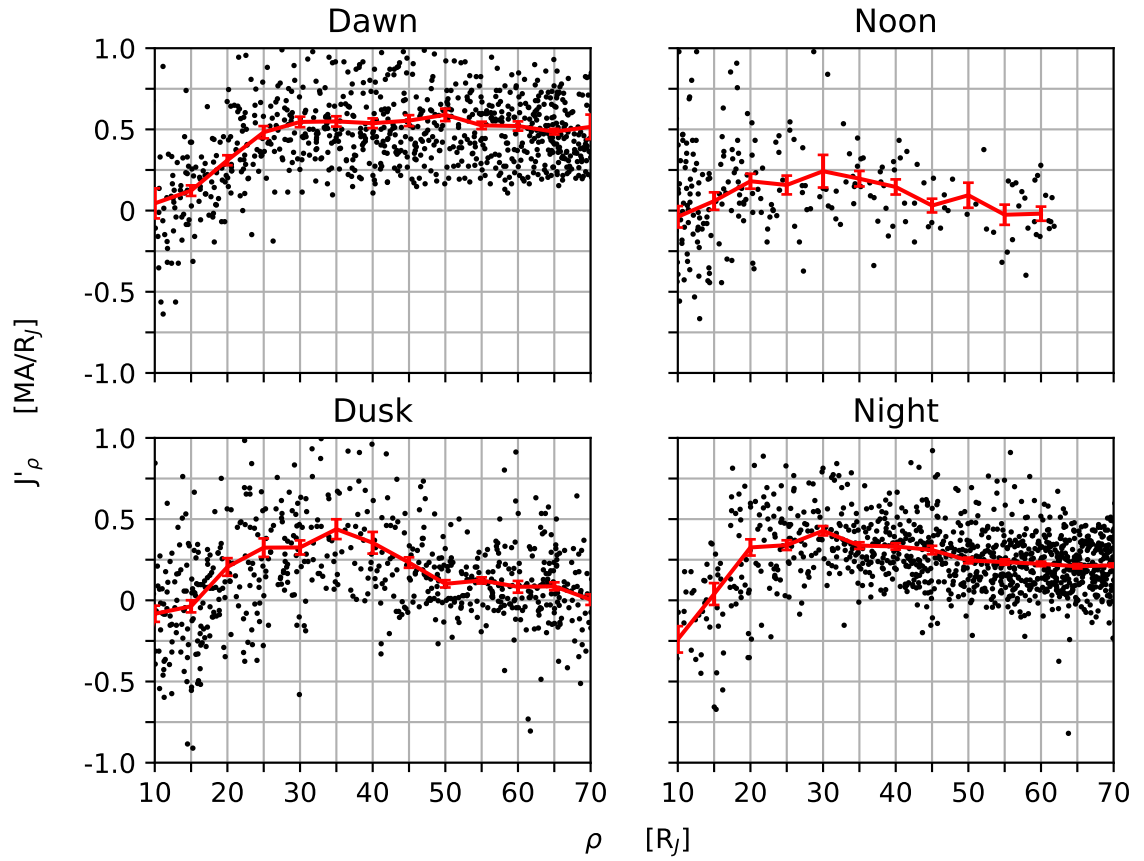


Figure 5.8: The radial HICD shown against radial distance from the planet binned in LT sectors. HICDs from lobe traversals are represented by black dots. The red line is the mean of the $5 R_J$ bins. Error bars represent the standard error of the mean.

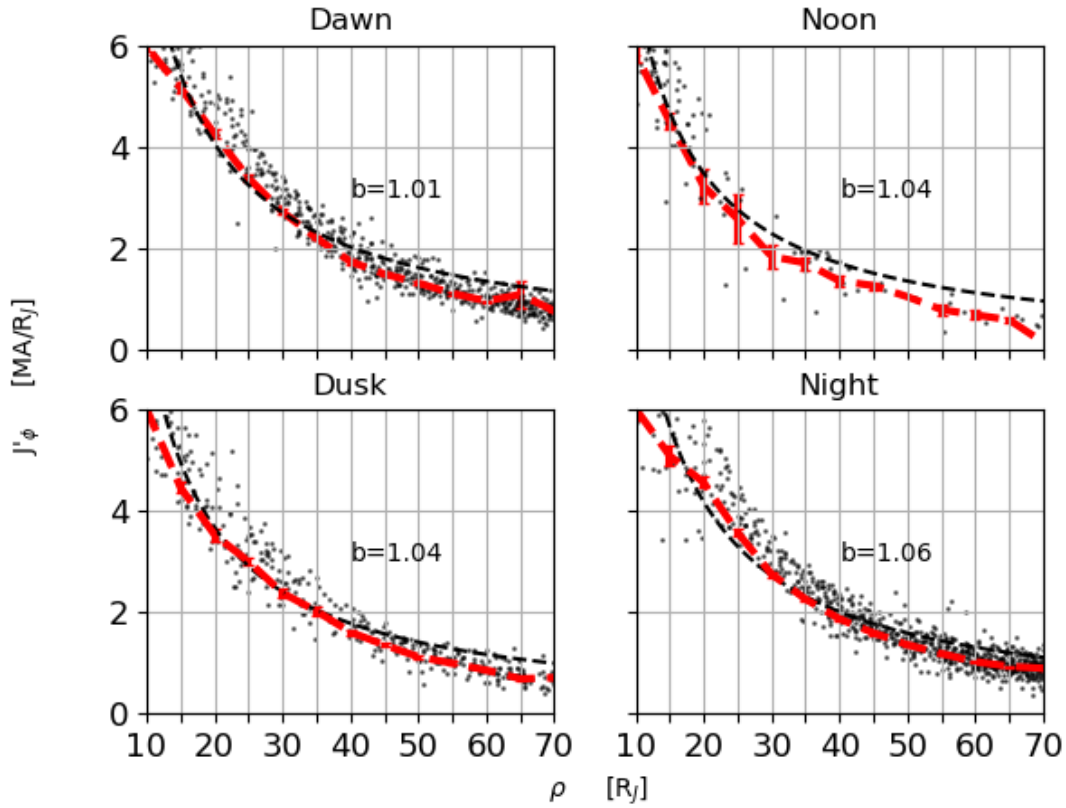


Figure 5.9: The azimuthal HICD shown against radial distance from the planet binned in LT sectors. HICDs from lobe traversals are represented as black dots. The red line is the mean of the $5 R_J$ bins. Error bars represent the standard error of the mean. The dashed black line is the fitted value to the function $\frac{a}{\rho^b}$, with the corresponding b value labeled.

5.4.2 Divergence of the Height Integrated Current Density

The current system coupling the Jovian magnetosphere to the ionosphere is expected to exhibit current continuity. Expressed mathematically, it states that the divergence

of the current density is 0:

$$\nabla \cdot J' = \nabla_{\perp} \cdot J'_{\perp} + \nabla_{\parallel} \cdot J'_{\parallel} = 0 \quad (5.12)$$

Hence it can be shown that the divergence of the radial and azimuthal components, $\nabla J'_{\rho}$ and $\nabla J'_{\phi}$, can be related to the divergence of the parallel currents. Substituting in values for the binned HICDs, these divergences were calculated and can be seen in Figure 5.10, which shows the divergence of the radial (5.10a), azimuthal (5.10b) and perpendicular (5.10c) HICD. Warmer colours in the diverging colour scale are indicative of current being added to the denoted component, while cooler colours represent a loss of current. In line with the previous work of Khurana (2001), it can be seen that radial currents are enhanced within the inner middle magnetosphere and depleted through noon and dusk, while azimuthal currents are fed in the dusk magnetosphere, and removed at dawn.

Equation 5.12 shows that the perpendicular and parallel divergence must equal 0. Therefore, the sum of the radial and azimuthal current divergence can be used to reveal the location of upward and downward FACs in Figure 5.10. Again warmer colours indicate upward FACs and cooler currents indicate downward FACs associated with auroral particle precipitation. The field-aligned current locations deduced in this study agree with those from Khurana (2001), however there is now complete coverage in the dusk and noon sector due to the additional data.

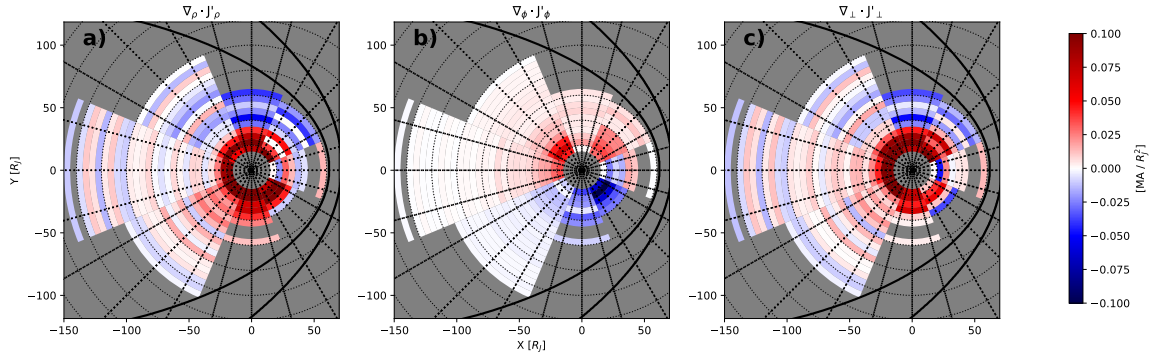


Figure 5.10: The divergence of the HICD for the (a) radial (b) azimuthal and (c) perpendicular components, in a similar format to Figure 5.6. The divergence of the perpendicular components is analogous to the parallel current density.

5.5 Discussion

7382 traversals are identified using data spanning nearly 5 decades. Over this time the solar wind conditions will have varied significantly over the long term solar cycle, as well as experiencing transient events. Though the orientation of the interplanetary magnetic field has little effect on asymmetries in the system, the dynamic pressure of the solar wind does (Cowley et al., 2001; Delamere et al., 2015b). For example, a compression of the magnetosphere due to an increase in solar wind dynamic pressure forces plasma radially inward. This increases its angular velocity and consequently decreases the corotation enforcement currents, altering the magnetic field geometry. Additionally, the location of the MAE can vary day-to-day by up to 3° of latitude. This has been attributed to changes in Io torus and plasma disk density associated with increased Io volcanism (Bonfond, 2012). Binning and averaging the available

data into individual sectors means temporal fluctuations can be neglected, such as those associated with variations in the solar wind dynamic pressure or perturbations in the current disk. Therefore, this analysis presents an average view of Jupiter's current disk where the variance in the data, captured in the error analysis, reflects some of these natural fluctuations.

The radial currents in Figures 5.6a and 5.6b are associated with corotation enforcement. Outward radial currents act to accelerate plasma towards corotation, whilst inward radial currents decelerate the plasma. Peaks occurring around $30 R_J$ in Figure 5.8 are consistent with the location of corotation breakdown inferred from auroral observations and numerous models (Nichols et al., 2004; Clarke et al., 2004; Ray et al., 2010; Ray et al., 2012). Azimuthal currents in Figure 5.6c and 5.6d are associated with the $\mathbf{J} \times \mathbf{B}$ forces acting to balance radial stresses. The presence of weaker radial and azimuthal currents at noon is in part due to the influence of solar wind on the Jovian magnetosphere. As plasma rotates through dawn into the dayside magnetosphere, it is constrained by the magnetopause and forced closer to the planet. As a consequence its velocity increases and $\mathbf{J} \times \mathbf{B}$ force required to keep the plasma in corotation is decreased (Walker et al., 2003; Kivelson et al., 2005a; Chané et al., 2017). Additionally, the solar wind dynamic pressure acts to balance the outward radial stresses and so weaker azimuthal currents are present in the dayside magnetosphere.

What is clear from these results is the obvious asymmetries prevalent throughout the magnetosphere. Such asymmetries arise from the influence of the solar wind on

the Jovian system. While these are strongest in the middle-to-outer magnetosphere, the inner magnetosphere is also affected. At 20 R_J , the nightside radial and azimuthal currents exceed the dayside by $\sim 30\%$ as shown in Figures 5.8 and 5.9. The asymmetries become more apparent with increasing radial distance. Outside 40 R_J the dawn-dusk asymmetry in the HICD is stark. Strong outward currents in the dawn sector transition to inward flowing currents through noon and into the dusk sector. These currents act to accelerate plasma through dawn into the dayside magnetosphere and decelerate it through the noon to post-dusk sector. Radial currents in the dawn sector have little variation with radial distance, but decrease steadily in the other three LT sectors, with the noon and dusk currents falling off more rapidly than the night sector. This could correspond with loaded flux tubes associated with the Vasyliunas cycle (Vasyliunas, 1983). It should be noted though that the choice of current disk thickness greatly influences the currents (up to $\pm 100\%$) around 50 R_J .

The development of LT asymmetries is highlighted in Figure 5.7. Transitioning from smaller to larger radial distances, radial HICD are seen to grow increasingly with radial distance. The weakest radial currents are observed between 12:00 - 18:00, agreeing with findings by Ray et al. (2014), who showed a region of weaker current density in the post noon sector. Azimuthal currents are seen to fall off with distance. The black profile illustrates the results of a curve fitting routine, fitting data to the form $a\frac{1}{r^b}$. As in Khurana (2001), a peak begins to develop in the radial and azimuthal HICD around 06:00LT and 00:00LT respectively, but now the weakest currents are present at noon. A similar development has also been reported at Saturn by Martin et al. (2019) where a minimum occurs in the HICD through the noon-dusk sector.

The asymmetries determined in the HICD calculation correspond with dynamics observed in other datasets. Variations in the plasma flow velocity have been observed in Galileo energetic particle data by Krupp et al. (2001). They showed pronounced LT asymmetry in plasma velocities within $50 R_J$, with dawn-noon velocities being greater than noon-dusk velocities. However, plasma data is limited outside $50 R_J$ in the dusk sector. Within the inner-to-middle magnetosphere, plasma flows derived by Bagenal et al. (2016) were slightly larger in the dawn sector than the dusk sector, however their study only extended to $30 R_J$. Results by Bunce et al. (2001) showed that the current disk field falls off more rapidly in the dayside than at similar distances in the nightside. The result of the functional fit in Figure 5.7 suggests that the night side falls off more rapidly than the dayside, however due to the limited data coverage on the dayside, this value may vary. Without access to more data, bootstrapping and re-sampling the data sample offers a solution to better estimate this rate of decrease, however this was beyond the scope of this study.

A variety of global MHD models have been applied in understanding Jupiter's magnetospheric interaction with the solar wind (Ogino et al., 1998; Walker et al., 2005; Fukazawa et al., 2006). Walker et al. (2003) applied a global magnetohydrodynamic (MHD) model to investigate the influence of the solar wind on the structure of currents within the Jovian magnetosphere. In their study they compared their simulated currents with the findings of Khurana (2001), however a system-wide comparison could not be made as a result of limited Galileo orbiter data. This study revealed the structure of currents within these regions. Though the simulated current densities are

overall much weaker than the observed HICDs in this study, the asymmetries present in the simulation are in qualitative agreement with these observations. Disparities in the magnitude of the currents between our study and simulations might be ascribed to the average state system being shown in our work. As a dynamically modeled system such as that in Walker et al. (2003) would see variations in the magnitude of the predicted current densities. In their simulation, outward radial currents are predicted in the pre-noon sector, and inward radial currents in the post-noon sector. This is consistent with the observations of a transition from outward to inward radial currents within the noon magnetosphere. However, the inward radial currents predicted in the midnight sector are not present in this study. Similarly, using a 3D global MHD simulation, Chané et al. (2018) investigated the cause of localised peaks in auroral emissions. They showed flux tubes being accelerated through dawn into noon before decelerating and moving in towards the planet. The presence of strong outward radial currents within the dawn sector calculated in this study agree with the results from the simulation.

Examining the divergences of the perpendicular currents, Figure 5.10a illustrates positive radial divergences present throughout all LTs within $30 R_J$ and up to $70 R_J$ in the dawn sector suggesting an increasing radial current, whilst current is being removed within the post-noon to dusk side magnetosphere outside of $30 R_J$. For the azimuthal component in 5.10b, results show the same dawn-dusk asymmetry reported by Khurana (2001), indicating an azimuthal current loss in the dawn magnetosphere and a gain in the dusk sector. This ring current like system is similar to that seen at Earth, although at Jupiter it can be seen to extend over a much larger radial range.

A strong, downward to the ionosphere current, region can be seen in the dayside magnetosphere. It is possible that this could be related to the auroral discontinuity observed by Radioti et al. (2008). Radial HICDs play a key role in determining the location of the FACs. As can be seen in Figure 5.10, the divergence of perpendicular currents are largely similar to the divergence of radial currents, with some variation in the inner regions due to a strong azimuthal divergence in the currents. This highlights the importance of considering both radial and azimuthal currents when describing the M-I coupling system responsible for Jupiter’s auroral emissions.

Mapping of the divergence of the perpendicular HICD was achieved through the use of the JRM09+CAN magnetic field models (Connerney et al., 2018; Connerney, 1981). When mapping the magnitude of the divergence of the perpendicular HICD to ionospheric altitudes, values were found within the range -1.38 to $0.51 \mu\text{A m}^{-2}$, which is comparable to, though slightly larger than, expected values from other studies (Hill, 2001; Cowley et al., 2001; Cowley et al., 2002). Therefore, the field-aligned currents found in this work are likely to be those associated with those responsible for main auroral emission.

A prominent feature in the tail region is an alternation between positive and negative divergences in the radial component, and subsequently the perpendicular current divergence. This effect, referred to as “striping” by Martin et al. (2019), is an artifact of the differencing method implemented in this study. Small variations between adjacent bins, containing low counts, result in the appearance of a larger divergence. This feature is more pronounced in the radial divergence due to the

smaller magnitude values. This effect can be mitigated by increasing the bin size to encompass more data points with the drawback of decreased resolution, or by bootstrapping data within the bins. The bin choice utilised in this study produced an agreeable trade off between the conservation of fine structures and minimising the striping effect.

Figure 5.11 presents a comparison of the radial and azimuthal divergences. Regions where the divergence of the azimuthal (radial) currents are greater than the radial (azimuthal) currents are coloured red (white), in white regions the divergence of perpendicular currents is determined largely by the radial currents. In all LT sectors, but not all radial sectors and with the exception of the pre dawn and dusk sector, the divergence of the azimuthal currents influences the presence of FACs to a similar degree as the divergence of the radial currents. When utilising M-I coupling models to describe the Jovian current system, it is therefore important to consider not only the effect on FACs by the azimuthal currents, but also the effect of LT asymmetries in determining their location and magnitude. Prevailing discrepancies between 1D M-I coupling models and observations could be a consequence of neglecting the effects of azimuthal currents in the Jovian system. Future M-I coupling models should strive to amalgamate both the influence of radial and azimuthal currents in order to obtain a more realistic description of the system. This could be done through an empirical description of the HICDs, however this is left for future work. At Saturn, the divergence of radial currents is much smaller in magnitude than the divergence of azimuthal currents. As such, the divergence of azimuthal currents largely determines the location of the FACs at Saturn (Martin et al., 2019) and should be strongly

considered.

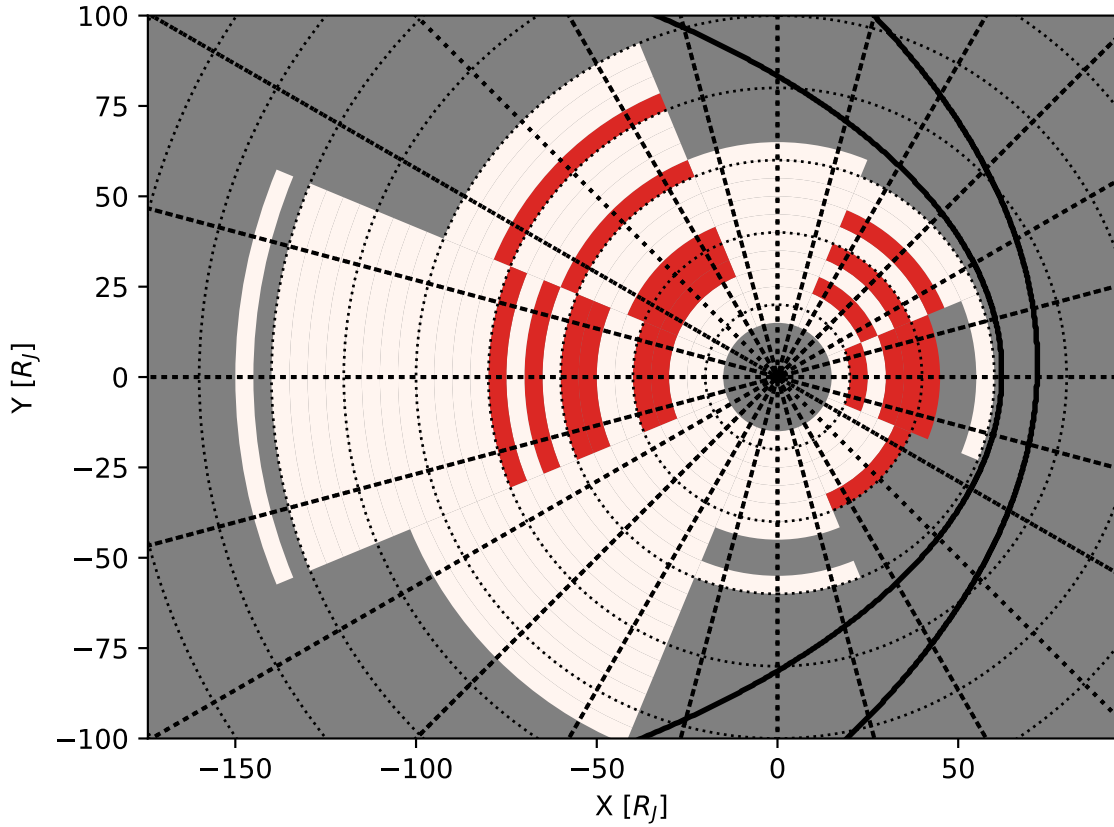


Figure 5.11: A comparison of the radial and azimuthal divergences. Red regions denote where $\nabla_{\phi} \cdot J'_{\phi} > \nabla_{\rho} \cdot J'_{\rho}$, white regions denote where $\nabla_{\rho} \cdot J'_{\rho} > \nabla_{\phi} \cdot J'_{\phi}$. (In similar format to Figure 5.6)

FACs, upward from the ionosphere, dominate the inner ($40 R_J$) region of the magnetodisk, however there are much stronger positive divergences between 16:30LT and 01:30LT, and weaker, sometimes negative divergences at approximately 07:30LT

to 13:30LT. Radioti et al. (2008) suggested that these return currents within the dayside magnetosphere would correspond to discontinuities observed in the main auroral emission. The strong upward FACs found in the dawn sector could be attributed to the shearing motion of flux tubes described by the Chané et al. (2018) simulation. As this is a common feature, it is expected it to appear in the time averaged results and would act to enhance FACs in the region. Again predictions made by Walker et al. (2003) are consistent with these findings. In the Khurana (2001) study, return FACs were not identified in the dusk-noon region due to the lack of available magnetometer data. The increased coverage used in this study is able to reveal evidence of current closure in outer dusk-noon magnetosphere, radially adjacent to regions of strong upward FACs.

By summing over the divergence of the perpendicular currents throughout the system, an overall positive divergence of 1.87 MA R_j^{-2} is calculated. As current continuity must be maintained, the missing return currents may exist in the unmapped regions of the system i.e. dayside and magnetopause regions. This value assumes that the effect of magnetopause currents is negligible in the current disk. As mentioned earlier, by working within the boundary of a compressed magnetosphere, the influence of these currents are limited in the results. Furthermore, the magnetopause currents are external to the current disk region and take the form of a Laplacian field inside the magnetosphere. For a Laplacian field the two terms of Eq 5.10 exactly cancel, providing no contribution to the local azimuthal currents. Variations in the current disk thickness would influence the strength of the azimuthal currents and alter this value. This demonstrates the need for a description of the spatial variation of current

disk thickness which could help to provide a more accurate representation of the azimuthal currents within $50 R_J$. This would further constrain the contribution of azimuthal currents to the location and magnitude of FACs.

5.6 Summary

An analysis of the current structure within the Jovian magnetodisk is presented using all magnetometer data available until 28th July 2018. This work built upon previous work by Khurana (2001) using the latest internal field model, current disk geometry model, and an automated lobe finding process. In doing so a high resolution, full LT coverage of the radial and azimuthal HICDs in the Jovian current disk. The following conclusions were made from the results:

1. Asymmetries in both radial and azimuthal HICDs exist within the inner portion of the middle magnetosphere, some manifesting within $20 R_J$.
2. Both radial and azimuthal currents are weakest in the dayside magnetosphere.
3. Azimuthal currents are shown to play a key role in determining the location of FACs.
4. By summing over all known perpendicular divergences a net positive divergence of $1.87 \text{ MA } R_J^{-2}$ is found. This is postulated to be balanced along the magnetopause and/or in the tail region.
5. When mapped to the ionosphere, parallel current densities have magnitudes within the range 9.27×10^{-3} to $1.38 \mu\text{A m}^{-2}$, comparable with other studies.

It is therefore suggested that future M-I coupling models should take into account not only the presence of radial currents but also azimuthal currents, and the asymmetries found in both. Furthermore, when utilising and constructing models of the current disk, it is paramount that the asymmetries be taken into consideration. Future work would aim to produce an empirical description of these asymmetries, such that they can be readily integrated into M-I coupling models, as well as producing a full spatial description of the variation in current disk thickness.

Chapter 6

Localised Mid-to-High Latitude Alfvénic Turbulence

This chapter contains work *Evidence of Alfvénic Activity in Jupiter’s Mid-to-High Latitude Magnetosphere* by Lorch et al. (2022). L.C. Ray was the primary academic supervisor. R.J. Wilson, F. Bagenal, F. Crary and F. Allegrini supported scientific discussions and analysis techniques used in processing the JADE plasma data. P.A. Damiano and P.A. Delamere supported in the analysis and interpretation of Alfvénic turbulence. C.E.J. Watt supported scientific discussion and understanding around the physics of Alfvén waves.

6.1 Introduction

The planet Jupiter exhibits unique and striking auroral displays. With emissions 100x more energetic than Earth’s, and with a surface brightness up to 10x higher, the Jovian aurora is the brightest and most powerful in the solar system (Clarke

et al., 2004). Jupiter’s aurora is comprised of three distinguishable components: polar emissions, the MAE and satellite footprints. This chapter focuses on one potential electron energisation mechanisms for the MAE: wave-particle interactions. The MAE is intrinsically linked with the planet’s plasma disk, a dense equatorial region of mostly ionised sulphur and oxygen originating from the volcanic moon Io.

A plethora of studies have been carried out using both ground based and *in situ* measurements to understand the coupling relationship between the generation of MAE and the processes in the plasma disk. Coupling is achieved through field-aligned currents, which close in the plasma disk through equatorially flowing currents and in the ionosphere via Pedersen currents. Electron precipitation into planetary atmosphere will enhance Pedersen conductance, acting as positive feedback mechanism to encourage transfer of momentum (Nichols et al., 2004; Ray et al., 2010). Variations in the structure of the field-aligned currents is expected to result in discontinuities and asymmetries in the subsequent MAE (Khurana, 2001; Radioti et al., 2008; Bonfond et al., 2015; Gustin et al., 2016; Lorch et al., 2020). However a number of discrepancies between magnetospheric measurements and auroral observations still remain.

For an isotropic plasma population travelling along the magnetic field, the current density carried to the ionosphere is defined by $j_{max} = env_{\parallel}$. Where a sharp decrease occurs in the plasma density, or the current density exceeds the limiting current density, a increase in plasma velocity is required to balance the system. An electric field, or potential drop, forms to accelerate the electrons and balance the equation.

Knight (1973) was the first to use a steady state one-dimensional model to estimate the electron current along a field line from the auroral zone to the plasma sheet. This became known amongst the community as the Knight relation, which quantified the relationship between the current density and the potential drop

$$j = \frac{e^2 n \Phi}{\sqrt{2\pi m_e T_e}} \quad (6.1)$$

where j , the field-aligned current density, is related to Φ , the field-aligned electric potential by a conversion factor made up of the electron charge e , electron mass, m_e and dependent on the electron density and temperature, n_e and T_e respectively. Applied with terrestrial values, the expected field-aligned potentials required to drive field-aligned currents would be around 10 kV. Knight found that the terrestrial current density and the electric potential followed a linear relationship. Additionally, the kinetic energy flux of accelerated electrons was squared when compared with the unaccelerated population (Lundin et al., 1978).

However a number of the underlying assumptions used in the derivation of the Knight relation are broken at Jupiter. For example, theoretical and observational studies (Cowley et al., 2003; Gustin et al., 2004), indicate that electrons must be accelerated from a few keV to around 100 keV and sometimes several hundreds of keV. Particles of this energy approach a relativistic regime and so adjustments to the Knight relation must be made to account for this. As it applies to a system with a monotonically varying potential structure along the magnetic field, the Knight relation is applicable to the Earth-based system, considering the mirror ratio between the ionosphere and the equatorial magnetosphere. At Jupiter, the

potential structure between the equatorial magnetosphere and the ionosphere is not monotonically varying due to the influence of the centrifugal forces, which confine heavy ions to the equatorial region and result in a minimum in the plasma density along the respective field line around 2-3 R_J from the planet's center. A number of studies have been carried out, applying and testing the Knight relation at Jupiter (Su et al., 2003; Cowley, 2006; Ray et al., 2009). The findings of Ray et al. (2009) in fact demonstrate that the terrestrial Knight relation is not applicable at Jupiter due to the non-monotonically variation of the potential structure. Figure 6.1 taken from Ray et al. (2009) shows a comparison of the Knight relation applied to Jupiter alongside a 1D spatial, 2D velocity space Vlasov model (Ergun et al., 2000) used to calculate the current-voltage relation. It shows that the Knight relation dramatically overestimates the current densities by not accounting for a high latitude current choke. Despite this however, there is relative agreement that field-aligned potentials of 100 kV or larger should be present based on the underlying theory that electric potentials are the main drivers of auroral particle acceleration.

Remote sensing observations provided information on the expected energies required for auroral generation. Spectral observations of FUV aurora from Hubble Space Telescope suggest a mean energy in the range of 30 - 200 keV for the main auroral emission (Gustin et al., 2004). This compared well with later Hisaki data which identified auroral electron energies to be in the tens to hundreds of keV range (Tao et al., 2016). Prior to the Juno era it was believed that strong field-aligned potentials accelerated electrons to the energies required to precipitate and generate auroral emissions. These occur at the plasma density minima when the demand

for currents to enforce corotation in the magnetospheric plasma exceed the thermal electron current density (Ray et al., 2009). Magnetospheric electrons were found to have insufficient energy flux or current density in the loss cone to account for the observed auroral emissions (Cowley et al., 2001; Bagenal et al., 2017) and as such required an acceleration mechanism to account for the observations.

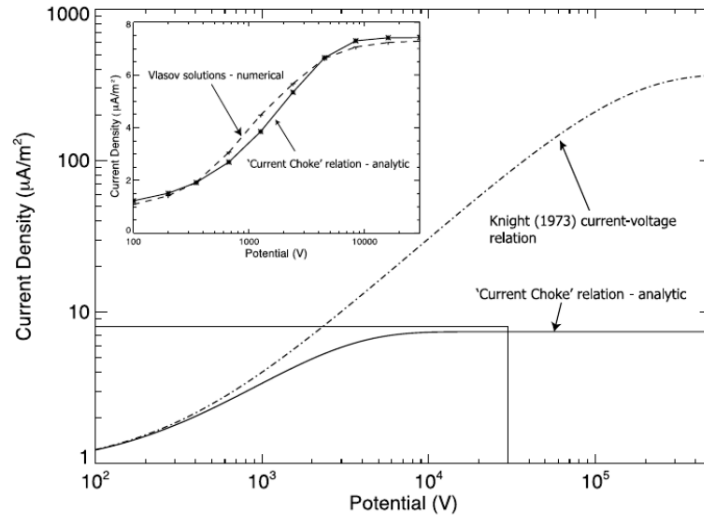


Figure 6.1: A comparison of the current-voltage relation derived by Knight (1973) (dot-dashed line) vs the analytical high latitude current choke result. The result of the Knight relation overestimates the current density saturation by almost a factor of 50. The insert is a comparison between the current-voltage relation derived from a 1D spatial, 2D velocity space Vlasov model and the analytical high latitude current choke solution. Taken from Ray et al. (2009)

Work by Ray et al. (2009), in which the terrestrial Knight relation (Knight, 1973) was adapted and applied to Jupiter, showed that parallel potentials of 100 kV are required in order to accelerate electrons to the observed energies. One of the goals of

the Juno mission was to identify these field-aligned potentials due to its polar orbit, which allows extended detailed measurements over all Jovian latitudes for the first time.

In situ observations by the various instruments on-board Juno have provided a unique insight into the planet's magnetospheric and auroral dynamics. The Waves instrument (Kurth et al., 2017) was used by Louis et al. (2019) to reveal the conjunction between kilometer to decameter wavelength radio emissions and the far ultraviolet wavelength emissions of the MAE, mapping to M-shells between 15 and 60 R_J , where $R_J = 71,492\text{km}$ is the Jovian equatorial radii. Gérard et al. (2019) presented comparisons between the precipitating electron flux and auroral brightness measurements made during several Juno perijoves. H_2 emission intensities were obtained from the UVS instrument by Gladstone et al. (2017), showing the intensity of the main auroral emissions exceeds, matches or falls below the intensity expected from JEDI measurements. These observations highlight a dependency on the location of the electron acceleration region relative to the spacecraft location, the findings of which were in agreement with theoretical expected acceleration regions. Plasma measurements from JEDI have further revealed the presence of MeV energised electrons over the polar cap and main auroral region (Mauk et al., 2020). Inverted V structures are energy enhancements observed in plasma data which appear in the shape of an inverted V (Frank et al., 1971). They correspond to regions of intense upward field-aligned currents, carried by hot magnetospheric electrons accelerated at relatively low altitudes by quasi-static electric fields (McFadden et al., 1999; Luízar et al., 2000) Not only have the presence of inverted V structures associated with field-

aligned potentials been identified in the JEDI data, but also broadband bi-directional electron beams (Mauk et al., 2017).

At Earth, broadband distributions are associated with electron acceleration in dispersive scale Alfvén waves (e.g. Chaston et al. (2002), Wahlund (2003), and Chaston (2006)) where global scale Alfvénic energy is thought to reach dispersive scale lengths via turbulent cascade (Chaston et al., 2008). Similarly, such features at Jupiter can be associated with the effects of propagating dispersive scale Alfvén waves (Watt et al., 2005; Watt et al., 2006; Hess et al., 2010; Damiano et al., 2019) and stochastic wave-particle interactions at dispersive scale lengths (e.g. Saur et al. (2003) and Allegrini et al. (2017)). New data from Juno is triggering a re-evaluation of our theories of electron acceleration within the Jovian system (see review of evidence by Bonfond et al. (2020)). It is now understood that dispersive Alfvén wave induced electron acceleration plays a significant part in the generation of the most intense Jovian aurora (Mauk et al., 2017). Figure 6.2 shows evidence of broadband and inverted V signatures within Jupiter’s polar region from the Juno Spacecraft. A later study by Gershman et al. (2019) provided observations of strong Alfvénic turbulence in Jupiter’s auroral region during perijove orbits.

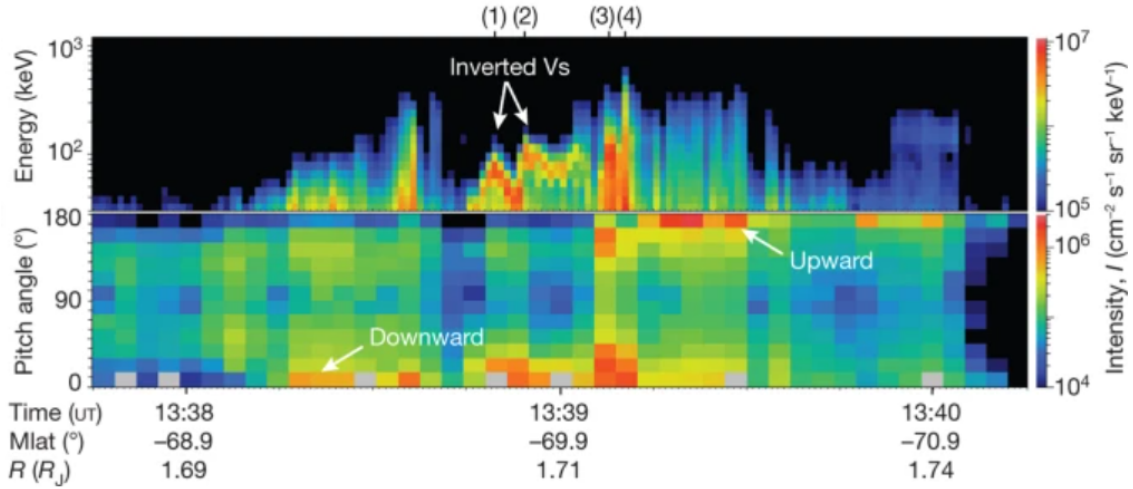


Figure 6.2: Two panels from Figure 2 in Mauk et al. (2017) showing Juno energetic electron plasma data from PJ4 over the polar region. Labeled are mono-directional inverted V signatures just prior to 13:39, and a bidirectional broadband signature just after 13:39. Inverted V signatures are associated with field-aligned potentials discussed in the Knight relation, while broadband signatures are associated with wave-particle interactions.

As per our discussion in Chapters 1 and 3, the fact that Alfvénic turbulence can feed energy to dispersive scale lengths to facilitate the wave particle interactions that result in the broadband energization is not a new revelation within the Jovian system. Saur et al. (2002) first identified weak MHD turbulence within the plasma disk of the middle magnetosphere. Evidence suggested that dissipation of the weak turbulence was the cause of increasing radial temperature profiles (Saur, 2004; Ng et al., 2018). The interaction between the Jovian ionosphere and magnetodisk results in a transfer of momentum. The decreasing angular momentum of radially moving

plasma exerts a stress on the magnetosphere which is balanced by $\mathbf{J} \times \mathbf{B}$ forces in the magnetosphere and ionosphere (Hill, 1979). Saur et al. (2018) stated that for field lines where stress balance is not maintained, Alfvén waves will transfer momentum between the magnetosphere and ionosphere to establish this force balance, and interactions between the Alfvén waves and the plasma can lead to stochastic acceleration. The dynamical processes occurring in Jupiter’s magnetosphere results in local areas falling out of this pressure balance, allowing such processes to occur. Beginning as a disturbance in the magnetospheric plasma by processes such as centrifugal radial interchange (Thomas et al., 2004), a process analogous to the gravity driven Rayleigh-Taylor instability, the large scale perturbations propagate along the magnetic field lines and reflect at the ionospheric boundary and the magnetodisk. The reverberating reflections interact non-linearly forming a turbulent cascade which, at small scales, dissipates its energy into the surrounding plasma. In the context of auroral observations, Saur et al. (2003) suggested that the field-aligned potential drop needed to accelerate electrons arises from the coupling of weak MHD turbulence with the global current system. Potentials of 160 kV were estimated to be generated through this process, which is within the range of predictions by Hubble Space Telescope and Hisaki observations.

This estimation was further supported by Clark et al. (2018), who showed that the energies in electron conics observed by Juno/JEDI matched the predictions made by Saur et al. (2003) as well as those of the Knight relation (Knight, 1973). Clark et al. (2018) also suggested that in order to account for the observed electron energies, it was entirely possible for additional processes to be occurring further along the field line.

The existence of turbulence within the magnetodisk (Tao et al., 2016) and at auroral regions has been well documented (Gershman et al., 2019), and extensive work has been done investigating the role of Alfvén waves along field lines threading the satellite footprints (Damiano et al., 2019). However few studies have been undertaken to investigate its presence within the deeper lobe, areas of the magnetosphere adjacent to, but threading, the current disc. This work investigates the presence of one potential acceleration mechanism within this previously unexplored area.

Before the arrival of Juno, Jovian missions were limited in their ability to provide full latitudinal coverage of the system. The Juno spacecraft orbits Jupiter in a polar orbit, with a perijove of $1.05R_J$ and apojove of $113R_J$ (Bolton et al., 2017). The tilt of Jupiter’s magnetic axis from its spin axis results in the Juno spacecraft weaving over several magnetic latitudes during a single perijove time frame. The orbital path of the Juno spacecraft makes it an ideal tool to study the variations in Jovian turbulence outside of the equatorial region. This study takes advantage of Juno’s unique perspective on the system, which for the first time gives us the opportunity to look for these mechanisms. The JADE-E instrument on-board Juno can detect the variation on electron plasma at the energy levels expected within this region (McComas et al., 2017). JADE coupled with the high-resolution magnetic field instrument (Connerney et al., 2017), has the potential to reveal never-before-seen features in the Jovian magnetosphere. The results of this study extends our understanding of turbulence to the mid-to-high latitude regions of the magnetosphere, revealing some of the additional processes occurring along the field lines threading the auroral region and the magnetodisk.

Our study reveals a sample of Alfvénic activity in the mid-to-high latitude regions of the Jovian magnetosphere. We define Alfvénic activity as a significant perturbation transverse to the ambient magnetic field. This study initially searched for discrete Alfvénic modes within the magnetosphere. These are assumed to accelerate particles in the mid latitude regions of the magnetosphere where the Alfvén velocity is comparable to the electron thermal velocity, however our search finds evidence of the processes occurring in the mid-to-high latitude regions. In Section 6.2 we explain the identification and analysis of our events. Section 6.3 discusses the results and implications towards the global system. We summarise and conclude our findings in Section 6.4.

6.2 Identification of Events

Alfvénic activity, manifesting as perturbations in the magnetic field, is expected to generate a parallel electric field at dispersive scale lengths (Lysak et al., 1996). These waves would thus act to accelerate charged particles. Such activity outside of the plasma disk is expected to be small and transient. Larger modes would be reflected at the plasma disk boundaries, while perturbations at smaller scales are able to traverse the field lines outside of the plasma disk (Hess et al., 2010). For this reason, high resolution magnetometer and plasma data is required to observe in detail these structures. Such a level of precision was not available before Juno. The Juno magnetometer instrument has the capacity needed to make such high-resolution measurements, at 64 vector measurements per second, and is in the ideal orbit for our study. This allows a uniquely detailed analysis of the plasma and magnetic field

within these regions.

Alfvénic perturbations are incompressible with respect to the background field (Alfvén, 1942), meaning while perturbations will exist in components of the magnetic field, there will be no associated increase in the magnitude of the magnetic field. It is therefore prudent to identify events using compressional and transverse power spectra of the magnetic field. Spectrograms are produced from high cadence magnetic field data. We apply a Hanning window to limit artificial effects owing to the signal being non-continuous (Eriksson, 2000). Hanning windows are a type of window function, a mathematical function with zero-values outside of a chosen interval, used in reducing edge effects of Fourier transforms performed on discrete time series data. They are best used in cases where the nature of a signal is not fully known, but a smoothing technique is required. The magnetic field is considered in the De Hoffmann-Teller frame of reference (De Hoffmann et al., 1950), defined in Chapter 4. For the scope of this study only the perpendicular component of the perturbation is considered, not the separate x and y components, therefore the x and y vectors are left free to rotate about the z axis. This frame of reference is chosen as to ascertain perturbations parallel and perpendicular to the background field. This is key to providing evidence of Alfvén wave activity, which is expected to exhibit a perturbation transverse to the magnetic field. To rotate into this frame we identify the background field using a 120s rolling average. A window of 120s was chosen as it is sufficiently large to capture the relatively slow variation of the magnetic field when compared with the variations of the perturbed field. Periods where the total transverse power undergoes a significant increase above the background level, in conjunction with significant

field perturbations, are recorded. Periods for use in the case study were selected by initially generating a pool of events by highlighting timestamps corresponding to a total increase in the transverse power spectra which was 2 standard deviations larger than the 120s rolling mean power in conjunction with magnetic field perturbations which were 2 standard deviations larger than the 120s rolling mean field strength. From this pool 12 periods were visually selected for use in the case studies. Events with visibly significant increases in the compressional power spectra were not included in this selection process. Figure 6.3 shows an example of one event used in this study at date 2017-138. Figure 6.3a) and b) have been detrended by subtraction of the 120s background average in order to highlight the transient perturbations. As the spectral power is prominent in the transverse component and not in the compressional component, see Figure 6.3d) and 6.3e), this gives evidence that these perturbations are Alfvénic in nature. Furthermore, broad increases in power over a range of frequencies is indicative of Alfvénic turbulence rather than discrete modes. This might be expected, as the reverberations of reflected Alfvén waves would interact non-linearly to form a turbulent structure. Quasi-periodic oscillations are seen in the number density obtained from the JADE-E instrument. This is believed to be due to the fact that only two of the three electrostatic analysers are functional, and so this introduces a degree of spin modulation into the observed results. This is not expected to significantly alter the result of this study, as the mean number density of the entire event period is used to calculate the plasma moments, thus smoothing out this modulation. This will not completely limit the quasi-periodic signature however, as it is expected that the quasi-periodic oscillations will affect the estimated error on the results through the variance, however as shall be shown later, these errors are

relatively very small. Finally, if there is an underestimation of the plasma density by, say 33%, this does not change our final conclusion when comparing spectral break scales to fundamental plasma scales.

It is necessary to characterise the length scales associated with turbulent features in order to discern possible energy dissipation mechanisms. The JADE plasma instrument on board Juno can provide the plasma parameters required to calculate these scales relatively accurately. For the regions within which the events are located, interactions are expected to occur at the electron plasma scale (Saur et al., 2018). In this study, high resolution data from the JADE-E instrument was used to obtain information about the local plasma population during transient events. In order to resolve temporally short events, Nyquist sampling theorem requires the resolution of comparable data to be at least half the duration of the observed event. For this reason, event selection is restricted to regions where the JADE-E plasma instrument is at its highest cadence.

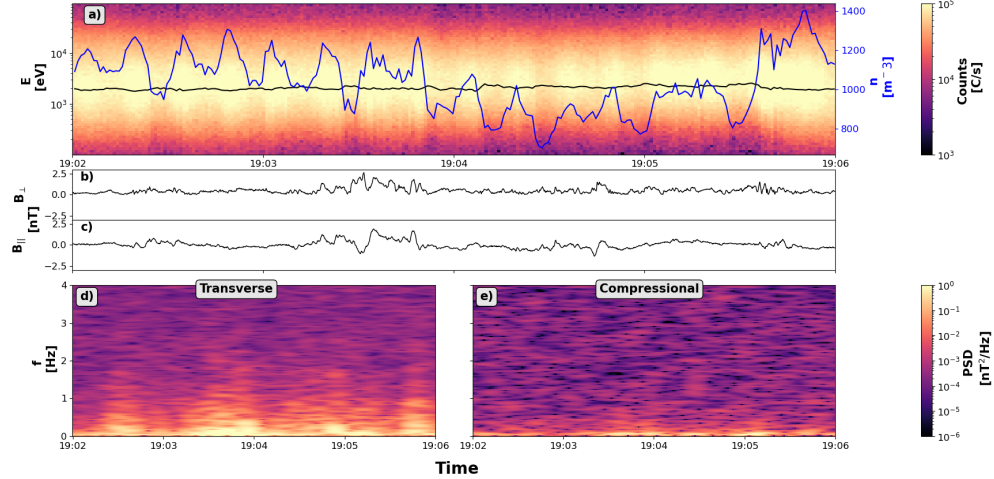


Figure 6.3: Electron plasma and magnetic field data in the dawn sector for a period during 2017-138. Panel a) shows the high resolution JADE-E electron plasma data. The temperature (black profile) and number density (blue profile) calculated from the plasma moments are overlaid. Panels b) and c) show the perpendicular and parallel components of the magnetic field in the De Hoffmann-Teller reference frame. A detrending procedure was implemented in order to highlight the transient perturbations in the field. Panels d) and e) show the power spectra of the transverse and compressional field respectively. Compressional signals appear absent from the event, while a clear, broad increase in transverse power indicates the presence of Alfvénic turbulence.

The events most comparable to Alfvénic activity were found in the mid-to-high latitudes, over 60° , with latitudes below this tending towards MHD turbulence containing compressional components. A subset of 12 events, which coincided with times where high resolution plasma data was available, were chosen for this study.

These events are spaced out over several orbits but are constrained to the dawn sector. The 12 events are quasi-discrete. Some events consist of individual perturbations spanning a few minutes while others exhibit several concurrent disturbances in the field. The distribution of the events used in this study can be seen in Figure 6.4, and tabulated in Table 6.1.

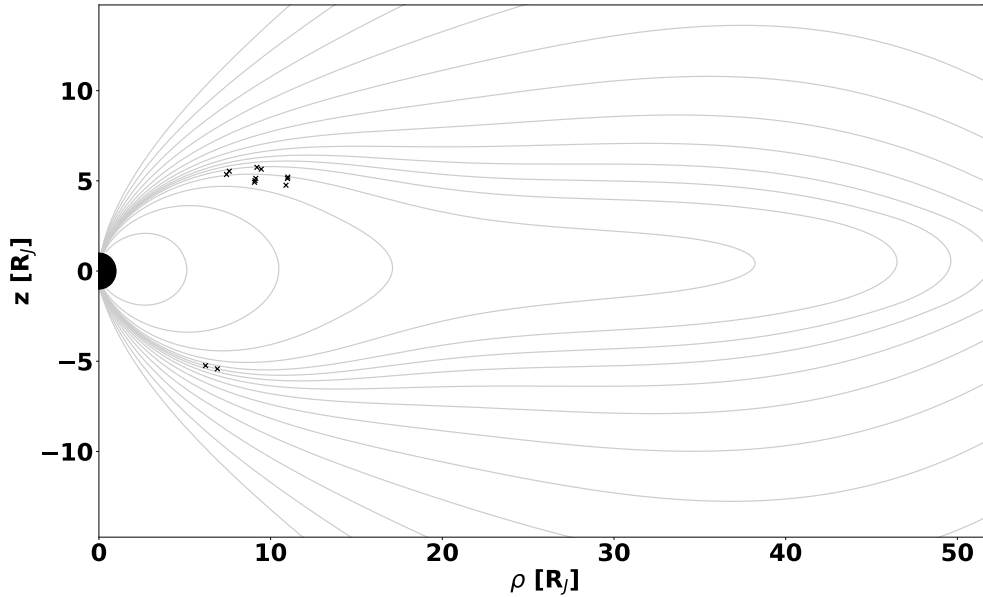


Figure 6.4: The location of the 12 identified events in the magnetic frame of reference. Events are localised in the mid-to-high latitude regions, mapping to equatorial radii, or M shells, between 20 - 50 R_J , conjugate with the main auroral emissions. Mapping was performed using the JRM09 magnetic field (Connerney et al., 2018) and CAN current disk (Connerney, 1981) models. Events used in this study are all within the dawn sector.

Event	Start Time [UT]	Duration [s]	M-shell [R _J]	JSM (X,Y,Z) [R _J]
1	2017-05-18 19:02:00	239	39.48	(-4.51,-10.40,4.44)
2	2017-05-18 19:06:00	1019	33.41	(-4.49,-10.38,4.37)
3	2017-05-18 19:24:00	359	23.82	(-4.39,-10.28,4.05)
4	2017-05-19 12:13:00	149	45.89	(-1.51,-5.95,-5.33)
5	2017-05-19 12:55:00	179	46.96	(-1.72,-6.44,-5.70)
6	2017-07-10 17:03:00	359	25.59	(-4.50,-8.29,4.55)
7	2017-07-10 17:10:00	239	23.28	(-4.46,-8.26,4.44)
8	2017-07-10 17:15:00	239	21.73	(-4.43,-8.23,4.36)
9	2017-09-01 12:18:00	419	32.01	(-5.44,-7.89,5.43)
10	2017-09-01 12:30:00	899	31.95	(-5.36,-7.69,5.47)
11	2017-09-01 14:13:00	239	26.14	(-4.57,-6.48,5.04)
12	2017-09-01 14:29:00	239	24.01	(-4.45,-6.36,4.87)

Table 6.1: The time, duration, M-shell mapping and Jupiter Solar Magnetic coordinates of the 12 events identified in this study.

6.3 Energy Regime of Turbulent Events

The initial search into identifying Alfvénic activity within the Jovian system yielded results that suggest the presence of Alfvénic turbulence rather than that of discrete wave-forms. Following the well-established work by Papen et al. (2014) and Tao et al. (2015), a wavelet analysis technique was applied to reveal the nature of the perturbations. A wavelet transformation was chosen in this instance as it allows for dynamic scaling with respect to temporal and frequency windows, whilst the window size for a windowed Fourier technique remains fixed, thus limiting both the time and frequency accuracy of the technique. A Fourier transform was used in the identification phase of the study as it provided sufficient detail to identify events and was much faster to run. The wavelet transform allows us to calculate the power

spectral density of our events. The transform, $W_i(t, \tau)$ is given as

$$W_i(t, \tau) = \sum_{j=1}^N B_i(t_j) \frac{1}{\sqrt{\tau}} \psi^* \left[\frac{(t_j - t)}{\tau} \right] \Delta t \quad (6.2)$$

where N is the length of the time array, B_i is a component of the detrended magnetic field signal, t_j indicates the time index, while τ is the inverse of the frequency and Δt is the time increment between measurements. ψ^* is the complex conjugate of the Morlet wavelet, defined by

$$\psi(x) = \pi^{-\frac{1}{4}} e^{i\omega_0 x - \frac{x^2}{2}} \quad (6.3)$$

where $\omega_0 = 6$. The results of a wavelet analysis for one event is shown in figure 6.5, where panel a) represents the parallel component, W_{\parallel} , and panel b) is the perpendicular component, W_{\perp} . W_{\parallel} shows little variation over the course of the event. However W_{\perp} exhibits a repeating increase in the power spectra over mid range frequencies. Again, a perpendicular power increase over a broad range of frequencies, such as those occurring between 19:03 - 19:04, is observed supporting the hypothesis that this event is an example of Alfvénic turbulence.

The results from the wavelet analysis are then used to calculate the power spectral density for the event with:

$$PSD_i(\tau) = \frac{2}{N\Delta t} \sum_{j=1}^N \Delta t |W_i(t_j, \tau)|^2 \quad (6.4)$$

In a turbulent system, large scale structures undergo a cascade to smaller and smaller scales, during this cascade through scales, energy can either enter, leave or

remain conserved in the cascade. The change in power spectral density with respect to frequency can be determined through fitting a power law to the given spectra. This provides information on how the energy within the turbulent system is changing. The point at which the power spectra gradient changes abruptly is referred to as the spectral break. The frequency at which the spectral break occurs can provide information on how energy is being gained or lost from the cascade.

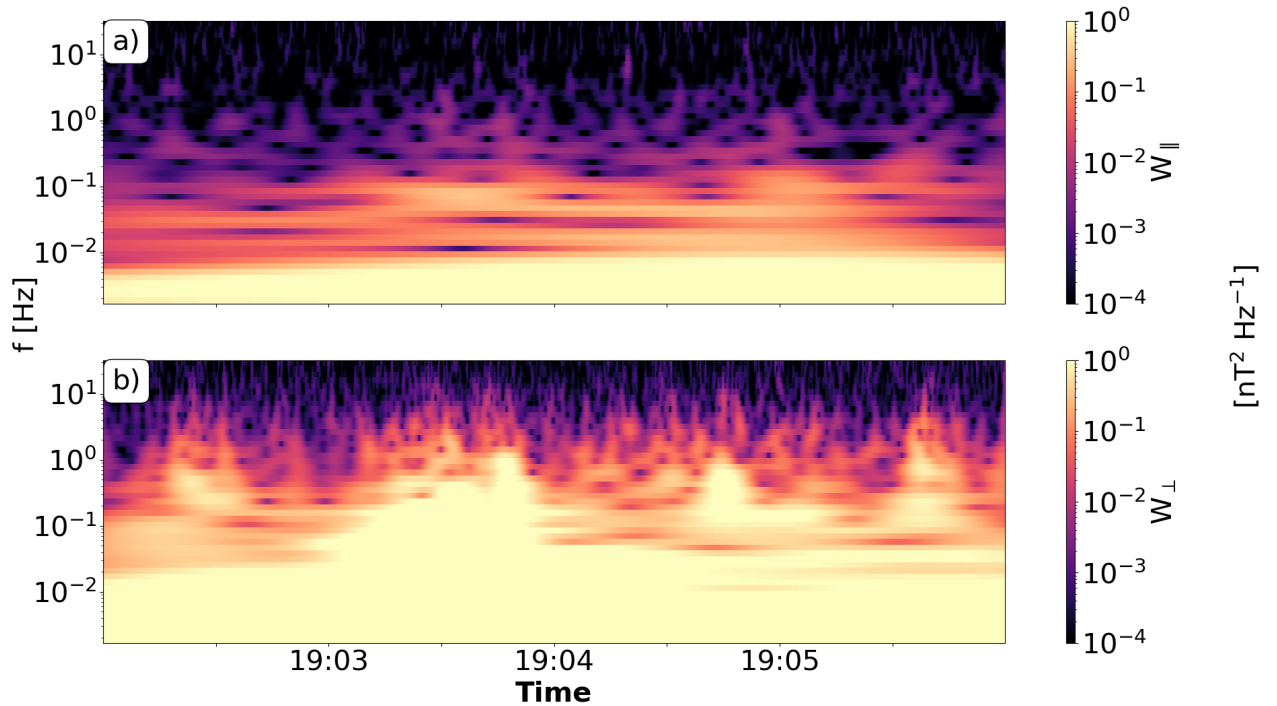


Figure 6.5: The results of the wavelet analysis from event during 2017-138 in the dawn sector. a) The parallel component of the power spectrum. b) the perpendicular component of the power spectrum

In order to ascertain the power law, and subsequent spectral break, associated

with the perturbations in this study an optimised fitting routine was applied with a sliding window to the spectral profiles. The frequency range over which the spectral index was most dissipative was determined by the sliding fit routine. By returning the fitted power laws for varying window sizes, one can identify a frequency range over which the power law reaches a local minima. A single power law value was returned based off an arbitrary, though sensible, choice of window size from the returned range of fitted gradients. As the power law did not vary significantly over a similar range of frequency windows, this method was assumed to give a reasonable estimate of the power law. Future work could look to implement a more advanced automated solution to determine the optimal window size and frequency range, however this was not within the scope of this project. Spectral indices between -1.87 and -2.71, representing a turbulent regime through which energy is dissipated (Leamon et al., 1999), were found to fit the profiles at the higher frequency range, approximately between 0.1 - 6 Hz. The sharp transition observed between the lower frequency and higher frequency fits may correspond to a transition into a dissipative regime. Lower frequency gradients were found by fitting a straight line to the profile between the lower frequency cut off and the start of the higher frequency gradient. Power laws in these ranges were much shallower, corresponding to an energy-containing scale (Goldstein et al., 1995). The fitting algorithm was not used here as the spectral break in the spectral profile had been located. The black lines in figure 6.6 show the fitted power laws before and after the spectral break.

The Alfvénicity, how Alfvénic an event is, can now be checked by calculating the compressibility of the event. This is given by the ratio of the parallel PSD component

over the total PSD, $\frac{PSD_{\parallel}}{PSD_{total}}$. Events with an isotropic power distribution would have a compressibility ratio of 0.33. Likewise, for a fully compressional signal we would expect a value of 1. Events with a low compressibility are more Alfvénic in nature, hence this method provides a way of confirming the initial assumption that the events are Alfvénic. Figure 6.7 shows the compressibility of all events. The frequency axis has been normalised by the spectral break frequency, providing a clear illustration that frequencies within the dissipative regime have a low compressibility.

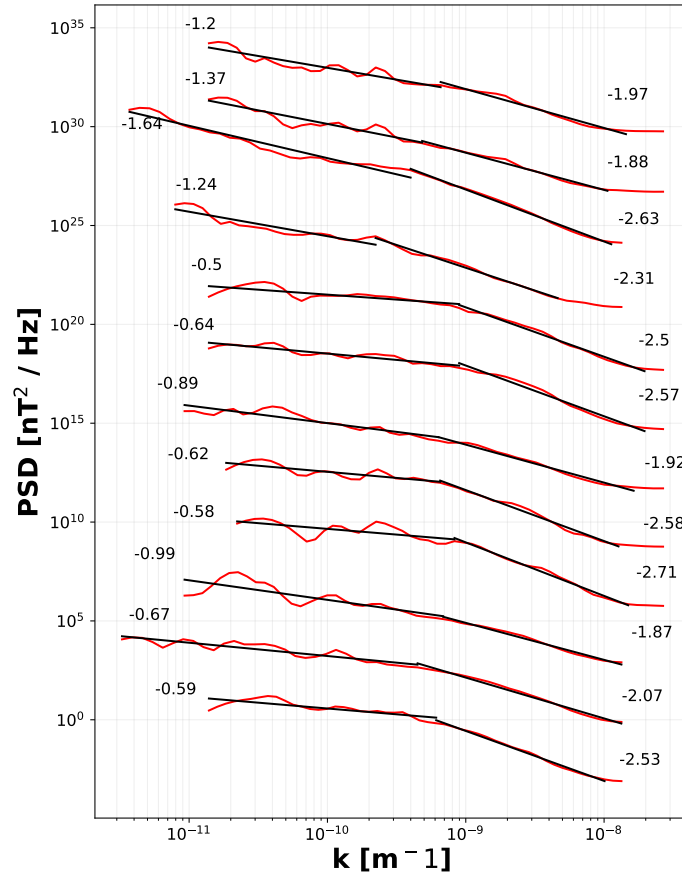


Figure 6.6: The calculated power spectral densities of each event. The PSD of each event, shown in red, are scaled by 10^{3n} where n is the number of the event. Scaling was used to aid visualisation. Black lines indicate the fitted power laws. The higher frequency power laws were fitted using the devised optimisation technique, while lower frequency gradients were fitted between the event specific lower frequency cut off and the higher frequency spectral break. The fitted power laws can all be seen to transition from a non-dissipative regime at lower frequencies to a dissipative regime at higher frequencies.

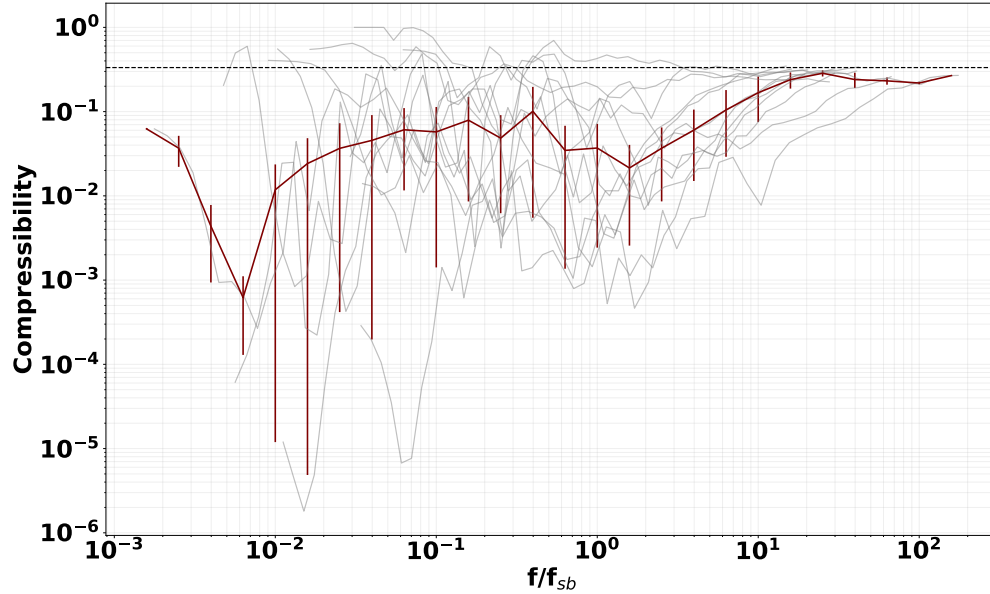


Figure 6.7: The compressibility of each event, represented by light grey lines, over frequency. The frequency has been normalised based off the spectral break in each event to highlight the compressibility within the energy dissipative regions. The black horizontal line marks the value expected for power isotropy. Values above this line indicate a more compressible signal, while values below it are more incompressible. The maroon profile represents the binned median value of each event, with error bars denoting the median absolute deviation.

Events in this study lie largely below the isotropic value, denoted by the horizontal dashed black line, for low to mid range frequencies. The maroon profile represents the binned median value of the events, with error bars indicating the median absolute

deviation, MAD , calculated by

$$MAD = Median(|X_i - \tilde{X}|) \quad (6.5)$$

where X_i is each respective value of the bin and \tilde{X} is the bin's median value. This trends asymptotically towards an isotropic distribution at higher relative frequencies. This result confirms the assumption that events are Alfvénic in nature. With this information it is then possible to estimate the Poynting flux of the events without knowledge of the electric field.

6.4 Discussion and Interpretation

6.4.1 Poynting Flux

A key comparison which can be made between these results and auroral observations is the Poynting flux. Sufficient Poynting flux can provide the energy which drives auroral particle precipitation and comparisons with observed values can indicate whether these events might result in auroral emissions. Usually this would require knowledge of the electric field, however by confirming the events are indeed Alfvénic in nature, the associated Poynting flux can instead be calculated purely with knowledge of the magnetic field:

$$S = \frac{(\delta B_{bp})^2 c}{\mu_0} \quad (6.6)$$

For a more suitable calculation of the Poynting flux, δB_{bp} is the root mean square of the amplitude of the magnetic perturbations. This was calculated using a 5th

order Butterworth band pass filter (Prêle, 2017). A Butterworth filter is a type of low-pass filter, which consists of a pass band, stop band and transition band. The Butterworth filter can transition rapidly from the pass band frequency range, where signals are returned as they appear, to the stop band, where the value of the returned signal is zero. The order of the filter determines how rapidly the transition from pass band to stop band occurs. Lower order filters capture the desired frequencies less uniformly, while having a higher sample rate of non-desired frequencies. The 5th order Butterworth filter used in this study was suitable for capturing the desired frequencies within the potentially dissipative regime, while rejecting the non-desired frequencies outside of this range. The filter used in this study had frequency cut-offs set at the upper and lower boundary of the optimised power law fit. The upper and lower frequency ranges varied depending on the result, but were between 0.06 - 0.27 Hz for the lower frequencies, and 1.5 - 4.5 Hz for the higher frequencies. The resultant variance was summed and the square root taken to give δB_{bp} . The values of δB_{bp} and the resultant localised Poynting flux are shown in Table 6.2.

This initial calculation returns the localised Poynting flux. To compare with auroral energy fluxes the result must be scaled to ionospheric altitudes. Assuming the perturbations are confined to an individual flux tube the area of said flux tube would be expected to scale with the mirror ratio. Using the JRM09 magnetic field model (Connerney et al., 2018) a magnetic field trace is made to the ionosphere (altitude of 1.1RJ) and a local mirror ratio is returned. By simply multiplying the local Poynting flux with the returned mirror ratio an estimation of the scaled Poynting flux is produced. These results are presented in the fourth column of Table 6.2.

In Gustin et al. (2016) mean auroral energy fluxes of 100 mW/m^2 were found to be sufficient in order to excite high intensity FUV emissions, while Saur et al. (2003) calculated an energy flux of 7 mW/m^2 corresponding to the region of maximum turbulent power at $20 R_J$. More recent estimates by Saur et al. (2018) place this value around 6 mW/m^2 , which correspond to 100 mW/m^2 at auroral altitudes. Auroral altitude Poynting flux from the events in this study are comparable to energy flux values observed by Gustin et al. (2016), and are within the $8 - 280 \text{ mW/m}^2$ range measured by JEDI (Mauk et al., 2017; Mauk et al., 2018). Assuming a dissipation efficiency of 10% (Hess et al., 2010) the scaled calculations of the Poynting flux are comparable to this value implying the events shown here have sufficient Poynting flux to generate auroral emissions. However, Gershman et al. (2019) found no traces of Alfvénic perturbations at perijoves over the main auroral emission. This might suggest that the turbulent fluctuations were reflected by the higher density gradients in the plasma disk before they reached these altitudes and as such turbulent energy within these latitudes contribute to magnetospheric plasma heating rather than auroral electron acceleration.

Event	δB [nT]	S_{local} [$\mu W / m^2$]	$S_{1.1\text{RJ}}$ [mW / m ²]
1	0.312	23.2	51.4
2	0.281	18.8	40.7
3	0.179	7.66	15.0
4	0.440	46.2	37.1
5	0.361	31.1	30.2
6	0.186	8.24	11.8
7	0.406	39.3	54.7
8	0.384	35.3	47.5
9	0.319	24.3	47.8
10	0.675	109	196
11	0.160	6.14	6.84
12	0.181	7.85	7.97

Table 6.2: A summary of the events' Poynting flux. Given for each event are the field perturbation, local and low altitude Poynting flux. The perturbed field was calculated as the sum of the variance of the band filtered magnetic field. The Poynting flux was scaled to ionospheric values by use of a mirror ratio calculated with the JRM09 magnetic field model.

6.4.2 Turbulent Scales

As discussed in Chapter 1 and 4, the power law associated with the power spectra indicates that at higher frequencies the turbulent perturbations are within the energy dissipative regime. Within this regime, energy can be lost to the environment, in this case the surrounding plasma. Dissipation of energy occurs in the form of dampening, the mechanism through which this occurs is determined by the scale of the turbulent perturbations. For the events in this study, the dissipation mechanism can be discerned through comparisons of fundamental plasma length scale with the spectral break length scale. Within these regions of the magnetosphere a semi-relativistic

approach must be considered in order to discern the respective length scales of the turbulent events (Gershman et al., 2019). Utilising the dispersion relation for semi-relativistic Alfvén waves, transformation between the frequency and length scales can be achieved. The respective dispersion relation is:

$$\omega = v_A k \cos(\theta) \approx ck_{\parallel} \quad (6.7)$$

For comparisons between the spectral break frequency and the fundamental length of the plasma it was necessary to utilise the high resolution JADE-E instrument. JADE-E enabled us to obtain plasma parameters during the transient perturbations in the magnetic field, providing a greater level of understanding of the events than model estimates alone. Assuming an isotropic distribution the plasma moments were calculated and used to obtain the respective frequencies. By using the mean value of the plasma moments over the observed period, it is assumed that the influence of the quasi-periodic oscillations, discussed earlier, are mitigated.

Figure 6.8 shows the comparison of several fundamental inverse plasma scales with the inverse spectral break length scale obtained through the optimisation algorithm. These correspond to length scales between 16 and 70 R_J . These scales are much larger than those observed within studies such as Papen et al. (2014), who observed ion inertial length scales between approximately $10^5 - 10^7$ m in Saturn's equatorial magnetosphere. This is believed to be due to the much lower number density, and much stronger magnetic field strength within the vicinity of these mid-to-high latitude events. Table 6.3 lists the parameters associated with each event. The dashed line here indicates unity. A χ^2 fitting and correlation analysis were used to quantify the closest

fit. The lower the χ^2 value, the closer the calculated scales are to the spectral break point, while the closer the correlation value is to 1, the higher the correlation between the two frequencies. The closest fit can be seen to be with the electron plasma scales, or electron inertial length. This suggests that energy from the turbulent fluctuations can be lost to electrons at this scale. It has been suggested by many sources that Alfvén wave energy would be dissipated at electron inertial scales, or skin depth, at high latitudes through wave particle interactions (e.g. Lysak et al. (1996), Chaston et al. (2002), Saur et al. (2003), Watt et al. (2005), Watt et al. (2006), Hess et al. (2010), and Damiano et al. (2019)). As can be seen in figure 6.8, the scale closest to the spectral break is indeed the electron inertial scale. The dissipative turbulent scales measured for these events is in agreement with theoretical scale predictions by Saur et al. (2018) for the same region.

Event	B [nT]	N [m ⁻³]	T [keV]	v [m s ⁻¹]	β	ω_{pe} [s ⁻¹]	λ_{De} [m]	ω_{ce} [s ⁻¹]	λ_{ce} [m]	Ω_e [s ⁻¹]	ρ_e [m]	Ω_i [s ⁻¹]	ρ_i [m]
1	299	1.04 × 10 ²¹	2.05	2.69 × 10 ⁷	9.60 × 10 ⁻¹²	0.289	1.04 × 10 ⁸	6.75 × 10 ²	4.44 × 10 ²	8.38 × 10 ⁷	3.21 × 10 ²	4.56	1.38 × 10 ²
2	302	1.88 × 10 ²¹	1.98	2.54 × 10 ⁷	1.05 × 10 ⁻¹¹	0.389	7.70 × 10 ⁷	9.09 × 10 ²	3.30 × 10 ²	8.44 × 10 ⁷	3.13 × 10 ²	4.60	1.34 × 10 ²
3	306	3.09 × 10 ²¹	1.36	2.19 × 10 ⁷	1.81 × 10 ⁻¹¹	0.499	6.00 × 10 ⁷	1.17 × 10 ³	2.57 × 10 ²	8.57 × 10 ⁷	2.55 × 10 ²	4.67	1.09 × 10 ²
4	120 × 10 ³	1.28 × 10 ²¹	2.74	3.10 × 10 ⁷	9.82 × 10 ⁻¹¹	0.321	9.33 × 10 ⁷	7.50 × 10 ²	4.00 × 10 ²	3.35 × 10 ⁷	9.25 × 10 ²	18.3	3.96 × 10 ²
5	993	1.01 × 10 ²¹	2.30	2.85 × 10 ⁷	1.08 × 10 ⁻¹²	0.286	1.05 × 10 ⁸	6.67 × 10 ²	4.50 × 10 ²	2.61 × 10 ⁷	1.09 × 10 ²	14.2	4.67 × 10 ²
6	490	1.07 × 10 ²¹	3.47	3.49 × 10 ⁷	6.19 × 10 ⁻¹²	0.293	1.02 × 10 ⁸	6.84 × 10 ²	4.38 × 10 ²	1.37 × 10 ⁷	2.55 × 10 ²	7.47	1.09 × 10 ²
7	497	1.81 × 10 ²¹	2.23	2.80 × 10 ⁷	6.61 × 10 ⁻¹²	0.382	7.84 × 10 ⁷	8.92 × 10 ²	3.36 × 10 ²	1.39 × 10 ⁷	2.02 × 10 ²	7.57	8.64 × 10 ²
8	502	2.48 × 10 ²¹	1.82	2.53 × 10 ⁷	7.22 × 10 ⁻¹²	0.447	6.71 × 10 ⁷	1.04 × 10 ³	2.87 × 10 ²	1.40 × 10 ⁷	1.80 × 10 ²	7.65	7.72 × 10 ²
9	481	1.20 × 10 ²¹	4.66	4.05 × 10 ⁷	9.70 × 10 ⁻¹¹	0.0982	3.05 × 10 ⁸	2.29 × 10 ²	1.31 × 10 ²	1.35 × 10 ⁷	3.01 × 10 ²	7.34	1.29 × 10 ²
10	519	3.35 × 10 ²¹	3.53	3.52 × 10 ⁷	1.76 × 10 ⁻¹²	0.164	1.83 × 10 ⁸	3.83 × 10 ²	7.82 × 10 ²	1.45 × 10 ⁷	2.42 × 10 ²	7.91	1.04 × 10 ²
11	765	1.56 × 10 ²¹	1.91	2.59 × 10 ⁷	2.05 × 10 ⁻¹¹	0.112	2.67 × 10 ⁸	2.62 × 10 ²	1.14 × 10 ²	2.14 × 10 ⁷	1.21 × 10 ²	11.7	5.18 × 10 ²
12	809	3.16 × 10 ²¹	1.84	2.54 × 10 ⁷	3.57 × 10 ⁻¹¹	0.160	1.88 × 10 ⁸	3.72 × 10 ²	8.05 × 10 ²	2.27 × 10 ⁷	1.12 × 10 ²	12.3	4.81 × 10 ²

Table 6.3: The parameters calculated for each event. From left to right: event number, mean magnetic field strength, mean number density, mean temperature, mean plasma thermal velocity, plasma beta, electron plasma frequency, electron inertial length, ion plasma frequency, ion inertial length, electron gyrofrequency, electron gyroradius, ion gyrofrequency, ion gyroradius

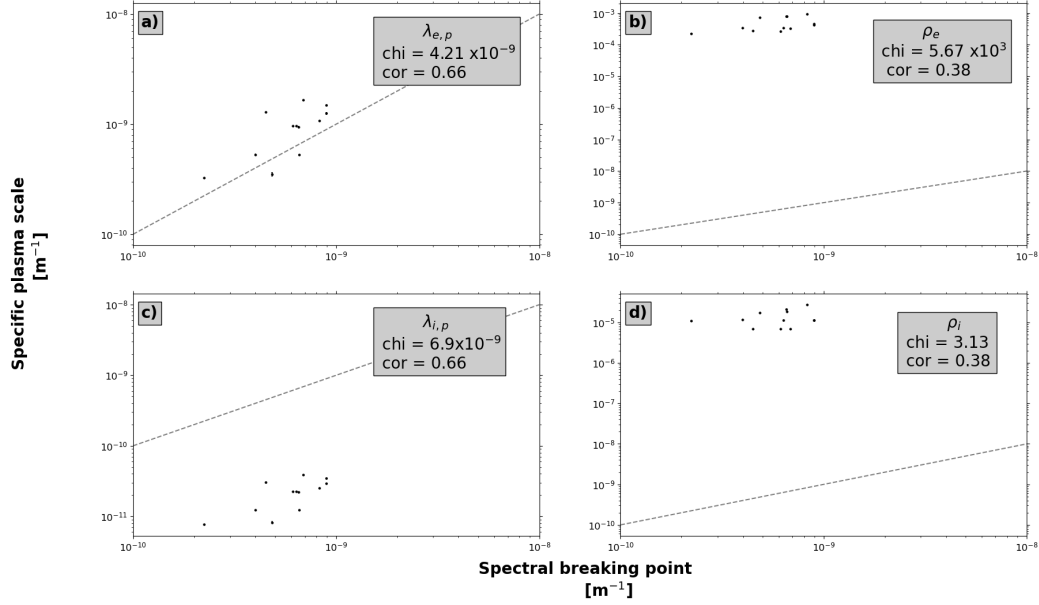


Figure 6.8: A comparison between the spectral breaking length scale and fundamental plasma lengths. a) Electron inertial length: $\frac{c}{\omega_{p,e}}$, b) electron gyro radius: $\frac{m_e v_{\perp}}{|q|B}$, c) ion inertial length $\frac{c}{\omega_{p,i}}$ and d) ion gyro radius: $\frac{m_i v_{\perp}}{|q|B}$. The χ^2 fit and correlation coefficient for each comparison are included in the upper right section of each panel. Error bars included here represent twice the standard error of the mean.

6.4.3 Intermittency

Turbulence must undergo a cascade from larger to smaller scales in order to facilitate energy transfers. In order to support the hypothesis that events in this study could lose energy to the surrounding plasma it is necessary to look for evidence of this cascade. Perturbations undergoing such a cascade would be expected to exhibit intermittency, seen as tails in probability density functions of the time lagged magnetic field (Carter,

2006), which have been associated with the presence of coherent structures in other studies (Veltri, 1999; Meyrand et al., 2015). A coherent structure is the term given to the relatively ordered structures within a turbulent flow, such as vortices, which are concurrent with a turbulent cascade (Fazle Hussain, 1986). The time lagged magnetic field, δB_t , is given by

$$\delta B_{i,t}(t, \tau) = \delta B_i(t + \tau) - \delta B_i \quad (6.8)$$

where τ is a time period consistent with the frequencies used in the wavelet analysis. Tails in the probability density function can be quantified by calculating the flatness or kurtosis of the function. This is carried out using structure functions of the 2nd and 4th order, $F_i(\tau) = \frac{\xi_i^4(\tau)}{|\xi_i^2(\tau)|^2}$. The m^{th} order structure function is given as:

$$\xi_i^m(\tau) = \frac{1}{N} \sum_{j=1}^N |\delta B_{i,t}(t_j, \tau)|^m \quad (6.9)$$

In the case of a Gaussian probability density function the corresponding flatness would be $F_i(\tau) = 3$. As such, a flatness of 3 would suggest there is no intermittency in the events and no energy transfers would be facilitated. Any values over this threshold suggests that intermittency is indeed present, that the events are undergoing a cascade and energy transfers are likely to occur.

For each event the mean flatness of the three components is taken to be the flatness of the probability density function, this is shown in Figure 6.9. Note that again, the frequency has been normalised by the spectral break frequency to aid in comparison. As can be seen in figure 6.9, the flatness of the events, over dissipative frequencies, are greater than that of a Gaussian profile. This demonstrates the

presence of intermittency, and hence the presence of a turbulent cascade which would dissipate energy to the surrounding plasma. This would also suggest that the turbulent cascade is facilitated outside of the magnetodisk at higher latitudes. The increasing gradient of the mean flatness indicates multifractal behaviour (Jiménez, 2006). Counter propagating Alfvén waves would be expected in the mid-to-high latitude regions as Alfvén wave reflections would likely occur where $\frac{B}{n}$ has a maximum at higher latitudes and at the magnetodisk boundary in the lower latitudes.

Analysis of turbulence in these mid-to-high latitude regions has not been done previously. However Tao et al. (2015) determined the nature of turbulence within the plasma disk and the lobe region beside the plasma disk boundary. They find large flatness values within the plasma disk, with high frequency values increasing exponentially reaching 100 at the upper cut-off, suggesting a strongly intermittent turbulence. Their lobe region values however, peak around the mid frequency range at a value of around 4, before settling at a Gaussian flatness value of 3 at the higher frequencies. This would indicate the noise floor of the instrument has been reached.

The mid-to-high latitude turbulence observed in this study displayed a greater level of intermittency than lobe values observed in Tao et al. (2015), but not as much as the plasma disk. This may be due to the mid-to-high latitude turbulence being more developed than that in the lobe regions, but not as developed as that observed in the plasma disk.

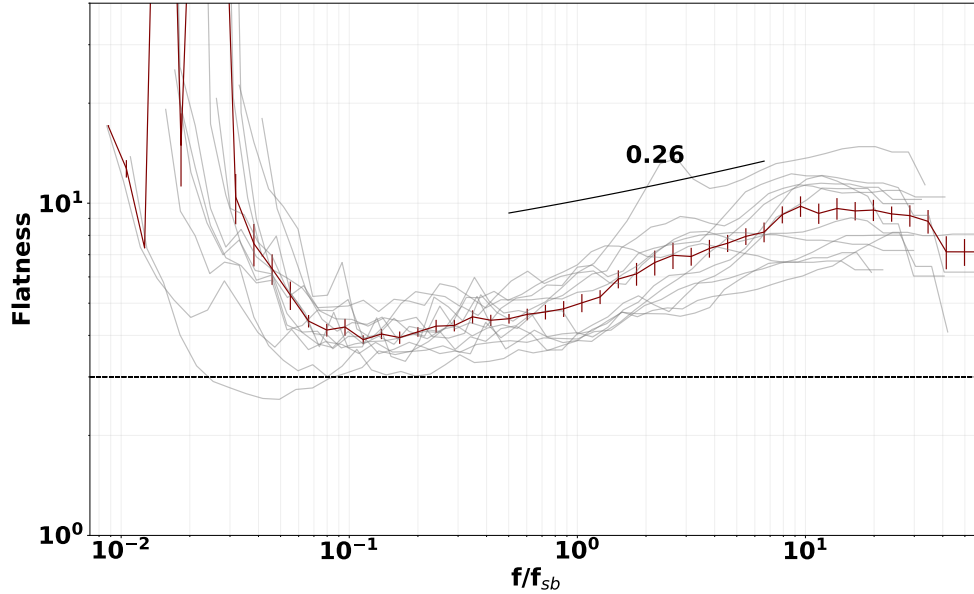


Figure 6.9: The flatness of each event normalised by the spectral break frequency of each event. The maroon profile indicates the mean flatness value, with error bars expressing the standard error of the mean. A dashed horizontal line represents a flatness of 3, for a Gaussian distribution. The large values towards the low frequency end are due to boundary effects, while the decrease at high frequencies is due to the instrument sampling boundary. The gradient fit over higher frequency ranges, with a positive value of 0.26, suggests that the turbulent events are multifractal in nature.

6.5 Summary

Using high resolution Juno magnetometer and plasma data, Alfvénic activity within the mid-to-high latitudes of the Jovian magnetosphere is investigated. 12 events

of interest were identified on field lines magnetically conjugate with Jupiter's main auroral emission and where both magnetometer data and plasma data were available at the desired resolution. These events provide a glimpse of a very dynamic system where turbulence and wave-particle interaction are energising the local plasma. Our key findings are:

1. Alfvénic turbulence exists in the mid-to-high latitude region of Jupiter's magnetosphere on field lines magnetically conjugate with the main auroral emission.
2. Wavelet analysis shows that the power spectral density of these events and associated power laws (-1.87 to -2.71) are consistent with turbulence in the energy dissipative regime.
3. PSD profiles in Figure 6.6 are show to exhibit spectral breaks at frequencies approaching the electron plasma frequency ($0.06 \leq \omega_{e,p} \leq 0.3$ Hz) in Figure 6.8. Fundamental frequencies were calculated from JADE-E plasma moments. This suggested that turbulent energy is dissipated into the local electron population and is in agreement with previous theoretical work (Saur et al., 2018).
4. Applying a Butterworth band pass filter over the magnetic field signal between dissipative frequencies, we estimate the Poynting flux and scale to the ionosphere. Our ionospheric values are comparable to those inferred from auroral observation and match well with predicted energy fluxes associated with turbulent acceleration of magnetospheric electrons (e.g. Saur et al. (2003)).
5. Analysis of the perturbed field indicates the presence of intermittency, a feature common in processes undergoing a turbulent cascade. The variation

in probability density flatness with frequency points towards turbulence of a multi-fractal nature.

These key findings paint an interesting picture. Alfvénic turbulence has the potential to energise electrons within regions of the magnetosphere outside the expected acceleration region for quasi-static electric fields. Future work should aim to systematically investigate and quantify the global variations in both Alfvénic and MHD turbulence within the Jovian magnetosphere. Juno’s exploration of non-equatorial latitudes offers the prime opportunity to carry out this investigation.

Chapter 7

Future Work and Conclusions

In the previous Chapter we identified evidence of Alfvénic turbulence in the mid-to-high latitude of the Jovian magnetosphere. The next stage in this degree was to apply a similar technique to all possible regions of the Jovian magnetosphere covered by magnetometer carrying spacecraft in order to quantify the spatial distribution of Alfvén waves. This work was unable to progress due to the Coronavirus pandemic. As such, this chapter presents a project roadmap outlining the considerations and techniques which could be applied to progress the work in Chapter 6.

7.1 Future work

7.1.1 Construction of a Suitable Dataset

A wide coverage of the planetary field, both in azimuth and latitude is critical to the success of this study. The Juno mission is a prime candidate to investigate the full spatial coverage of turbulent perturbations within the Jovian magnetosphere. Figure

7.1 shows the range of magnetic latitudes the Juno mission can cover, with magnetic field measurements taken over all orbital trajectories. It may also be more favourable that over time, the spacecraft spends more time traversing the southern hemisphere than the northern, as it has been suggested that the southern auroral emission is more representative of the magnetospheric dynamics than the northern emission, owing to its magnetic anomaly (Bonfond et al., 2015).

Though the results of other spacecraft, such as Galileo and the flyby missions utilised in Chapter 4, could provide additional data, it is important to consider factors such as long term changes in the Jovian magnetic and plasma environment, as well as the measurement capability of the various spacecraft in drawing conclusions. For example, the lower cadence of the Galileo spacecraft magnetometer when compared with Juno means transient events will not be detected in the Galileo orbits. This brings the risk of observation bias, where conclusions would be made that transient perturbations would not be present regions exclusively covered by the Galileo mission, when in fact the Galileo probe simply cannot detect such small scale features which Juno can.

Whilst there is currently no proposal for a constellation system at Jupiter, such as the Cluster mission at Earth, one can still perform suitable turbulent analysis with just one satellite. In fact, examining the anisotropy within turbulent perturbations over a wide range of scales is best achieved with a single satellite, as multi-satellite technique is best for scales close to satellite separation scale. The wave perturbations observed in Chapter 6 were of the order of tens of R_J . For comparison, the greatest

separation achieved by the cluster mission was around 10,000km, less than 2 Earth radii (Opgenoorth et al., 2005).

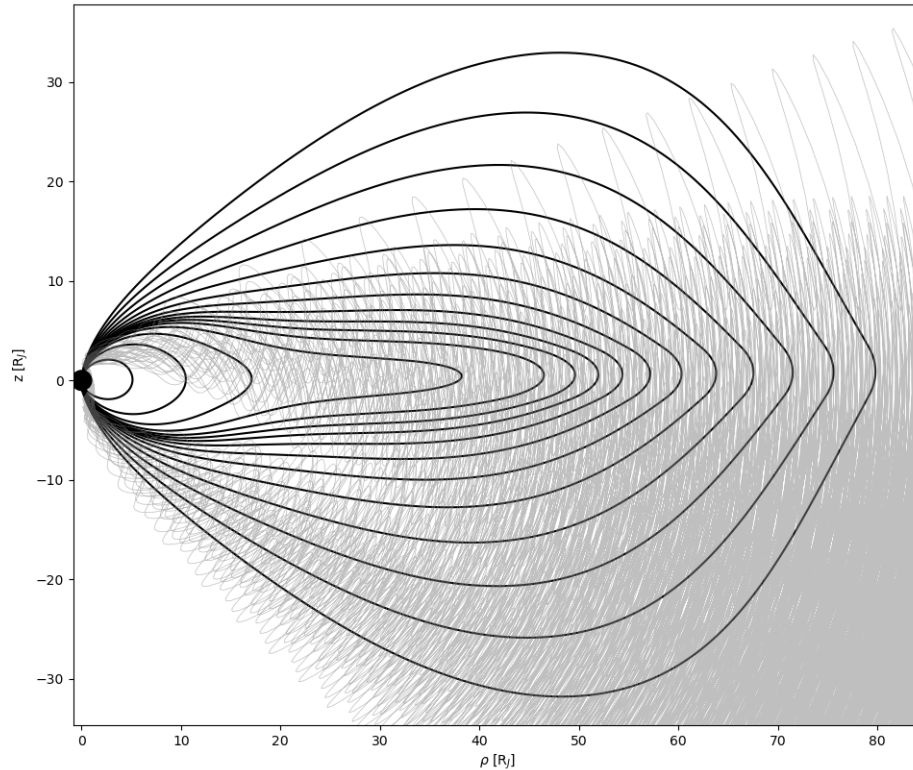


Figure 7.1: A two dimensional projection of the Juno orbits (grey) overlaid in the magnetic frame of reference. Solid black lines represent magnetic field line traces. The Juno orbital trajectory provides a dense coverage over a wide range of magnetic latitudes, making it an ideal candidate for providing a full spatial description of turbulent perturbations.

The limiting factor in the fulfillment of this study is the application of a robust

perturbation detection algorithm. When applying the algorithm employed in Chapter 6, 720 instances of “turbulent” activity were returned between July 2016 and June 2022, including those events identified in Chapter 6, and whilst some of these were potential candidates for study, the majority were clearly not. Figure 7.2 demonstrates two events, visually selected for illustrative purposes, highlighting a potential use case, and a likely false return from the algorithm. The main cause of this was due to the nature of the magnetic field varying significantly depending on the location of the spacecraft. One would need to create an adaptive algorithm to vary the search criteria within specific locations in order to return relevant measurements of the magnetic field. The algorithm could be made adaptive based on characteristic plasma properties, such as the local plasma beta. Alternatively, one could attempt a machine learning approach to the problem by visually identifying a training and testing set of known perturbations over a variety of spatial locations. This dataset could then be used to train a supervised machine learning algorithm as a potential identification mechanism for turbulent events. This method would require careful consideration of the variables to input into the algorithm however, and would require a vigorous analysis of the algorithm’s output to ensure a trustworthy result. Careful selection of the observation period is essential to obtain informative results. The algorithm outlined in Chapter 6 relied on 120s averaged magnetic field data, in conjunction with plasma data of a similar temporal resolution. In order to investigate the role of Alfvén waves throughout a range of latitudes, certain limitations must be accepted. Knowledge of the magnetic field is the main requirement for determining the Alfvénicity of field perturbations. Therefore, a future investigation would focus solely on the magnetic field over a range of temporal averages in order to understand

the variety and distribution of Alfvén waves within the system.

7.1.2 Numerical Analysis of Wave Evolution

Similar physical phenomena to those observed in the solar wind and terrestrial magnetosphere can be identified within different data sets through the use of similar analytical techniques. For a large number of plasma instabilities, large scale turbulent perturbations are governed by MHD theory, while the microscales are governed by kinetic theory. If a wide range of scales are identified in future work, one will need to determine which of these methods will be the most suitable to apply.

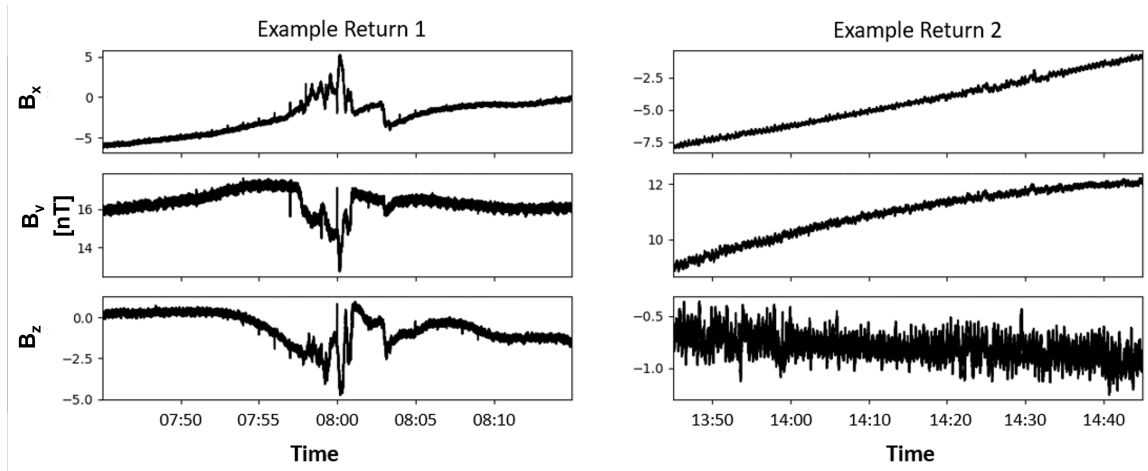


Figure 7.2: Two examples of the “turbulent” magnetic field measurements when applying the algorithm outlined in Chapter 6 to the entire Juno magnetometer dataset. (Left) A potentially successful result, as the magnetic field is seen to be fairly constant, and is significantly perturbed in all components over a relatively short period of time. (Right) A likely false return, as the magnetic field is very noisy, and no significant perturbations exist within this window.

In order to appropriately scale perturbations, and make comparisons with other studies it is paramount that the Taylor hypothesis be examined throughout the analysis of the data. As mentioned earlier, successful application of the Taylor assumption means power spectra computed as a function of frequency are equivalent to power spectra computed as a function of the wavevector. In expanding the study to all regions traversed by Juno, it may be likely that the Taylor hypothesis can be successfully applied. Due to the sheer magnitude of the Jovian magnetic field however, this seems unlikely. As such, future work would need to successfully categorise the recorded wave activity and apply the necessary dispersion relationship in order to

obtain a realistic wavevector.

At kinetic scales, where charged particles interact with wave modes, the particle distribution function distorts (Valentini et al., 2016). The application of a drift-kinetic 1D (DK-1D) model has been used to infer the interaction of waves within the terrestrial magnetosphere. This could be applied at Jupiter and compared to observations at certain spatial instances to infer similarities and understanding of the evolution of magnetospheric waves. However, as constraints on the resolution of plasma data have been lessened in this study, one must rely on diffusive equilibrium equations to estimate the plasma density and temperature. This will introduce a degree of uncertainty into the results, which could be partially quantified through a comparison of the diffusive equilibrium results with measured plasma temperatures from JEDI and JADE.

One new element to investigate in this study would be to see if observed turbulence exhibits some dominant right or left handed polarisation, such as that carried out by Czaykowska et al. (2001). One may be able to apply a hodogram analysis similar to that performed by Manners et al. (2019) to obtain the polarisation of a given perturbation. This would require an adaptation to the field-aligned reference frame defined in Chapter 6, such that the x and y axis are defined based on some fixed direction, e.g. the direction of relative bulk plasma velocity. If the perpendicular components were allowed to rotate about the z axis as they do in Chapter 6, then it would not be possible to determine the polarisation of any perturbations through this method. This analysis would also require knowledge of the plasma energy distribution

in calculating the ratio of perpendicular to parallel ion temperatures. This can be achieved with the JADE instrument however, as mentioned in the end of Chapter 4, the precession of Juno over time will limit the angle of the viewing cone until parallel plasma velocities will be unresolvable. Therefore this analysis will only be applicable in the dawn magnetosphere.

7.2 Conclusions

This thesis is dedicated to the investigation of the acceleration of particles within the Jovian magnetosphere, which eventually lead to the energisation of aurora. This was achieved through the investigation of the M-I coupled system, and an observation of an acceleration process within a region of the magnetosphere. This began with the outlining of fundamental physical concepts needed to understand planetary magnetospheres. Building upon this, a description is provided for some of the more complex dynamics present in the Jovian magnetosphere. Following this, we review the relevant instrumentation and techniques used in analysing *in situ* spacecraft data. This is then applied in the following chapters to reveal new insights into the Jovian magnetosphere.

We map the locations of upward and downward FACs in the Jovian magnetodisk, and show that $1.87 \text{ MA } R_J^{-2}$ amount of current density is unaccounted for. This is theorised to close either in the magnetopause or downtail. This work provides future researchers with a visual tool for identifying and quantifying the magnitude of FACs, which can be cross referenced with new Juno data and auroral observations in identifying magnetodisk interaction regions.

We then go on to show the existence of dissipative turbulent activity in the mid-to-high latitude regions of the Jovian magnetosphere. Through the application of an optimised fitting algorithm, spectral breaks were found at the electron plasma frequency scale, showing a transition to a dissipative regime. This shows tangible evidence that Alfvénic turbulence can supply energy to the surrounding plasma around the electron plasma frequency which is in agreement with theoretical predictions. Dissipative turbulence is found to have a Poynting flux consistent with observations associated with Auroral emissions.

Finally, we provide a theoretical project roadmap which outlines the future application of this work. When such future work is undertaken, its results may have implications in the development of project proposals for future missions to the other outer planet systems. It is further expected that the arrival of JUICE and Europa Clipper may be able to expand our understanding of turbulence in the Jovian system.

Appendix A

JRM09 Internal Magnetic Field Model Coefficients

JRM09 coefficients							
n	m	g_n^m	h_n^m	n	m	g_n^m	h_n^m
1	0	410244.7	0	7	6	-2892.9	-1526
1	1	-71498.3	21330.5	7	7	2968	-5684.2
2	0	11670.4	0	8	0	10059.2	0
2	1	-56835.8	-42027.3	8	1	1934.4	-2409.7
2	2	48689.5	19353.2	8	2	-6702.9	-11614.6
3	0	4018.6	0	8	3	153.7	9287
3	1	-37791.1	-32957.3	8	4	-4124.2	-911.9
3	2	15926.3	42084.5	8	5	-867.2	2754.5
3	3	-2710.5	-27544.2	8	6	-3740.6	-2446.1
4	0	-34645.4	0	8	7	-732.4	1207.3
4	1	-8247.6	31994.5	8	8	-2433.2	-2887.3
4	2	-2406.1	27811.2	9	0	9671.8	0
4	3	-11083.8	-926.1	9	1	-3046.2	-8467.4
4	4	-17837.2	367.1	9	2	260.9	-1383.8
5	0	-18023.6	0	9	3	2071.3	5697.7
5	1	4683.9	45347.9	9	4	3329.6	-2056.3
5	2	16160	-749	9	5	-2523.1	3081.5
5	3	-16402	6268.5	9	6	1787.1	-721.2
5	4	-2600.7	10859.6	9	7	-1148.2	1352.5
5	5	-3660.7	9608.4	9	8	1276.5	-210.1
6	0	-20819.6	0	9	9	-1976.8	1567.6
6	1	9992.9	14533.1	10	0	-2299.5	0
6	2	11791.8	-10592.9	10	1	2009.7	-4692.6
6	3	-12574.7	568.6	10	2	2127.8	4445.8
6	4	2669.7	12871.7	10	3	3498.3	-2378.6
6	5	1113.2	-4147.8	10	4	2967.6	-2204.3
6	6	7584.9	3604.4	10	5	16.3	164.1
7	0	598.4	0	10	6	1806.5	-1361.6
7	1	4665.9	-7626.3	10	7	-46.5	2031.5
7	2	-6495.7	-10948.4	10	8	2897.8	1411.8
7	3	-2516.5	2633.3	10	9	574.5	-714.3
7	4	-6448.5	5394.2	10	10	1298.9	1676.5
7	5	1855.3	-6050.8				

Table A.1: The spherical harmonic coefficients used in calculation of the JRM09 internal magnetic field model. Values obtained from Connerney et al. (2018).

References

- Achilleos, N. et al. (2015). “1. Transport of Mass, Momentum and Energy in Planetary Magnetodisc Regions”. In: *Space Sci Rev* 187, pp. 229–299. DOI: 10.1007/s11214-014-0086-y.
- Acuña, M.H. (2002). “Space-based magnetometers”. In: *Review of Scientific Instruments* 73.11, pp. 3717–3736. DOI: 10.1063/1.1510570.
- El-Alaoui, M. et al. (2021). “Magnetohydrodynamic Turbulence in the Earth’s Magnetotail From Observations and Global MHD Simulations”. In: *Frontiers in Astronomy and Space Sciences* 8.620519. DOI: 10.3389/fspas.2021.620519.
- Alexandrova, O. et al. (2006). “Alfvén vortex filaments observed in magnetosheath downstream of a quasiperpendicular bow shock”. In: *J. geophys. Res.* 11.A11208. DOI: 10.1029/2006JA011934.
- Alexandrova, O. et al. (2008). “Spectra and Anisotropy of Magnetic Fluctuations in the Earth’s Magnetosheath: Cluster Observations”. In: *Ann. Geophys.* 26.11, pp. 3585–3596. DOI: 10.5194/angeo-26-3585-2008.
- Alfvén, H. (1942). “Existence of Electromagnetic-Hydrodynamic Waves”. In: *Nature* 150, pp. 405–406. DOI: 10.1038/150405d0.

References

- Allegrini, F. et al. (2017). “Electron beams and loss cones in the auroral regions of Jupiter”. In: *Geophysical Research Letters* 44, pp. 7131–7139. DOI: 10.1002/2017GL073180.
- Amatucci, W.E. (2006). “A Review of Laboratory Investigations of Space Plasma Waves”. In: *IEEE*, pp. 32–66.
- Badman, S.V. et al. (2015). “Auroral Processes at the Giant Planets: Energy Deposition, Emission Mechanisms, Morphology and Spectra”. In: *Space Sci Rev* 187, pp. 99–179. DOI: 10.1007/s11214-014-0042-x.
- Bagenal, Fran et al. (2016). “Survey of Galileo plasma observations in Jupiter’s plasma sheet: Galileo Plasma Observations”. In: *Journal of Geophysical Research: Planets* 121.5, pp. 871–894. ISSN: 21699097. DOI: 10.1002/2016JE005009. URL: <http://doi.wiley.com/10.1002/2016JE005009>.
- Bagenal, F. et al. (2011). “Flow of mass and energy in the magnetospheres of Jupiter and Saturn”. In: *Journal of Geophysical Research: Space Physics* 116.A5, pp. 1–17. DOI: 10.1029/2010JA016294.
- Bagenal, F. et al. (2017). “Magnetospheric Science Objectives of the Juno Mission”. In: *Space Science Reviews* 213, pp. 219–287. DOI: 10.1007/s11214-014-0036-8.
- Bagenal, F. et al. (n.d.). “Magnetospheres of the Outer Planets Group Website”. In: URL: <https://lasp.colorado.edu/home/mop/files/2012/04/1Msphere.jpg>.
- Barbosa, D.D. (1981). “Dissipation and Turbulent Heating of Plasma in Jupiters Magnetosphere”. In: *Geophysical Research Letters* 8.10, pp. 1111–1114. DOI: 10.1029/GL008i010p01111.

References

- Barbosa, D.D. et al. (1984). “On the Acceleration of Energetic Ions in Jupiters Magnetosphere”. In: *Journal of Geophysical Research: Space Physics* 89.NA6, pp. 3789–3800. DOI: 10.1029/JA089iA06p03789.
- Baron, R.L. et al. (1996). “Solar wind control of Jupiter’s H₃⁺ auroras”. In: *Icarus* 120. DOI: 437--442.
- Bauer, T.M. et al. (1995). “Low-frequency waves in the near-Earth’s plasma sheet”. In: *Journal of Geophysical Research* 100, pp. 9605–9617. DOI: 10.1029/95JA00136.
- Belcher, J.W. et al. (1971). “Large amplitude Alfvén waves in the interplanetary medium”. In: *J. Geophys. Res.* 76, pp. 3534–3563. DOI: 10.1029/JA076i016p03534.
- Belcher, J.W. et al. (1975). “Alfvén waves and directional discontinuities in the interplanetary medium”. In: *J. Geophys. Res.* 80, pp. 181–186. DOI: 10.1029/JA080i001p00181.
- Bhattacharya, B. et al. (2005). “Diffuse Auroral Precipitation in the Jovian Upper Atmosphere and Magnetospheric Electron Flux Variability”. In: *Icarus* 178.2, pp. 406–416. DOI: 10.1016/j.icarus.2005.06.013.
- Bolton, S.J. et al. (2017). “The Juno Mission”. In: *Space Science Reviews* 213, pp. 5–37. DOI: 10.1007/s11214-017-0429-6.
- Bonfond, B. (2012). “When Moons Create Aurora: The Satellite Footprints on Giant Planets”. In: *Auroral Phenomenology and Magnetospheric Processes: Earth and Other Planets*. (Am. Geophys. Union, Washington: Geophysical Monograph Series, pp. 133–140.

References

- Bonfond, B. et al. (2015). “The Far-Ultraviolet Main Auroral Emission at Jupiter - Part 1: Dawn-Dusk Brightness Asymmetries”. In: *Annales Geophysicae* 33.10, pp. 1203–1209. DOI: 10.5194/angeo-33-1203-2015.
- Bonfond, B. et al. (2020). “Six Pieces of Evidence Against the Corotation Enforcement Theory to Explain the Main Aurora at Jupiter”. In: *Journal of Geophysical Research: Space Physics* 125.11. DOI: 10.1029/2020JA028152.
- Borovsky, J.E. et al. (1997). “The Earth’s plasma sheet as a laboratory for flow turbulence in high- β MHD”. In: *J. Plasma Phys* 57. DOI: 10.1017/S0022377896005259.
- Borovsky, J.E. et al. (2003). “Role of Solar Wind Turbulence in the Coupling of the Solar Wind to the Earth’s Magnetosphere”. In: *Journal of Geophysical Research* 108.A6, pp. 1246–1271. DOI: 10.1029/2002JA009601.
- Bourouaine, S. et al. (2013). “Observational Test of Stochastic Heating in Low-beta Fast-solar-wind Streams”. In: *The Astrophysical Journal*. DOI: 10.1088/0004-637X/774/2/96.
- Breuillard, H. et al. (2018). “New Insights into the Nature of Turbulence in the Earth’s Magnetosheath Using Magnetospheric MultiScale Mission Data”. In: *The Astrophysical Journal* 859.127. DOI: 10.3847/1538-4357/aabae8.
- Brice, N. et al. (1973). “Jupiter’s Radiation Belts”. In: *Icarus* 18, pp. 206–219. DOI: 10.1016/0019-1035(73)90204-2.
- Broadfoot, A.L. et al. (1979). “Extreme Ultraviolet Observations from Voyager 1 Encounter with Jupiter”. In: *Science* 204.4396, pp. 979–982. DOI: 10.1126/science.204.4396.979.

References

- Bunce, E. J. et al. (2001). "Divergence of the equatorial current in the dawn sector of Jupiter's magnetosphere: analysis of Pioneer and Voyager magnetic field data". In: *Planetary and Space Science* 49, p. 25. ISSN: 10891113.
- Bunce, E.J. et al. (2005). "Solar Wind-Magnetosphere-Ionosphere Coupling at Jupiter". In: *Advances in Space Research* 36, pp. 2090–2099. DOI: 10.1016/j.asr.2005.04.016.
- Carter, T.A. (2006). "Intermittent Turbulence and Turbulent Structures in a Linear Magnetized Plasma". In: *Physics of Plasmas* 13.010701. DOI: 10.1063/1.2158929.
- Case, N.A. (n.d.). "Solar Wind-Magnetosphere Interactions: A Statistical Analysis of Spacecraft Measurements". In: DOI: 10.13140/2.1.2588.8321.
- Chandran, B.D.G. et al. (2013). "Stochastic Heating, Differential Flow, and the Alpha-to-Proton Temperature Ratio in the Solar Wind". In: *The Astrophysical Journal* 776.45. DOI: 10.1088/0004-637X/776/1/45.
- Chandrasekhar, S. (1957). "The Partition of Energy in Hydromagnetic Turbulence". In: *Annals of Physics* 2. DOI: 10.1016/0003-4916(57)90051-9.
- Chané, E. et al. (2017). "How is the Jovian main auroral emission affected by the solar wind?" In: *Journal of Geophysical Research: Space Physics*. ISSN: 21699380. DOI: 10.1002/2016JA023318. URL: <http://doi.wiley.com/10.1002/2016JA023318>.
- Chané, E. et al. (2018). "Periodic shearing motions in the Jovian magnetosphere causing a localized peak in the main auroral emission close to noon". In: *Planetary and Space Science* 158, pp. 110–117. ISSN: 00320633. DOI: 10.1016/j.pss.2018.04.023. URL: <https://linkinghub.elsevier.com/retrieve/pii/S0032063317304737>.

References

- Chapman, S. (1931). “The Absorption and Dissociative or Ionizing Effect of Monochromatic Radiation in an Atmosphere on a Rotating Earth”. In: *Proc. Phys. Soc.* 43.1, pp. 26–45. DOI: 10.1088/0959-5309/43/1/305.
- Chapman, S. et al. (1930). “A New Theory of Magnetic Storms”. In: *Nature* 126, pp. 129–130. DOI: 10.1038/126129a0.
- Chaston, C.C. (2006). “ULF waves and Auroral Electrons”. In: *Magnetospheric ULF Waves: Synthesis and New Directions*. Ed. by K. Takahashi et al. Geophysical Monograph Series 169, pp. 239–257. DOI: 10.1029/169GM16.
- Chaston, C.C. et al. (2002). “Driven Alfvén waves and electron acceleration: A FAST case study”. In: *Geophysical Research Letters* 29.1535. DOI: 10.1029/2001GL013842.
- Chaston, C.C. et al. (2004). “Auroral ion acceleration in dispersive Alfvén waves”. In: *Journal of Geophysical Research* 109.A04205. DOI: 10.1029/2003JA010053.
- Chaston, C.C. et al. (2008). “The Turbulent Alfvénic Aurora”. In: *Phys. Rev. Lett.* 100.17, p. 175003. DOI: 10.1103/PhysRevLett.100.175003.
- Chen, C.H.K. et al. (2012). “Density Fluctuation Spectrum of Solar Wind Turbulence between Ion and Electron Scales”. In: *Physical Review Letters* 109.3. DOI: 10.1103/PhysRevLett.109.035001.
- Chen, L. et al. (2001). “On resonant heating below the cyclotron frequency”. In: *Physics of Plasmas*. DOI: 10.1063/1.1406939.
- Clark, G. et al. (2018). “Precipitating Electron Energy Flux and Characteristic Energies in Jupiter’s Main Auroral Region as Measured by Juno/JEDI”. In: *Journal of Geophysical Research: Space Physics* 123, pp. 7554–7567. DOI: 10.1029/2018JA025639.

References

- Clarke, J.T. et al. (2004). “Jupiter’s Aurora”. In: *Jupiter The Planet, Satellites and Magnetosphere*. Ed. by Fran Bagenal et al. Cambridge: Cambridge University Press. Chap. 26, pp. 639–670.
- Clarke, J.T. et al. (2009). “The response of Jupiter’s and Saturn’s auroral activity to the solar wind.” In: *Journal of Geophysical Research* 114 (A05210). DOI: 10.1029/2008JA013694.
- Coleman, P.J. (1968). “Turbulence, Viscosity and Dissipation in the Solar-Wind Plasma”. In: *Astrophysical Journal* 153. DOI: 10.1086/149674.
- Collinson, G.A. et al. (2010). “On variable geometric factor systems for top-hat electrostatic space plasma analyzers”. In: *Meas. Sci. Technol* 21, pp. 1–16. DOI: 10.1088/0957-0233/21/10/105903.
- Connerney, J. E. P. (1981). “The magnetic field of Jupiter: A generalized inverse approach”. In: *Journal of Geophysical Research: Space Physics* 86 (A9), pp. 7679–7693. ISSN: 01480227. DOI: 10.1029/JA086iA09p07679. URL: <http://doi.wiley.com/10.1029/JA086iA09p07679> (visited on 10/12/2018).
- Connerney, J. E. P. et al. (1998). “New models of Jupiter’s magnetic field constrained by the Io flux tube footprint”. In: *J. of Geophys. Res.: Space Physics* 103 (A6), pp. 11929–11939. ISSN: 01480227. DOI: 10.1029/97JA03726.
- Connerney, J. E. P. et al. (2018). “A New Model of Jupiter’s Magnetic Field From Juno’s First Nine Orbits”. In: *Geophysical Research Letters* 45.6, pp. 2590–2596. ISSN: 00948276. DOI: 10.1002/2018GL077312.
- Connerney, J.E.P. et al. (2017). “The Juno Magnetic Field Investigation”. In: *Space Sci Rev* 213, pp. 39–138. DOI: 10.1007/s11214-017-0334-z.

References

- Coulomb, C.-A. (1785). “Premier mémoire sur l’électricité et le magnétisme”. In: *Histoire de l’Académie Royale des Sciences*, pp. 569–577.
- Cowley, S.W.H. (2006). “Current-voltage and kinetic energy flux relations for relativistic field-aligned acceleration of auroral electrons”. In: *Ann. Geophys.* 24, pp. 325–338. DOI: 10.5194/angeo-24-325-2006.
- Cowley, S.W.H. et al. (2001). “Origin of the main auroral oval in Jupiter’s coupled magnetosphere–ionosphere system”. In: *Planetary and Space Science* 49.10, pp. 1067–1088. ISSN: 00320633. DOI: 10.1016/S0032-0633(00)00167-7.
- Cowley, S.W.H. et al. (2002). “Distributions of Current and AUroral Precipitation in Jupiter’s Middle Magnetosphere Computed from Steady-State Hill-Pontius Angular Velocity Profiles: Solutions for Current Sheet and Dipole Magnetic Field Models.” In: *Planetary and Space Science* 50, pp. 717–734. DOI: 10.1016/S0032-0633(02)00046-6.
- Cowley, S.W.H. et al. (2003). “Origin’s of Jupiter’s main oval auroral emissions”. In: *Journal of Geophysical Research* 108.A4. DOI: 10.1029/2002JA009329.
- Cramer, N.F (2001). “Waves in Uniform Plasmas”. In: *Physics of Alfvén Waves*. Verlag Berlin GmbH, Berlin: Wiley-VCH, pp. 11–63. DOI: 10.1002/3527603123.
- Czaykowska, A. et al. (2001). “Magnetic Field Fluctuations Across the Earth’s Bow Shock”. In: *Ann. Geophys.* 19.275–287. DOI: 10.5194/angeo-19-275-2001.
- Damiano, P.A. et al. (2019). “Kinetic Simulations of Electron Acceleration by Dispersive Scale Alfvén Waves in Jupiter’s Magnetosphere”. In: *Geophysical Research Letters* 46, pp. 3043–3051. DOI: 10.1029/2018GL081219.
- D’Amicis, R. et al. (2020). “The Effect of Solar-Wind Turbulence on Magnetospheric Activity”. In: *Front. Phys.* 8.604857. DOI: 10.3389/fphy.2020.604857.

References

- De Hoffmann, F. et al. (1950). “Magneto-Hydrodynamic Shocks”. In: *Physical Review* 80.4, pp. 692–703. DOI: 10.1103/PhysRev.80.692.
- Delamere, P.A. et al. (2013). “Magnetotail Structure of the Giant Magnetospheres: Implications of the Viscous Interaction with the Solar Wind”. In: *Journal of Geophysical Research* 118, pp. 7045–7053. DOI: 10.1002/2013JA01917.
- Delamere, P.A. et al. (2015a). “Magnetic Flux Circulation in the Rotationally Driven Giant Magnetospheres”. In: *Journal of Geophysical Research: Space Physics* 120, pp. 4229–4245. DOI: 10.1002/2015JA021036.
- Delamere, P.A. et al. (2015b). “Solar Wind and Internally Driven Dynamics: Influences on Magnetodiscs and Auroral Responses”. In: *Space Science Reviews* 187. DOI: 10.1007/s11214-014-0075-1.
- Dubinin, E. et al. (2005). “Nonlinear inertial and kinetic Alfvén waves”. In: *Journal of Geophysical Research* A10S04 (110). DOI: 10.1029/2004JA010770.
- Dungey, J.W. (1961). “Interplanetary Magnetic Field and the Auroral Zones”. In: *Physical Review Letters* 6.2, pp. 47–48. DOI: 10.1103/PhysRevLett.6.47.
- Eastwood, J.P. et al. (2003). “On the Existence of Alfvén Waves in the Terrestrial Foreshock”. In: *Ann. Geophys.* 21, pp. 1457–1465. DOI: 10.5194/angeo-21-1457-2003.
- Ebert, R.W. et al. (2017). “Spatial Distribution and Properties of 0.1-100 keV Electrons in Jupiter’s Polar Auroral Region”. In: *Geophysical Research Letters* 44.18, pp. 9199–9207. DOI: 10.1002/2017GL075106.
- Echer, E. et al. (2020). “Statistical analysis of solar wind parameter variation with heliospheric distance: Ulysses observations in the ecliptic plane”. In: *Adv. Space Res.* 65.12, pp. 2846–2856. DOI: 10.1016/j.asr.2020.03.036.

References

- Ergun, R.E. et al. (2000). “Parallel electric fields in discrete arcs”. In: *Geophysical Research Letters* 27, pp. 4053–4056. DOI: 10.1029/2000GL003819.
- Ergun, R.E. et al. (2002). “Recent M-I coupling discoveries and how they apply to the outer planets”. In: *paper presented at Conference on Magnetospheres of the Outer Planets, NASA, Laurel, Md.*
- Eriksson, A.I. (2000). “Spectral Analysis”. In: *Analysis Methods for Multi-Spacecraft Data*. Ed. by G. Paschmann et al. ESA Publications Division, Keplerlaan 1, 2200 AG Noordwijk, The Netherlands: ISSI Scientific Report SR-001, pp. 5–42.
- Espinosa, S. et al. (2000). “Periodic perturbations in Saturn’s magnetic field”. In: *Geophysical Research Letters* 27, pp. 2785–2788. DOI: 10.1029/2000GL000048.
- Fazle Hussain, A.K.M. (1986). “Coherent Structures and Turbulence”. In: *J. Fluid Mech.* 173, pp. 303–356. DOI: 10.1017/S0022112086001192.
- Fiksel, G. et al. (2009). “Mass-dependent ion heating during magnetic reconnection in a laboratory plasma”. In: *Physical Review Letters* 103.14. DOI: 10.1103/PhysRevLett.103.145002.
- Frank, L.A. et al. (1971). “Observations of charged particle precipitation into the auroral zone”. In: *Journal of Geophysical Research* 76, pp. 3612–3643.
- Frank, L.A. et al. (2002). “Galileo Observations of Electron Beams and Thermal Ions in Jupiter’s Magnetosphere and their Relationship to Auroras”. In: *Journal of Geophysical Research: Space Physics* 107.A12. DOI: 10.1029/2001JA009150.
- Fukazawa, K. et al. (2006). “Configuration and dynamics of the Jovian magnetosphere”. In: *Journal of Geophysical Research* 111 (A10207). DOI: 10.1029/2006JA011874.

References

- Gérard, J.-C. et al. (2019). “Contemporaneous Observations of Jovian Energetic Auroral Electrons and Ultraviolet Emissions by the Juno Spacecraft”. In: *Journal of Geophysical Research: Space Physics* 124.11, pp. 8298–8317. DOI: 10.1029/2019JA026862.
- Gershman, D.J. et al. (2017). “Juno observations of large-scale compressions of Jupiter’s dawnside magnetopause”. In: *Geophysical Research Letters* 44. DOI: 10.1002/2017GL073132.
- Gershman, D.J. et al. (2019). “Alfvénic Fluctuations Associated with Jupiter’s Auroral Emissions”. In: *Geophysical Research Letters* 46, pp. 7157–7165. DOI: 10.1029/2019GL082951.
- Gladstone, G.R. et al. (2017). “The Ultraviolet Spectrograph on NASA’s Juno Mission”. In: *Space Science Reviews* 213.447–473. DOI: 10.1007/s11214-014-0040-z.
- Gold, T. (1959). “Motions in the magnetosphere of the Earth”. In: *Journal of Geophysical Research* 64, pp. 1219–1224. DOI: 10.1029/JZ064i009p01219.
- Goldreich, P. et al. (1995). “Toward a theory of interstellar turbulence. II. Strong Alfvénic turbulence”. In: *Astrophys. J.* 438, pp. 763–775. DOI: 10.1086/175121.
- Goldreich, P. et al. (2007). “Spontaneous axisymmetry breaking of the external magnetic field at Saturn”. In: *Journal of Geophysical Research: Space Physics* 112.A05225. DOI: 10.1029/2006JA012163.
- Goldstein, B.E. et al. (1995). “Properties of magnetohydrodynamic turbulence in the solar wind as observed by Ulysses at high heliographic latitudes”. In: *Geophysical Research Letters* 22.23, pp. 3393–3396. DOI: 10.1029/95GL03183.

References

- Gonzalez, W.D. et al. (1999). “Interplanetary origin of geomagnetic storms”. In: *Space Sci. Rev.* 88, pp. 529–562. DOI: 10.1023/A:1005160129098.
- Goossens, M. (2003). *An Introduction to Plasma Astrophysics and Magnetohydrodynamics*. Springer. ISBN: 978-1-4020-1433-8.
- Grodent, Denis et al. (2008a). “Auroral evidence of a localized magnetic anomaly in Jupiter’s northern hemisphere”. In: *J. of Geophys. Res.: Space Physics* 113 (A9), n/a–n/a. ISSN: 01480227. DOI: 10.1029/2008JA013185.
- Grodent, D. et al. (2003). “Jupiter’s Polar Auroral Emissions”. In: *Journal of Geophysical Research* 108.A10. DOI: 10.1029/2003JA01001.
- Grodent, D. et al. (2008b). “Auroral evidence of a localized magnetic anomaly in Jupiter’s northern hemisphere”. In: *Journal of Geophysical Research: Atmospheres* 113.A9. DOI: 10.1029/2008JA013185.
- Guillot, T. et al. (2004). “The Interior of Jupiter”. In: *Jupiter The Planet, Satellites and Magnetosphere*. Ed. by Fran Bagenal et al. Cambridge: Cambridge University Press. Chap. 3, pp. 35–57.
- Gurnett, D.A. et al. (2009). “Discovery of a north-south asymmetry in Saturn’s radio rotation period”. In: *Geophysical Research Letters* 36.L16102. DOI: 10.1029/2009GL039621.
- Gustin, J. et al. (2004). “Energy-flux relationship in the FUV Jovian aurora deduced from HST-STIS spectral observations”. In: *Journal of Geophysical Research: Space Physics* 109.A10. DOI: 10.1029/2003JA010365.
- Gustin, J. et al. (2006). “Characteristics of Jovian morning bright FUV aurora from Hubble Space Telescope/Space Telescope Imaging Spectrograph imaging and spectral observations”. In: *Journal of Geophysical Research* 111 (A9). ISSN: 0148-

References

0227. DOI: 10.1029/2006JA011730. URL: <http://doi.wiley.com/10.1029/2006JA011730> (visited on 03/11/2019).
- Gustin, J. et al. (2016). “Characteristics of north Jovian aurora from STIS FUV spectral images”. In: *Icarus* 268, pp. 215–241. DOI: 10.1016/j.icarus.2015.12.048.
- Hasegawa, H. et al. (2004). “Transport of solar wind into Earth’s Magnetosphere through rolled-up Kelvin-Helmholtz vortices”. In: *Nature* 430, pp. 755–7758. DOI: 10.1038/nature02799.
- Hess, S. L. G. et al. (2011). “Model of the Jovian magnetic field topology constrained by the Io auroral emissions”. In: *J. of Geophys. Res.: Space Physics* 116 (A5). ISSN: 01480227. DOI: 10.1029/2010JA016262. URL: <http://doi.wiley.com/10.1029/2010JA016262> (visited on 10/12/2018).
- Hess, S.L.G. et al. (2010). “Power transmission and particle acceleration along the Io flux tube”. In: *Journal of Geophysical Research* 115.A06205. DOI: 10.1029/2009JA014928.
- Hess, S. et al. (2012). “Satellite-Induced Electron Acceleration and Related Auroras”. In: *Geophysical Monograph Series* (197), pp. 582–592. DOI: 10.1029/2011GM001175.
- Hill, T. W. et al. (1976). “Heavy ions from the Galilean satellites and the centrifugal distortion of the Jovian magnetosphere”. In: *Journal of Geophysical Research* 81.25. ISSN: 01480227. DOI: 10.1029/JA081i025p04561. URL: <http://doi.wiley.com/10.1029/JA081i025p04561>.
- Hill, T.W. (1979). “Inertial limit on corotation”. In: *J. of Geophys. Res.* 84 (A11), p. 6554. ISSN: 0148-0227. DOI: 10.1029/JA084iA11p06554.

References

- Hill, T.W. (2001). “The Jovian auroral oval”. In: *Journal of Geophysical Research* 106, pp. 8101–8107. DOI: 10.1029/2000JA000302.
- Hill, T.W. et al. (1983). “Magnetospheric models”. In: *Physics of the Jovian Magnetosphere*. Ed. by A.J. Dessler. New York: Cambridge University Press. Chap. 10, pp. 353–394.
- Hoshino, M. et al. (1994). “Turbulent magnetic field in the distant magnetotail: bottom-up process of plasmoid formation?” In: *Geophysical Research Letters* 21, pp. 2935–2938. DOI: 10.1029/94GL02094.
- Howes, G.G. et al. (2013). “Alfvén wave collisions, the fundamental building block of plasma turbulence, I. Asymptotic solution.” In: *Phys. Plasmas*. 20.072302. DOI: 10.1063/1.4812805.
- Hughes, W.J. (1995). “The Magnetopause, Magnetotail, and Magnetic Reconnection”. In: *Introduction to Space Physics*. Ed. by M.G. Kivelson et al. Cambridge: Cambridge University Press. Chap. 9, pp. 227–287.
- Imperial College London (n.d.). “How a fluxgate works”. In: URL: <https://www.imperial.ac.uk/space-and-atmospheric-physics/research/areas/space-magnetometer-laboratory/space-instrumentation-research/magnetometers/fluxgate-magnetometers/how-a-fluxgate-works/>.
- Iroshnikov, P.S. (1964). “Turbulence of a conducting fluid in a strong magnetic field”. In: *Sov. Astron.* 7, p. 566.
- Jia, X. et al. (2010). “Magnetic Fields of the Satellites of Jupiter and Saturn”. In: *Space Science Reviews* (152), pp. 271–305. DOI: 10.1007/s11214-009-9507-8.
- Jiménez, J. (2006). “Intermittency in turbulence”. In: *Physics*. DOI: 10.1016/B0-12-512666-2/00368-0.

References

- Johnson, J.R. et al. (2001). “Stochastic ion heating at the magnetopause due to kinetic Alfvén waves”. In: *Geophysical Research Letters*. DOI: 10.1029/2001GL013509.
- Johnson, T.V. et al. (1992). “Space Science Reviews Volume on Galileo Mission Overview”. In: *Space Sci Rev* 60, pp. 3–21. DOI: 10.1007/BF00216848.
- Joy, S. P. et al. (2002). “Probabilistic models of the Jovian magnetopause and bow shock locations”. In: *J. of Geophys. Res.* 107 (A10). ISSN: 0148-0227. DOI: 10.1029/2001JA009146.
- Kaeppler, S.R. et al. (2012). “Current Closure in the Auroral Ionosphere: Results From the Auroral Current and Electrodynamics Structure Rocket Mission”. In: *Auroral Phenomenology and Magnetospheric Processes: Earth and Other Planets*. Ed. by A. Keiling et al. Washington, DC: AGU Books Board. Chap. 15, pp. 183–192.
- Karimabadi, H. et al. (1994). “Ion scattering and acceleration by low frequency waves in the cometary environment.” In: *Washington DC American Geophysical Union Geophysical Monograph Series*. DOI: 10.1029/GM084p0221.
- Kelley, M.C. (2003). “Ionosphere”. In: *Encyclopedia of Atmospheric Sciences*. Ed. by J.R. Holton. London: Academic Press, pp. 1022–1030.
- Kepko, L. et al. (2003). “Observations of Discrete, Global Magnetospheric Oscillations Directly Driven by Solar Wind Density Variations”. In: *Journal of Geophysical Research: Space Physics* 108.A6. DOI: 10.1029/2002JA009676.
- Khurana, K.K. (2001). “Influence of solar wind on Jupiter’s magnetosphere deduced from currents in the equatorial plane”. In: *J. of Geophys. Res.: Space Physics* 106 (A11), pp. 25999–26016. ISSN: 01480227. DOI: 10.1029/2000JA000352.
- Khurana, K.K. et al. (1998). “Induced Magnetic Fields as Evidence for Subsurface Oceans in Europe and Callisto”. In: *Nature* 395, pp. 777–780.

References

- Khurana, Krishan K. (1992). “A generalized hinged-magnetodisc model of Jupiter’s nightside current sheet”. In: *J. of Geophys. Res.* 97 (A5), p. 6269. ISSN: 0148-0227. DOI: 10.1029/92JA00169.
- Khurana, Krishan K. et al. (1993). “Inference of the angular velocity of plasma in the Jovian magnetosphere from the sweepback of magnetic field”. In: *Journal of Geophysical Research: Space Physics* 98 (A1), pp. 67–79. ISSN: 01480227. DOI: 10.1029/92JA01890. URL: <http://doi.wiley.com/10.1029/92JA01890> (visited on 11/15/2018).
- Khurana, Krishan K et al. (2004). “The Configuration of Jupiter’s Magnetosphere”. In: *Jupiter The Planet, Satellites and Magnetosphere*. Ed. by Fran Bagenal et al. Cambridge: Cambridge University Press. Chap. 24, pp. 593–616.
- Khurana, Krishan K. et al. (2005). “Global structure of Jupiter’s magnetospheric current sheet”. In: *J of Geophys. Res.* 110 (A7). ISSN: 0148-0227. DOI: 10.1029/2004JA010757.
- Kita, H. et al. (2019). “Jovian UV Aurora’s Response to the Solar Wind: Hisaki EXCEED and Juno Observations”. In: *Journal of Geophysical Research: Space Physics* 124.12, pp. 10209–10218. DOI: 10.1029/2019JA026997.
- Kivelson, M. G. et al. (2005a). “Dynamical consequences of two modes of centrifugal instability in Jupiter’s outer magnetosphere”. In: *Journal of Geophysical Research* 110 (A12). ISSN: 0148-0227. DOI: 10.1029/2005JA011176. URL: <http://doi.wiley.com/10.1029/2005JA011176>.
- Kivelson, M.G. (2005). “The Current Systems of the Jovian Magnetosphere and Ionosphere and Predictions for Saturn”. In: *Space Science Reviews* 116, pp. 299–318. DOI: 10.1007/s11214-005-1959-x.

References

- Kivelson, M.G. et al. (1992). “The Galileo Magnetic Field Investigation”. In: *Space Science Reviews* 60, pp. 357–383. DOI: 10.1007/BF00216862.
- Kivelson, M.G. et al. (1995). *Introduction to Space Physics*. Cambridge University Press. ISBN: 0-521-45714-9.
- Kivelson, M.G. et al. (1997). “Intermittent short-duration magnetic field anomalies in the Io torus: evidence for plasma interchange?” In: *Geophysical Research Letters* 24.2127. DOI: 10.1029/97GL02202.
- Kivelson, M.G. et al. (1999). “Europa and Callisto: Induced or intrinsic fields in a periodically varying plasma environment”. In: *J. Geophys. Res* 104, pp. 4609–46225. DOI: 10.1029/1998JA900095.
- Kivelson, M.G. et al. (2000). “Galileo Magnetometer Measurements Strengthen the Case for a Subsurface Ocean at Europa”. In: *Science* 289.5483, pp. 1340–1343. DOI: 10.1126/science.289.5483.1340.
- Kivelson, M.G. et al. (2005b). “Dynamical consequences of two modes of centrifugal instability in Jupiter’s outer magnetosphere”. In: *Journal of Geophysical Research* 110.A12209, pp. 1–13. DOI: 10.1029/2005JA011176.
- Kiyani, K.H. et al. (2015). “Dissipation and heating in solar wind turbulence: from the macro to the micro and back again”. In: *Phil. Trans. R. Soc. A*. 373. DOI: 10.1098/rsta.2014.0155.
- Klimas, A. et al. (2010). “Multiscale auroral emission statistics as evidence of turbulent reconnection in Earth’s midtail plasma sheet”. In: *Journal of Geophysical Research* 115.A06202. DOI: 10.1029/2009JA014995.
- Knight, S. (1973). “Parallel electric fields”. In: *Planetary and Space Science* 21.5, pp. 741–750. DOI: 10.1016/0032-0633(73)90093-7.

References

- Kotsiaros, S. et al. (2019). “Birkeland Currents in Jupiter’s Magnetosphere Observed by the Polar-Orbiting Juno Spacecraft”. In: *Nature Astronomy* 3, pp. 904–909. DOI: 10.1038/s41550-019-0819-7.
- Kraichnan, R.H. (1965). “Inertial-range spectrum of hydromagnetic turbulence”. In: *Phys. Fluids*, pp. 1385–1387.
- Krupp, N. et al. (2001). “Global flows of energetic ions in Jupiter’s equatorial plane: First-order approximation”. In: *J. of Geophys. Res.: Space Physics* 106, pp. 26017–26032. ISSN: 01480227. DOI: 10.1029/2000JA900138.
- Krupp, N et al. (2004). “Dynamics of the Jovian Magnetosphere”. In: *Jupiter The Planet, Satellites and Magnetosphere*. Ed. by Fran Bagenal et al. Cambridge: Cambridge University Press. Chap. 25, pp. 617–638.
- Kurth, W.S. et al. (2017). “The Juno Waves Investigation”. In: *Space Science Reviews* 213, pp. 347–392. DOI: 10.1007/s11214-017-0396-y.
- Kuznetsov, V.D. et al. (2016). “The Sun and Heliosphere Explorer - the Interhelio-probe mission”. In: *Geomagnetism and Aeronomy* 56.7, pp. 781–841. DOI: 10.1134/S0016793216070124.
- Lakhina, G.S. et al. (2000). “Broadband plasma waves in the boundary layers”. In: *Journal of Geophysical Research* (105). DOI: 10.1029/2000JA900054.
- Larrodera, C. et al. (2020). “Bimodal distribution of the solar wind at 1 AU”. In: *Astronomy and Astrophysics* 635.A44. DOI: 10.1051/0004-6361/201937307.
- Leamon, R.J. et al. (1999). “Dissipation range dynamics: Kinetic Alfvén waves and the importance of β_e ”. In: *Journal of Geophysical Research* 104.A10, pp. 22331–22344. DOI: 10.1029/1999ja900158.

References

- Lee, L.C. et al. (2020). “Fluid and Kinetic Aspects of Magnetic Reconnection and Some Related Magnetospheric Phenomena”. In: *Reviews of Modern Plasma Physics* 4.9. DOI: 10.1007/s41614-020-00045-7.
- Lhotka, C. et al. (2019). “Kinematic models of the interplanetary magnetic field”. In: *Ann. Geophys.* 37.3, pp. 299–314. DOI: 10.5194/angeo-37-299-2019.
- Li, W. et al. (2017). “Understanding the Origin of Jupiter’s Diffuse Aurora Using Juno’s First Perijove Observations”. In: *Geophysical Research Letters* 44, pp. 10162–10170. DOI: 10.1002/2017GL075545.
- Lorch, C.T.S. et al. (2020). “Local Time Asymmetries in Jupiter’s Magnetodisc Currents”. In: *Journal of Geophysical Research: Space Physics* 125. DOI: 10.1029/2019JA027455.
- Lorch, C.T.S. et al. (2022). “Evidence of Alfvénic Activity in Jupiter’s Mid-To-High Latitude Magnetosphere”. In: *Journal of Geophysical Research: Space Physics* 127 (6). DOI: 10.1029/2021JA029853.
- Louis, C.K. et al. (2019). “Jovian Auroral Radio Sources Detected In Situ by Juno/Waves: Comparisons With Model Auroral Ovals and Simultaneous HST FUV Images”. In: *Geophysical Research Letters* 46.21, pp. 11606–11614. DOI: 10.1029/2019GL084799.
- Luhmann, J.G. (1995). “Ionospheres”. In: *Introduction to Space Physics*. Ed. by M.G. Kivelson et al. Cambridge: Cambridge University Press. Chap. 7, pp. 183–202.
- Luizar, O. et al. (2000). “Experimental study of the formulation of inverted-V structures and their stratification using AUREOL-3 observations”. In: *Ann. Geophysicae* 18, pp. 1399–1411.

References

- Lundin, R. et al. (1978). “Some characteristics of the parallel electric field acceleration of electrons over discrete auroral arcs as observed from two rocket flights”. In: *Symposium on European Rocket Research* ESA SP-135, p. 125.
- Lundquist, S. (1949a). “Experimental Investigations of Magneto-hydrodynamic waves”. In: *Physical Review* 76.12, pp. 1805–1809. DOI: 10.1103/PhysRev.76.1805.
- Lundquist, S (1949b). “Experimental Demonstration of Magneto-hydrodynamic Waves”. In: *Nature* 164.4160, pp. 145–146. DOI: 10.1038/164145a0.
- Lysak, R.L. (2008). “On the dispersion relation for the kinetic Alfvén wave in an inhomogeneous plasma”. In: *Physics of Plasmas* 15.062901. DOI: 10.1063/1.2918742.
- Lysak, R. et al. (1996). “On the kinetic dispersion relation for shear Alfvén waves”. In: *Journal of Geophysical Research* 101.5085. DOI: 10.1029/95JA03712.
- Mangeney, A. et al. (2006). “Cluster observations in the magnetosheath—Part 1: Anisotropies of the wave vector distribution of the turbulence at electron scales.” In: *Ann. Geophys.* 24, pp. 3507–3521. DOI: 10.5194/angeo-24-3507-2006.
- Manners, H. et al. (2019). “First Evidence for Multiple-Harmonic Standing Alfvén Waves in Jupiter’s Equatorial Plasma Sheet”. In: *Geophysical Research Letters* 46.16, pp. 9344–9351. DOI: 10.1029/2019GL083899.
- Manners, H. et al. (2020). “The Global Distribution of Ultralow-Frequency Waves in Jupiter’s Magnetosphere”. In: *Journal of Geophysical Research: Space Physics* 125.10. DOI: 10.1029/2020JA028345.
- Martin, C. J. et al. (2019). “Current Density in Saturn’s Equatorial Current Sheet: Cassini Magnetometer Observations”. In: *Journal of Geophysical Research: Space*

References

- Physics* 124.1, pp. 279–292. ISSN: 21699380. DOI: 10.1029/2018JA025970. URL: <http://doi.wiley.com/10.1029/2018JA025970>.
- Masters, A. (2017). “Model-based assessments of magnetic reconnection and Kelvin-Helmholtz instability at Jupiter’s magnetopause”. In: *Journal of Geophysical Research: Space Physics* 112.11, pp. 11154–11174. DOI: 10.1002/2017JA024736.
- Mauk, B.H. et al. (1999). “Storm-like Dynamics of Jupiter’s Inner and Middle Magnetosphere”. In: *Journal of Geophysical Research* 104, pp. 22759–22778. DOI: 10.1029/1999JA900097.
- Mauk, B.H. et al. (2004). “Energetic Ion Characteristics and Neutral Gas Interactions in Jupiter’s Magnetosphere”. In: *Journal of Geophysical Research* 109.A09S12. DOI: 10.1029/2003JA010270.
- Mauk, B.H. et al. (2017). “Juno observations of energetic charged particles over Jupiter’s polar regions: Analysis of mono- and bi-directional electron beams”. In: *Geophysical Research Letters* 44.10, pp. 4410–4418. DOI: 10.1002/2016GL072286.
- Mauk, B.H. et al. (2018). “Diverse electron and ion acceleration characteristics observed over Jupiter’s main aurora.” In: *Geophysical Research Letters* 45.3, pp. 1277–1285. DOI: 10.1002/2017GL076901.
- Mauk, B.H. et al. (2020). “Energetic Particles and Acceleration Regions Over Jupiter’s Polar Cap and Main Aurora: A Broad Overview”. In: *Journal of Geophysical Research: Space Physics* 125.3. DOI: 10.1029/2019JA027699.
- McChesney, J.M. et al. (1987). “Observation of fast stochastic ion heating by drift waves”. In: *Physical Review Letters*. DOI: 10.1103/PhysRevLett.59.1436.
- McComas, D.J. et al. (2003). “The three-dimensional solar wind around solar maximum”. In: *Geophysical Research Letters* 30.10. DOI: 10.1029/2003GL017136.

References

- McComas, D.J et al. (2008). “Weaker Solar Wind from the Polar coronal Holes and the Whole Sun”. In: *Geophysical Research Letters* 35.18. DOI: 10.1029/2008GL034896.
- McComas, D.J. et al. (2017). “The Jovian Auroral Disrtibutions Experiment (JADE) on the Juno Mission to Jupiter”. In: *Space Science Reviews* 213, pp. 547–643. DOI: 10.1007/s11214-013-9990-9.
- McComb, W.D. (1990). “The physics of fluid turbulence”. In: *Oxford University Press*.
- McFadden, J.P. et al. (1999). “Microstructure of the auroral acceleration region as observed by FAST”. In: *Journal of Geophysical Research* 104, pp. 14453–14480.
- Meyrand, R. et al. (2015). “Weak Magnetohydrodynamic Turbulence and Intermittency”. In: *J. Fluid Mech.* 770.R1. DOI: 10.1017/jfm.2015.1441.
- Morel, X. et al. (2017). “Electrostatic Analyzer with a 3-D Instantaneous Field of View for Fast Measurements of Plasma Distribution Functions in Space.” In: *Journal of Geophysical Research: Space Physics* 112.3, pp. 3397–3410. DOI: 10.1002/2016JA023596.
- Mottez, F. (2015). “Plasma acceleration by the interaction of parallel propagating Alfvén waves”. In: *J. Plasma Physics* 81.325810104. DOI: 10.1017/S0022377814000580.
- Ng, C.S. et al. (2018). “Radial Transport and plasma heating in Jupiter’s magnetodisc”. In: *Journal of Geophysical Research: Space Physics* 123, pp. 6611–6620. DOI: 10.1029/2018JA025345.
- Nichols, J. D. et al. (2004). “Magnetosphere-ionosphere coupling currents in Jupiter’s middle magnetosphere: effect of precipitation-induced enhancement of the ionospheric Pedersen conductivity”. In: *Annales Geophysicae* 22.5, pp. 1799–1827.

References

- ISSN: 1432-0576. DOI: 10.5194/angeo-22-1799-2004. URL: <http://www.ann-geophys.net/22/1799/2004/>.
- Nichols, J.D. et al. (2007). “Response of Jupiter’s UV auroras to interplanetary conditions as observed by the Hubble Space Telescope during the Cassini flyby campaign”. In: *Journal of Geophysical Research* 112(A11) (A02203). DOI: 10.1029/2006JA012005.
- Nichols, J.D. et al. (2009). “Variation of different components of Jupiter’s auroral emission”. In: *Journal of Geophysical Research* 114 (A06219). DOI: 10.1029/2009JA014051.
- Nichols, J.D. et al. (2017). “Response of Jupiter’s auroras to conditions in the interplanetary medium as measured by the Hubble Space Telescope and Juno”. In: *Geophysical Research Letters* 44.15, pp. 7643–7652. DOI: 10.1002/2017GL073029.
- Nishida, A. (1976). “Outward diffusion of energetic particles from the Jovian radiation belt”. In: *Journal of Geophysical Research* 81, pp. 1771–1773. DOI: 10.1029/JA081i010p01771.
- Nykyri, K. et al. (2006). “Origin of the turbulent spectra in the high-latitude cusp: Cluster spacecraft observations”. In: *Ann. Geophys.* 24, pp. 1–20. DOI: 10.5194/angeo-24-1057-2006.
- Ogino, T. et al. (1998). “n, A global magnetohydrodynamic simulation of the Jovian magnetosphere”. In: *Journal of Geophysical Research* 103 (255). DOI: 10.1029/97JA02247.
- Onofri, M. et al. (2004). “Three-dimensional Simulations of Magnetic Reconnection in Slab Geometry”. In: *Physics of Plasmas* 11, pp. 4837–4846. DOI: 10.1063/1.1791638.

References

- Opgenoorth, H. et al. (2005). “Cluster spacecraft reach greatest separation at fifth anniversary”. In: *ESA*. URL: https://www.esa.int/Science_Exploration/Space_Science/Cluster/Cluster_spacecraft_reach_greatest_separation_at_fifth_anniversary%7D.
- Owens, M. (2020). “Solar Wind Structure”. In: *Oxford Research Encyclopedia of Physics*. DOI: 10.1093/acrefore/9780190871994.013.19.
- Owens, M.J. et al. (2005). “An event-based approach to validating solar wind speed predictions: High-speed enhancements in the Wang-Sheeley-Argé model”. In: *Journal of Geophysical Research* 110.A12105. DOI: 10.1029/2005JA011343.
- Papen, M. von et al. (2014). “Turbulent magnetic field fluctuations in Saturn’s plasma sheet.” In: *Journal of Geophysical Research: Space Physics* 119, pp. 2797–2818. DOI: 10.1002/2013JA019542.
- Papen, M. von et al. (2016). “Longitudinal and local time asymmetries of magnetospheric turbulence in Saturn’s plasma sheet”. In: *Journal of Geophysical Research: Space Physics* 121, pp. 4119–4134. DOI: 10.1002/2016JA022427.
- Paranicas, C.P. et al. (1991). “Pressure Anisotropy and Radial Stress Balance in the Jovian Neutral Sheet”. In: *Journal of Geophysical Research* 96.21135. DOI: 10.1029/91JA01647.
- Parker, E.N. (1958). “Dynamics of the Interplanetary Gas and Magnetic Fields”. In: *Astrophysical Journal* 128, pp. 664–676. DOI: 10.1086/146579.
- Parks, G.K. (2015). “Magnetosphere”. In: *Encyclopedia of Atmospheric Sciences*. Ed. by G.R. North et al. Elsevier Ltd., pp. 309–315.

References

- Perri, S. et al. (2012). “Detection of Small-Scale Structures in the Dissipation Regime of Solar-Wind Turbulence”. In: *Phys. Rev. Lett.* 109.191101. DOI: 10.1103/PhysRevLett.109.191101.
- Phipps, P. et al. (2020). “Centrifugal Equator in Jupiter’s Plasma Sheet”. In: *Journal of Geophysical Research: Space Science* 126. DOI: 10.1029/2020JA028713.
- Pine, Z.B. et al. (2020). “Solar Wind Turbulence from 1 to 45 AU. I. Evidence for Dissipation of Magnetic Fluctuations using Voyager and ACE Observations”. In: *The Astrophysical Journal* 900.2. DOI: 10.3847/1538-4357/abab10.
- Podesta, J.J. et al. (2008). “Correlation length of large-scale solar wind velocity fluctuations measured tangent to the Earth’s orbit: First results from Stereo”. In: *Journal of Geophysical Research* 113.A09104. DOI: 10.1029/2007JA012865.
- Pontius, D.H. et al. (1982). “Departure from corotation of the Io plasma torus: Local plasma production”. In: *Geophysical Research Letters* 9 (12). DOI: 10.1029/GL009i012p01321.
- Prêle, D. (2017). “Advanced Electronic Systems”. In: p39. DOI: ce1-00843641v6.
- Primdahl, F. (1979). “The Fluxgate Magnetometer”. In: *J Phys. E: Sci. Instrum* 12.1979, pp. 241–253. DOI: 10.1088/0022-3735/12/4/001.
- Provan, G. et al. (2009). “Polarization and phase of planetary-period magnetic field oscillations on high-latitude field lines in Saturn’s magnetosphere”. In: *Journal of Geophysical Research: Space Physics* 114.A02225. DOI: 10.1029/2008JA013782.
- Radioti, A. et al. (2008). “Discontinuity in Jupiter’s main auroral oval”. In: *J. of Geophys. Res.: Space Physics* 113. ISSN: 01480227. DOI: 10.1029/2007JA012610.
- Ray, L. C. et al. (2010). “Magnetosphere-ionosphere coupling at Jupiter: Effect of field-aligned potentials on angular momentum transport”. In: *Journal of Geophysical*

References

- Research: Space Physics* 115 (A9). ISSN: 01480227. DOI: 10.1029/2010JA015423.
URL: <http://doi.wiley.com/10.1029/2010JA015423>.
- Ray, L. C. et al. (2012). “Magnetosphere-ionosphere coupling at Jupiter: A parameter space study”. In: *Journal of Geophysical Research: Space Physics* 117 (A1). ISSN: 01480227. DOI: 10.1029/2011JA016899. URL: <http://doi.wiley.com/10.1029/2011JA016899>.
- Ray, L. C. et al. (2014). “Local time variations in Jupiter’s magnetosphere-ionosphere coupling system”. In: *J. of Geophys. Res.: Space Physics* 119.6, pp. 4740–4751. ISSN: 21699380. DOI: 10.1002/2014JA019941.
- Ray, L.C. et al. (2009). “Current-Voltage relation of a centrifugally confined plasma”. In: *Journal of Geophysical Research: Space Physics* 114.A4. DOI: 10.1029/2008JA013969.
- Richardson, J.D. (1987). “Ion distributions in the dayside magnetosheaths of Jupiter and Saturn”. In: *J. Geophys. Res.* 92.A6. DOI: 10.1029/JA092iA06p06133.
- Russell, C.T. et al. (2007). “Ion-cyclotron Wave Generation by Planetary Ion Pickup”. In: *Journal of Atmospheric and Solar-Terrestrial Physics* 69.14, pp. 1723–1738. DOI: 10.1016/j.jastp.2007.02.014.
- Saur, J. (2004). “Turbulent heating of Jupiter’s middle magnetosphere”. In: *The Astrophysical Journal* 602, pp. 137–140. DOI: 10.1086/382588.
- (2021). “Turbulence in the Magnetospheres of the Outer Planets”. In: *Frontiers in Astronomy and Space Sciences* 8.624602. DOI: 10.3389/fspas.2021.624602.
- Saur, J. et al. (2002). “Evidence for weak MHD turbulence in the middle magnetosphere of Jupiter”. In: *Astronomy & Astrophysics* 386, pp. 699–708. DOI: 10.1051/0004-6361:20020305.

- Saur, J. et al. (2003). “An acceleration mechanism for the generation of the main auroral oval on Jupiter”. In: *Geophysical Research Letters* 30.5. DOI: 10.1029/2002GL015761.
- Saur, J. et al. (2018). “Wave-Particle Interactions of Alfvén Waves in Jupiter’s Magnetosphere: Auroral and Magnetospheric Particle Acceleration”. In: *Journal of Geophysical Research: Space Physics* 123. DOI: 10.1029/2018JA025948.
- Schekochihin, A.A. (2022). “MHD Turbulence: A Biased Review”. In: *J. Plasma Phys.* DOI: 2010.00699v3.
- Schneider, N.M. et al. (2007). “Io’s neutral clouds, plasma torus and magnetospheric interactions”. In: *Io after Galileo: A New View of Jupiter’s Volcanic moon*. Ed. by R.M.C. Lopes et al. Chichester, UK: Praxis Publishing Ltd. Chap. 11, pp. 265–286.
- Schubert, G. et al. (2004). “Interior Composition, Structure and Dynamics of the Galilean Satellites”. In: *Jupiter The Planet, Satellites and Magnetosphere*. Ed. by Fran Bagenal et al. Cambridge: Cambridge University Press. Chap. 13, pp. 281–306.
- Schulz, M. (1979). “Jupiter’s Radiation Belts”. In: *Space Sci Rev* 23, pp. 277–318. DOI: 10.1007/BF00173813.
- Sckopke, N. et al. (1983). “Evolution of Ion Distributions Across the Nearly Perpendicular Bow Shock: Specularly and Non-specularly reflected-gyrating ions”. In: *Journal of Geophysical Research: Space Physics* 88.A8, pp. 6121–6136. DOI: 10.1029/JA088iA08p06121.
- Seki, K. et al. (2015). “A Review of General Physical and Chemical Processes Related to Plasma Sources and Losses for Solar System Magnetospheres”. In: *Space Science Reviews* 192, pp. 27–89. DOI: 10.1007/s11214-015-0170-y.

References

- Smith, E. J. et al. (1974). “The planetary magnetic field and magnetosphere of Jupiter: Pioneer 10”. In: *Journal of Geophysical Research* 79.25, pp. 3501–3513. ISSN: 01480227. DOI: 10.1029/JA079i025p03501. URL: <http://doi.wiley.com/10.1029/JA079i025p03501>.
- Sorriso-Valvo, L. et al. (1999). “Intermittency in the Solar Wind Turbulence Through Probability Distribution Functions of Fluctuations”. In: *Geophysical Research Letters* 26. DOI: 10.1029/1999GL900270.
- Sorriso-Valvo, L. et al. (2001). “Intermittency in Plasma Turbulence”. In: *Planetary and Space Science* 49, pp. 1193–1200. DOI: 10.1016/S0032-0633(01)00060-5.
- Southwood, D. J. et al. (2001). “A new perspective concerning the influence of the solar wind on the Jovian magnetosphere”. In: *Journal of Geophysical Research: Space Physics* 106 (A4). ISSN: 01480227. DOI: 10.1029/2000JA000236. URL: <http://doi.wiley.com/10.1029/2000JA000236>.
- Southwood, D.J. et al. (1987). “Magnetospheric Interchange Instability”. In: *J. Geophys. Res.* 92, pp. 109–116. DOI: 10.1029/JA092iA01p00109.
- Spitzer, L. (2006). “Physics of Fully Ionized Gases”. In: Dover Publications Inc.
- Stallard, Tom S. et al. (2018). “Identification of Jupiter’s magnetic equator through H₃⁺ ionospheric emission”. In: *Nature Astronomy* 2.10, pp. 773–777. ISSN: 2397-3366. DOI: 10.1038/s41550-018-0523-z.
- Stone, R.G. et al. (1992). “Ulysses Radio and Plasma Wave Observations in the Jupiter Environment”. In: *Science* 257.5076, pp. 1524–1531. DOI: 10.1126/science.257.5076.1524.
- Su, Y.-J. et al. (2003). “Io-related Jovian auroral arcs: Modeling parallel electric fields”. In: *Journal of Geophysical Research* 108.A2. DOI: 10.1029/2002JA009247.

References

- Suess, S.T. et al. (2003). “Solar Winds”. In: *Encyclopedia of Atmospheric Sciences*. Ed. by J.R. Holton. London: Academic Press, pp. 2078–2085.
- Sundkvist, D. et al. (2005). “In situ multi-satellite detection of coherent vortices as a manifestation of Alfvénic turbulence”. In: *Nature* 11.436, pp. 825–828. DOI: 10.1038/nature03931.
- Tao, C. et al. (2005a). “Magnetic Field Variations in the Jovian Magnetotail Induced by Solar Wind Dynamic Pressure Enhancements”. In: *Journal of Geophysical Research* 110.A11208. DOI: 10.1029/2004JA010959.
- (2005b). “Magnetic field variations in the Jovian magnetotail induced by solar wind dynamic pressure enhancements”. In: *Journal of Geophysical Research* 110.A11208. DOI: 10.1029/2004JA010959.
- Tao, C. et al. (2015). “Properties of Jupiter’s magnetospheric turbulence observed by the Galileo spacecraft”. In: *Journal of Geophysical Research: Space Physics* 120.4, pp. 2477–2493. DOI: 10.1002/2014JA020749.
- Tao, C. et al. (2016). “Variations of Jupiter’s aurora observed by Hisaki/EXCEED: 2. Estimations of auroral parameters and magnetospheric dynamics”. In: *Journal of Geophysical Research: Space Physics* 121, pp. 4055–4071. DOI: 10.1002/2015JA021272.
- Taylor, G.I. (1938). “The Spectrum of Turbulence”. In: *Proc. Roy. Soc. London* A132, pp. 476–490. DOI: 10.1098/rspa.1938.0032.
- Thomas, N. et al. (2004). “The Io Neutral Clouds and Plasma Torus”. In: *Jupiter The Planet, Satellites and Magnetosphere*. Ed. by F. Bagenal et al. Cambridge: Cambridge University Press. Chap. 23, pp. 261–292.

References

- Thomsen, M.F. et al. (1988). “Comment on ‘Ion distributions in the dayside magnetosheaths of Jupiter and Saturn’ by J.D. Richardson”. In: *J. Geophys. Res.* 93.A4. DOI: 10.1029/JA093iA04p02761.
- Tsurutani, B.T. et al. (1981). “Upstream waves and particles: An overview of ISEE results”. In: *Journal of Geophysical Research* 86.A6, pp. 4317–4324. DOI: 10.1029/ja086ia06p04317.
- Tu, C.-Y. et al. (1995). “MHD Structures, Waves and Turbulence in the Solar Wind: Observations and Theories”. In: *Space Science Reviews* 73, pp. 1–210. DOI: 10.1007/BF00748891.
- Valentini, F. et al. (2016). “Differential kinetic dynamics and heating of ions in the turbulent solar wind”. In: *New J. Phys.* 18.125001. DOI: 10.1088/1367-2630/18/12/125001.
- Vasyliunas, V.M (1983). “Plasma Distribution and Flow”. In: *Physics of the Jovian Magnetosphere*. Ed. by A.J Dessler. Cambridge: Cambridge University Press. Chap. 11, pp. 395–453.
- Veltri, P. (1999). “MHD turbulence in the solar wind: self-similarity, intermittency and coherent structures”. In: *Plasma Physics and Controlled Fusion* 41.A787. DOI: 10.1088/0741-3335/41/3A/071.
- Verscharen, D. et al. (2019). “The multi-scale nature of the solar wind”. In: *Living Reviews in Solar Physics* 16.5. DOI: 10.1007/s41116-019-0021-0.
- Wahlund, J.-E. (2003). “Observations of auroral broadband emissions by Cluster”. In: *Geophysical Research Letters* 30.1535. DOI: 10.1029/2002GL016335.

References

- Waite, J.H.Jr. et al. (1983). “Electron precipitation and related aeronomy of the Jovian thermosphere and ionosphere”. In: *Journal of Geophysical Research* (88), pp. 6143–6163. DOI: 10.1029/JA088iA08p06143.
- Walker, Raymond J et al. (2003). “A simulation study of currents in the Jovian magnetosphere”. In: *Planetary and Space Science* 51.4, pp. 295–307. ISSN: 00320633. DOI: 10.1016/S0032-0633(03)00018-7.
- Walker, R.J. et al. (2001). “Magnetohydrodynamic simulations of the effects of the solar wind on the Jovian Magnetosphere”. In: *Planetary and Space Science* 49, pp. 237–245. DOI: 10.1016/S0032-0633(00)00145-8.
- Walker, R.J. et al. (2005). “The locations and shapes of Jupiter’s bow shock and magnetopause”. In: *AIP Conference Proceedings* 781.
- Walt, M. (1994). *Introduction to Geomagnetically Trapped Radiation*. Cambridge: Cambridge University Press.
- Wan, M. et al. (2015). “Intermittent Dissipation and Heating in 3D Kinetic Plasma Turbulence”. In: *Phys. Rev. Lett.* 114.175002. DOI: 10.1103/PhysRevLett.114.175002.
- Watt, C.E.J. et al. (2005). “Self-consistent electron acceleration due to inertial Alfvén wave pulses”. In: *Journal of Geophysical Research: Space Physics* 110.A10S07. DOI: 10.1029/2004JA010877.
- (2006). “Inertial Alfvén waves and acceleration of electrons in nonuniform magnetic fields”. In: *Geophysical Research Letters* 33.L02106. DOI: 10.1029/2005GL024779.

References

- Wilson, R.J. et al. (2000). “Evidence Provided by Galileo of Ultra Low Frequency Waves in Jupiter’s Middle Magnetosphere”. In: *Geophysical Research Letters* 27.6, pp. 835–838. DOI: 10.1029/1999GL010750.
- Woodfield, E.E. et al. (2014). “The origin of Jupiter’s outer radiation belt”. In: *Journal of Geophysical Research: Space Physics* (119), pp. 3490–3502. DOI: 10.1002/2014JA019891.
- Yang, Y. (2019). “Energy Cascade in Compressible MHD Turbulence. In: Energy Transfer and Dissipation in Plasma Turbulence”. In: *Springer Theses*. DOI: 10.1007/978-981-13-8149-2_4.
- Yelle, R.V. et al. (2004). “Jupiter’s Thermosphere and Ionosphere”. In: *Jupiter The Planet, Satellites and Magnetosphere*. Ed. by Fran Bagenal et al. Cambridge: Cambridge University Press. Chap. 9, pp. 185–218.
- Yermolaev, Y.I. et al. (2005). “Statistical Studies of Geomagnetic Storm Dependencies on Solar and Interplanetary Events: A Review”. In: *Planet Space Sci* 53, pp. 189–196. DOI: 10.1016/j.pss.2004.09.044.
- Yordanova, E. et al. (2008). “Magnetosheath plasma turbulence and its spatiotemporal evolution as observed by the cluster spacecraft”. In: *Phys. Rev. Lett.* 100.205003. DOI: 10.1103/PhysRevLett.100.205003.
- Zhang, X.Y. et al. (2010). “ULF waves excited by negative/positive solar wind dynamic pressure impulses at geosynchronous orbit”. In: *Journal of Geophysical Research: Space Physics* 115.A10. DOI: 10.1029/2009JA015016.
- Zhao, M.X. et al. (2012). “Nonlinear Dispersive Scale Alfvén Waves in Magnetosphere-Ionosphere coupling: Physical processes and Simulation Results”. In: *Chinese Science Bulletin* 57.12, pp. 1384–1392. DOI: 10.1007/s11434-011-4905-1.

References

Zimbardo, G. et al. (2010). "Magnetic Turbulence in the Geospace Environment". In:
Space Science Reviews 156. DOI: 10.1007/s11214-010-9692-5.